Photo-induced Structural Dynamics of Molybdenum Disulfide

A Dissertation

SUBMITTED TO THE FACULTY OF

UNIVERSITY OF MINNESOTA

BY

Alyssa Jennifer McKenna

IN PARTIAL FULFILLMENT OF THE REQUIREMENTS

FOR THE DEGREE OF

DOCTOR OF PHILOSOPHY

David J. Flannigan, Advisor

May 2017

Acknowledgements

First and foremost, I would like to thank my advisor, David Flannigan, for providing guidance and support during my five years at the University of Minnesota. It was an incredible opportunity to work with a novel, state-of-the-art, unique instrument. Maybe one day other scientists will understand it is not just a fast camera.

I secondly must thank the past and present members of the Flannigan Research Group – Dan C., Dayne, Karl (Boo), Jess, Tom, Kyle, Spencer, Ryan, Pranav, David V., Jeff E., Elisah, Daniel D., and Yichao – for helpful discussions and lively, diverting conversations in the several offices and labs we have inhabited. In particular, thank you to Daniel Cremons, Dr. David Valley, and Dayne Plemmons for helpful discussions about acoustic phonons and modeling and to Dr. Jeff Eliason for helping with the analysis and editing of my first, first-author paper. Thank you, Ryan Gnasbasik, for writing the space-time-intensity analysis scripts that I modified to analyze the data in Chapters 3 and 4. Thank you, Dayne Plemmons, for writing the MATLAB scripts to analyze the plasma lensing experiments.

I must also thank my fellow graduate student and postdoctoral cohort for discussions and support. Specifically, thank you to Dr. Jeff Peterson for a six-hour discussion on finite element modeling, and thank you to Tom Fielitz for helping me think out loud, discuss my project endlessly, and provide advice on the best ways to write code in MATLAB. Thank you, Dan, Boo, Spencer, and Tom, for reading different chapters

and providing feedback quickly.

Finally, I would like to thank my family – my mother (Ping), my father (Brian), my brother (Brent), and my partner in life and in scientific pursuit (Tom). Thank you for believing in me when I did not believe in myself.

Parts of this work were carried out in the Characterization Facility, University of Minnesota, which receives support from the National Science Foundation (NSF) through the MRSEC program under Award Number DMR-1420013. My project is supported by the Donors of the American Chemical Society Petroleum Research Fund under Award Number 53116-DNI7 and by the Arnold and Mabel Beckman Foundation in the form of a Young Investigator Award. This material is based upon work supported by the National Science Foundation Graduate Research Fellowship Program under Grant No. DGE-1348264.

Dedication

To my family. I promise not to do this again.

Abstract

In this dissertation, the photo-induced structural dynamics of molybdenum disulfide (MoS_2) have been imaged over seven orders of magnitude in time – picoseconds (ps, 10^{-12} seconds) to tens of microseconds (10^{-5} seconds) – and in real space with up to 2 nanometer (nm, 10^{-9} meter) spatial resolution. Molybdenum disulfide, a heavily studied layered material due to its tunable electronic bandgap, is of interest for a variety of device applications and due to the tunability of many of its properties with strain (*e.g.*, thermal properties and electronic bandgap). Ultrafast electron microscopy (UEM) combines the nanometer spatial resolution of transmission electron microscopy with the femtosecond temporal resolution of ultrafast pump-probe spectroscopy and was used to directly image the photo-excited dynamics in a freestanding, micrometer-size, multilayer MoS_2 flake viewed along the [001] direction.

Following photo-excitation with a 515-nm, 700-femtosecond laser pulse, individual wave trains were observed to emerge from nanoscale morphological features, particularly the vacuum-specimen interface. The strain waves propagated in-plane along or near contrast features at approximately the speed of sound (7 nm per ps) and at frequencies in the tens of gigahertz (GHz), which identified them as Lamb modes (quasi-shear plate waves). Using the dispersion relation for 50-nm thick MoS_2 plate and the cut-off frequencies of an anisotropic plate, the waves were identified as second-order anti-symmetric or symmetric Lamb modes, which are differentiated by their symmetry with respect to the mid-plane of the specimen. The change in contrast was attributed to the tilting of planes into or out of the diffraction condition for anti-symmetric waves or a change in in-plane inter-planar spacing for the longitudinal wave coupled to the symmetric waves. The strain waves were then imaged on the nanosecond (ns, 10^{-9} seconds) timescales and found to undergo phonon-phonon scattering. This scattering resulted in the damping of the high-GHz oscillations and the emergence of incoherent oscillations with frequencies on the order of single GHz. On microsecond timescales, three megahertz (MHz, 10^6 hertz), whole-flake mechanical resonances were observed. These mechanical modes were found to have microsecond lifetimes and were simulated using finite element modeling. This work provides insight into the photoexcitation of high-velocity elastic strain waves and the subsequent mode-coupling processes and whole-flake oscillations.

Work to understand the factors needed for high resolution ultrafast electron imaging is also presented. High-resolution ultrafast imaging first requires that the specimen drift is low in the requisite acquisition time at high magnifications. Thus, average specimen drift rates and the required acquisition times at these magnifications were measured. To produce the high temporal resolution in UEM, electron packets rather than a continuous beam of electrons are produced *via* the photoelectric effect upon irradiation with laser pulses. Next, the stability in the number of electrons in the packets was probed. The lattice fringes of tungsten disulfide nanoparticles (6 Å spacing) were successfully imaged.

Table of Contents

List of Tables

List of Figures

1 | INTRODUCTION

The work in this dissertation is motivated by a need to understand the propagation, dissipation, and trapping of heat in realizable, nanoscale materials and the coupling of that thermal energy to the structure. The effects of improved understanding of thermal processes can be readily observed on large spatial and slow temporal scales in daily life. For instance, new materials and designs of rotor blades and vanes in modern aircraft engines allow them to sustain significant thermal stresses without catastrophic failure.[1-3] The release of thermal stresses in the earth's crust, accumulated over years due to temperature fluctuations,[4] is correlated to earthquake launch and magnitude,[5] which scientists hope to use to predict earthquake occurrence.

As shown in Figure 1.1, this dissertation is concerned with the other end of the spectrum – small spatial and fast temporal scales. In this phase space, our current understanding of the thermal physics has allowed electronics to shrink in size and cycle time. For instance, transistors with lateral dimensions as small as seven nanometers (nm)[6] and with cycle times as fast as two picoseconds (ps) can be produced.[7] Microelectromechanical (MEM) and nanoelectromechanical (NEM) devices, named for the spatial dimensions of their components, are used as mass and chemical sensors.[8] On such spatiotemporal scales, the dissipation of heat, especially in electronics,[9] and the effects of thermal fluctuations on material properties, as in sensors,[10-13] are major

challenges to further miniaturization and enhanced performance. Moreover, confinement, defects, and morphology, not usually accounted for in macroscopic, ensemble-averaging models,[14] significantly affect or even determine material behavior.[15-29] Consequently, characterization techniques that offer access to the relevant phase space, outlined in red in Figure 1.1, must be employed to study realizable materials.

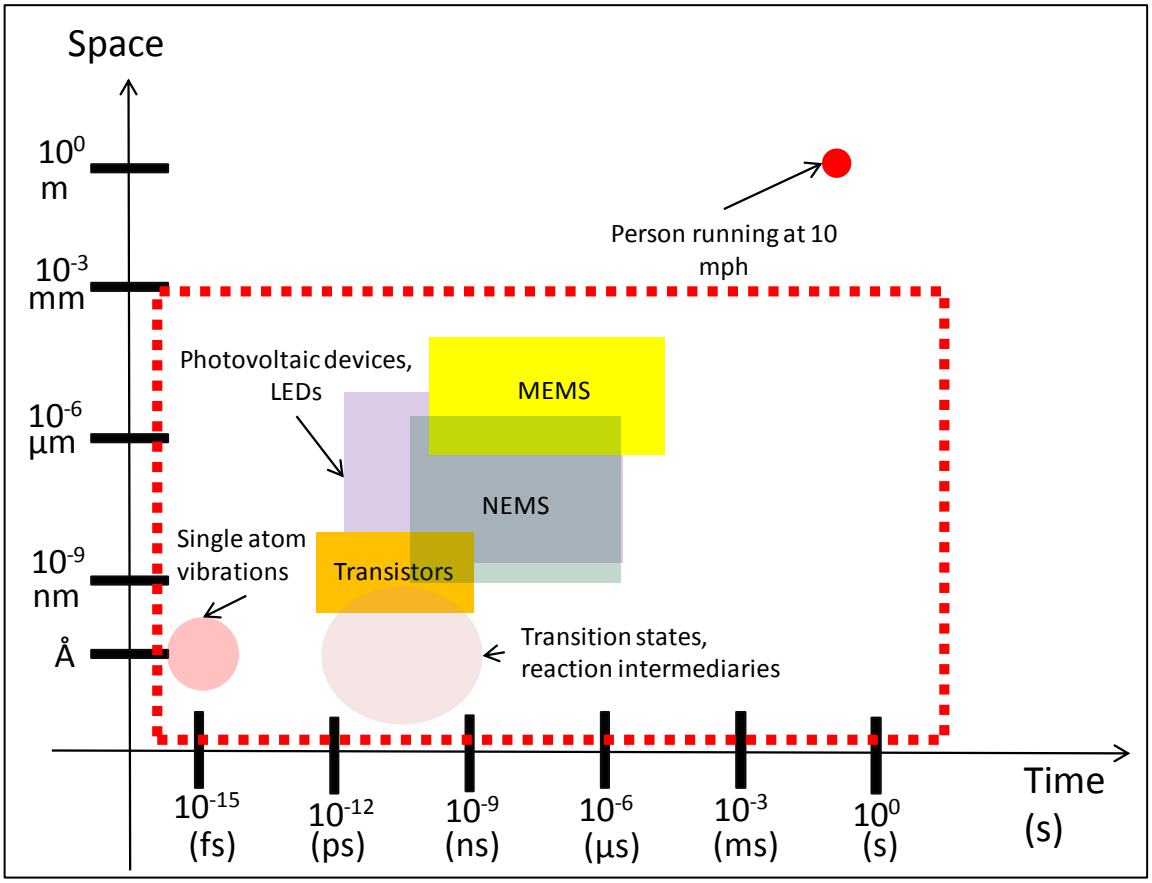

Figure 1.1 | **Spatiotemporal phase space of modern applications and fundamental research interests.** Modern technologies such as photovoltaic devices, light-emitting diodes (LEDs), and transistors have critical physics on spatial scales smaller than millimeters and temporal scales faster than microseconds. Fundamental physics such as single atom vibrations, transition states, and reaction intermediaries occur on angstrom spatial scales and picosecond or femtosecond time scales. The spatiotemporal phase space in realizable materials is outlined in red.

In this chapter, I will provide the background to understand the material system studied, discuss ultrafast carrier and structural dynamics studies, and outline the instrument utilized. First, I will introduce transition metal dichalcogenides (TMDs) and detail the properties and potential applications of a heavily studied TMD, molybdenum disulfide (MoS_2). I will then review the ultrafast photo-carrier dynamics and the resulting structural dynamics in MoS_2 and other important two-dimensional materials. Next, the fundamental operating principles of ultrafast electron microscopy (UEM) – used in this dissertation to access the seven orders of magnitude in temporal space (individual ps to tens of microseconds (μs)) and four orders of magnitude in spatial phase space (tens of nanometers (nm) to individual micrometers (μm)) – will be outlined. Finally, I will briefly summarize the findings of this dissertation.

1.1 | Transition Metal Dichalcogenides

Since the first exfoliation of graphene,[30] two-dimensional materials are studied as model systems to elucidate physics in low-dimensional systems and to construct atomically thin devices. After graphene, the family of compounds known as the layered TMDs is the most heavily studied due to the thickness-dependence of many material properties and numerous potential applications, including electronics, sensors, photovoltaics, and catalysis.[8,31-36] In this section, I will introduce layered TMDs. I will then focus on MoS_2, which was chosen for this study due to its device applications and to the large mass of literature that make it a model system.

1.1.1 | Layered TMDs

Transition metal dichalcogenides are a family of compounds named for their chemical formula TX_2, where T is a transitional metal from groups four through ten and X is a chalcogen (one of the elements in group 17 of the periodic table; usually sulfur, selenium, or tellurium). Most of the TMDs where T is from groups four through seven form layered crystals in which each plane of transition metal atoms is covalently bonded to two sandwiching planes of chalcogen atoms, most commonly with trigonal prismatic or octahedral coordination. Between planes of chalcogen atoms, only weak van der Waals forces exist. These layered crystals are thus strong laterally[37-43] but can be easily separated into discrete, atomically-thin, chemically stable layers.[31-36,44-46] They were best-known as lubricants until their unusual electrical properties were discovered.[47-49] Because MoS_2 is a layered TMD, I will restrict my discussion to the layered TMDs.

Two families of approaches can be used to fabricate few- to mono-layer TMD specimens, which have been reviewed extensively.[31-36,44-46] The first set, the top-down approaches, starts with a bulk sample and removes layers. The most famous such method is micromechanical exfoliation, in which a piece of adhesive tape is used to peel away layers, which are then transferred to the desired substrate. Although simple, low-cost, and swift, this method is low-throughput and offers little control over the thickness and number of flakes.[16-17,30,37,50-55] Another top-down approach is liquid exfoliation, which includes sonication of the TMD in the appropriate solvent[56-59] and ion (*e.g.*, alkali metal ions) intercalation.[60] This approach is often accompanied by a phase change or a

physical, periodic deformation, which can drastically change the electrical properties.[31-32,35] The second set (the bottom-up approach) is chemical vapor deposition (CVD) and is an active area of investigation to produce consistent growth of large, pristine flakes.[61-66] This set has been thoroughly reviewed elsewhere.[31-36,44,67-75]

The chemical composition and polymorph (*i.e.*, specific crystal structure and layer stacking sequence) determine many of the properties of these layered TMDs. The polymorphs of layered TMDs are notated *nK-TX*$_2$, where *n* is a number between 1 and 3 indicating the number of TX_2 units (*i.e.*, number of layers) in each unit cell and *K* is a letter denoting the symmetry within the unit cell. The most common polymorphs are 2H, 1T, and 3R, where H denotes hexagonal, T trigonal, and R rhombohedral symmetry in the unit cell. The specific stacking sequence and geometry depends on the compound. The chemical composition of the TMDs determines the filling of the d-bands, and the positions of the non-bonding d-bands between the bonding and anti-bonding bands depend on the polymorph and associated coordination of the transition metal. These two characteristics lead to a wide range of electronic character from semimetallic or metallic to semiconducting and of magnetic character from diamagnetic to paramagnetic.[32,76] Combined with the strong electron-phonon coupling, certain combinations of polymorph and composition results in exotic electronic behavior, such as charge density waves (CDWs) and superconductivity in metallic d^1 (*e.g.*, Ta and Nb) TMDs.[77-82]

As specimens are thinned, interlayer coupling, quantum confinement, and symmetry change, which result in layer-dependent properties. When a semiconducting

MoX_2 and WX_2, where X denotes a chalcogen, is thinned to a single layer, quantum confinement results in an indirect-direct electronic bandgap transition,[17,83] leading to the emergence of photoluminescence.[16,84-86] This transition is also observed upon the application of strain.[87-91] For few-layer molybdenum diselenide ($MoSe_2$), the indirect and direct bandgap are so close in energy that heating produces an indirect-to-direct bandgap transition.[92] Recently, a bandgap transition with thickness was observed in rhenium disulfide (ReS_2). In contrast to MoS_2, bilayer ReS_2 displays the direct bandgap, and monolayer and bulk samples retain the indirect bandgap.[93]

The layer-dependent properties make TMDs attractive for a variety of applications.[31-36,67-74] Because semiconducting TMDs retain their electronic bandgap and optical properties even at the monolayer limit, they are of interest for photovoltaics,[34,67,94-99] transistors, logic circuits,[53,62,67,100-113] photodectectors,[36,114-116] light-emitting devices,[36,67,72,117] and lasers.[36] Another example is the emergence of piezoelectricity with the breaking of inversion symmetry in 2H-polymorphs (*i.e.*, odd number of layers), which may be utilized to create nano-power generators[118-121] and to tune photoluminescence in monolayers.[122] Thin layers are also more efficient catalysts in hydrogen evolution reactions, since they contain more edge sites that are catalytically active.[18,25-26,123-124] For TMDs where the transition metal is from group six, strong spin-orbit coupling leads to control over the valley degree of freedom in noncentrosymmetric samples (*e.g.*, odd number of layers). In such samples, the electrons can be excited to specific valleys depending on the helicity of the incident circularly polarized light, which

has made TMDs of interest for valleytronic (analogous to spintronics) devices.[125-136]

1.1.2 | Molybdenum Disulfide (MoS_2)

Molybdenum disulfide, known as molybdenite when found in nature,[137] is a heavily studied layered TMD. The useful properties stem from its structure. The three common polymorphs of MoS_2 are 2H, 3R, and 1T and are shown in Figure 1.2.[76] The 2H-MoS_2, shown on the left in Figure 1.2, has trigonal prismatic coordination of the transition metal atoms in each layer. Its space group is $P6_3/mmc$ or D_{6h}, depending on the notation convention. The two layers in each unit cell are offset so that the chalcogen atoms in the layers above and below are directly above the transition metal atoms in the surrounding layers. The 3R-MoS_2 polymorph, which also has trigonal prismatic symmetry, has three layers in each unit cell, as seen in the center structure in Figure 1.2. The layers are offset such that the chalcogen atoms in the second layer are directly above the transition metal atoms in the layer below, but the transition metal atoms in the second layer are not above the chalcogen atoms in the first. The chalcogen atoms in the third layer fall above the metal atoms in the second, and the transition metal atoms in the third fall above the chalcogen atoms in the first. In contrast, the 1T-MoS_2 polymorph has octahedral coordination where one plane of chalcogen atoms is rotated sixty degrees with respect to the other, and each layer is stacked directly on top of the other, as shown on the right in Figure 1.2. The most common polymorph, 2H-MoS_2, was used in this study, and the 2H notation will henceforth be omitted. The symmetry notation will be included only if denoting a different polymorph.

Due to this layered structure, the mechanical properties of this material are transversely isotropic.[43] For monolayers, the in-plane Young's modulus has been measured to be 0.22[138] and 0.27 terapascal (TPa).[37] For samples ranging from 5 to 25 layers, the in-plane Young's modulus extracted from atomic force microscopy measurements ranges from 0.21 to 0.42 TPa and has an average value of 0.33 ± 0.07 TPa, similar to that of graphene. The variation was attributed to changes in defect density and adhesion to the substrate.[39] The purely elastic deformation of the samples extended to tens of nanometers for both few- and monolayer samples.[39,138] MoS_2 undergoes brittle

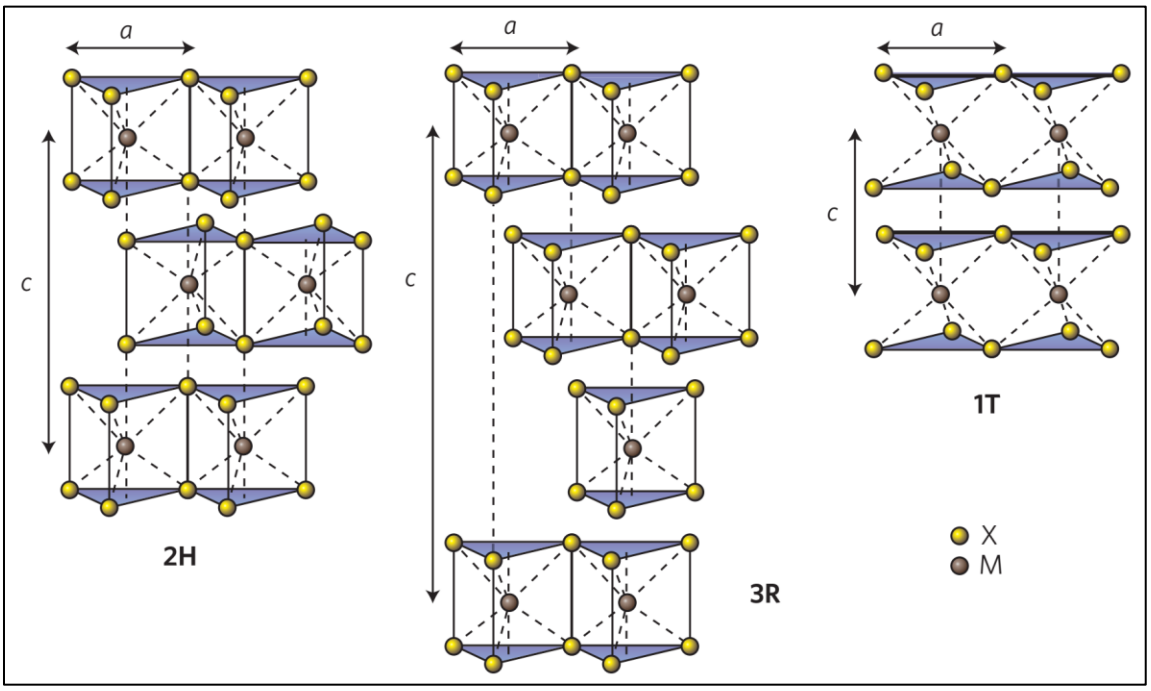

Figure 1.2 | **Common polymorphs of MoS_2.** The three most common polymorphs of MoS_2 – 2H (H indicates hexagonal symmetry), 3R (R indicates rhombohedral symmetry), and 1T (T indicates trigonal symmetry) – are shown above, where the number denotes the number of layers in each unit cell. The M here is Mo, and X is the chalcogen. Adapted by permission from Macmillan Publishers Ltd: *Nature Nanotechnology*, Ref [31]), © 2012.

fracture, with a breaking strength of 16-30 gigapascal (GPa) or breaking strain of ~0.06-0.11 for several layers.[37,138] The elastic bending modulus has been calculated to range between 6.62 and 13.42 eV.[38,42,139-140] These mechanical properties make MoS_2 appealing for high-frequency resonators and mass sensors.[141-143]

The electronic band structures of MoS_2 of varying thicknesses are shown in Figure 1.3, calculated using density functional theory. In the bulk MoS_2 band structure, the indirect bandgap occurs between the Γ point in the valence band and about halfway between the Γ and Λ (also called Q) points in the conduction band.[144-145] The direct optical

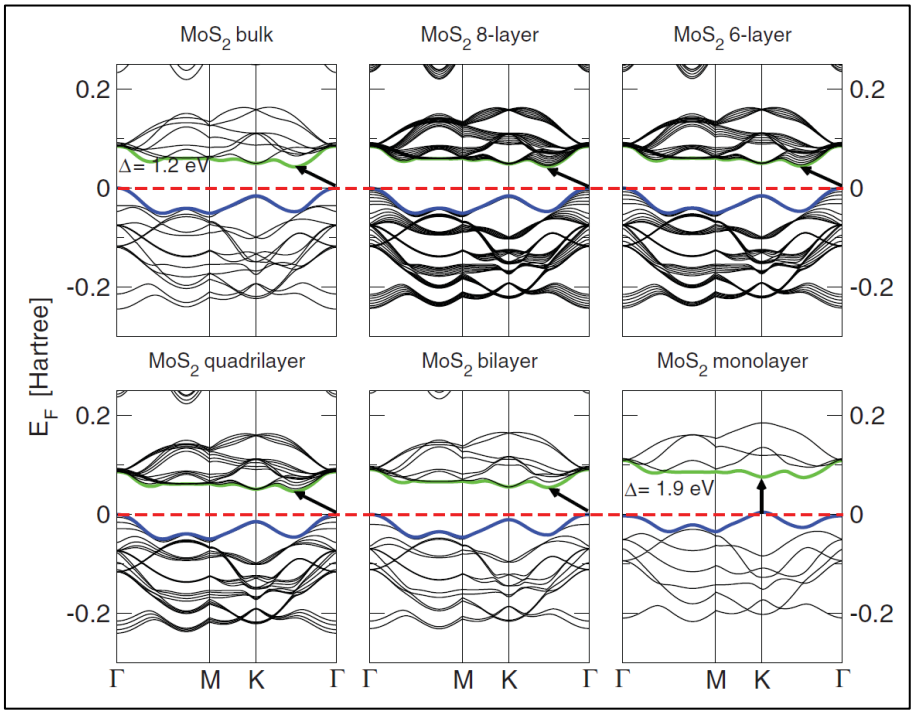

Figure 1.3 | **Electronic bandstructures for bulk to monolayer MoS_2.** The electronic bandstructures were calculated for bulk, 8-layer, 6-layer, 4-layer, bilayer, and monolayer samples. The conduction band minimum between the K and Γ points slowly rises as the number of layers decreases, where the minimum at the K point is relatively unaffected. The result is a transition from a 1.2 eV indirect bandgap in bulk to a 1.9 eV direct bandgap in the monolayer. Reprinted figure with permission from Kuc, A.; Zibouche, N.; Heine, T. *Phys. Rev. B* **2011**, *83*, 245213. © 2011 by the American Physical Society.

bandgap occurs at the K points, which are at the edges of the hexagonal Brillion zone. The bottom of the conduction band and top of the valence band are made up of hybridized molybdenum *d*-orbitals and sulfur *p*-orbitals. Calculations indicate that the majority of the *d*-orbitals that form the states at the conduction band minimum are strongly localized on the Mo atoms, which are enclosed by planes of S atoms. Thus, these *d*-orbitals are minimally affected by changes in interlayer coupling with thickness changes. The *d*-orbitals that form the valence and conduction band states at the Γ point and between Γ and Λ points, respectively, responsible for the indirect bandgap are linearly combined with antibonding p_z orbitals on the S atoms. Thus, as the number of layers decreases, the interlayer coupling causes the conduction band minimum to rise significantly. In the limit of a monolayer, the conduction band minimum between the Γ and Λ points rises higher than the minimum at the K point, resulting in the bandgap transition from indirect (1.23 eV) to direct (1.79 eV).[16,144] The bandgap can also be tuned using strain.[87-88,146-147] The presence and tunability of the electronic bandgap even in atomically-thin layers make MoS_2 appealing for a variety of nano-electronics, including transistors and light-emitting diodes.[31,36,114-115]

Three excitonic features – traditionally named A, B, and C excitons in order of increasing energy – emerge if spin-orbit coupling and interlayer interaction are included in band structure calculations. As shown in Figure 1.4, strong spin-orbit coupling for monolayer MoS_2 and interlayer interaction for multi-layer and bulk MoS_2 split the valence band maxima at the K point into two states – K_{v1} and K_{v2} – regardless of the

thickness. The A and B excitons correspond to transitions from the K_{v1} and K_{v2} states, respectively, to the conduction band. Their ground state transition energies are 1.85 eV (670 nm) and 1.98 eV (627 nm).[16,148-151] The C excitons correspond to transitions in the region between the Γ and Λ points.[145] The Rydberg states of the B exciton were observed in a monolayer MoS_2 specimen, and a binding energy of 0.44 eV was deduced for the B exciton.[152] A binding energy of 0.54 eV has been calculated for the A exciton.[153]

Due to the combination of the decreased dielectric screening in two-dimensional crystals and heavy band masses in monolayer MoS_2, trions (charged excitons), which comprise either two electrons and a hole or two holes and an electron,[154] are formed with a binding energy of ~20 meV. In this case, the trions

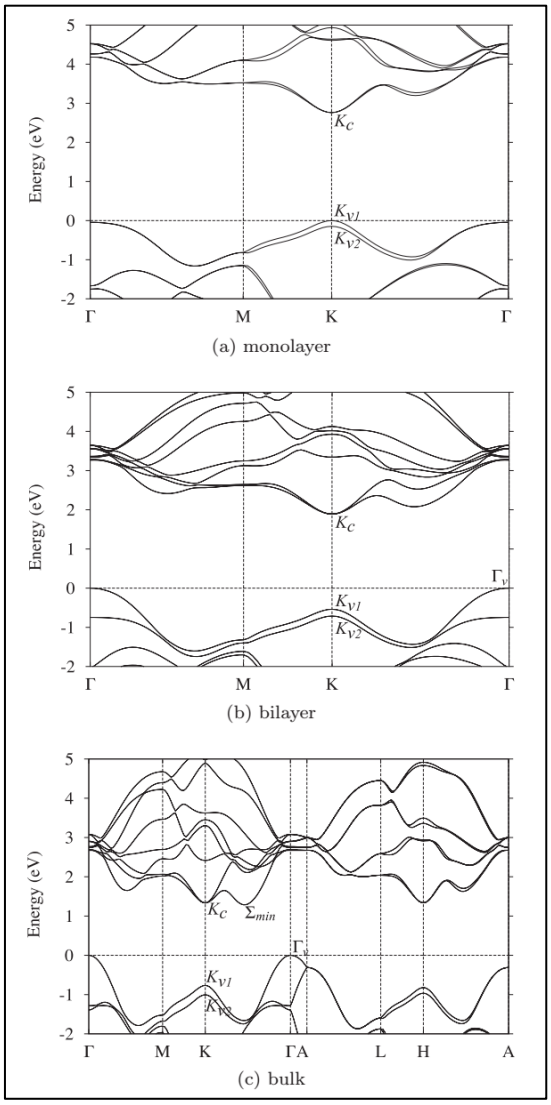

Figure 1.4 | **Electronic bandstructure of monolayer, bilayer, and bulk MoS_2 with spin-orbit coupling and interlayer interactions.** Spin-orbit coupling and interlayer interactions result in large splitting in the valence band at the K-point for (a) monolayer, (b) bilayer, and (c) bulk MoS_2. Reprinted figure with permission from Cheiwchanchamnangij, T.; Lambrecht, W. R. L. *Phys. Rev. B* **2012**, *85*, 205302. © 2012 by the American Physical Society.

comprise two electrons and one hole. In contrast to excitons for which only one state is allowed (*e.g.*, hole spin up and electron spin down in the K-valley for A excitons), multiple trion states are allowed. The lowest energy state is two electrons spin down and one hole spin up, and the lifetime of the hole was found to be much longer than the trion lifetime.[153,155] Trions can repel each other and decrease the photoconductivity transiently.[156]

In monolayer MoS_2, strong spin-orbit coupling and breaking of inversion symmetry splits the valence band valley at the K points by ~160 meV and creates two valleys, the K and K' valleys, with different spin character. Spin-degeneracy at the K-point requires both time reversal and inversion symmetry, which is lacking in the noncentrosymmetric monolayer, for the 1H monolayer is now in the D_{3h} space group. Consequently, the two bands are of different spin character, and left circularly polarized light excites carriers into the K valleys whereas right circularly polarized light excites carriers into the K' valleys.[131,133-134,157] Trions can also be selectively excited into the K- or K'-valleys with different light helicities.[153,155] This circular dichroism has spurred applications in valleytronics.[131-136,143]

Even in very thin layers, MoS_2 and all the other TMDs with transition metals from group six exhibit unexpectedly strong optical absorption[158] due to a feature of the electronic bandstructure known as band nesting. Band nesting refers to regions in the band structure in which the conduction and valence bands are parallel in energy[159] and occurs approximately halfway between the Γ and Λ points for monolayer MoS_2, as seen

in Figure 1.5.[83,158-159] Band nesting corresponds to van Hove singularities in the density of states, which results in strongly enhanced optical conductivity.[83] The photocarriers excited to regions with band nesting propagate at the same speed but in opposite directions, resulting in swift carrier separation.[83,159-160] The long lifetimes of C excitons relative to that of A and B excitons have been attributed to band nesting.[145] These optical features have made MoS_2 appealing for solar cells and photodetectors.[94-96,99,114,116,161-163]

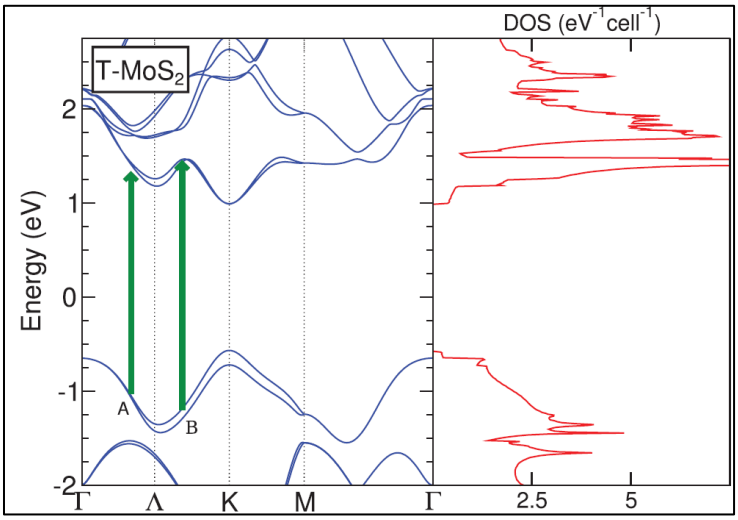

Figure 1.5 | **Band nesting in MoS_2.** Electronic bandstructure showing band nesting between the two green arrows on the left, and the density of states on the right showing van Hove singularities. Adapted with permission from Ref [83] © American Physical Society.

As the number of layers decreases, the changing interaction between layers shifts the phononic band structure, shown in Figure 1.6. The corresponding phonon modes are shown in Figure 1.7. The E^1_{2g} and A_{1g} modes are Raman-active. Compared to bulk positions, each mode frequency shifts toward the other by 3 cm^{-1} for a monolayer specimen. This shift decreases with increasing layer number until the peaks have returned to their bulk positions (382 cm^{-1} and 408 cm^{-1}, respectively) at six layers.[51] This significant shift in position has become the standard method to determine the number of layers in a sample.[164-165]

Due to the dependence on the phononic bandstructure, thermal conductivity has been found to also vary with layers. For single crystal MoS_2, the thermal conductivity is strongly anisotropic and has been reported to be 85-100 W m^{-1} K^{-1} for the in-plane direction and 2 W m^{-1} K^{-1} for the perpendicular direction for bulk single crystals,[167] 34.5 for single crystal, and 44-55 W m^{-1} K^{-1} for few-layer MoS_2.[168-170] For polycrystalline films, the conductivity has been measured to be much lower (1.5[171] and 0.73 W m^{-1} K^{-1} for in-plane[172] and 0.25 W m^{-1} K^{-1} for cross-plane directions[171]) due to the reduced boundary conductance across grains, calculated to be 87.5 ± 1.5 megawatts m^{-2} K^{-1}.[172]

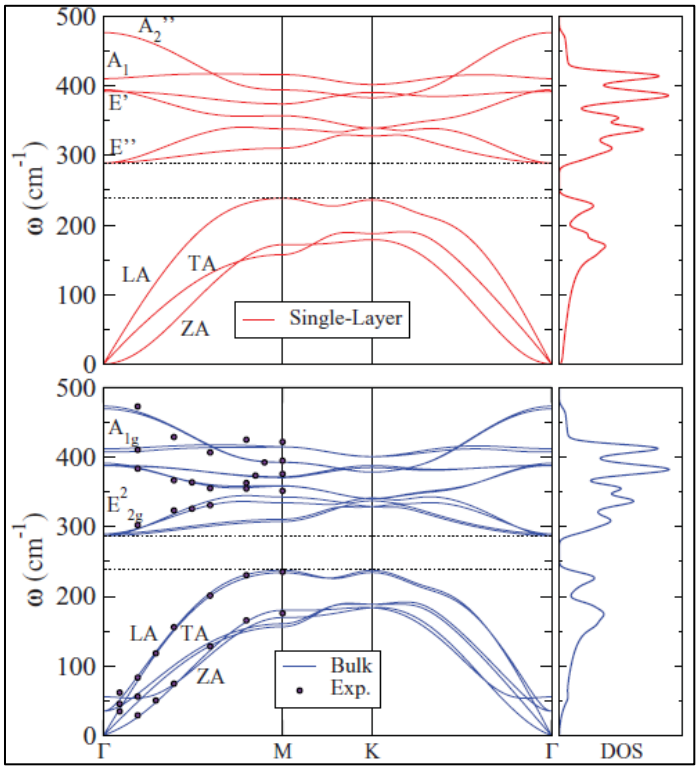

Figure 1.6 | **Phononic bandstructure of monolayer and bulk MoS_2.** Phononic bandstructure and density of states for (upper panels) monolayer and (lower panels) bulk MoS_2. The experimental data is from N. Wakabayashi, N.; Smith, H. G.; and Nicklow, R. M. *Phys. Rev. B* **1975**, *12*, 659-663. Adapted with permission from Ref [166] © American Physical Society.

In samples with odd numbers of layers, lack of the inversion symmetry leads to piezoelectricity,[118-119] which can be harnessed for energy conversion and power generators.[120-121,173] The piezoelectricity has been harnessed to manipulate exciton

relaxation pathways. A surface acoustic wave was applied to a mono-layer specimen, and the electric field due to the mechanical deformation forced excitons to dissociate. The electron and hole were then trapped in different extrema of the conduction and valence bands, preventing direct recombination and quenching the photoluminescence. In addition, the electric fields possessed enough energy to force trion dissociation into excitons and further increase quenching. The authors postulated that water molecules present at the edges reduced the electric field and resulted in the observed relatively strong photoluminescence. At higher acoustic wave powers, the samples were calculated to heat significantly and thus reduce the bandgap, increasing quenching through a different mechanism.[122] This work suggests that the relaxation pathways depend on the local heating and specimen condition.

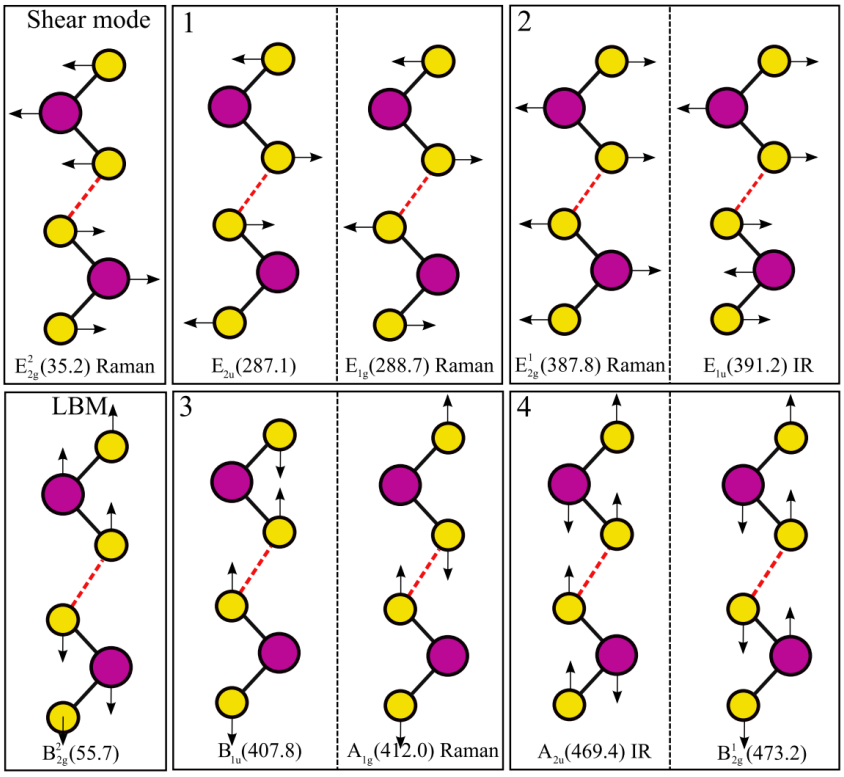

Figure 1.7 | **Optical phonon modes of multi-layer MoS_2.** Frequencies are in cm^{-1}. Raman/IR indicates whether the mode is Raman- or IR-active. Reprinted with permission from Ref [174].

Although

monolayers have gained the most attention, research has indicated that few-layer MoS_2 may be better suited for some applications. For instance, the signal from field effect transistors (FETs) with few-layer MoS_2 used as gas sensors was found to be more stable and sensitive than monolayer-MoS_2 devices.[175] In addition, multi-layer MoS_2 has higher optical absorption, higher carrier mobility,[176] higher density of states at the conduction band minimum,[177-178] and longer photo-carrier lifetimes[179-180] than monolayer MoS_2, which makes multi-layer MoS_2 better suited for photo-devices.[181] These experiments suggest that study of few- to many layer MoS_2 properties is valuable not only for fundamental understanding but also for devices.

The electrical and optical properties of MoS_2 have been found to depend on strain as well as number of layers.[87-88] The strain dependence has been measured by shifts in micro-Raman and photoluminescence peak positions[182] and calculated using atomistic tight binding[183] and an analytical bond length model.[184] Up to a strain of 0.2 in the plane, the optical bandgap of monolayer MoS_2 decreases approximately linearly by ~50 meV per percent strain under in-plane uniaxial strain[88,184-186] and by 99 meV per percent strain under biaxial strain[187] but increases under out-of-plane uniaxial tensile strain.[188] Above that strain, the bandgap energy stabilizes at 0.45 eV. Monolayer MoS_2 has been calculated to undergo a semiconductor-to-metal transition under ~10% tensile strain or ~15% compressive biaxial strain.[189-191] Bulk MoS_2 was calculated to undergo the transition at 10% compressive strain.[191] This transition is due to tensile strain increasing the overlap of the d_{xy} and $d_{x^2+y^2}$ orbitals with the chalcogen p states at the K point while

decreasing the overlap of the d_{z^2} and chalcogen *p* states at the Γ point. As for thickness, the conduction band minimum is not affected by strain.[192] Atomistic tight binding simulations suggested that the dieletric function can red-shift under uniaxial tensile strain in monolayer MoS_2.[183] In-plane strain also enhances interface coupling.[193] Strain thus constitutes a useful knob to tune the properties of MoS_2. All of the studies above, however, examined steady-state or stationary effects of strain over a whole sample, which raises several questions. Could these properties be tuned dynamically or over short time scales? What would those time scales be, and how can we harness this knob in real-time? Moreover, could the properties be tuned locally? What are the appropriate spatial scales?

1.2 | Ultrafast Photo-carrier Dynamics in MoS_2 and Other Two-dimensional Materials

Perhaps the most expedient way to add strain to a system is through heat, and the most expedient way to heat a nanoscale material is through ultrafast laser irradiation. Pulsed lasers now offer access down to attoseconds (10^{-18}),[194-195] and tuning the repetition rate to allow full relaxation of the system back to the same initial state enables consistent, repeated excitation in every cycle.[196] Ultrafast (<1 ps) pulse durations enable access to time scales that challenge our understanding of heat and its dynamics, for the specific dynamics of photo-carriers (*e.g.*, excitation mechanisms and relaxation pathways) become significant on these spatial and temporal scales.[14,197] Photo-carrier dynamics are generally determined by two properties: electronic character and quantum confinement. The most heavily studied two-dimensional material is graphene, a single plane of carbon

atoms in a hexagonal lattice.[30,198-199] Its bulk counterpart is graphite. In contrast to MoS_2, graphene is metallic. With the application of an external electric field, bilayer graphite (also known as bilayer graphene) can develop a small tunable bandgap and finite electron mass.[200-202] Thus, the photo-carrier response exhibits different characteristics from the semiconducting MoS2. Although also a layered TMD, tungsten ditelluride (WTe_2) exhibits magnetoresistance and thus different photo-carrier dynamics in certain temperature ranges. This section will outline the photo-carrier dynamics in paradigmatic graphene, graphite, and WTe_2 and review the literature on photo-carrier dynamics in MoS_2.

Photo-carrier dynamics are generally characterized with pump-probe methods. In all cases, an optical – usually a laser pulse with a duration of tens to hundreds of femtoseconds (fs) – excitation pulse is directed onto the sample. The techniques can then be grouped depending on the probing signal collected at different time delays between the arrivals of the excitation laser pulse and the probing pulse. For the first group, the sample generates a signal – photoluminescence or second harmonic generation – in which changes in energy, peak shape, or peak area indicate dynamics. Another group directs a second probing laser pulse of the same or different wavelength onto the sample and measures the transient change in transmission, reflection (*e.g.*, time-resolved transient reflectivity), or energy (*e.g.*, ultrafast spectroscopy). A final set of techniques uses electron packets (*e.g.*, ultrafast electron diffraction or UED) or X-ray pulses to probe the specimen dynamics and measures changes in the intensities, peak positions, or peak

widths in the resulting diffraction patterns (DPs).

1.2.1 | Ultrafast Photo-carrier Dynamics in Two-Dimensional Materials: Graphene, Graphite, WTe_2

For graphene and graphite, photo-excited electrons are promoted from the π band to the π^* band. For graphene, the electrons appear or are assumed to thermalize quickly, as would be expected of a metal.[203-206] For graphite, some experiments have supported that electrons thermalize in tens of femtoseconds,[200,207-208] whereas others have suggested that the electrons in graphite immediately couple to strongly coupled optical phonons (SCOPs) – the E_{2g} mode at the Γ point and the A_1' mode at the K point[209-210] – in the first 200 fs or that hot SCOPs and electrons are generated by the photo-excitation pulse instead. The hot electron and SCOP populations then relax without clear thermalization.[210-211]

Assuming electron thermalization, hot electrons diffuse and cool on a 100 fs timescale.[208,212] In graphene and to a lesser extent in graphite,[206] the dominant scattering mechanisms are scattering from charged impurities,[213] from ripples,[214-215] and from midgap states created by point defects.[207,216-218] If defects are minimized, intrinsic scattering from optical and acoustic phonons – those intrinsic to graphene and the substrate optical modes if the graphene is supported[203,206,219-221] – and supercollisions – disorder-assisted two-phonon emission that enhances relaxation rates[204,207,216,222-223] – dominate.[203,207,212,216,219-220,223-224]

The scattering by phonons is grouped into two regimes depending on carrier

density. Unlike conventional metals, graphene has a small Fermi surface, which restricts the acoustic phonons in momentum space that can couple to electrons. Thus, acoustic phonon scattering dominates at low electron densities (10^{11} – 10^{13} cm^{-2} per layer), whereas optical phonon (which have large energies in graphene), particularly SCOPs, emission, usually within 500 fs of excitation,[225] and supercollisions dominate above those densities.[203,206-207,212,216,220,224] Using a two-temperature model – in which extent of electronic and phononic excitation is quantified with electron and phonon temperatures – this restriction can be expressed by a threshold electronic temperature, known as the Bloch-Grüneisen temperature. Below the Bloch-Grüneisen temperature, the relaxation is dominated by electron-acoustic phonon coupling, and above that temperature, electron-optical phonon coupling and/or supercollisions dominate.[223] This temperature can be tuned with charged impurity, defect, and disorder densities. In particular, the temperature will decrease for lower carrier density and higher disorder.[226] Supercollisions have been found to be the dominant relaxation pathway when the time to cool graphene decreases as the carrier temperature increases,[207,222] ranging from ~200 ps below 50 K and ~10 ps at 300 K,[207] and the cooling times are much faster than achieved by phonon scattering.[222]

For graphite, the carrier cooling is much faster than in graphene. For instance, the carrier cooling is two to three times faster in bilayer than monolayer graphene due to an increased sensitivity to the carrier density. Like in graphene, the carrier energy loss rate in bilayer graphite depends on carrier density. In contrast to monolayer graphene, the electron-phonon coupling time also depends on the carrier density. Supercollisions have

not been observed in bilayer graphene.[200] At higher electron temperatures[206] and longer timescales,[208] the hot phonon effect – in which a high density of hot phonons suppresses further phonon emission – is found to be substantial in bilayer graphite.[206] For 20- to 30-nm thick graphite, the intraband carrier-carrier scattering occurs in ~30 fs, and the intraband carrier-phonon scattering occurs in ~100 fs.[208]

Tungsten ditelluride (WTe_2) has similar dynamics except at low temperatures, where the influence of its giant, non-saturating magnetoresistance appears to have significant influence on the observed properties. Electron-electron thermalization and electron-phonon thermalization occur within a picosecond and are relatively independent of excitation fluence. Phonon-assisted electron-hole recombination, intervalley electron-phonon scattering followed by recombination, occurs in the next 5-15 ps. The ultimate cooling to the substrate is much longer than the experimental range (300 ps) and was not studied further. During relaxation, two coherent lattice modes are observed with frequencies of 0.25 and 2.4 terahertz (THz), which correspond to the A_1 optical phonons. Between temperatures of 300 and 50 K, the recombination time gradually increases because the phonon population decreases and thereby slows the recombination. Between temperatures of ~50 and 5 K, however, the recombination time suddenly increases, which is attributed to the electronic structure change characteristic of magnetoresistance. Specifically, the electron-hole pockets in the Fermi surface that are believed to produce the magnetoresistance have been calculated to expand at low temperatures, thereby increasing the density of states and changing the interband e-ph scattering coupling

strength.[227]

1.2.2 | Ultrafast Photo-carrier Dynamics in MoS_2 and Other Semiconducting TMDs

Due to its many applications in electronics, the initial, photo-induced electronic carrier dynamics of MoS_2 and other semiconducting TMDs is an active area of study, particularly in monolayers. By far the most researched carrier dynamics belong to MoS_2, and the trends often extend to other semiconducting TMDs, which are isoelectric with MoS_2. Thus, MoS_2 photo-carrier dynamics will be detailed in this section, and the parallels between WS_2 and MoS_2 briefly illustrated.

Because MoS_2 is a semiconductor, electrons undergo direct optical excitation into the conduction band, leaving holes behind in the valence band.[228-229] Injection of these charge carriers can then suppress further optical absorption.[228,230-232] These carriers then undergo intraband relaxation or thermalization, which involves both intra- and inter-valley scattering, and interband relaxation or carrier cooling, which is accomplished by indirect or direct recombination, depending on the position of the carrier in the Brillion zone. At higher excitation fluences (corresponding to a carrier density of 10^{13} cm^{-2} in the monolayer), MoS_2 undergoes a Mott transition and behaves metallically, at least in the initial dynamics.[52,132] These high carrier concentrations correspond to high electron temperatures, such as 16,000 K for a carrier concentration of ~10^{22} m^{-3} and a fluence of 10 milliJoule (mJ) per cm^2. Such high transient electron temperatures do not lead to structural modification, unlike much lower temperatures achieved with steady-state

heating.[233] In WS_2, the high optical energies have also resulted in a Mott transition, and the photo-generated dense electron-hole plasma screens the Coulomb interaction, which reduces the exciton binding energy to zero, decreases quasi-particle energy so that the bandgap shifts in energy to below the initial exciton energy (*i.e.*, bandgap renormalization), and shifts the quasi-Fermi levels into the bands (*i.e.*, population inversion).[234] Since WS_2 are isoelectric with MoS_2, similar trends can be expected. At low optical excitation or longer timescales, the relaxation pathways for MoS_2 are described below.

Upon optical excitation, the observed time and spatial scales vary widely in the literature, but the photo-induced response can be split into two categories due to the layer-dependence of the electronic band structure – bulk and thin (few- to monolayer). For bulk crystals (~100 nm thick), the relaxation pathways can be listed in order of increasing timescales as intravalley relaxation, intervalley relaxation, and indirect recombination. One study found that hot electrons relaxed through both carrier-carrier and carrier-phonon scattering. In the temperature range studied (*i.e.*, below the Debye temperature of 570 K), the dominant mechanism was found to be electron-electron scattering, which resulted in hot carrier lifetimes of below 65 fs depending on the excess carrier energy.[235] Another study attributed a biexponential rise (1.8 ± 0.6 ps and 20 ± 2 ps) in the transmission of the probe pulses to carrier-carrier and carrier-phonon intravalley scattering, respectively. The intervalley scattering was fit with a single exponential decay (~2.6 ns), and the indirect recombination time scale was longer than

that probed by the experiments (~4 ns).[231] Other studies have reported intervalley scattering occurs in <1 ps and that the ultimate carrier lifetime is on the order of hundreds of picoseconds.[229] Such disparities could be due in part to the varying or unreported number of layers and defect densities in bulk samples.

Photocarriers in mono- and few-layer MoS_2 also undergo intraband relaxation but much more quickly (<500 fs) than bulk samples.[231] For monolayer and bilayer MoS_2, the electron-hole pairs excited between A and B exciton energies thermalize and relax to the K-point. Due to band-nesting, excitation above ~2 eV for monolayers and ~2.4 eV for bilayers, which corresponds to the C exciton energy, results in rapid dissociation and intraband scattering to the D* (close to Λ) valley for electrons and Γ hill for holes for the majority of carriers.[145,159] The time scales and mechanisms for intraband scattering vary widely in the literature. Two recent studies on five-layer MoS_2 with 10 fs laser pulses found that hot electrons thermalize in less than 20 fs. At all temperatures, carrier-carrier scattering is significant.[236-237] At low temperatures (<200 K),[52,178] carrier-charged impurity scattering is more significant than carrier-phonon scattering. At higher temperatures, however, carrier-phonon scattering becomes more important than carrier-charged impurity scattering. Intravalley relaxation was found to be mediated by acoustic phonons rather than optical phonons due to the suppression of the latter by the hot phonon effect. Intervalley scattering is mediated by carrier-phonon scattering, in which two phonons are involved. Holes relaxing from the K-valley involve two acoustic phonons, whereas electrons relaxing from the K-valley emit two longitudinal optical

phonons.[236-237] In another study, the fast intraband relaxation in monolayer and few-layer MoS_2 has been attributed to a non-phonon mechanism – defect scattering – because Auger-type electron-hole scattering relies on substantial disparity between the electron and hole effective masses,[231] which are very similar in MoS_2.[147] Other studies have found that exciton-exciton repulsion and scattering also contribute to the intraband relaxation, although these samples may not have been the 2H-polymorph.[232]

Studies have suggested a wide range of hot carrier cooling mechanisms and timescales. For the monolayer, the majority of electrons and holes are expected to relax *via* nonradiative recombination (single to tens of ps) and intervalley scattering where both electron and hole relax to the K point (where they then radiatively recombine) rather than indirect radiative recombination from the Λ/Γ state (hundreds of picoseconds). For the bilayer, the latter case is now more likely.[159] This theory is supported by the much lower optical phonon energy in MoS_2 than in graphene, and coupling to optical phonons is much more efficient, reducing the influence of coupling to substrate phonon modes. At low temperatures below the optical phonon energy (below 50-75 K), the hot carrier cooling is dominated by emission of acoustic phonons; at higher temperatures, optical phonon emission dominates. Like graphene, the carrier dynamics can also be described by a Bloch-Grüneiesen temperature, above which phonon emission is limited. Below this temperature, the coupling is two orders of magnitude larger than for graphene. The Bloch-Grüneiesen temperature is lower in MoS_2 than graphene or bilayer graphene, and optical phonons are susceptible to the hot phonon effect, which decreases the cooling

rate.[238] One study reported that carrier-optical phonon coupling times were 640 and 650 fs for the A and B exciton, respectively,[236] whereas another claimed that the electron-phonon coupling time was on the order of tens of picoseconds.[233] Yet another study reported three distinct decay times for carrier cooling. The fast decay on the order of single picoseconds was attributed to enhanced trapping of excitons by surface trap states. The intermediate time on the order of tens of picoseconds was attributed to interband carrier-phonon relaxation (*i.e.*, indirect recombination). The slow decay on the order of hundreds of picoseconds is attributed to direct recombination at K or K' valleys.[231] For high exciton populations in monolayers, the exciton-exciton annihilation was found to limit the lifetimes. The scattering rate was found to vary quadratically with population of excitons. Radiative decay was calculated to be on the order of ten nanoseconds and thus considered irrelevant.[228,230-232]

The long carrier lifetimes in both bulk and few-layer MoS_2 allow the carriers time to diffuse. Inter-layer carrier diffusion is expected to be low due to the different bonding environment between layers. Carrier diffusion within the layers has been modeled with the ambipolar diffusion equation and maintains the excitation pulse profile (*i.e.*, Gaussian function). The diffusion coefficient is calculated to be 4.2 ± 0.4 cm^2/s. For hot carriers, the diffusion coefficient was deduced to be much higher (18 cm^2/s).[229] For bi- and tri-layer specimens, the diffusion coefficient was measured to be 20 ± 10 cm^2/s, and the diffusion length was estimated to be 450 nm for a carrier lifetime of 100 ps.[131]

Tungsten disulfide (WS_2) shows similar dynamics at low carrier densities. For

relatively low excitation fluences, the carrier density stays below the Mott threshold so that the dynamics are generally those of excitons. Within hundreds of femtoseconds, A and B excitons (at the K/K' points) are excited and thermalize, and their lifetimes are on the order of 1 to 15 ps, depending on the excitation fluence. The dominant relaxation pathways are expected to be nonradiative recombination *via* Auger exciton-exciton annihilation and defect scattering, with the emittance of phonons and heating of the lattice. The cooling of the lattice was found to be determined by heat transfer to the supporting substrate, taking ~250 ps.[239] At high carrier densities ($\geq 10^{14}$ cm^{-2} per layer), optical excitation results in a Mott transition in mono- and bilayer WS_2 on picosecond timescales, as in MoS_2. The onset of the Mott transition was within the instrument resolution (hundreds of femtoseconds), and the population inversion was found to decay in ~1 ps through radiative and non-radiative channels. After this decay, the optical response follows the same trends as described above.[234]

1.3 | Structural Response in MoS_2 and Other Two-dimensional Materials

The structural response immediately following the photocarrier response – from electron-phonon coupling through mechanical oscillations – affects the carrier relaxation pathways and is separately of interest for sensor applications. Moreover, phonons are, by definition, local strain waves, and strain has been shown to tune the material properties in MoS_2, as discussed previously. In contrast to other two-dimensional materials like graphene, the ultrafast structural response of thin MoS_2 is a nascent area of study.

Experimentally, the structural response in a material is measured using UED or ultrafast electron crystallography in both transmission and reflection geometries,[210,240-245] ultrafast electron microscopy (UEM) which is described in more detail in Section 1.4,[246-247] ultrafast X-ray diffraction, time-resolved spectroscopy,[225,248-249] angle-resolved photoelectron spectroscopy,[250] transient reflectivitiy,[251] and time-resolved transient reflectivity.[249] Briefly, UEM operates using the same principles as UED but allows all the imaging capabilities of a TEM rather than just diffraction information.[192,245-253] The structural response has also been calculated using density functional theory and density-functional perturbation theory.[209] In this section, I will briefly review the research on the structural response of paradigmatic two-dimensional materials including graphite, graphene, and other TMDs and review in detail the structural response of MoS_2.

1.3.1| Structural Responses of Two-dimensional or Thin Materials: Graphene, Graphite, WTe_2, TaS_2, $TaSe_2$, WSe_2, and Germanium

The structural responses of the most heavily studied two-dimensional material, graphene, and of its bulk counterpart, graphite, are of interest for understanding electron-phonon dynamics in carbon-based devices and for understanding structural mechanics in thin systems.[210] At moderate fluences (*e.g.*, between 0.5 and 21 mJ/cm^2), the electrons quickly thermalize and couple to phonons. The phonons then thermalize in ~10 ps (*i.e.*, the lattice heats) in both in- and out-of-plane directions.[242-243] At higher fluences nearing the ablation threshold, graphite contracts in the initial picoseconds. The timescale of the contraction is inversely proportional to the excitation fluence and is as short as 500 fs.

The contraction is attributed to strong electron-phonon coupling, in which ~90% of the laser excitation energy excites both incoherent and coherent high-momentum SCOPs. The lattice next undergoes expansion with a time constant of several picoseconds, where the exact number depends on the sample geometry and thickness.[209-210,240-243,245,248] The dominant mode is attributed to the A_1' mode rather than E_{2g} because the A_1' exhibits stronger electron-phonon coupling and has more decay channels through acoustic phonons, making it more susceptible to hot phonon effects and thus limiting the electron relaxation rate.[209] The expansion is attributed to thermalization of the SCOPs with the phonon population *via* mode conversion, particularly decay into lower energy acoustic phonons, and further electron-phonon coupling.[209,225,240-241,248,250] Graphene is expected to undergo similar behavior, although the magnitudes will vary depending on the coupling strength.[209]

On long time scales, graphite relaxes into mechanical oscillations that ultimately dissipate the photo-excited thermal energy. For a 75-nm thick graphite crystal, the movement was tracked *via* motion of contrast in time-resolved electron micrographs out to tens of microseconds. During the initial five microseconds, multiple mechanical modes were evident in the chaotic motion of the image contrast. After tens of microseconds, the crystal vibrates at a fundamental global resonance of 1.08 megahertz (MHz), which was used to extract the mechanical properties. The lifetimes of these modes were found to be determined by mechanical damping.[246]

Similarly, the optical phonons of tungsten ditelluride (WTe_2) were measured with

time-resolved transient reflectivity and found to decay into acoustic phonons with a rate dependent on the temperature. The reflectivity was found to undergo an instrument-limited change followed by a multiexponential decay combined with periodic oscillations. The exponential decay was attributed to photocarrier relaxation and not studied further. The oscillations were fit with a damped sinusoidal function, and the dominant frequency was found to be 0.27 THz, suggesting the oscillation corresponded to the A_1 optical phonon. This attribution is further supported by the dependence of the optical phonon frequency on the probe laser polarization. Acoustic phonons were calculated to oscillate at a frequency one order of magnitude lower. The optical phonon frequency was found to decrease with temperature increases, which was attributed to anharmonic decay of optical phonons. The damping increased with pump fluence, which was attributed to lattice anharmonicity. These results suggested that WTe_2 may have unobserved CDW character, which would contribute to the phonon frequency softening.[252]

The structural dynamics of 1T-tantalum disulfide (TaS_2) and both 1T- and 2H-tantalum diselenide ($TaSe_2$) are of particular interest due to the occurrence of phase transitions of an entirely different type – the formation of different CDW phases. Connected with superconductivity, CDWs are a combined lattice distortion and electron density re-distribution into a periodic structure. The three phases of CDWs are the commensurate CDW (CCDW) characterized by high resistivity and a very ordered lattice distortion (*i.e.*, the deformation of 12 Ta atomic cores around a thirteenth Ta core to form

a star-of-David structure in TaS_2 and the deformation of 6 Ta cores around a seventh Ta core in 2H-$TaSe_2$),[82] the nearly commensurate CDW (NCCDW) characterized by a less-ordered distortion and a lower resistivity, and the incommensurate CDW (ICCDW) characterized by disordered lattice distortion and a further drop in resistivity. The phase diagram is shown in Figure 1.8 for TaS_2. At ambient pressure, the Mott (insulating) state – characterized by a localization of the electronic distribution around the atomic cores without a lattice distortion – and CCDW coexist below 180 K,[253] the NCCDW occurs between 180 and 350 K, and the ICCDW occurs between 350 and 550 K. Above 550 K, TaS_2 is metallic. At low temperatures and high pressures, superconductivity is observed due to the non-metallic low-temperature phase due to the NCCDW phase.[79] Electron-electron and electron-phonon interactions drive transitions or stabilize a mosaic of different phases upon application of external voltage pulses.[253]

While some studies claim to have observed nonequilibrium phase transitions from CCDW and ICCDW in $TaSe_2$[254] and ICCDW and NCCDW in TaS_2[255] upon optical excitation, many questions remain. First and foremost, it is not currently known whether the lattice distortion or the electron density re-distribution occurs first. Moreover, ultrafast electron diffraction studies averaged signal from large sample areas, which does not account for the significant influence of defects on phase transitions.[256-257] These puzzles show the importance of understanding the interplay of electronic and structural deformation and interactions.

Recently, the launch and propagation of acoustic phonons in tungsten diselenide

(WSe_2), germanium (Ge), and TaS_2 were imaged in real-space by coworkers in the Flannigan group.[247,258] Using the imaging capabilities of UEM, they were able to resolve acoustic wavetrains by tracking the changes in the contrast due to changes in the local Bragg diffraction condition. It was observed that the acoustic phonons appear to be launched from step-edges in WSe_2, where the thickness changed abruptly. Specifically, it was observed that the intensity increased for ~10 ps before a traveling wave was launched in a direction approximately normal to the step-edge. This time

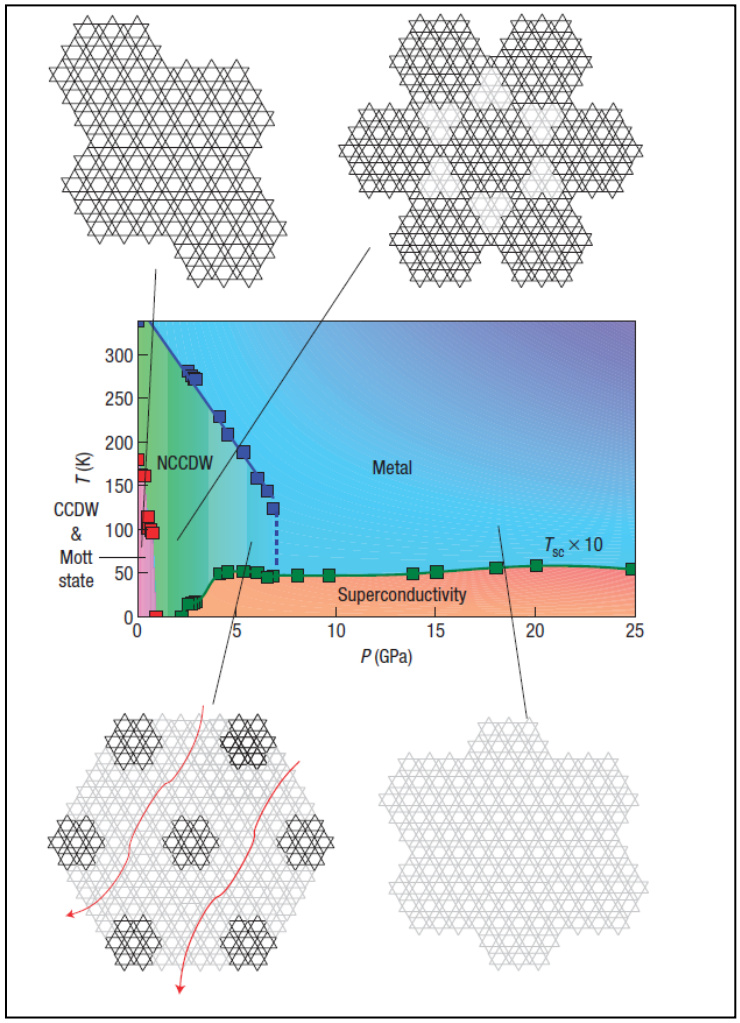

Figure 1.8 | **Phase diagram of 1T-TaS_2 with the metallic, superconducting, and CDW phases indicated.** The drawings surrounding the phase diagram indicate the deformation in the CDW phases, where the darker lines indicate star-of-David deformations, and the lighter lines indicate decreased deformation. Clockwise from top left, the structures are CCDW, NCCDW, metallic, and coexistence of metallic and NCCDW. Reprinted by permission from Macmillan Publishers Ltd: *Nature Materials*, Ref [79], © 2008.

interval is believed to correspond to the dephasing time of longitudinal waves traveling in the cross-plane direction. Several traveling strain wave modes were observed, depending on the location on the specimens. The highest frequency modes were found to emerge from the vacuum-crystal interface, from which they traveled at phase velocities of 6.5 and 5.5 nm/ps for Ge and WSe_2, respectively. Slightly lower-frequency waves were found to be launched from step edges. In both cases, the image intensity oscillated with frequencies in the tens of gigahertz (GHz) for both materials. Similarly high-frequency waves have been observed in electron diffraction patterns taken on silicon[259] and in time-resolved transient reflectivity measurements on WSe_2, which were ascribed to the A_{1g} mode at the Γ point (7.448 THz) for monolayer specimens as well as the interlayer B_1 mode (frequency was found to depend on thickness) for multilayer specimens. In monolayer specimens, the A_{1g} phonons were found to decay anharmonically into longitudinal acoustic (LA) modes (3.7 THz) in several picoseconds, depending on the thickness, but the LA modes were not observed in multi-layer specimens.[249] The GHz frequencies observed in the UEM study were attributed to the longitudinal acoustic phonons traveling in the cross-plane direction and the dilatational Lamb-wave mode, respectively. This work exposes the rich potential of a technique that offers imaging capabilities with the temporal resolution of pump-probe spectroscopy and the spatial resolution of transmission electron microscope (TEM) in elucidating strain dynamics and coupling with morphological or defect structures.[247,258]

1.3.2 | Photo-induced Structural Response of MoS_2

Ge and coworkers[251] observed the launch and propagation of the out-of-plane coherent longitudinal acoustic phonon mode in MoS_2 samples with 10 to 1,314 layers. The sample reflectivity suddenly changed at time zero followed by a slow decay overlaid with damped oscillations, with a single frequency for each sample. The change – the sign of which depended on the number of layers – and subsequent decay were attributed to photo-carrier relaxation and were outside the scope of the study. The oscillation frequency was inversely proportional to the number of layers because this mode produced a standing acoustic wave; the frequency ranged from 0.226 THz for 11 layers to 0.038 THz for 1,314 layers. The oscillations were fit with exponentially damped sinusoids. In contrast, the oscillation period was found to be linearly proportional to number of layers only for samples thinner than 122 layers, which is consistent with the establishment of a standing wave. The sound velocity was calculated to be 7.11 kilometers (km)/s. The oscillation period was consistently ~30 ps for samples thicker than that threshold, which was deduced to be the transition to a surface acoustic wave rather than a standing wave, and the damping time constant increased. This trend could be accounted for by considering the effect of the substrate. The damping by the substrate can be expected to be more pronounced for thinner samples, which is reflected in the trend for the damping time. Oscillations were not observed in samples thinner than 10 layers, which was attributed to low signal.

The ultrafast structural response of supported monolayer MoS_2 was studied by

Mannebach *et al.* using UED, which was described in Section 1.2.[244] In this study, the evolution of the intensities and positions of different peaks in the electron diffraction pattern were tracked. In 1.7 ± 0.3 ps, the intensity decreased, which is attributed to electron-phonon coupling and electron-phonon thermalization. The peak positions oscillate and are found to be consistent with thermal stress release. The intensity recovers in a biexponential form (53 ± 9 ps and an unspecified longer time constant), which was attributed to heat transfer from the MoS_2 to the amorphous carbon support film and from the support film to the surrounding heat sink (copper TEM grid), respectively. At increased pump fluence, the peaks were observed to broaden in those initial ~2 ps, which is consistent with the onset of rippling. The magnitude of this rippling was calculated to be ~3° deviation from flat normal. This study examined only the diffraction pattern of monolayer MoS_2 and thus had to extrapolate to real-space imaging. Furthermore, it did not investigate the relaxation pathways of the thermal oscillations.

The mechanical structural deformation, resonance frequencies, and quality factors in MoS_2 have been studied due to the interest to use thin flakes of MoS_2 as mass or chemical sensors. On these timescales, the structural dynamics of MoS_2 are accurately described by membrane or plate mechanics, depending on the thickness.[260] Generally, the resonance frequencies of circular, free-standing MoS_2 membranes are in the MHz range (10-300 MHz) with quality factors in the range of tens to hundreds and displacement sensitivities of tens of femtometers per $Hz^{1/2}$ depending on the boundary

conditions, thickness, and mechanical properties of the membranes.[142,260-261] These values vary slightly in the literature but are generally comparable to other two-dimensional thin materials.[40] The time-domain response of a circular monolayer MoS_2 membrane gave a mechanical ring-down lifetime of 0.6 μs for the 22.2 MHz resonant mode with a quality factor of 42.[12]

The bridge between the phonon dynamics and classical plate or membrane dynamics has not been explored in these thin materials. Such dynamics, however, are of fundamental interest as well as of interest to understand how to make sensors more sensitive or rapid. Moreover, understanding both the phonon and mechanical dynamics and their interaction with the structure in real materials – defects such as step edges – is paramount to understand how pure or perfect the material must be to attain a particular device performance. Elucidating that relationship requires exquisite spatiotemporal resolution, such as that attained by UEM.

1.4 | Ultrafast Electron Microscopy

Ultrafast techniques that use optical probes are diffraction-limited to a spatial resolution of hundreds of nanometers, although various techniques have circumvented this limit for specific systems.[262-264] Moreover, optical techniques are sensitive to only optically active states and transitions. Conventional transmission electron microscopes (TEMs) have a diffraction limit of fractions of an angstrom due to the small wavelength of the electrons traveling at relativistic speeds.[265] However, the continuous beam of electrons used restricts the temporal resolution to that of the frame readout rate of the

camera; one state-of-the-art camera can take only 300 images a second, which corresponds to one image every 3 milliseconds (ms).[266] To probe the influence of spatial inhomogeneity of a specimen on dynamic properties, a technique is needed that combines the high spatial resolution of TEMs with the temporal resolution of pump-probe spectroscopy. Such a technique that achieves simultaneous femtosecond temporal and nanometer spatial resolution is called ultrafast electron microscopy (UEM).[196,267-275] This section describes the operating principles of the different modalities, with emphasis on the stroboscopic mode which I used in this research project.

1.4.1 | Operating Principles of UEM

Ultrafast electron microscopy is a pump-probe technique, in which the excitation or pump pulse is an ultrafast laser pulse and the probe pulse is an electron packet. The instrument itself is a combination of an ultrafast laser system, which requires a femtosecond and/or nanosecond laser and an optical delay stage or delay generator, and a TEM that has been modified with two optical periscopes – collections of optics that guide pulses into the microscope – that enable laser access to the electron source and to the specimen, respectively. The instrument is shown schematically in Figure 1.9.

A typical UEM experiment begins with the emission of an ultrafast laser pulse, usually hundreds of femtoseconds or a nanosecond in duration depending on the time scales of interest, which is passed through nonlinear optics and split into two pulses. The first pulse is tuned further if necessary to provide the appropriate excitation energy for the material system and is passed into a conventional TEM, where it is directed onto the

specimen. The specimen absorbs the pump pulse, and dynamics are initiated. Meanwhile, the second pulse is frequency-doubled into the ultraviolet (UV) range and then directed onto the TEM electron source. This UV pulse extracts a short electron packet, which is accelerated to the operating voltage and directed down the column. The electron packet then arrives a certain time interval from the arrival of the pump pulse at the specimen, which determines at what point in the dynamics the electron packet captures the dynamics. The packet in this case acts as a short flash and interacts with the specimen only over its short duration. This probe packet is collected on the detector (here, a charge-coupled device (CCD) camera) and begins to form an image. The time interval between the relative arrivals of the pump pulse and probe packet is varied to probe the entire process at discrete intervals.[196,267-275]

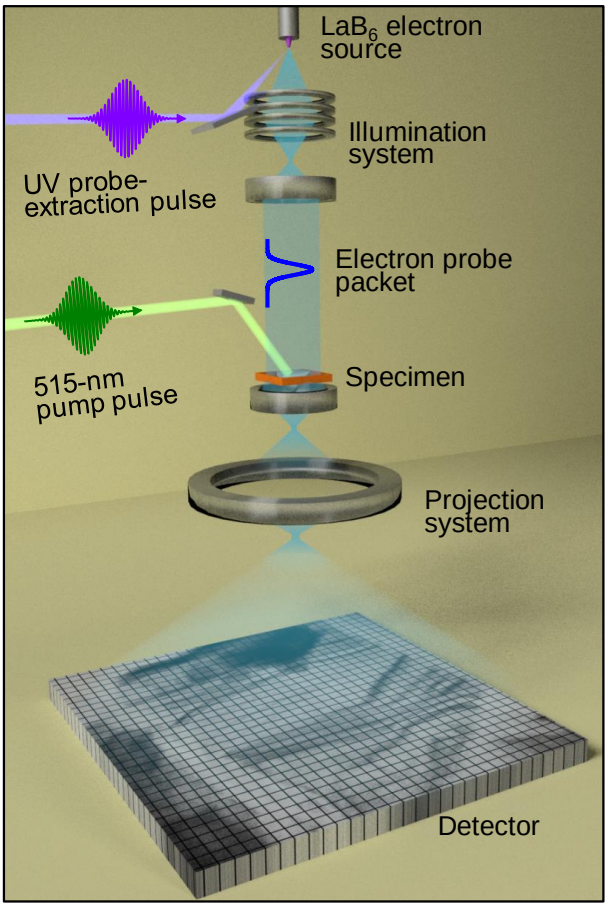

Figure 1.9 | **Schematic of a UEM experiment.** Schematic of the laser beam paths for the 257.5-nm probe extracting pulse (violet), the 515-nm excitation pulses (green), the important lenses, the electron probe packet (sapphire), and the detector, which is greatly exaggerated here for illustrative purposes.

Due to space-charge effects or Coulombic repulsion, the number of electrons in the probe packets must be limited to preserve the ultrafast temporal resolution and TEM spatial resolution. The maximum resolution can be acheived in the limit of a single electron per packet, in which the Coulomb repulsion would be minimized.[196,276] However, one electron is hardly enough to produce a meaningful image or diffraction pattern. Generally, a minimum of 10^6 to 10^7 electrons are needed to produce an image or diffraction pattern with an appreciable signal-to-noise ratio.[277-278] Thus, the pump-probe cycle must be repeated millions of times in order to collect enough electrons for an image or diffraction pattern of a single point in the dynamic process. The relative time interval is then adjusted, and the pump-probe cycle repeated. Therefore, this characterization technique can probe only reversible processes. A large impact on the spatial resolution is the thermal drift of the specimen as it is repeatedly pumped and probed. Thus, the process can be expedited by including greater than one electron per packet, with two limiting caveats. First, the number of electrons will then be constrained by the desired temporal resolution. Second, the repetition rate of the laser must be adjusted to allow the process to be truly reversible. In other words, the specimen must be allowed to relax to the same initial state before the arrival of the next pump pulse, which limits how quickly the signal can then be accumulated. Both of these are determined by the process being probed.[196]

Stroboscopic UEM has been employed to study materials phenomena in a broad range of specimens, from organic and inorganic to biological, with a broad range of

signals, from bright-field (BF) images to photon-induced near-field electron microscopy (PINEM). Stroboscopic UEM has been used to visualize phase transitions, such as structural phase transitions in a single Fe(pyrazine)$Pt(CN)_4$ nanoparticule[279] and the metal-insulator transition in polycrystalline VO_2,[280] by observation of changes in both real- and reciprocal-space signals. In addition, changes in macromolecular ordering was mapped for helical poly(ethylene) oxide.[281] Diffraction signals have been used to image elastic displacements in carbon nanotubes,[282] which were further elucidated using electron energy-loss spectroscopy (EELS)[283] and to track electron-phonon coupling in graphite.[243] The MHz mechanical drumming of graphite[246] and silicon cantilevers[284] have been imaged on microsecond timescales. Recently, acoustic phonons were imaged in real space on picosecond timescales in WSe_2, Ge, and TaS_2 thin films[247,258] and in MoS_2 in this work,[285-286] and acoustic-plasmonic vibrations were imaged in real-space in gold nanoparticles.[287] Other capabilities, particularly tomography[288-290] and spectroscopy,[291-293] have been demonstrated in a UEM. Finally, PINEM[294-297] has allowed the imaging of evanescent fields around nanostructures and the interactions with nearby nanostructures,[298-299] investigation of electron-plasmon interactions,[268,300] and detailed characterization of the instrument response.[297]

An overview of the UEM system at the University of Minnesota is given in Chapter 2, and details for specific experiments will be included in the chapters describing those experiments.

1.4.2 | Other Modalities

To image irreversible processes, two other modalities – single-shot and movie-mode dynamic TEM (DTEM) – have been developed and applied with great success to elucidate important processes, such as ablation and re-crystallization.[301-303] Because irreversible processes must be completely captured in a single pulse, each pulse in both of these modalities contains 10^6 or more electrons, depending on the information to be captured as described in Section 1.4.1. Per the previous discussion, the primary disadvantage is the reduced temporal resolution, usually to several nanoseconds rather than hundreds of femtoseconds, as achieved with stroboscopic UEM. In single-shot DTEM, a single probe pulse with 10^6-10^8 electrons follows a pump pulse at some time interval and captures the time point in the process.[304] The electron beam is then moved to another region in the specimen, nominally identical to the original, now irreversibly altered area, and a probe pulse follows another pump pulse but at some different time interval.[305] A way to circumvent the potential variations in the specimen is to install a set of deflection coils and send a train of electron probe packets after a single pump pulse. Each electron packet is then deflected to a separate region of the camera. Once read out and re-assembled in the correct order, these images form a movie of the process, from which movie-mode DTEM derives its name.[306-307]

A modality that offers sensitivity to surface processes is scanning ultrafast electron microscopy (SUEM). In contrast to UEM, SUEM employs a scanning electron microscope (SEM) rather than a TEM, and thus the signals are back-scattered electrons,

secondary electrons, and X-rays. The stroboscopic pump-probe process is otherwise identical to UEM. The SUEM system probes surface properties and does not require an electron-transparent specimen. It has been applied to study carrier dynamics in semiconductors.[275,308-317]

A final modality is ultrafast electron diffraction (UED). These systems are similar to UEM and DTEM, except that the only signal that can be collected is diffraction from the specimen. Consequently, the systems do not require a TEM and instead generally comprise an ultrafast laser system as in UEM and a high-vacuum chamber with a photo-activated electron source and detector, with generally fewer lenses than in a TEM.[277] Due to the slightly lower complexity, methods to compress electron pulses to circumvent space-charge effects for large pulses have been developed and implemented in such systems, which is not trivial to achieve in a UEM.[318-324] This technique has provided unique insights into structural and carrier dynamics in a range of systems – such as electron-electron thermalization, electron-phonon coupling,[325] phonon dynamics,[326] phase transitions,[279-280,327-338] and structural changes.[244,339-340]

1.5 | Chapter and Project Summary

In this chapter, I have introduced MoS_2, the most heavily studied member of the layered TMDs, and its structure. Its semiconducting nature, relatively large optical absorption, chemical stability at atomically thin layers, robust mechanical properties, and tunability of its material properties with strain or layer number have made it appealing for applications in transistors, photo-detectors, photovoltaics, gas sensors, mass sensors, and

flexible nanoelectronics. In particular, the tunability of its electrical properties with strain has raised the possibility that strain could be harnessed to tune properties dynamically in both space and time. Such dynamics, however, would need to be resolved on the ultrafast timescales (< μs) and device-relevant spatial scales (≤ nm). One such way to accomplish this dynamical tuning is through the use of optical excitation. Photo-excited electrons and excitons undergo intra- and inter-band relaxation, during which time they emit acoustic phonons, which are, by definition, strain waves, or optical phonons, which then relax into acoustic phonon modes. The excitation of electrons and the electron-phonon coupling have been studied in MoS_2, but the structural dynamics and propagation of those phonons have not been studied due to limitations in the spatiotemporal resolution of conventional pump-probe techniques. The UEM – a combination of a TEM and pump-probe optical system – at the University of Minnesota offers access to temporal scales from hundreds of femtoseconds to seconds simultaneously with access to sub-nanometer spatial regimes.

These capabilities have been harnessed in this research project to image the structural dynamics from launch of acoustic phonons through full mechanical relaxation in MoS_2 over seven orders of magnitude in time (individual picoseconds to tens of microseconds) and nanometer spatial scales. In the next chapter, I will discuss the specific experimental protocols and instrument components that make this work possible. I will also introduce the specimen studied and its static characterization, as well as my work determining the spatial resolution of the microscope when operated in pulsed-

electron mode, which is the highest spatial resolution achieved with the UEM in the Flannigan research group to date. In Chapter 3, I will discuss image sequences acquired that track the launch and propagation of acoustic phonons in MoS_2. In particular, I observe coherent acoustic phonons that appear to be launched at the edge of the flake and propagate away from that interface at approximately the speed of sound in MoS_2. I then discuss potential launch mechanisms and the modeling used to understand the dominant mechanisms, as well as modeling to understand how the acoustic phonons cause changes in image contrast. I present preliminary work in understanding the launch mechanisms, such as development of the measurement capabilities for determining time zero on the 515-nm beam line. In Chapter 4, I discuss image sequences that show a transition from propagation of coherent acoustic phonons into chaotic motion and the appearance of lower-frequency (single gigahertz) modes that dominate as the higher-frequency modes are damped out. In Chapter 5, I will discuss image sequences showing the final relaxation of the flake through mechanical oscillations. The frequencies of these oscillations appear to depend on geometric constraints, which supports the idea that these modes are the fundamental mechanical modes of the flake. Modeling with COMSOL supports this hypothesis. In Chapter 6, I will discuss the future work that these projects suggest.

2 | METHODS

This chapter details the alignment and operation of the UEM at the University of Minnesota necessary to observe the photo-actuated material response in this dissertation. In particular, I will discuss the instrument components, operation, alignment, and basic control experiments. Some observations of the effects of specimen drift, electron source fluctuations, and source quality on the spatial resolution achievable as well as characterization of the limit of the spatial resolution in a UEM will then be discussed. Next, I will discuss the fabrication and characterization of an electron-transparent specimen from a bulk MoS_2 crystal, particularly thickness and sources of contrast. Finally, I will summarize standard procedures to convert image formats, to drift correct image sequences, and to quantify dynamics. I will include any details pertaining to specific experiments in the subsequent chapters that discuss them.

2.1 | UEM at the University of Minnesota

The UEM operated by the Flannigan research group comprises a conventional TEM with several modifications to integrate an ultrafast, pulsed laser system containing a delay stage or electronic delay generator, as shown in Figure 2.1. This combination enables stroboscopic imaging of ultrafast processes, the principles of which were

described in Section 1.4.1.

2.1.1 | FEI Tecnai Femto

The TEM is the Tecnai Femto manufactured by FEI (recently acquired by Thermo Fisher Scientific) and is a modified version of the Tecnai T20 microscope. The FEI Tecnai Femto may be operated at a range of voltages with a maximum at 200 kV. All of the experiments in this work were conducted with the microscope operating at that maximum voltage. The FEI Tecnai Femto differs from a T20 in that it has been outfitted with two optical periscopes, as shown in Figure 2.1(a). As shown by the purple arrow, the upper periscope allows a laser beam access to the electron source, in this case a lanthanum hexaboride (LaB_6) crystal. The lens before the entrance to that periscope allows the operator to change the size and location of the incoming laser relative to the

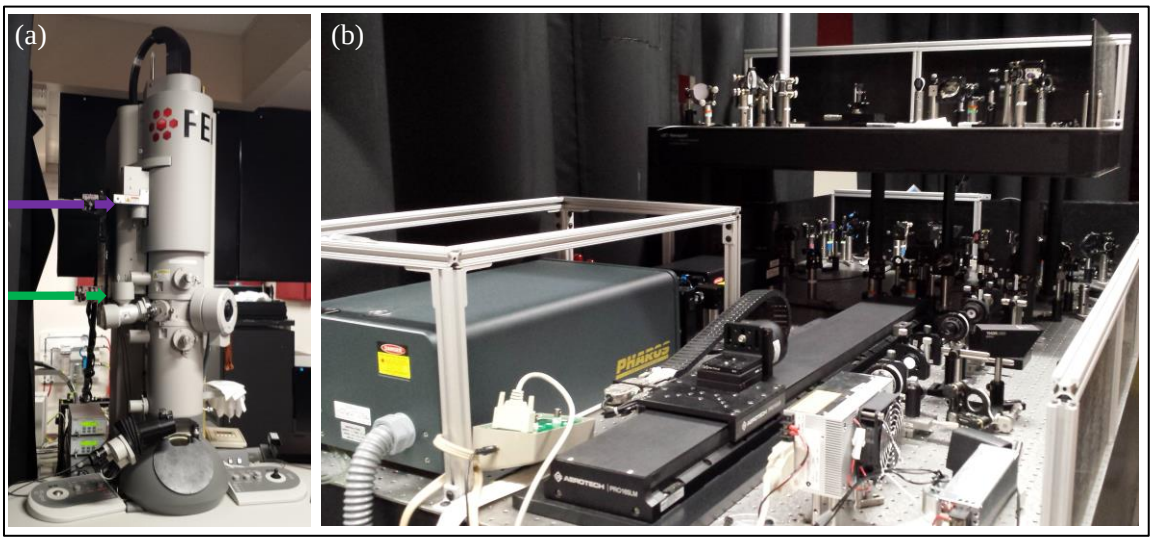

Figure 2.1 | **The UEM at the University of Minnesota.** (a) The FEI Tecnai Femto. The upper optical periscope (purple arrow) allows laser access to the electron source, and the lower optical periscope (green arrow) allows laser access to the specimen. (b) The ultrafast laser system and optics.

electron source inside the Tecnai Femto, ultimately allowing alignment of the laser onto the LaB_6 at an incident angle of 4° from the optic axis. As shown by the green arrow, the lower periscope allows the laser beam to access the specimen, with an incident angle of 4° from the optic axis in the TEM; as before, the lens before the periscope allows the user to change the size and relative location of this laser in the TEM on the specimen. The procedures to align the lasers through the periscopes and onto the electron source and the specimen are described in Sections 2.1.6 and 2.1.7, respectively.

A second modification that differentiates this TEM from others is the source shape. The FEI Tecnai Femto contains a LaB_6 source so that it can be operated thermionically, but whereas most thermionic sources are conical LaB_6 crystals, the LaB_6 here is terminated by a flat surface with a diameter ranging from 50 to 150 μm and is encased in 80 μm of graphite. The exact tip size used in the experiments will be noted in the relevant chapters. This large flat surface allows the user to align the laser to the source to extract electrons more easily and to extract more electrons per pulse for ultrafast experiments. The graphite provides thermal stabilization when operated as a UEM, reducing tip movement due to thermal fluctuations during hours-long experiments.

None of these modifications, however, affects the electromagnetic lenses within the FEI Tecnai Femto, and the standard alignment procedures for conventional TEM are followed when the microscope is operated thermionically. Because the number of electrons and shape of the beam changed when the microscope was operated as a UEM, I will discuss those modifications in Section 2.1.8.

2.1.2 | Laser System Components

The laser system employed is shown in Figure 2.1(b), and schematics of the important components for the femtosecond and nanosecond experiments can be found in Figure 2.2 and Figure 2.3, respectively. For both femtosecond- and nanosecond-timescale experiments, a femtosecond laser was used to generate the pump pulses, and these pulses followed the same paths on the laser table, shown in green from the beam splitter onto the delay stage. For the femtosecond experiments, the laser also generated the electron-extracting laser pulses. The femtosecond laser in these experiments is the

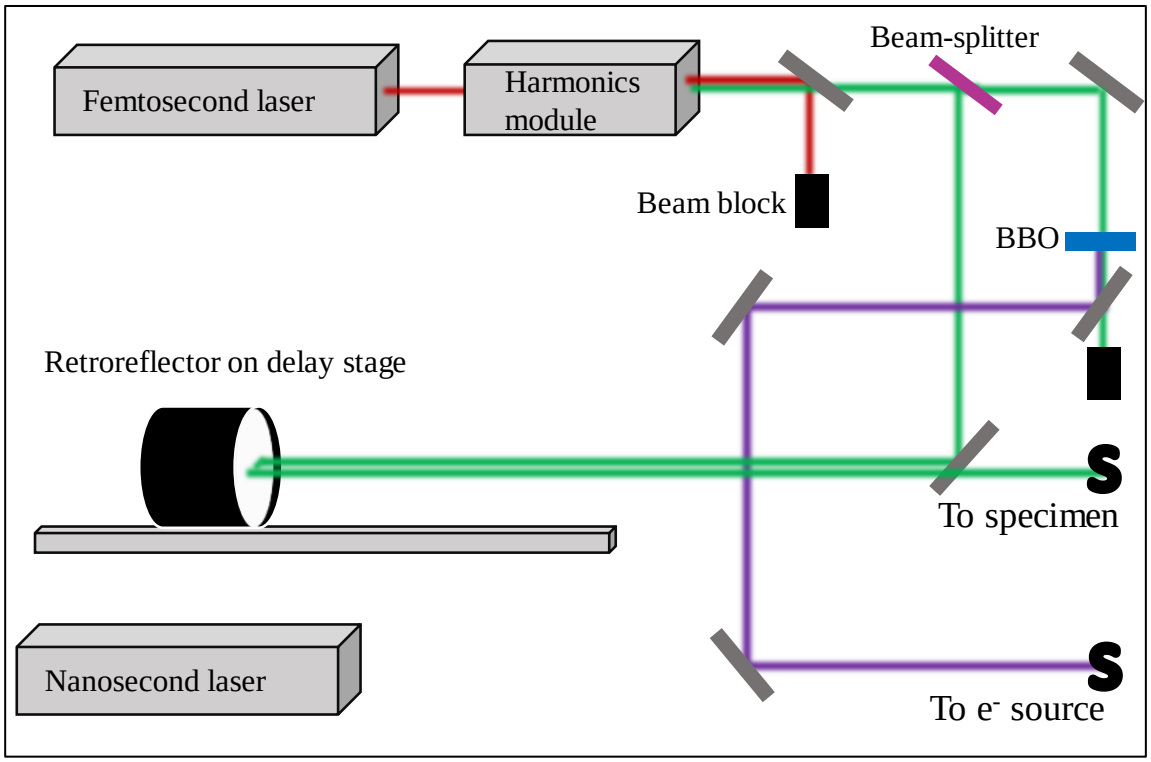

Figure 2.2 | **Schematic of laser lines involved in a femtosecond experiment.** The PHAROS femtosecond laser (Yb:KGW) outputs a base wavelength of 1030 nm (shown in red), which is then frequency-doubled in the harmonics module to 515 nm (shown in green). Part of the green light is frequency-doubled in a beta barium borate (BBO) crystal (257.5 nm). Any unlabeled components are mirrors.

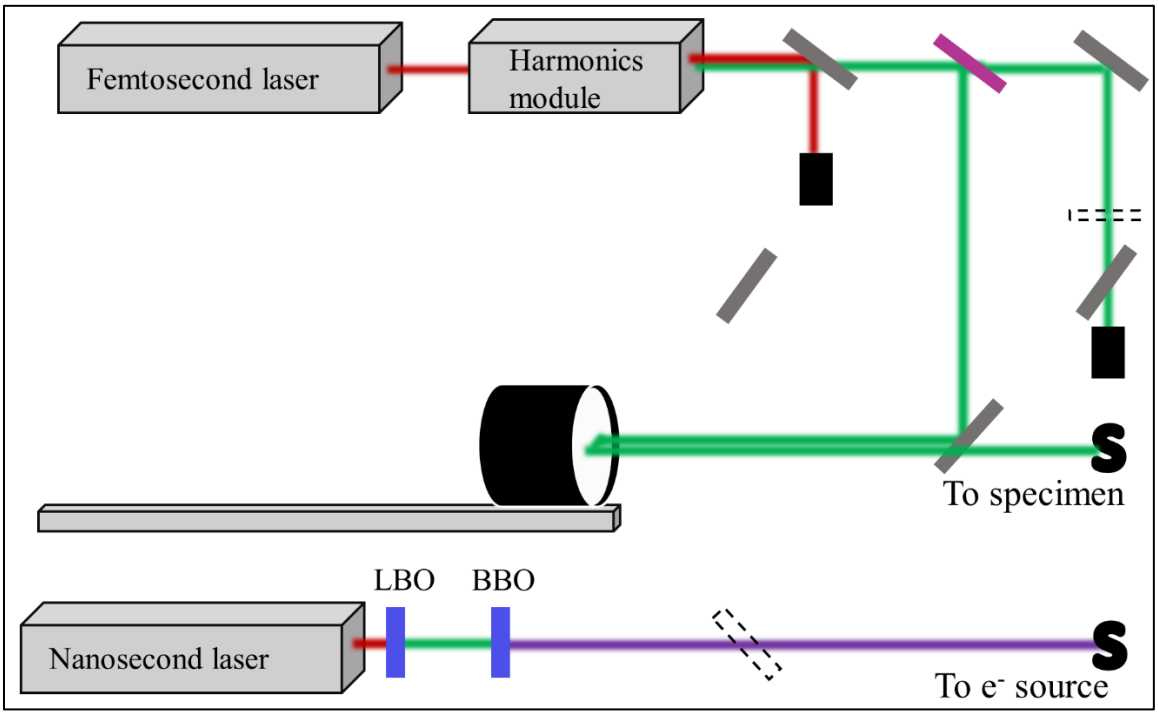

Figure 2.3 | **Schematic of the laser setup in nanosecond experiment.** The base wavelength from the Wedge nanosecond laser (Nd:YAG, base wavelength of 1064 nm) is passed through a lithium triborate (LBO) and then BBO crystals to produce 266 nm (shown in purple). The femtosecond laser is used to generate the 515-nm pump pulses.

PHAROS from Light Conversion. The PHAROS (Yb:YGW) has a base wavelength of 1030 nm ± 5 nm and a maximum pulse energy of 200 micro-Joules (μJ) at most repetition rates. Its repetition rate may be tuned from 1 kilohertz (kHz) to 1 MHz and may be tuned further using a pulse picker, an electro-optical modulator consisting of a Pockels cell and polarizers.[341] The laser pulse duration was measured using an auto-correlator as 700 fs near the entrance to the pump periscope.[276] For nanosecond experiments, the electron-extracting pulses were generated with the Wedge Laser from Bright Solutions (Nd:YAG), with a base wavelength of 1064 nm. The repetition rate of this Q-switched laser may be tuned from a single pulse to 100 kHz, and its maximum

pulse energy is reported to be 4 mJ.

Two types of frequency-doubling crystals are used. A frequency-doubling lithium triborate LiB_3O_5 (LBO) crystal is used to produce 532-nm pulses on the nanosecond line. Beta barium borate β-BaB_2O_4 (BBO) crystals are used to convert 515-nm into 257-nm light on the femtosecond line and 532-nm into 266-nm light on the nanosecond line. In both cases, the fourth harmonic, with a wavelength in the ultraviolet (UV) range, is used as the electron-extracting pulses.

Polarizers on the nanosecond line have been omitted for simplicity. The nanosecond laser pulses are initially circularly polarized but are converted to linear polarization before being sent into the microscope. The femtosecond laser pulses are linearly polarized and are not altered for these experiments.

Two delay generators are used to vary the time interval while acquiring image sequences. For femtosecond experiments, the one-meter long linear motor stage PRO165LM-1000 from Aerotech, Inc, with accuracy of ±2.5 μm (±8.3 fs) is used. For nanosecond experiments, a DG535 digital delay/pulse generator from Stanford Research Systems is used to coordinate pulse train timing between nanosecond probe pulses and femtosecond pump pulses. The manufacturer claims a typical timing jitter of 50 ps.

2.1.3 | Theoretical Versus Experimental Time Zero

Time zero has two definitions, termed theoretical and experimental time zero. Theoretical time zero is the time delay at which the laser pump pulse and electron probe packet overlap exactly in time at the specimen. The method offering the closest

experimental measurement of theoretical time zero and the instrument response requires an electron energy-loss (EEL) spectrometer due to the fast rise time falling nearly within the electron envelope.[297] Since the FEI Tecnai Femto is currently not equipped with an EEL spectrometer, experimental time zero, defined as the time at which dynamics are first observed, is used in this study unless otherwise specified. In particular, a procedure to determine theoretical time zero was recently applied in the Flannigan research group using a phenomenon called plasma lensing.[276] This procedure and the measurements of theoretical time zero and of the instrument response are discussed in Section 3.3.2.

2.1.4 | Pulsed Femtosecond Experiment Flow and Logic

For femtosecond-timescale experiments, pulses from the PHAROS are first converted to the appropriate wavelengths. The 1030-nm pulses are first frequency-doubled to 515 nm in a harmonics generation module called the HIRO from Light Conversion. The 515-nm pulses are directed into a beamsplitter, where approximately thirty percent of the light is directed into a BBO crystal. This light is partly frequency-doubled to 257 nm, which now has enough energy to extract electrons from the LaB_6 source via the photoelectric effect. The unconverted 515-nm light is directed into a beam block for safety. The UV pulses are directed onto the upper laser table and through the directional lens, where it is focuses and directs the pulses onto the electron source. Via the photoelectric effect, each UV pulse extracts an ultrashort electron probe packet.

The remaining seventy percent of the green light incident on the beam splitter are the pump pulses. From the beamsplitter, they are directed onto one-meter long delay

stage. Multiple jogs in this line were added to allow for switching to different wavelengths with similar path lengths and to ensure that time zero is actually in the microscope. The similar path lengths are important for the concept of ensuring that the start of dynamics is actually observable in the TEM. The retroreflector mounted on the delay stage extends the temporal delay range of the stage to two meters, which using the speed of light corresponds to approximately 7 nanoseconds (ns). Changing the position of the retroreflector on the delay stage produces a shift in the relative arrival times of the electron packet and pump pulse corresponding to the distance moved. The pump pulse is next directed onto the upper laser table before being directed through the lens into the lower periscope and onto the specimen.

The position and movement of the delay stage and timing of image acquisition are controlled by a set of LabVIEW programs. These programs automate the image acquisition process and allow the user to spend as little time as possible in the UEM room to minimize temperature fluctuations. One program coordinates the movement of the delay stage and sends signals to the second LabVIEW program to acquire images. In all experiments, the user inputs the exposure time for each image into the latter program and the exposure time plus two to three seconds into the first program to allow the first program time to move the delay stage completely before the next image is acquired.

2.1.5 | Pulsed Nanosecond Experiment Flow and Logic

As in the previous section, the PHAROS generates the femtosecond laser pump pulse at a repetition rate set according to standard procedure. Two microseconds before

the next pulse is set to be emitted, the PHAROS sends an electrical signal to the DG535 delay generator, which then triggers the nanosecond laser to emit a nanosecond pulse. This nanosecond pulse is then frequency-doubled twice though first an LBO and then a BBO crystal, which results in 266-nm pulses.

Two photodetectors shown in Figure 2.4 are used to tune the timing. One photodetector is placed on the nanosecond line after the steering optic that directs the 266-nm pulses to the top table and captures the 515-nm signal remaining from the frequency doubling. A second photodetector, placed on the infrared (as seen in Figure

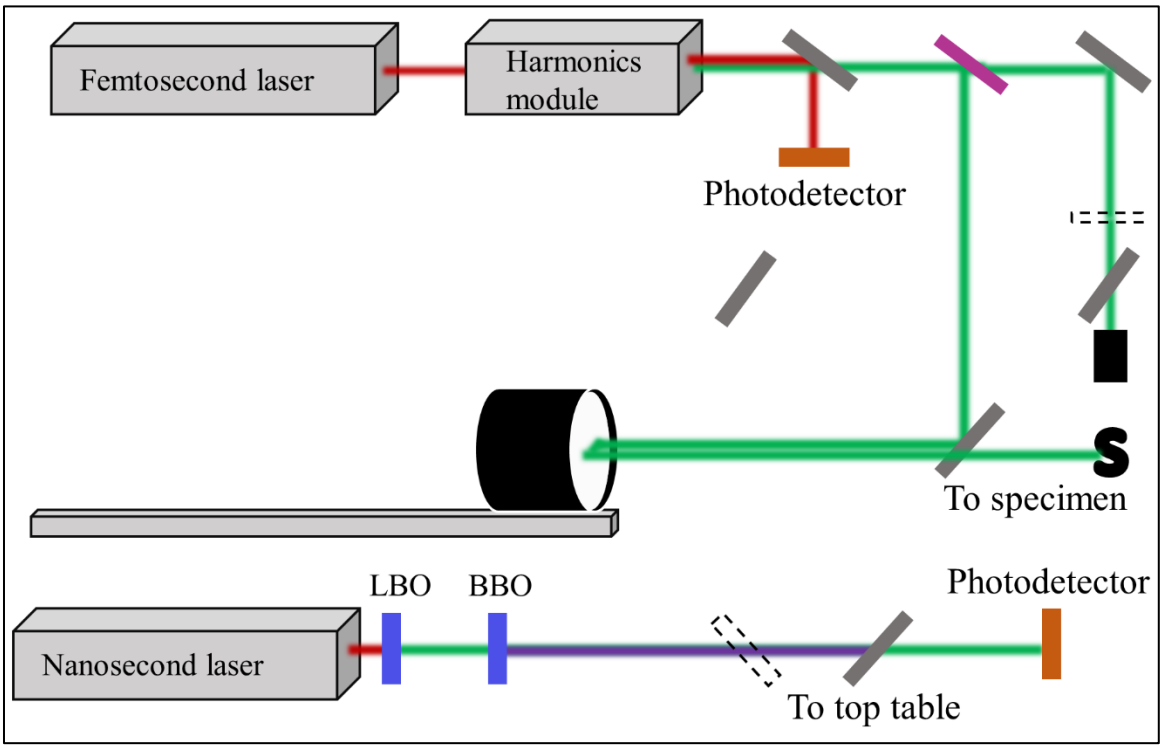

Figure 2.4 | **Nanosecond laser system with photodetector positions.** Photodetectors used to tune timing of ns probe-extracting 266-nm pulse and fs 515-nm pulse are shown in orange, along with the mirror used to direct the 266-nm light onto the top table and on the electron source.

2.4) or 343-nm femtosecond line, is used to track the timing of the pump pulses. The delay stage is then moved to its front-most position to minimize the path-length differences between the pump and probe-extracting pulses, and the pulses are viewed on an oscilloscope. In the LabVIEW program used to coordinate the delay generator and the camera on the TEM, a second delay is set so that the two pulses arrive at the photodetectors at the same time. This second delay adjusts the triggering of the nanosecond laser to minimize the delay between the user-set time zero and experimental time zero. The second delay varies depending on the environmental conditions and the repetition rate chosen for the experiment and is thus manually set at the beginning of experiments.

2.1.6 | Alignment Procedure for the Pump Laser

Aligning the pump laser is accomplished by incremental shifts of the pump focusing lens just before the beginning of the pump periscope to center a damaged spot in a holey (a regularly perforated, amorphous) carbon film on a TEM grid. The laser power of the pump is measured using a power meter (Newport 1918-R) just before passing through the focusing lens and generally adjusted to a pulse energy between 0.5 and 1 μJ. The TEM is operated thermionically to provide enough signal for rapid, relatively easy alignment. The electron beam is aligned to the optic axis using standard procedure, and eucentric height is determined for the holey carbon film on the TEM grid. As the TEM shifts between the lower magnification range (18.5 to 1850x, hereafter labeled LM) to medium magnification range (1500 to 250,000x hereafter labeled M-SA), the image

significantly shifts and rotates due to the precession of the electrons as they travel through the magnetic fields in the electron lenses. The experiments in this dissertation were performed in the M-SA range, but this range does not offer a large enough field of view to find or center the laser. Thus, a distinguishing feature – the asymmetric center marker of the TEM grid – is first centered on the camera in the M-SA range. The magnification is then minimized (18.5x on the phosphor screen or 21x on the camera) so that the majority of the squares is visible, and a marker is placed on the camera live-feed marking the location on the specimen that is centered in the appropriate magnification range. The TEM stage is then moved so that the marker is in the middle of a TEM grid square, and the histogram adjusted to include only the peak at the lowest intensity values to increase contrast.

The position of the retroreflector on the delay stage is then adjusted depending on the timescales to be probed in the experiment. For femtosecond experiments, the delay stage is moved to experimental time zero. For nanosecond experiments, the delay stage is moved as close to the front of the stage as possible. This adjustment minimizes the relative path-length difference between the pump pulse traveling down the femtosecond beam line and the electron-extracting pulses traveling down the nanosecond beam line.

The shutter blocking the pump laser from entering the column is then opened, and the carbon film on the TEM grid is exposed to the pump laser briefly before being blocked again. The operator inspects the carbon film for evidence of contrast changes, which indicates interaction of the laser and the carbon. An undamaged carbon support

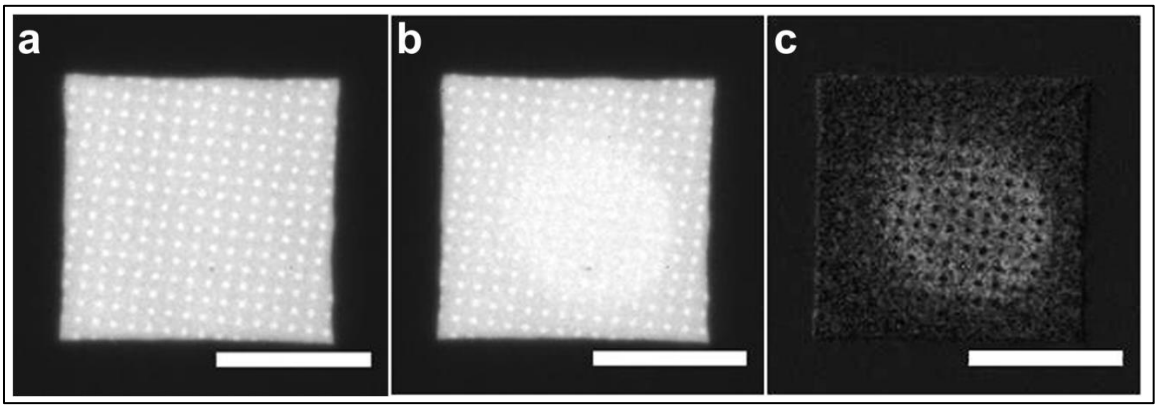

Figure 2.5 | **Alignment of pump laser on carbon support film.** (a) Carbon support film before laser exposure. (b) Carbon support film after exposure. (c) (b) subtracted from (a) to show damage due to laser exposure more clearly. Scale bars represent 50 μm. Images courtesy of Daniel Cremons.

film is shown in Figure 2.5(a), and the same support film is shown in Figure 2.5(b). The damaged region is particularly obvious in the difference image in Figure 2.5(c), in which Figure 2.5(b) is subtracted from Figure 2.5(a). All images were acquired at 21x magnification. The distance to be moved can be measured on the camera, and the lens moved incrementally. Each small tick on the lens micrometers corresponds to about 10 μm movement of the laser on the quantifoil. Although the x- and y-micrometers move orthogonally with respect to one another, these movements are often rotated with respect to the desired directions of movement. Before movement, the lens positions are noted to provide a starting point in case the pump laser – after movement – is no longer visible. The stage is then moved until the marker is centered in an undamaged grid square, and the carbon film is exposed again to the laser to determine the new position. This procedure is repeated until the damaged spot is centered on the marker. The laser power can then be reduced, and the position checked more precisely.

If the laser spot needs to be radically realigned or cannot be found with the above

method, two actions can be taken. If possible, lens micrometer positions from previous users are consulted and tested. Next, the laser power is checked. For pulse energies less than ~0.5 μJ, contrast changes are observed only after exposures of several seconds. Above 1 μJ, the damaged spot is generally larger than one square, and the beam outline is convolved with the damage from the heated copper grid bars, which makes the center challenging to determine. If neither of these alternatives work, after noting the initial lens positions, the operator may increase magnification and begin to systematically vary the lens x- and y-positions, watching the grid bar position for sudden changes in position. These changes indicate a change in temperature in the grid and thus the laser being present on the grid. The laser is then blocked, and the grid scanned for damage. If a new damaged spot is located, the lens micrometers are moved as described previously until the pump laser is aligned.

Once the pump laser is aligned at experimental time zero, the laser alignment over the stage range and thus temporal range to be used in the experiment is checked. The laser is blocked, and the TEM stage is adjusted so that an undamaged carbon film grid square is centered on the marker. The delay stage is moved to the end of the time range of interest, and the laser is unshuttered. The laser spot must remain within the same square; otherwise, the two mirrors just before the delay stage are adjusted to minimize laser beam movement as the delay stage is scanned over its entire range. After moving to a new grid square, the delay stage is moved to at least a hundred picoseconds before experimental time zero, and the laser alignment again checked.

Once the pump is aligned, the power meter is placed in front of the lens directing the pump laser into the TEM, and the power is adjusted using either an attenuator wheel or with the laser itself to the desired pump fluence for the experiment. The full-width at half-maximum (FWHM) of the pump beam was measured to be 124 μm using a knife-edge experiment on a reflection from the pump beam from inside the TEM. The FWHM was converted to a beam radius of 105 μm, and the average fluence used in the following experiments was thus 0.76 ± 0.04 mJ/cm^2. Calculation of the beam radius and average pump fluence is shown in Appendix D.

2.1.7 | Alignment Procedure for the Probe-extracting Laser

The first step in the alignment procedure is to operate the TEM thermionically and complete the alignments as per standard procedure. This procedure is followed to ensure that the beam is visible and aligned so that when the laser does strike the source, photo-generated electrons, following the same path, will be visible on the screen. Next, the source temperature is reduced toward room temperature until the thermionic beam is barely visible on both the phosphor screen at the bottom of the column and on the camera. The magnification is decreased so that the entire source is visible because the laser extracts electrons from the source, its sides, and the Wehnelt aperture, as shown in Figure 2.6. For the images in Figure 2.6, the nanosecond laser was scanned across a 50-μm diameter flat surface LaB_6 at 1700x magnification. Each image was acquired for 2 s. The outer ring is emission from the Wehnelt aperture, and the inner disk is emission from the LaB_6. To align the laser on the source, the lens before the probe periscope is scanned

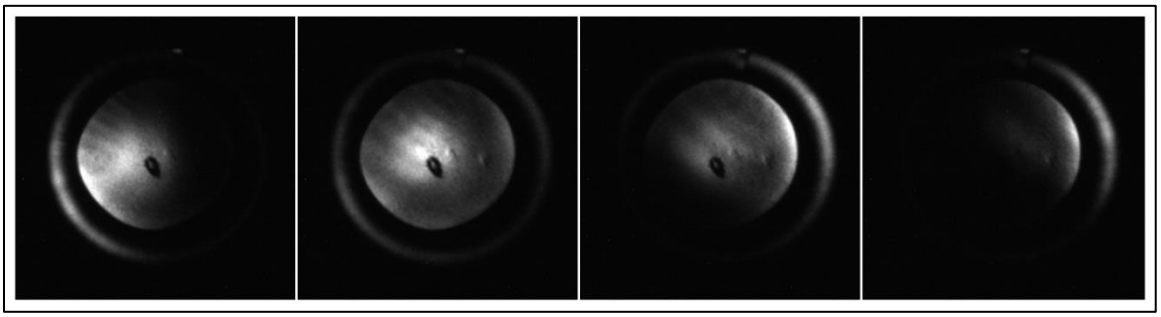

Figure 2.6 | **Photoelectron emission from the gun.** Photoelectron emission as the nanosecond laser is scanned across the gun region. The outer ring is emission from the Wehnelt aperture, and the inner disk is the 50-μm diameter flat surface LaB_6. Images courtesy of Daniel Cremons.

methodically until additional intensity is visible on the screen. The electrons extracted from the Wehnelt aperture often appear as flashes on the camera and serve as landmarks that the lens micrometers are near their optimal position. At this point, small adjustments are needed to optimize the position of the laser on the LaB_6, which are carried out at higher magnifications. Empirically, electrons extracted from the LaB_6 have been noted to decrease in intensity throughout long experiments compared to those from the sides of the source crystal and the Wehnelt aperture.

2.1.8 | Alignment of the Photoelectron Beam

Once the pump laser and probe-extracting laser are aligned, the source is brought to room temperature unless otherwise stated, and the photoelectron beam is aligned. The gun tilt (tilting of the electron beam to be parallel to the TEM optic axis) and gun shift (shift of the electron beam onto the optic axis) are not usually noticeably improved if further adjusted when the Femto is operated with photoelectrons. However, these two alignments can sometimes be re-adjusted to compensate slightly for a non-circular

crossover, as is the case for a source near the end of its lifetime. Next, the appropriate condenser aperture is chosen. For the experiments in this thesis, one of the two larger apertures was used because, for most of the experiments, the limiting factor was signal rather than coherency. The largest aperture is three millimeters in diameter, and the second largest diameter is 200 μm. Once the aperture for the experiments is chosen, the condenser astigmatism is corrected, and the specimen returned to its previously saved eucentric height. For these experiments, the photoelectron beam was not generally aligned further since high spatial resolution was not required. For many of the experiments, contrast was further enhanced by inserting and aligning an objective aperture (usually with a diameter of 100 or 40 μm), which allows only electrons that have been directly transmitted or scattered into small angles around the direct beam to form the image. Thus, areas of the specimen that scatter into Bragg angles or high angles will be excluded and appear dark.

2.1.9 | Environmental Instabilities and Effect on Experiments

For the last two years of my doctoral studies, a temperature monitoring system has offered continuous recording of the environmental temperature. Three temperature probes are placed throughout the room. One is placed on the laser table, another on the TEM by the cold finger dewar, and the third by the door. The TEM cold finger is a metal rod extending into the TEM column close to the specimen. When cooled by liquid nitrogen, the rod collects contaminants from the specimen and specimen insertion process *via* condensation. The temperature from all three probes is logged and recorded

continuously and can be compared to experimental data to correlate instabilities in photoelectron intensity with temperature swings. In addition, the image acquisition process is automated so that the user can leave the room and minimize temperature swings with the user present.

2.1.10 | Measures to Minimize Environmental Impacts on Dynamics

Before any of the laser system was aligned, the lasers were allowed to pass through the entire optical system, including the focusing lens before the periscopes for thirty to sixty minutes to allow the room temperature to stabilize as close as possible to the experimental conditions. The temperature is also continuously monitored to compare to image sequences if desired. Finally, the amount of time spent in the room and the number of times the door was opened and closed were minimized to help stabilize the temperature and prevent frequent temperature swings.

To deconvolute any change in imaging conditions associated with the room environment from the change in images due to the dynamics, up to four control experiments were performed. The first was to acquire ten or more images before experimental time zero. These images exposed whether the repetition rate had been correctly chosen so that the dynamics were truly reversible (*i.e.*, the specimen relaxed to its initial state before the arrival of the next pump pulse). The second measure was to randomize the order in which the time points were acquired. For most experiments, the electron beam would drift or decrease in intensity due to laser drift, most often due to changes in the room temperature or other environmental impacts (*e.g.*, HVAC cycles,

opening and closing of the door). Image sequences were then played in both time point order and acquisition order and compared. Changes in image intensity that trended with the acquisition order could then be identified as resulting from environmental factors, such as large oscillations in room temperature or specimen drift, and removed if possible. Changes in image intensity that occurred randomly or even before time zero due to specimen drift or beam instability could be used to identify noise and its effect on observed dynamics.

The next two measures are more traditional control experiments. Images were acquired in which the pump beam was placed at a time point where dynamics would normally be observed. The acquire series function offered by the CCD camera manufactuer Gatan was activated to acquire a series of images at this time point for the same exposure times and for a similar total length of time that an individual scan with pump movement would require. This image sequence showed whether changes in the image intensity were due to changes in imaging conditions rather than a material response. An image sequence was also acquired in which the pump beam was removed from the specimen. Similarly, the acquire series function was activated for the same exposure time and time needed to acquire a scan with pump movement to elucidate the impact of specimen drift and thus changing imaging conditions on the image intensity.

2.2 | Determining the Ultimate Spatial Resolution of Nanosecond UEM Experiments

The FEI Tecnai Femto can achieve 1.4 angstrom (Å) resolution when operated

thermionically with a 15 μm-diameter LaB_6 (not graphite-coated) and 6 Å when operated with electron packets with 50 μm-diameter LaB_6 (not graphite-coated). One of the first projects I undertook after the microscope was operational in January 2015 was to determine the spatial resolution of the microscope. The very first UEM, developed in 2005 in the lab of Dr. Ahmed Zewail, achieved resolution of 3.4 Å but did not provide a procedure.[342-343] The challenges to overcome included the low number of photoelectrons relative to thermionic operation, the specimen drift, the stability of the electron source, and the spatial coherency of the electron pulses. The specimen used here was WS_2 nanoparticles and nanotubes, which have an interplanar spacing of 6 Å, dropcast onto a lacey carbon support film on a TEM grid.

The number of photoelectrons in a train of packets is dramatically lower than a thermionic beam. This reduction stems from the pulsed nature of the beam, the intense, localized laser heating which can ablate material from the source and create non-emitting regions, and – most importantly – electron-electron repulsion within large electron pulses. This repulsion is responsible for the spreading of the electron pulses in both space and time, reducing the achievable spatial and temporal resolution. Higher spatial resolution requires fewer electrons in each pulse and thus dimmer illumination, which necessitates completing alignments and focusing on the camera, which has a lower refresh rate than the human eye and thus increases the length of time needed to complete alignments. In addition, the nanosecond laser system was used to generate an order of magnitude more photoelectrons than the femtosecond laser.

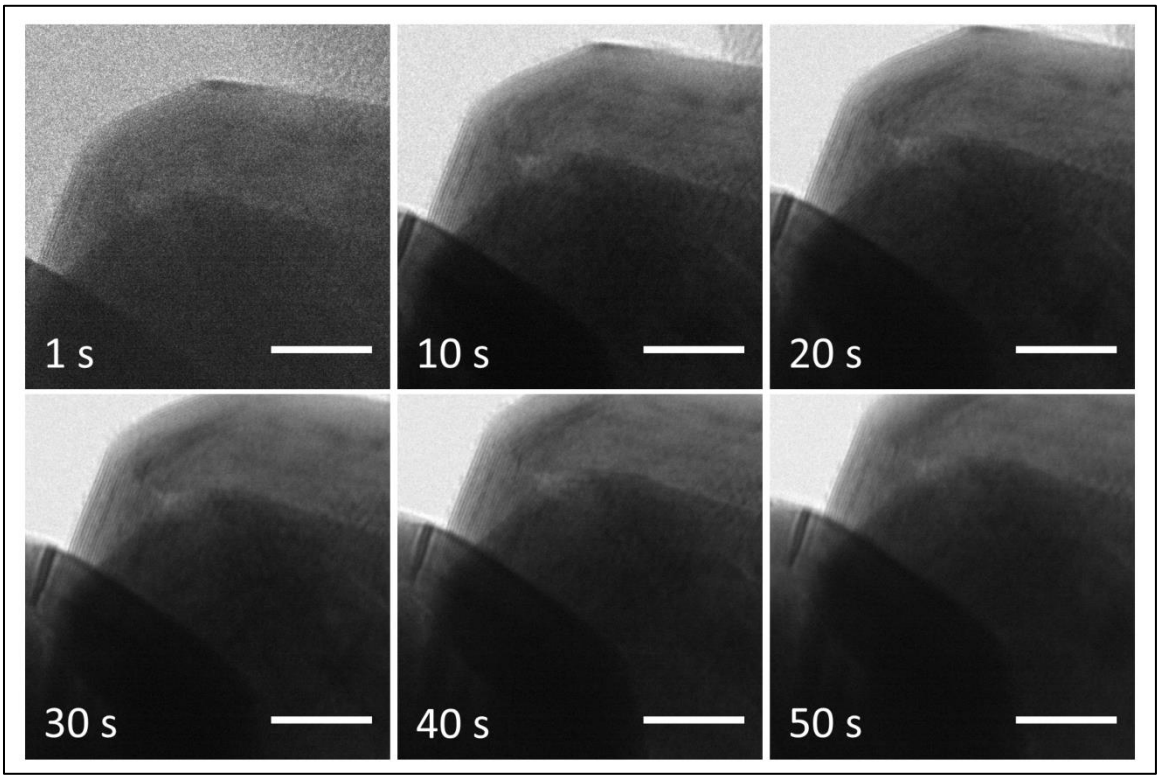

Figure 2.7 | **Specimen drift vs. acquisition time.** The same particle is imaged with 1, 10, 20, 30, 40, and 50 s acquisition times. The lattice fringes along the edge of WS_2 nanoparticle become more visible with acquisition time until acquisition times longer than 20 s, after which they are blurred as the specimen drifts. The lattice fringes along the drift direction remain clear regardless of acquisition time. Scale bar represents 20 nm.

Because of the lower number of photo-electrons than thermionic beams, the required acquisition times are constrained by the specimen drift rates. In Figure 2.7, a WS_2 nanoparticle is imaged at various acquisition times but otherwise the same imaging conditions. In particular, the magnification is 150,000x, which corresponds to 0.07 nm per pixel, and a condenser aperture of diameter 100 μm and objective aperture of diameter 40 μm were used with spot size 3. At 1-s acquisition times, the lattice fringes are not visible. The fringes become clearer for 10 s and become most clear when the image is acquired for 20 s. The fringes quickly lose clarity at longer acquisition times

(30, 40, and 50 s) due to specimen drift because the fringes in the direction of the direction of the specimen drift remain clear throughout.

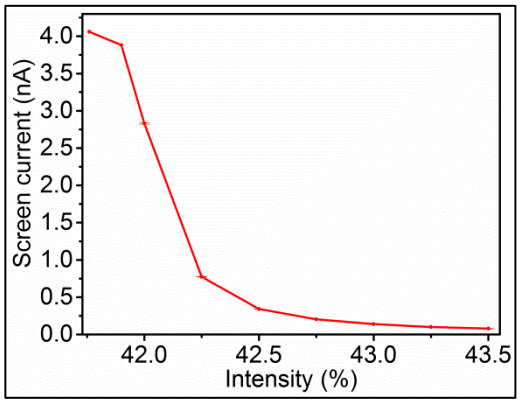

Figure 2.8 | **Screen current vs. intensity setting**. Current measured at the phosphor viewing screen relative to the intensity (percentage of total condenser lens strength).

To estimate the appropriate acquisition times, the beam was spread to produce currents similar to that observed for bright photoelectron beams, and images were acquired at various acquisition times and magnifications. Figure 2.8 shows the average current measured at the phosphor viewing screen before the camera versus the intensity (percentage of the condenser lens strength) with the condenser and objective apertures and spot size listed above. The magnification was 71,000x. The closest camera magnification is 80,000x. The screen current values do not exactly correlate with the current incident on the camera but do reflect the trend of the current with intensity.

To determine the appropriate acquisition time, the images in Figure 2.9 were acquired at 80,000x, which corresponds to 0.13 nm/pixel, with the same condenser aperture, objective aperture, and spot size as Figure 2.7 and Figure 2.8, at various acquisition times. The two images outlined in red were acquired at 42.23% intensity, which corresponds to ~0.8 nA of screen current in Figure 2.8. At this relatively high current, the lattice fringes are visible even with acquisition times as small as 2 s. The images outlined in green were acquired at 43.00% intensity, which corresponds to ~0.1

nA of screen current or an eightfold reduction in the number of electrons, and the lattice fringes are not visible until the image is acquired for at least 20 s, approximately eight times the acquisition time required for the higher current.

As seen in Figure 2.10, images acquired at 100,000x, which corresponds to 0.11 nm per pixel, with the same condenser and objective apertures and spot size as before show a similar trend in Figure 2.9. The two images outlined in red were acquired at 42.23% intensity (~0.8 nA), and the lattice fringes are again visible even at low acquisition times. The images outlined in green were acquired at 43.00% intensity (~0.1 nA), and the lattice fringes are most obvious at 20 s. For the 30 s acquisition, the lattice

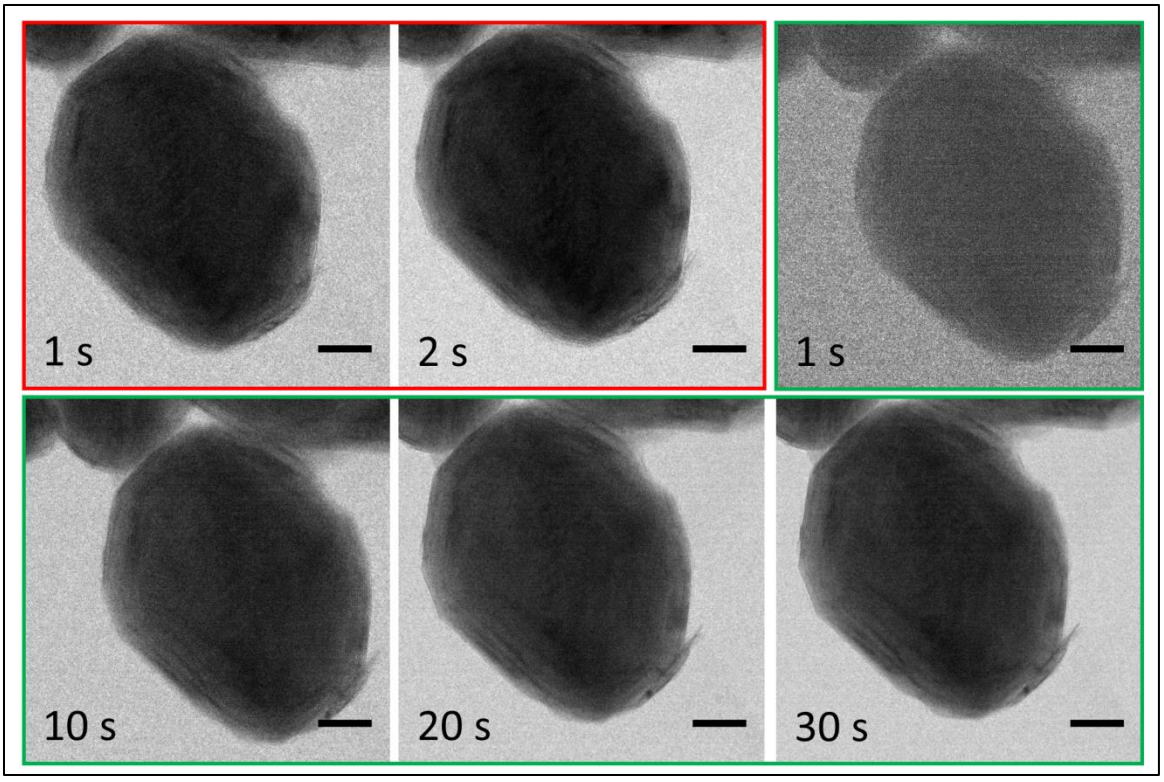

Figure 2.9 | **Acquisition time vs. intensity at 80,000x magnification.** The images outlined in red were acquired at 42.23% of the total lens strength, and the images outlined in green were acquired at 43.00%. All scale bars represent 20 nm.

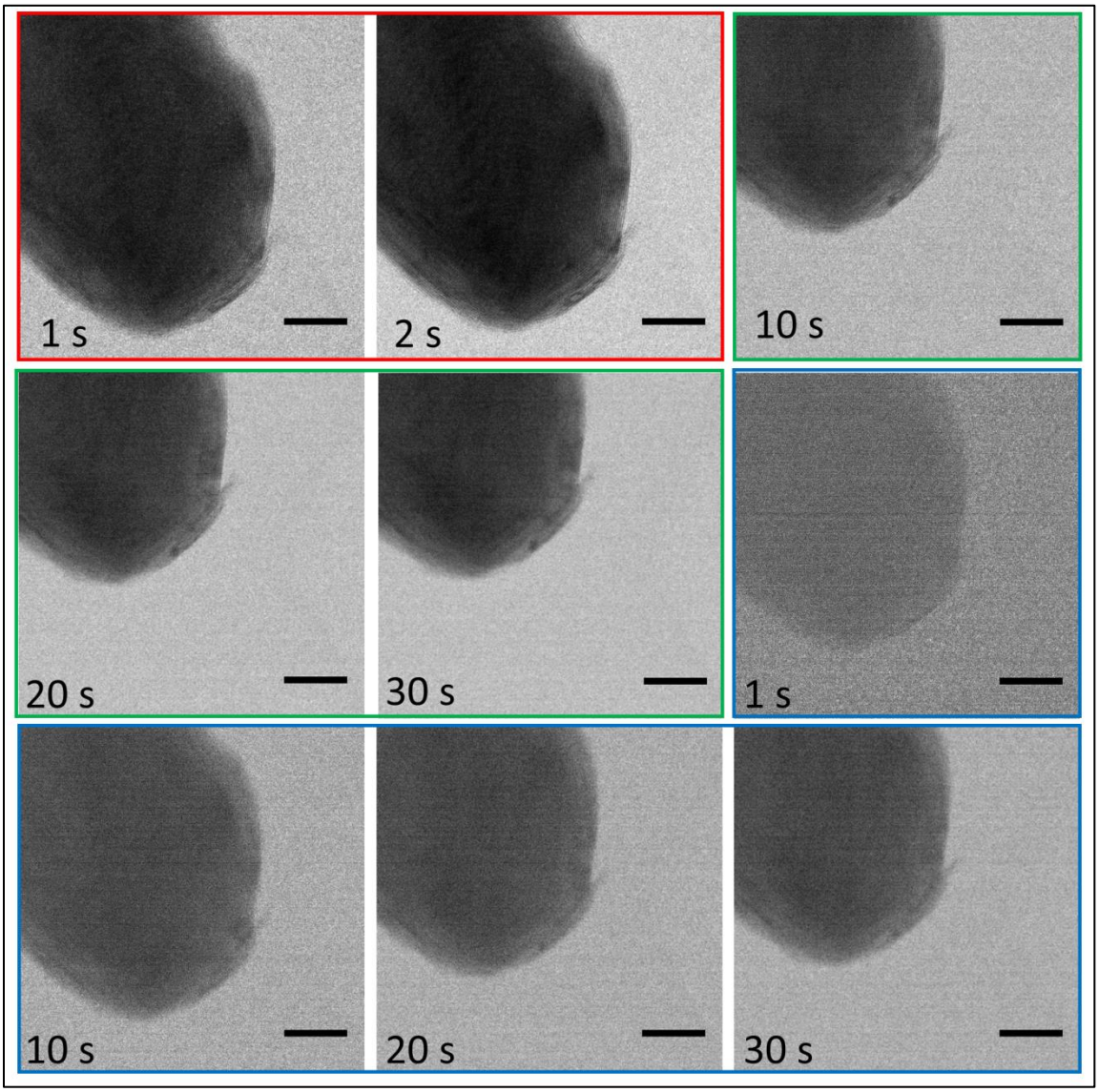

Figure 2.10 | **Acquisition time vs. intensity at 100,000x magnification.** The images outlined in red were acquired at 42.23% of the total lens strength, and the images outlined in green were acquired at 43.00%. The images outlines in blue were acquired at 43.47%. All scale bars represent 20 nm.

fringes are blurred by specimen drift but still somewhat visible. The images outlined in blue were acquired at 43.47% intensity, which corresponds to a screen current of ~0.08 nA. At such low electron counts, the lattice fringes are not visible even for 30 s acquisitions, suggesting that extremely low photoelectron counts are not conducive to

lattice fringe imaging.

Because of the importance of high photoelectron count, the next step was to determine the laser repetition rate that could maximize the UV power. At 46% of the total power on the nanosecond laser, I varied the repetition rate from 1 to 100 kHz and measured the average UV power, as plotted in Figure 2.11. The maximum UV power is obtained for 20 kHz for this wedge power. A higher percentage on the nanosecond laser may be optimized at a different repetition rate.

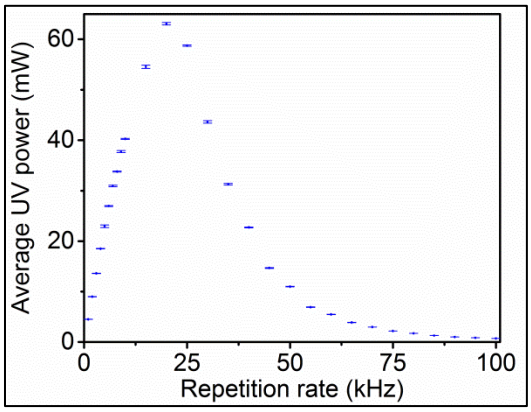

Figure 2.11 | **Average UV power vs. nanosecond repetition rate.** The average UV power in mW as the repetition rate is changed at 46% total power on the nanosecond laser.

The other limiting factor on lattice fringe imaging is the specimen drift rate. Average specimen drift rates for a nanotube and nanoparticle were measured. Two series of images were acquired for the nanotube shown in Figure 2.12(a); the first set of 50 images was acquired immediately after the stage was moved to capture the maximum drift due to the stage. The first image in the second set of 50 images was acquired 93 seconds after the last image in the first set. A representative image of the nanoparticle is shown in Figure 2.12(c). All sets of images were acquired with 5 s intervals between acquisitions, 1 s exposure time, and at 150,000x magnification (0.0342871 nm per pixel). The images were drift-corrected using the procedure described in Section 2.4.1, and the drift corrections along with linear fits with intercepts set to 0 are plotted in Figure 2.12.

For the nanoparticle drift in Figure 2.12(d), the drift corrections in the *x*- and *y*-directions were converted to polar length coordinate *R*:

$$R = \sqrt{x^2 + y^2} \tag{2.1}$$

where *x* is the drift correction in the horizontal direction and *y* is the drift correction in the vertical direction. The slopes of those fits are 0.03 nm/s for Figure 2.12(b) and 0.02 nm/s for Figure 2.12(d). At these drift rates, the maximum acquisition time is between 23 and 35 s. For specimens where the stage has been allowed to equilibrate after movement, the maximum acquisition time will be higher.

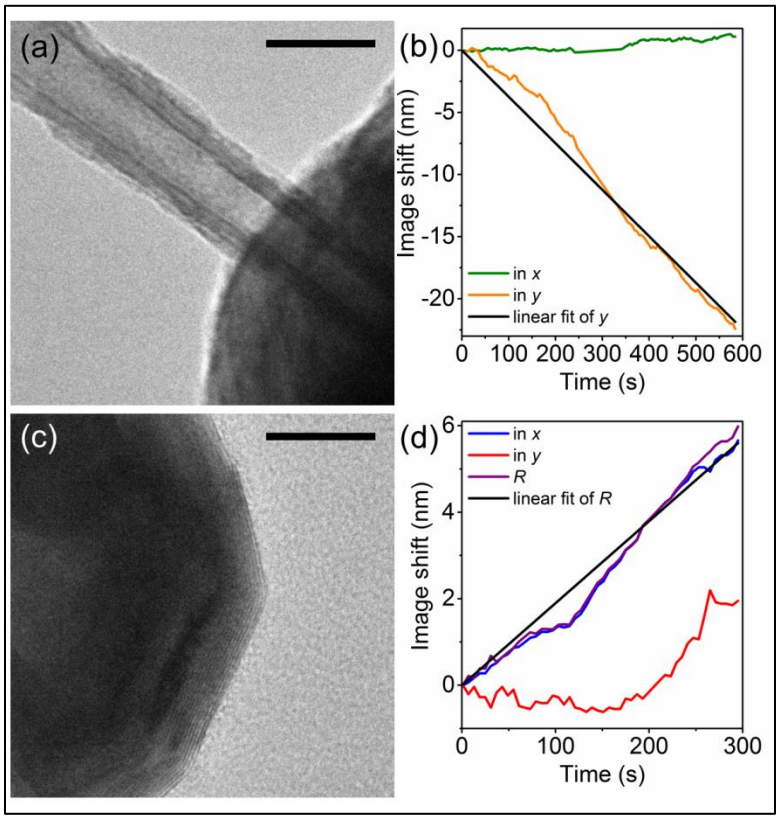

Figure 2.12 | **Drift rates.** (a) Representative image of nanotube for which the drift correction is plotted in (b). Scale bar is 20 nm. (b) Drift correction in horizontal (*x*) or green direction and in vertical (*y*) or yellow direction. The linear fit to vertical drift correction is plotted in black. (c) Representative image of nanoparticle for which drift correction is plotted in (d). Scale bar is 20 nm. (d) Drift correction in *x*- (blue) and *y*-directions (red). The total drift in polar coordinate of length *R* is plotted in purple and fit with a linear equation with the intercept set to zero.

Because of the low number of photoelectrons and thus the long time to align the microscope for high-magnification work, the number of photoelectron emitted must be

stable. Changes in the non-graphite-coated LaB_6 temperature caused source movement, necessitating re-alignment of the probe-extracting laser and re-alignment of the photoelectron packets. I monitored the photoelectron count versus time over three separate time intervals on two separate days, which are plotted in Figure 2.13. Images of the crossover were captured at a magnification of 5,000x (1.04 nm per pixel) for 0.5 s. Representative crossovers for three image sequences are shown in Figure 2.13(a), (c), and (e). The total counts in each image

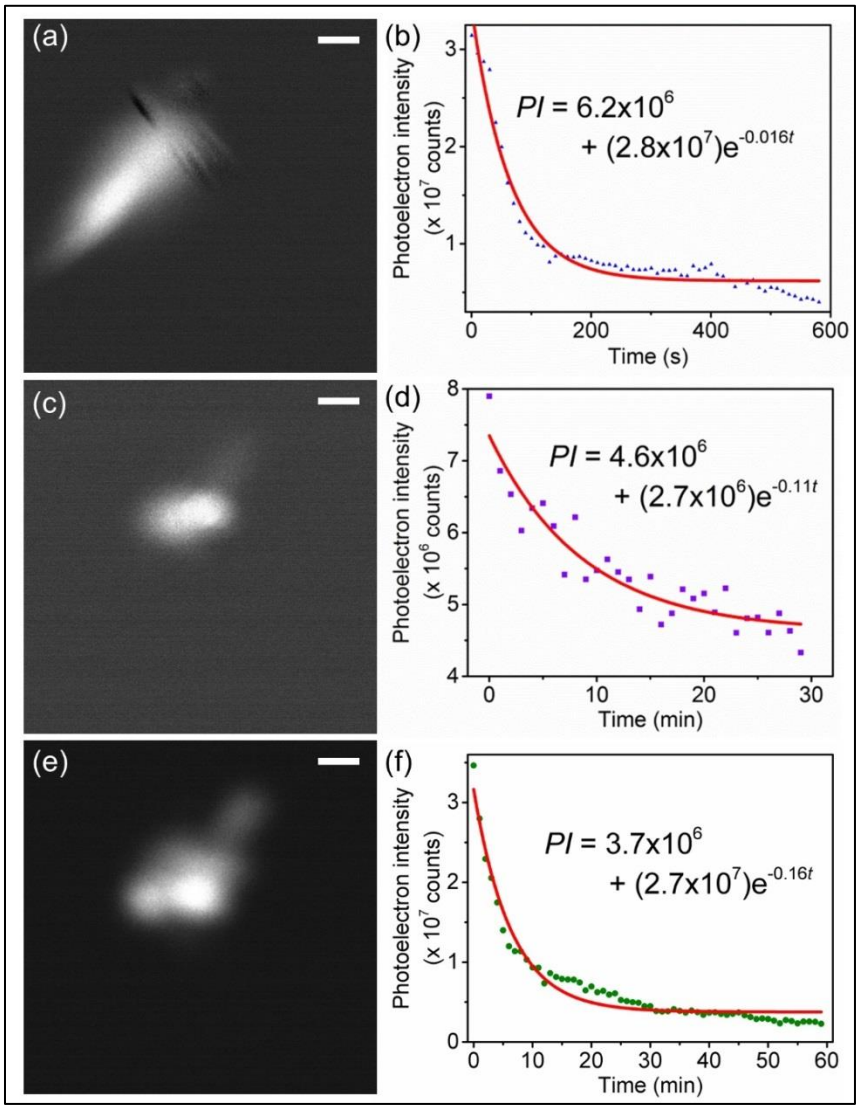

Figure 2.13 | **Photoelectron intensity decay.** (a), (c), and (e) Representative images of photoelectron crossovers. Scale bars represent 250 nm. (b), (d), and (f) are the total number of counts in the images vs. time with exponential decay fits. Photoelectron intensity is abbreviated *PI*, and time is abbreviated *t*.

were summed and plotted versus the time during which they were acquired in Figure 2.13(b), (d), and (f). The MATLAB code computing these sums is included in Appendix H.1. These points were fit with exponential decays, shown on the plots, in Origin. The images in Figure 2.13(a) and (b) were acquired at a heat-to value of 20, which produced some thermionic emission, with 10 s between the beginning of each camera exposure. The thermionic emission was captured after the image series was acquired, and the counts in that image were summed and subtracted from each sum in the series to extrapolate the photoelectron intensity. The nanosecond laser was set to 25 kHz with 44% power. A sapphire sampling crystal sent some of the UV power to a detector rather than the source. The images in Figure 2.13(c)-(f) were acquired with acquisition intervals of 60 s, and the nanosecond laser was set to 20 kHz, with 50% power. Images (c) and (d) came from different laser positions on the electron source than images (e) and (f) due to the photoelectrons fading to undetectable between image sequences.

The widely varying photoelectron lifetimes show the importance of a stable electron source as well as high emittance from the source. The three 1/*e* lifetimes of the photoelectron crossovers are 1.04 minutes, 10 minutes, and 6 minutes, respectively. As well as having the longest lifetime, the photoelectron crossover in Figure 2.13(c) and (d) also begins with the highest number of counts, which means that even as it decays, the beam still provides enough counts ($> 10^7$) to build up signal in a reasonable time.

The shape of the crossover can be affected by changing the step size. The step size is a measure of the Wehnelt bias and thus the crossover location. The nanosecond

laser was set to 50 kHz at 55% power, and the source was completely cooled for these experiments. Images of the photoelectron crossover were acquired at 14,500x (0.36 nm per pixel) for 1 s as the step size was varied over its full range (1-6) and are shown in Figure 2.14. The total number of counts in each image appeared to decrease with increasing step size, but this trend could be due to the decay of the photoelectron density with time, as discussed above. This change in shape with bias is also observed in graphite-coated tips, as reported recently.[276]

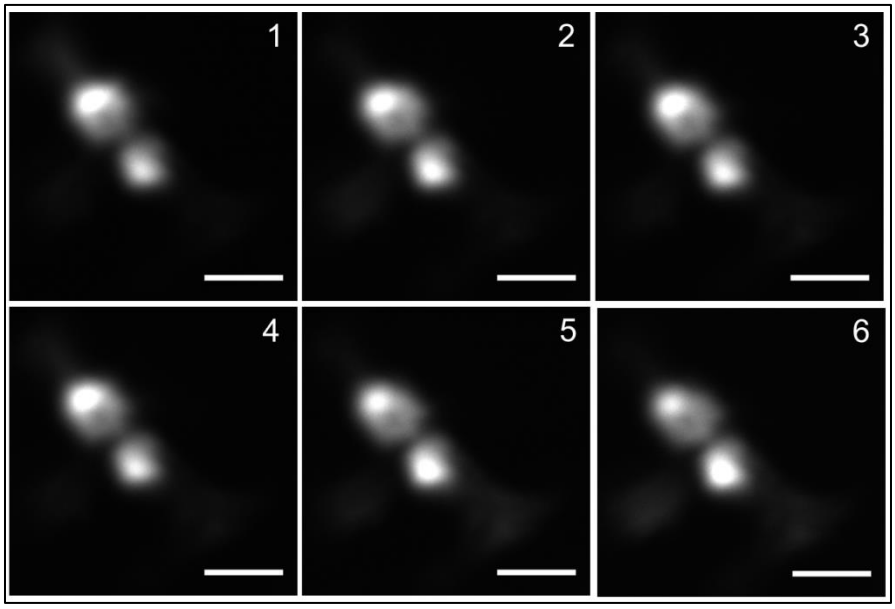

Figure 2.14 | **Step size effect on crossover.** Images of the crossover at different step size values (in upper right hand corner of each image). All scale bars represent 200 nm.

The number of photoelectrons can be increased by heating the electron source to a level below thermionic emission. As shown in Figure 2.15, the photoelectron crossover is imaged at different heat-to values, where saturated thermionic emission is achieved at a heat-to value of 28. The onset of thermionic emission is 19. The nanosecond laser is set to 50 kHz, with 55% power, and the laser was irised down to 30.165 mW of ultraviolet light on the source. As the heat-to value

increases, the number of counts increases, from $3x10^8$ to $2x10^9$ total counts, and the shape of the crossover changes to include more emission spots.

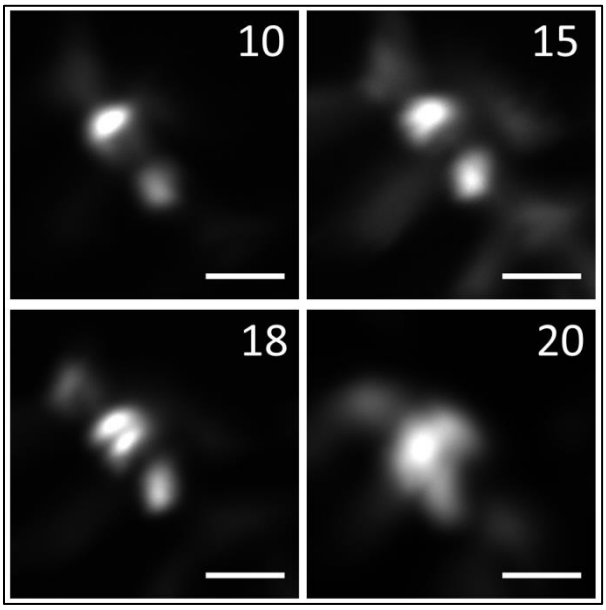

Figure 2.15 | **Photoelectron crossover shape at different heat-to values.** Images of the photoelectron crossover at different heat-to values given in the upper right hand corners. Scale bars represent 200 nm.

Crossover size and shape affect lattice fringe imaging due to changes in spatial coherence. Even under bright illumination, lattice fringes are still not consistently observed, which indicates that the spatial coherence of the source plays an important role in determining spatial resolution. Spatial coherence is a measure of the phase relationship between different probing electrons. Because electrons are fermions, each wave can interfere only with different parts of itself. The detector then sees an incoherent average of these interference patterns. With a completely spatially coherent source, the electron waves are all emitted with the same wavelength and produce identical interference patterns at the detector, producing interference fringes like lattice fringes, which are phase contrast, with perfect contrast. A real source is only partially coherent, meaning that the electrons are emitted with a spectrum of wavelengths that produce slightly different interference patterns at the source. A larger range of wavelengths decreases the contrast in the averaged interference pattern and eventually

leads to no contrast at all. Moreover, it can be shown that coherence between points extends to only a small region around those points.[344] Thus, multiple disjointed or broad sources, as seen in Figure 2.15, severely limit the resolution of the instrument. These multiple point emitters are particularly present near the end of the source's useful lifetime, and, thus, high-resolution imaging is best conducted near the beginning of the source's lifetime. Further work is needed to characterize the coherence of the source and the necessary coherence to image lattice fringes consistently.

All of these factors came together in the experiment in which lattice fringes in a WS_2 nanotube were imaged. The nanosecond laser was set to 10 kHz, 69% total power. The laser was irised down to give 33 mW of UV incident into the top periscope. The images in Figure 2.16 are both taken at 150,000x, which corresponds to 0.07 nm per pixel. The condenser aperture of diameter 100 µm was used. The thermionic image, on the left in Figure 2.16, was acquired for 1 s and binned by 2, and the photoelectron image, on the right in Figure 2.16, was acquired for 25 s and also binned by 2. The lattice fringes are clearest in the

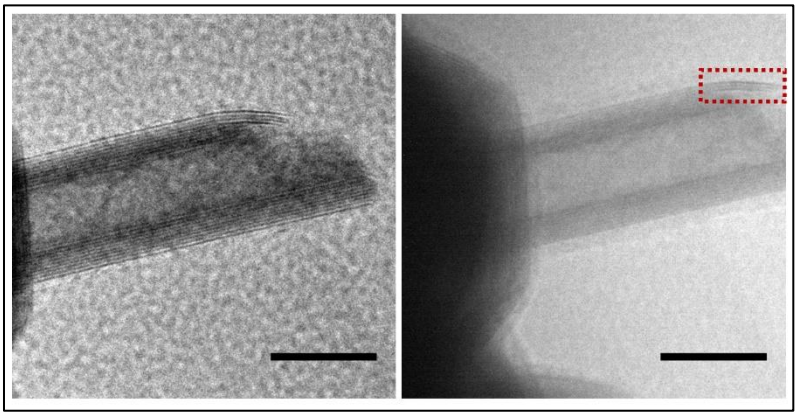

Figure 2.16 | **Lattice fringe imaging with thermionic and photoelectron beams.** Lattice fringes of a WS_2 nanotube are imaged with thermionic (left) and photoelectron (right) sources. On the right, the lattice fringes are clearest in the red box. Scale bars represent 20 nm.

photoelectron image in the area outlined in the red box.

Once I could image lattice fringes, I turned my attention to the study of material dynamics in TMDs. The first step in that process is to fabricate a specimen that is suited for study with UEM. In addition to the requirements for a TEM specimen, namely electron transparency and lateral dimensions of less than 3 mm (the diameter of the TEM column), ideal UEM specimens dissipate heat quickly so that higher repetition rates and thus lower acquisition times can be used. In the next section, I discuss the fabrication procedure for the MoS_2 specimen that I studied in this dissertation.

2.3 | Preparation of MoS_2 Specimen

Reliable, controlled fabrication of TMD specimens is an active area of research. The most famous method is micromechanical exfoliation, in which layers are peeled from a bulk specimen and then thinned further with strips of tape. Although it certainly does not offer the most control over the number of layers in the resulting specimen, this method is still the simplest technique to produce thin specimens, and thus it was used in this dissertation. The exfoliation and transfer procedure used will be explained in depth here.

2.3.1 | Micromechanical Exfoliation and Transfer to a TEM Grid

Synthetic MoS_2 was purchased from 2D Semiconductors in the 2H polymorph and is shown in Figure 2.17(a). A piece of Scotch tape was used to exfoliate thin flakes of MoS_2, and Scotch tape was applied sixteen subsequent times to those initially

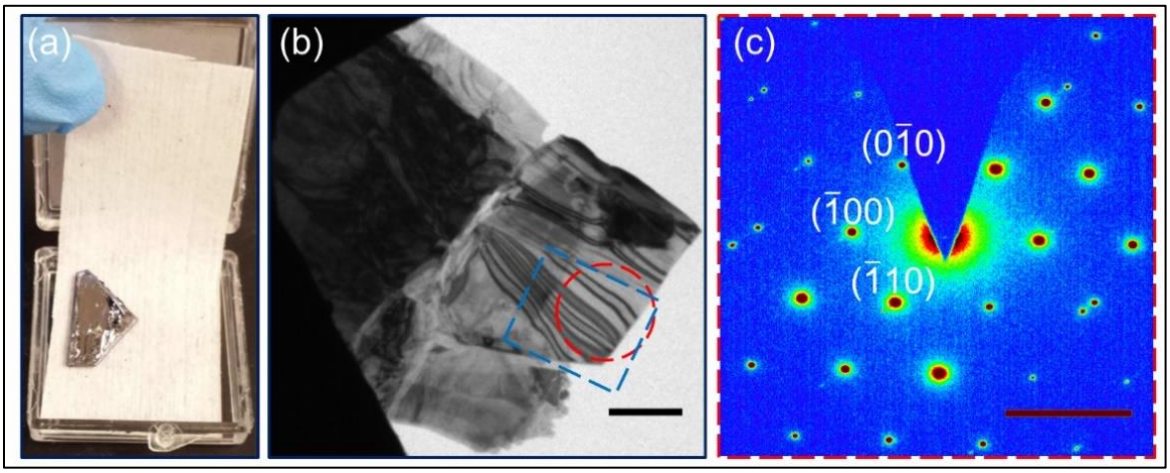

Figure 2.17 | **MoS_2 specimen examined in this thesis.** (a) Bulk specimen from which TEM specimen was exfoliated. (b) Bright-field image of MoS_2 flake studied. Flake in the upper right was examined in detail, particularly the area outlined in blue. The red circle indicates the position of the selected area diffraction (SAD) aperture when the diffraction pattern in (c) was collected. Scale bar is 1 μm. (c) SAD pattern taken of the flake in (b), where the SAD aperture was positioned as indicated by the red circle. The scale bar is 5 nm^{-1}.

exfoliated flakes to produce electron-transparent flakes interspersed with optically opaque flakes. Next, the tape was placed on a NaCl crystal, and the back of the tape was rubbed firmly with tweezers to transfer some flakes to the crystal. The crystal was dipped twice in methanol and dried on a hotplate at 85°C. This step was repeated three more times, with the final heating temperature at 60°C. The tape was rubbed a final time on the crystal, and 40 μL of 4 wt% polymethylmethacryalate (PMMA)-anisole solution was dropcast onto the surface of the crystal with the flakes. The sample was cured for 5 minutes at 100°C, and the salt was dissolved in deionized water. The PMMA film was rinsed in methanol several times and then placed in a viewing glass with a shallow methanol bath under the optical microscope while the film was positioned over a 2000-mesh copper grid. Acetone was gently added to dissolve the PMMA with minimal

movement of the film, and the grid was left in an acetone bath to dissolve remaining PMMA for approximately two hours.

2.3.2 | Characterization of Specimen

The BF TEM image in Figure 2.17(b) was taken at a magnification of 1700x (3.159 nm per pixel) and acquired for 15 seconds with an objective aperture of diameter 40 μm to illustrate the geometry of the specimen. As evident from the image, the specimen comprises three flakes. The one on the left is relatively thick compared to the other two as seen by the lower intensity present, and the one at the bottom of the image does not have well-defined geometry. The flake suspended on the other two was chosen for the dynamic experiments because it displayed distinct, highly visible bands of contrast but less mass-thickness contrast than the other two. The BF images taken at different alpha-tilt angles in Figure 2.18 show that the flake is resting on the other two. These images were acquired at 2,500x for 1 s, with a 200 μm diameter condenser aperture and 40-μm diameter objective aperture centered on the unscattered beam in the diffraction pattern. In addition, the tilt series shows that the contrast moves significantly with tilt and is thus not associated with a defect but rather with bending. The diffraction pattern in Figure 2.17(c) was collected by placing a selected area diffraction (SAD) aperture with a diameter of 40 μm as shown by the red, dotted-line circle in Figure 2.17(b) and switching to diffraction mode. The magnification was 200 mm, and the acquisition time was 20 seconds. This diffraction pattern viewed along the [001] zone axis displays the characteristic hexagonal symmetry of the 2H polymorph.

The dark-field (DF) images shown in Figure 2.19 further indicate that the contrast mechanism is diffraction contrast, varying intensity in BF images due to varying degrees of diffraction across the specimen.[345] The images were all acquired with spot size 1 and a condenser aperture of diameter 200 µm. The first image is a bright-field (BF) image acquired at 2,500x for 3 s, with an objective aperture of 20 µm centered on direct beam in the diffraction pattern in the second panel, which is covered by the beam block. The

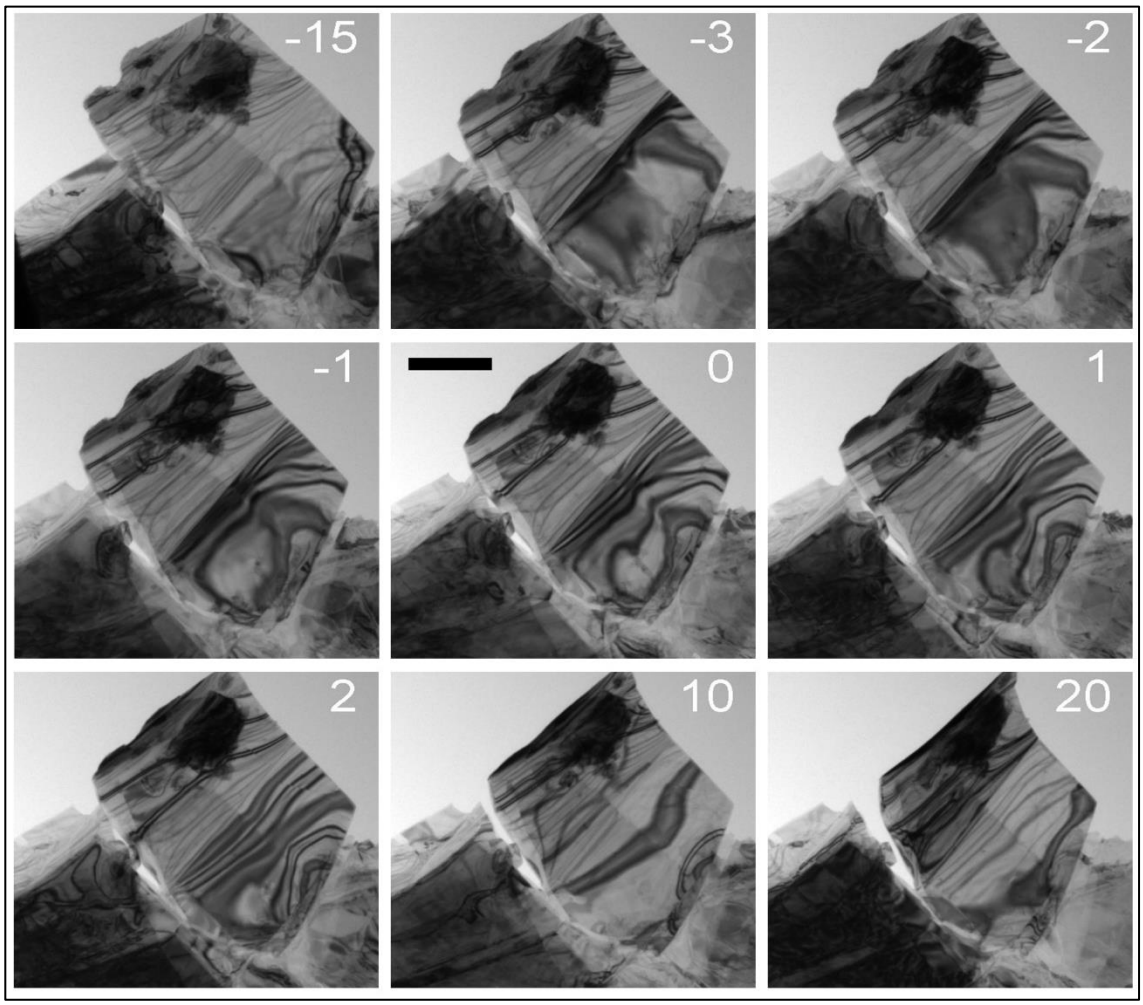

Figure 2.18 | **Bright-field (BF) images of flake at different tilt angles.** BF images of flake at different alpha-tilt angles, which are indicated in the upper right corner in each image. Scale bar represents 1 µm and is the same for all images.

diffraction pattern was captured using an SAD aperture of diameter 200 μm centered over the flakes at a camera length of 200 mm. The DF images were then captured by centering the 20-μm diameter objective aperture on the spots indexed in the upper left corner of each panel. Different contrast features appear bright because electrons from individual diffraction spots are used to produce the image, which indicates that the contrast is diffraction contrast. Combined with the observation of the significant movement of these features with specimen tilt, these DF images suggest that the contrast features are bend contours, diffraction contrast that appears due to the movement of the planes into or out of the diffraction condition with bending in the specimen.[41]

The specimen thickness was measured using EELS. The high-angle annular dark-field (HAADF) image is shown in Figure 2.20 on the far left. Because HAADF images are formed using electrons scattered at large angles, contrast is reversed from BF images; sample regions that scatter strongly are bright whereas those that scatter to small angles are dark. The area outlined in green was used to drift correct the images as a series of EEL spectra was collected on the area outlined in red, and the resulting spectra are shown in the rectangle with four quadrants labeled, where the grayscale value corresponds to number of electrons at 17.25 eV, chosen for clarity. The thicknesses were computed from those spectra using the Gatan log-ratio absolute algorithm, which uses the equation:

$$t = \lambda \ln\left(\frac{I_t}{I_0}\right) \tag{2.2}$$

where t is thickness, λ is the inelastic mean free path (IMFP), I_t is the area under spectrum,

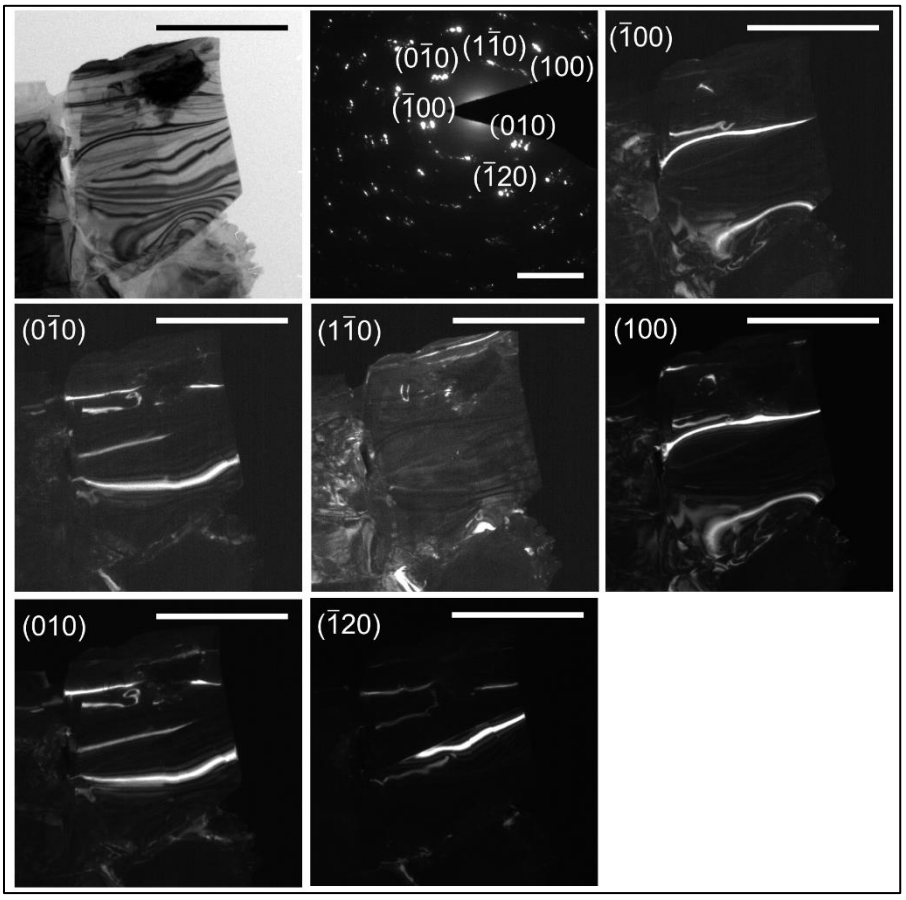

Figure 2.19 | **Dark-field images of MoS_2 flake.** The first panel is the BF image, where the objective aperture is centered on the direct beam. The second panel is the SAD pattern of the entire flake. The remaining images are DF images where the objective aperture is centered on the diffraction spot indexed in the upper left corner. Scale bars in bright- and DF images are 2 μm, and scale bar in the diffraction pattern is 5 nm^{-1}.

and I_0 is the area under the zero loss peak.[346-348] I input the beam energy $E_0 =$ 300 keV, the approximate convergence semi-angle $\beta =$ 10 millradians (mrad), the collection semi-angle (5.78 mrad), and the effective atomic number $Z_{eff} =$ 25 calculated by

$$Z_{eff} = \sum_i f_i Z_i \tag{2.3}$$

where f_i is the fraction of component *i* in the compound and Z_i is the atomic number of component *i*. The exact algorithm used to calculate the IMFP and thus thickness is

proprietary. The thicknesses in the four quadrants were then averaged to give the thickness values shown in the table. Variations in calculation of Z_{eff} and in the semi-angles due to instrument instability were found to give thicknesses within 10 nm of the values in Figure 2.20. The spectra and images were collected on an FEI Tecnai F30 at the University of Minnesota Characterization Facility.

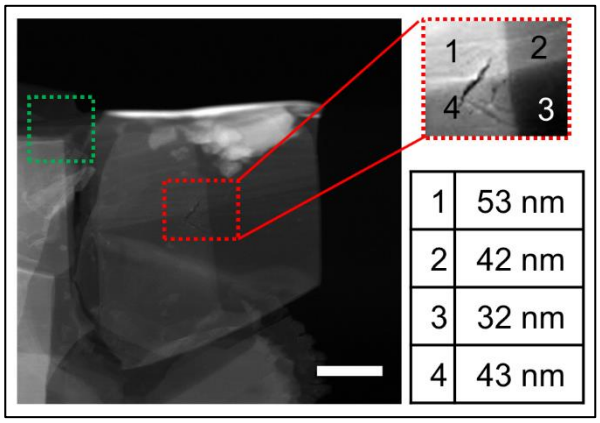

Figure 2.20 | **EELS thickness map.** HAADF image showing the area used to correct for drift outlined in green and the area over which EELS spectra were collected in red. Scale bar represents 1 μm. Average thicknesses in the four quadrants are shown in the table.

2.4 | Image Analysis Methods

The data from all of these experiments were thousands of images. Procedures and code to quantify changes in images were developed in collaboration with my collegaues in the Flannigan Research Group. The type of change varied from local changes in intensity to movement of existing intensity features. Thus, a brief, general description of the principles of analysis will be given here, with more details in the following chapters and specific codes included in Appendix H. All images had to be converted from different formats, the intensity scaled or normalized, and the specimen drift corrected for. Those procedures will be described in detail here without long descriptions in the following chapters.

2.4.1 | Conversion and Drift Correction

During long experiments, the specimen drifted in position, and images needed to be corrected to differentiate movement from the material response. Images were first batch-converted from .dm4 to .dm3 file formats using Digital Micrograph. The .dm4 file format is proprietary to Gatan, the camera manufactuer, and, until recently, could not be read in any software besides Digital Micrograph, which has its own coding language and is not optimized for batch processing as in MATLAB or ImageJ/Fiji.[349] The .dm3 files could be imported into and read by Fiji with the appropriate plugin, and outliers were removed with the built-in feature in Fiji ("Remove Outliers…"). This feature finds individual pixels whose value deviates from the median in its neighborhood by more than the user-specified threshold (0.4% in this dissertation) and applies a median filter.[192] The images were then converted to 16-bit file sizes. The contrast was enhanced using the built-in function ("Enhance Contrast…") using the normalization option. This option scales the intensity at each pixel in each image so that it fits into the range for 16-bit images (0 to 65,535), setting any pixel values below 0 to 0 and above 65,535 to 65,535.[350] The images were drift-corrected using the template-matching plugin for Fiji, which matches a template (region of interest) selected from one image to a region in the other images in the image sequence. Next, either the drift-corrected images were saved as tiffs, or the shifts in horizontal and lateral directions were saved to be imported into MATLAB later.

2.4.2 | Image Analysis

MATLAB was chosen to analyze images due to its computational power, transparency, and ease of code construction. After images were imported into MATLAB, they were drift-corrected if necessary, and then an area was selected over which a normalization factor was computed. In some cases, an area over vacuum in each image was averaged to produce the normalization factor for each image, and the same area used for each image in the sequence. In others in which the area over vacuum was small, the average intensity over the entirety of each image was used as the normalization factor. The exact approach taken for each image sequence in the subsequent chapters will be noted. Typically, a median filter was applied to reduce the noise.

For images in which the intensity oscillates in one location or high intensity appears and disappears, the changes are plotted and tracked in space-time-intensity plots. First developed by Dayne Plemmons, these three-dimensional graphs are generated by tracking the intensity variations in time along a line of pixels in an image. The ordinate is usually the distance along that line, the abscissa is the delay value at which the image was taken, and the perpendicular axis is the intensity. Slicing a space-time-intensity plot at one spatial location produces a plot of intensity versus time at one spatial location. Slicing a space-time-intensity plot at one point in time produces a plot of intensity along the line in one image/time point. These plots are useful in that they clearly capture and plot the appearance and movement of intensity through both space and time. Ridges correspond to high intensity regions travel along the line. Moreover, the slopes of the ridges corresponded to the speed at which the intensity feature moved in the direction that

the line was drawn, which was important in identifying the origin of the dynamics. The code used to produce these plots in this thesis was initially written by Ryan Gnabasik, which I have modified where necessary to more clearly capture the intensity dynamics in my experiments. For instance, I added the code necessary to analyze the raw image files (.dm3 file formats) and counts rather than the scaled intensity produced when converting to tif or jpeg formats. In addition, I added code to drift-correct the images using the shifts produced by template-matching in Fiji and to use a user-selected area to compute the normalization factor for that image.

Useful image analysis code that I developed tracks the movement of a contrast feature that stayed relative constant in shape and is given in Appendix H.3. For such features, the intensity was averaged across a small rectangle to reduce the noise, and the feature was identified as either a peak or a dip in the intensity, depending on whether that feature was a bright or dark intensity feature, respectively. The intensity was smoothed using a Savitzky-Golay filter with an order of three and various window sizes, and the peak or dip was then identified using the MATLAB function findpeaks, which identifies local maxima and minima. The peak (dip) in each image was then fit with a pseudo-Voigt with a positive (negative) amplitude. Accurately fitting the peak (dip) depended on restricting the fitting window to include only that peak (dip) and usually required identifying nearby minima (maxima). The analysis method was effective only when the contrast of and around the feature that did not change appreciably; otherwise, the correct feature was not identified consistently. Where necessary, outliers were examined

individually, and the fitting window adjusted to fit the correct feature. The centers of the fitted pseudo-Voigt functions were used as the position of the feature and plotted over time.

For both the space-time-intensity plots and the feature-position tracking plots, fast Fourier transforms (FFTs) were used to quantify frequency. The sequences were padded out to 2^{17} values with the average of the final fifty or hundred values of the intensity to allow better detection of the frequency peaks. In some cases, windowed FFTs were performed to quantify lifetimes of the different modes. These windowed FFTs were also padded to increase the frequency resolution.

2.5 | Summary

In this chapter, I have discussed the instrument, spatial resolution characterization, specimen preparation, specimen characterization, and image analysis methods used in this thesis. First, I described the two optical periscopes added to an FEI T20 TEM to produce the FEI Tecnai Femto, the first commercially available UEM, the variation in the electron source needed to make ultrafast experiments more stable, and the ultrafast laser system integrated into the TEM which includes a femtosecond and a nanosecond laser. In addition, I described the alignment procedure for the pump and probe beams and the effects of temperature on the system, as well as control experiments to deconvolute those effects from material dynamics. I have also described my work in measuring the spatial resolution of the UEM and the understanding I gained about the source characteristics and beneficial instrument practices to conduct experiments near or

at the spatial resolution limit. Next, I discussed the exfoliation and transfer procedure to prepare the main specimen of MoS_2 studied in this work and characterization of that specimen. In particular, the contrast features were identified as bend contours. Finally, drift correction, intensity normalization, space-time-intensity plots, and feature tracking were described briefly. Details pertaining to specific experiments will be given in subsequent chapters.

3 | PROPAGATION OF ACOUSTIC PHONONS

In this chapter, I will discuss my research on imaging the launch and propagation of acoustic phonons in MoS_2. Parts of this chapter are passages from the publication by A. J. McKenna, J. K. Eliason, and D. J. Flannigan titled "Spatiotemporal Evolution of Coherent Elastic Strain Waves in a Single MoS_2 Flake," which was recently accepted for publication in *Nano Letters*.[286] The properties of extended sheets of MoS_2, a heavily-studied transition-metal dichalcogenide (TMD) semiconductor, have been shown to be dependent on both layer number and structural morphology.[16-17,51,189,351-353] This has led to the development of methods aimed specifically at tuning and controlling its electronic, optical, and mechanical responses.[354-355] Among these methods, elastic deformation is particularly effective and versatile, stemming (in part) from widely-varying linear-elastic tensor values and highly direction-dependent transport properties, both of which are directly linked to the structurally-anisotropic bonding in the layered lattice type. For example, application of a tensile, compressive, or shear stress, or a substrate-induced strain, has been shown to alter the electronic and phononic band structures, as well as the effective charge-carrier masses, of few- and single-layer specimens.[87-88,146,185,187,189,352,356-361] Additionally, the elastic constitutive properties, resonant responses, and phonon-transport behaviors (*e.g.*, Young's modulus, piezoelectricity, thermoelectricity, *etc.*) have

attracted attention for energy-harvesting and energy-conversion applications, wherein the number of layers plays a distinct role owing to the effect on crystal symmetry.[37,39,120,139,142,176,362-363]

In addition to direct-contact manipulation, optical excitation offers a means to (remotely) modulate and control the structural and transport properties of MoS_2, either through the charge carriers or via the resulting lattice response.[131,134,364] Accordingly, development of a comprehensive view of the time-dependent response of MoS_2 to optical excitation – in addition to advancing fundamental understanding – could potentially influence the application space. While charge-carrier and exciton dynamics of MoS_2 have been extensively studied with ultrafast spectroscopy,[130,132,228,231,233,236,365-370] the concomitant photoexcited low-energy lattice dynamics (*e.g.*, low-frequency acoustic-phonon excitation and launch, transient thermoelasticity, optomechanical oscillation, *etc.*) have received far less attention. Indeed, most studies within this particular parameter space have focused on understanding interlayer shear and breathing modes with frequencies of ~1 THz using time-averaged Raman spectroscopy.[371-374]

Importantly, evolution of relatively low-energy coherent structural dynamics having MHz to GHz frequencies is particularly amenable to study with ultrafast electron and X-ray scattering techniques. This is due, in part, to such techniques being sensitive to atomic-scale vibrations, nanoscale elastic deformation, and mesoscale mechanical motion.[247,284,287,325,375-377] Specifically with respect to TMDs, most studies employing such methods have focused on materials that exhibit charge-density waves (*e.g.*, $TaSe_2$

and TaS_2),[255,378-383] though more-recent work has begun to focus on the semiconductors.[247,384] For MoS_2, Lindenberg and co-workers used MeV ultrafast electron diffraction to study the reciprocal-space dynamics of a monolayer specimen in a parallel-beam configuration, as detailed in Section 1.3.2.[244] In this way, they were able to measure picosecond in-plane photoinduced wrinkling, electron-phonon coupling times, and rates of thermal-energy transfer to a substrate. To date, however, the spatiotemporal evolution of photoexcited coherent elastic strain waves in MoS_2 – spanning picoseconds to microseconds (GHz to MHz) and nanometers to micrometers – has not been reported.

In this chapter, I will describe how I have used an ultrafast electron microscope (UEM)[196,273,276] to directly image the spatiotemporal dynamics of photoexcited propagating strain waves in individual, micrometer-size multilayer flakes of MoS_2. I find that the observed strain-wave dynamics can be categorized into three distinct regimes, the total temporal ranges of which span from picoseconds to microseconds, with concomitant frequencies of observed coherent oscillatory motion relaxing from GHz to MHz values. In the first regime detailed in this chapter, spanning the first few hundred picoseconds following photoexcitation, individual coherent wave trains, having distinct wave vectors and frequencies of tens of GHz, emerge and propagate at the approximate in-plane speed of sound. As previously observed in multilayer flakes of WSe_2,[247] the wave trains originate at structurally dissimilar features (*e.g.*, vacuum/crystal and crystal/crystal interfaces) and propagate along wave vectors oriented normal to, and away from, the interface. Wave-train interference effects mark the onset of the second distinct temporal

regime. Here, such effects are first observed 140 ps after photoexcitation and are characterized by the interference of two wave trains propagating along two distinct wave vectors. This continues and evolves into incoherent lattice motion across the entire flake over the span of a few nanoseconds, which will be detailed in the following chapter. I will then discuss simulations of the Lamb modes of an orthotropic plate that help explain the frequencies observed and of the changes to the diffraction contrast observed in images upon compressional and dilatational modes. I will also briefly present preliminary work to probe the launch mechanism of the acoustic phonons.

3.1 | Experimental Observation of Tens of GHz Acoustic Phonons

3.1.1 | Initial Observation of Tens of GHz Oscillations in Image Contrast

The ultrafast structural dynamics are most clearly captured in an image sequence with 1 ps time steps. The first image sequence (314 images in 1 ps time steps, seen in Figure 3.1 and Figure 3.2) was acquired at 3,500x magnification. The other two image sequences (151 images, seen in Figure 3.3, Figure 3.4, and Figure 3.5) were acquired at 6,500x magnification. All images were acquired for 50 seconds using a 2-mm diameter condenser aperture, spot size 1, and an objective aperture with a diameter of 100 μm, which was centered on the direct beam in the diffraction pattern. The source was a 50-μm diameter LaB_6 flat surface. Because these sequences correspond to the initial observation of the dynamics, the time zero in this section does not correspond to the true experimental time zero, which was determined later. The repetition rate of the femtosecond laser was set to 10 kHz for all the image sequences in this chapter. Figure

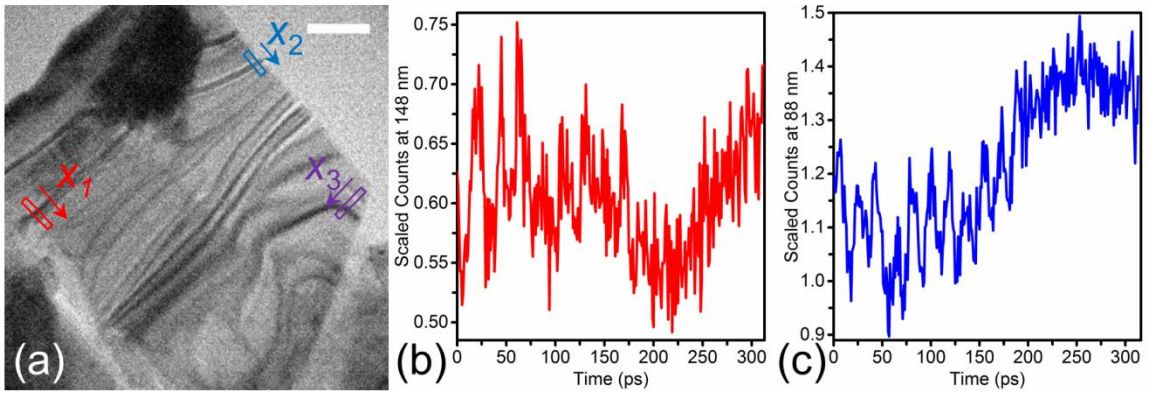

Figure 3.1 | **Observation of high-GHz oscillations.** (a) Representative BF UEM image from the sequence showing the positions of the three boxes. Scale bar is 500 nm. (b) Variation in counts at pixel 148 nm along x_1.

3.1(a) is a representative BF UEM image from the first image sequence.

To quantify the motion, the intensity over time was tracked in three small spatial areas outlined in Figure 3.1(a). The images were batch-converted and drift-corrected as described in Section 2.4.1. The drift-corrected raw image files were then loaded into MATLAB and rotated to various angles so that the dark fringes in each rectangle were approximately perpendicular to the long edge of the boxes then drawn. The counts in each image were divided by the mean of the counts in the entire image to exclude intensity changes due to photoelectron intensity variations. For each pixel along the long edge of the rectangles in each image, the normalized counts within 5 pixels of either side of the line were averaged together, corresponding to the short dimension of the rectangles, which produced an average intensity trace for each image. The scaled counts at 148 nm along x_1 is plotted in Figure 3.1(b) and captures the damped high-frequency oscillations present in the image counts over time. Similar oscillations are observed in Figure 3.1(c), which displays the counts at 89 nm along x_2 over time. This feature is on

the other side of the flake, which suggests that these oscillations are generated at all interfaces (*e.g.*, specimen-vacuum interface). The intensity traces for each box are plotted over time and space in Figure 3.2(a), (c), and (e), respectively, and hereafter called space-time-intensity plots. The color or *z*-axis corresponds to the normalized intensity, and the *x*- and *y*-axes correspond to the time steps and spatial extent analyzed in the sequence. If sliced perpendicular to the *y*-axis, the resulting graph plots the intensity versus time at one pixel, as observed in Figure 3.1(b) and (c). If sliced perpendicular to the *x*-axis, the resulting graph shows the intensity variation across the rectangle at one point, as would be observed in an intensity trace in a static TEM image.

The space-time-intensity plots indicate that the oscillations are most clearly captured in the red and blue rectangles. To quantify the oscillations, FFTs were performed on the space-time-intensity plots and are given in Figure 3.2 (b), (d), and (f). For the regions outlined in red and blue, the oscillations occur at frequencies of 44 and 54 GHz. The oscillations in the purple rectangle are not clear, and the noise in the FFT is high. This region was thus not further investigated in these image sequences.

As observed in Section 2.3.2, the contrast features correspond to bend contours. As will be explained in more detail in Section 3.2.2, the strain waves observed in this chapter can either tilt or alter the interplanar spacing so that the planes near the diffraction condition (*i.e.*, near the bend contours) are brought into or farther from the Bragg angle and thereby change the contrast. This observation implies that the image planes deformed by the strain waves must be near the diffraction condition in order for

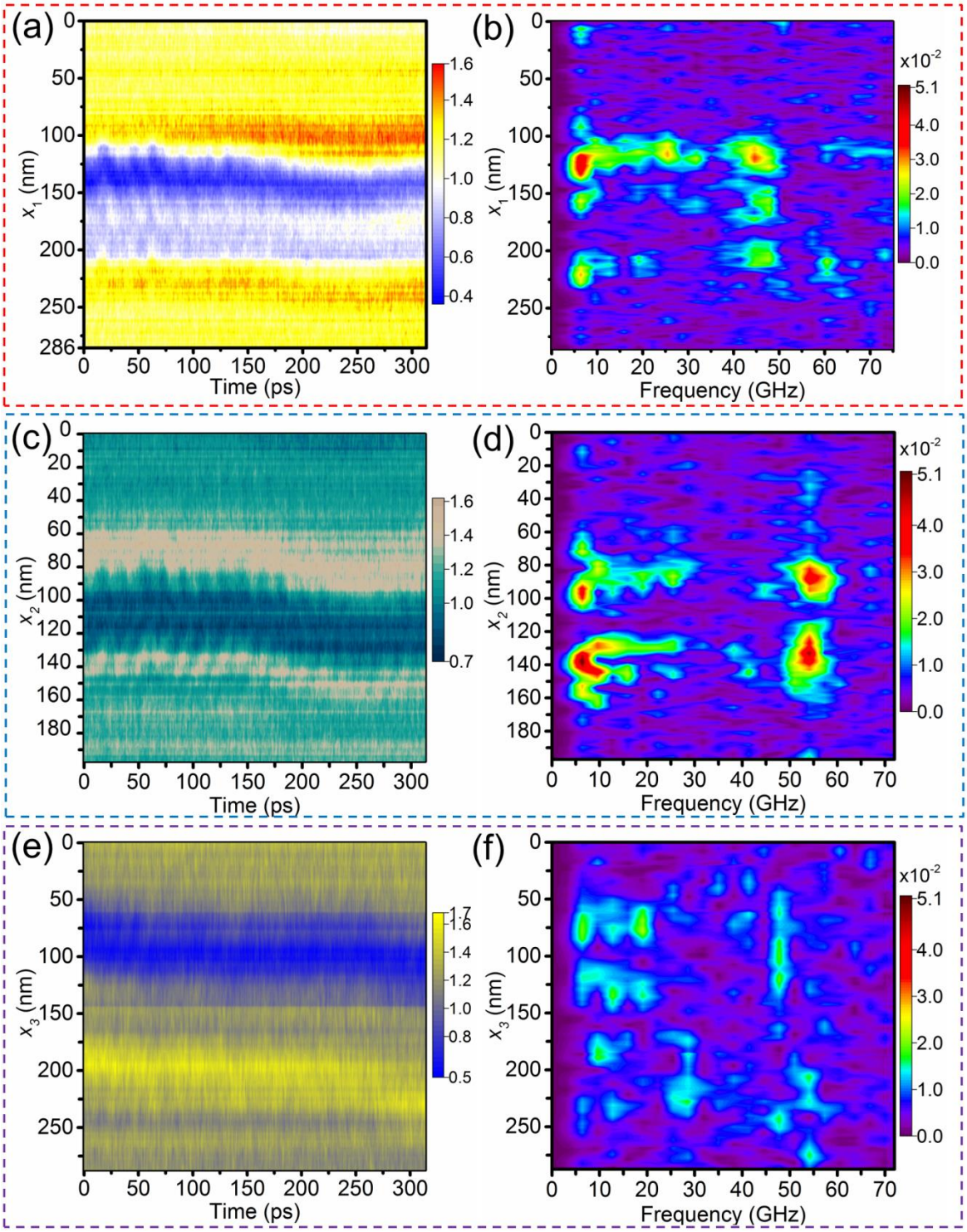

Figure 3.2 | **Quantification of high-GHz oscillations in Figure 3.1.** (a), (c), and (e) Scaled counts (color) plotted versus distance along x_n in Figure 3.1 and time, where n is 1

(red), 2 (blue), or 3 (purple), respectively. (b), (d), and (f) FFT magnitude (color) plotted versus distance along x_n and time, where n is 1 (red), 2 (blue), or 3 (purple), respectively.

their strain to be imaged, which will be important in later image sequences.

The oscillations in the upper left region (near the red rectangle in Figure 3.1(a)) were investigated in an image sequence at higher (6,500x) magnification, which corresponds to 0.79 nm per pixel. A representative image from that image sequence is shown in Figure 3.3(a). As before, the images were batch converted and drift corrected before being imported into MATLAB. The drift-corrected raw images were then rotated so that the contrast fringes were approximately perpendicular to the vertical direction. The regions indicated with red and purple rectangles in Figure 3.3(a) were analyzed as described previously. The scaled intensity at pixels 127 nm along x_1 and 70 nm along x_2 are plotted versus time in Figure 3.3(b) without offset. The dotted lines are plotted at 27 and 55 ps and indicate the first observation of oscillations at these locations. The delay between these values suggests

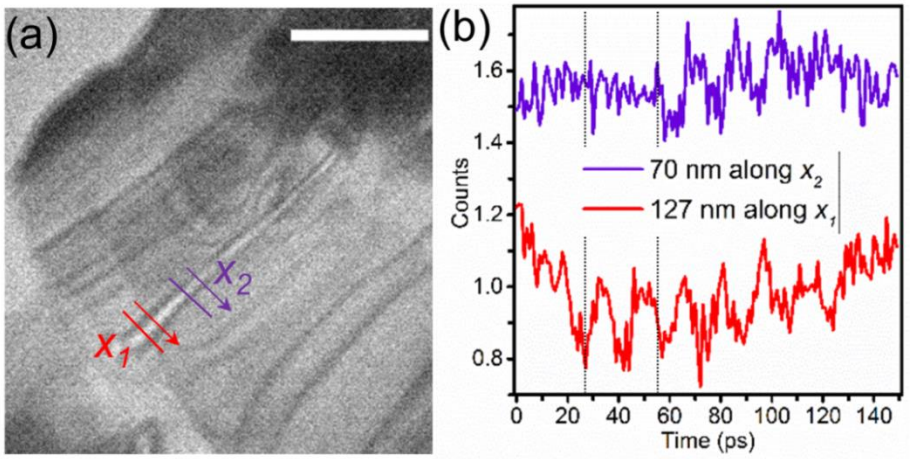

Figure 3.3 | **High-GHz oscillations at higher magnification.** (a) Representative BF UEM image at 6,500x magnification, showing the two regions analyzed, outlined in red and purple. Scale bar is 500 nm. (b) Relative intensity vs. time for a pixel 127 nm along x_1 in red and for a pixel 70 nm along x_2. The dotted lines indicate 27 and 55 ps.

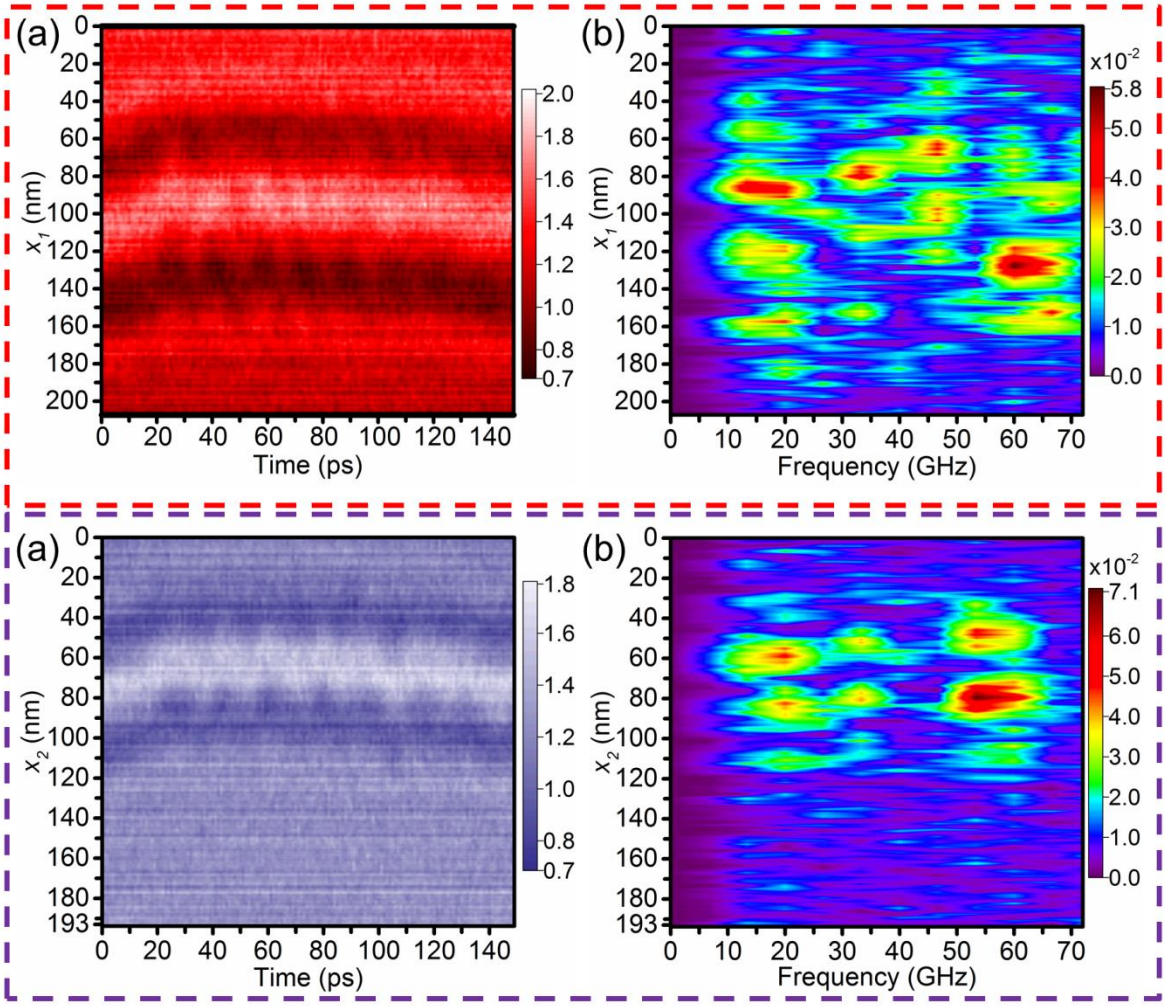

Figure 3.4 | **High-GHz oscillations at higher magnification.** (a) Intensity at each pixel along x_1 plotted as color over x_1 and time. (b) FFT magnitude as color at every pixel along x_1 for frequencies out to 72 GHz. (c) Intensity at each pixel along x_2 plotted as color over x_2 and time. (d) FFT magnitude as color at every pixel along x_2 for frequencies out to 72 GHz.

that the disturbance travels from the first box inward toward the second box, and because the approximate distance between the lines is 150 nm, the estimated speed is 5 nm/ps. The space-time-intensity plots in Figure 3.4(a) and (c) capture the oscillations of the entire contrast feature over time, and the FFTs in Figure 3.4 (b) and (c) indicate the presence of frequencies between 40 and 60 GHz.

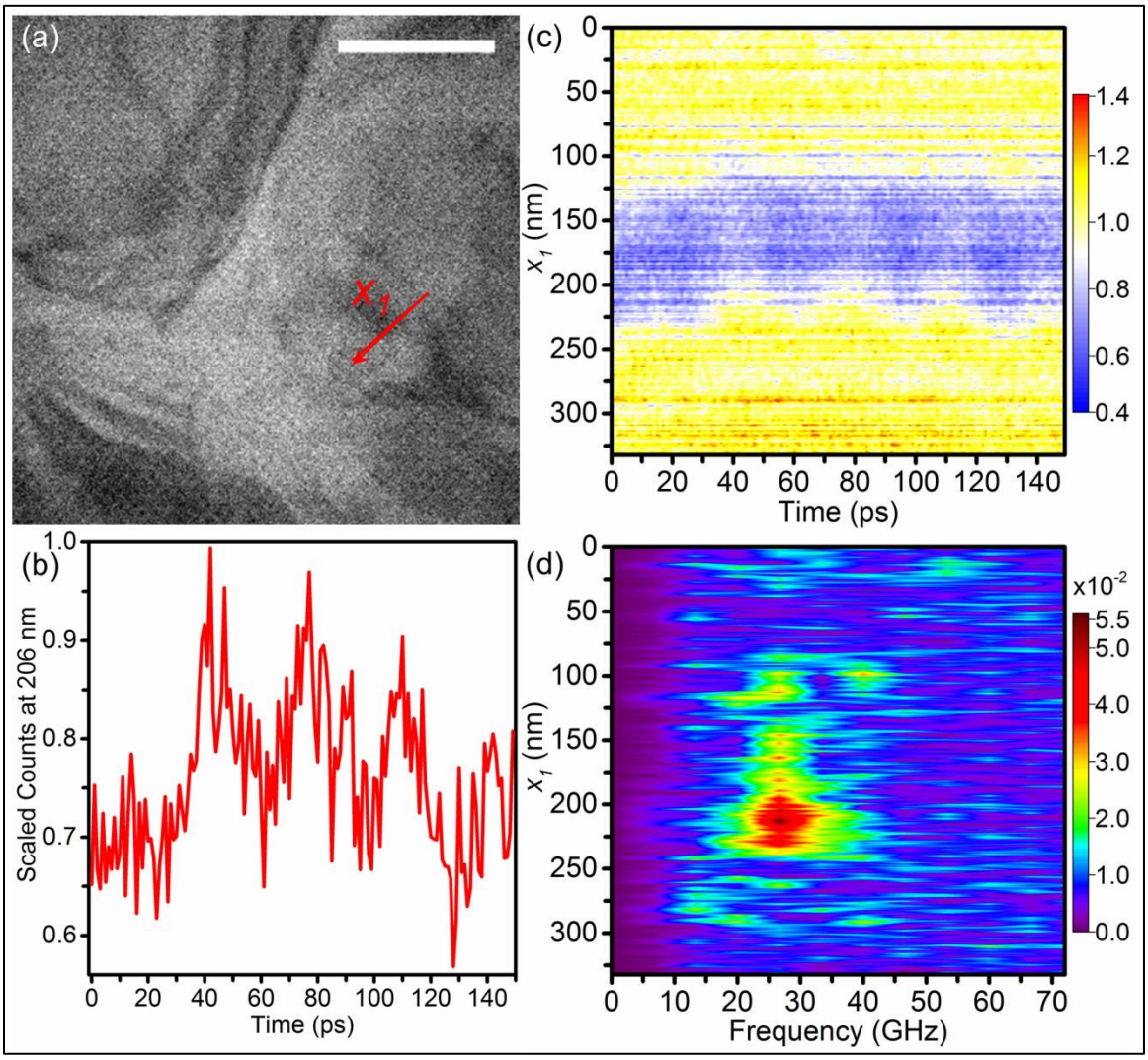

Figure 3.5 | **27 GHz oscillations observed in lower flake.** (a) Representative BF UEM image at 6,500x magnification of lower flake in Figure 2.17, where flake otherwise analyzed seen in upper left corner. Scale bar represents 500 nm. (b) Oscillations in Counts at 206 nm along x_1. (c) Scaled counts plotted along each pixel of x_1 at each time point. (d) FFT of (c) showing the frequency of oscillation = 28 GHz.

The same analysis is completed for the flake below the main flake in Figure 2.17, as shown in Figure 3.5. This image sequence was captured at the same magnification and time points as the image sequence above under the same imaging parameters. A representative BF UEM image is shown in Figure 3.5(a). The triangular lower end of the

main flake is visible in the upper left hand corner. The oscillations are visible in Figure 3.5(b), which is 206 nm along x_1. To understand more of the oscillations, the space-time-intensity plot is shown in Figure 3.5(c), which, as in Figure 3.5(b), shows much slower oscillations than observed in the main flake in Figure 3.1 and Figure 3.3. The FFT computed for the space-time-intensity plot is shown in Figure 3.5(d), and shows that the frequency observed is indeed much lower, 28 GHz. This difference in frequency may be due to differences in thickness or the degree to which the diffraction condition is met. In other words, higher frequency oscillations may be present but not close to the diffraction condition and thus not visible.

This initial observation, though interesting, was flawed in that the experimental time zero was not known. Pre-time zero images were thus not available to aid in distinguishing between environmental fluctuations changing imaging conditions and thus presenting dynamic changes in image contrast rather than the material response. Moreover, determining how the oscillations propagated after the first observation was not possible without pre-time zero images. On a later day, experimental time zero was determined. Soon after, the image sequence in the next section was acquired, in which propagation of these 50-GHz oscillations was observed, and the oscillations were able to be identified.

3.1.2 | Observation of Acoustic Phonons

The ultrafast structural dynamics are most clearly captured in an image sequence with 1 ps time steps. This image sequence (-36 to 358 ps in 1 ps time steps) is a

compilation of three image sequences, all acquired on the same day. The laser extracting the photoelectrons from the electron source drifted during the scan and caused the beam to fade in brightness between image sequences. Therefore, I stitched together 240 images (-36 to 139 ps) from the first sequence, 74 images (140 to 212 ps) from the second, and 146 images (213 to 358 ps) from the last sequence, where I adjusted the beam between the acquisition of each sequence to maximize brightness of the photoelectron packets. The image sequences were all acquired using a 2-mm diameter condenser aperture, spot size 1, and an objective aperture with a diameter of 100 μm, which was centered on the direct beam in the diffraction pattern. All image sequences were acquired at 3,500x magnification, which corresponds to 1.5 nm per pixel. Each image was acquired for 30 seconds. Zero picoseconds was set to be the earliest time dynamics in this specimen were observed on an earlier date because theoretical time zero had not been determined when these image sequences were captured. This experimental "time zero" is consistent for the remaining image sequences in Chapters 3 and 4 unless otherwise noted.

The dynamics were best captured by the changes in image contrast. The images were batch-converted and drift-corrected as described in Section 2.4.1. Figure 3.6(a) is a magnified area of the region outlined in blue in Figure 2.17(b) at 0 ps in this image sequence. In MATLAB, these images where the intensity was scaled from 0 to 264 were loaded and rotated 78° counterclockwise so that the diffraction contrast feature was observed to be approximately horizontal. A line was then drawn in the observed direction of propagation of the diffraction contrast feature to determine the area in which

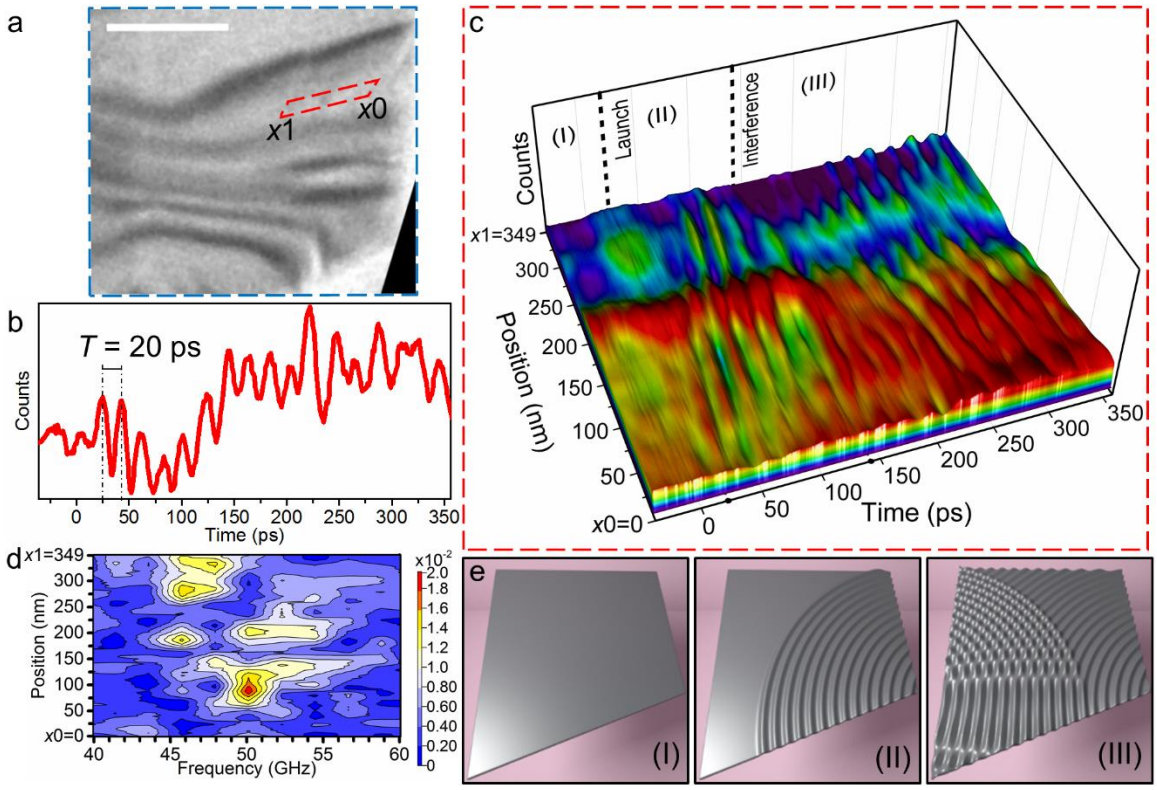

Figure 3.6 | **Acoustic-phonon launch and propagation.** (a) Representative UEM BF image of the MoS_2 region of interest outlined in Figure 2.17(b). The scale bar represents 500 nm. The dashed red parallelogram, spanning positions *x*0 to *x*1 (349 nm in length), is the region in which the subsequent analysis was performed. (b) Single-pixel counts, at a position 66 nm from *x*0 along the length of the parallelogram, as a function of time. The oscillation period within the time window is T = 20 ps. (c) Surface contour plot of the counts at each pixel position between *x*0 and *x*1, averaged along the short axis of the parallelogram, as a function of time. At the magnification used here (3500x), each pixel corresponds to 1.5 nm. Three regions displaying distinct dynamics are noted: (I) = before phonon wave-train launch, (II) = launch (t = 0 ps) and initial, single-wave-train propagation along a vector oriented roughly along *x*0 to *x*1, and (III) = observed wave interference effects beginning at approximately t = 140 ps. (d) Spatial Fourier transform of the surface contour plot in panel (c). The color bar represents magnitude. (e) Simplified illustration of in-plane wave-train propagation, reflection, and interference.

the average intensity would be tracked; this line corresponds to the long edge of the red parallelogram in Figure 3.6(a). For each pixel along the long edge from *x*0 to *x*1 in each image, the intensity within 25 pixels of either side of the line were averaged together,

corresponding to the short dimension of the red parallelogram, and then divided by the mean intensity over the whole area enclosed in the red parallelogram. The intensity versus time plot for the pixels 66 nm from *x*0 toward *x*1 in Figure 3.6(b) is representative of intensity variations and shows that the intensity oscillates at a high frequency with a period of approximately 20 ps.

In Figure 3.6(c), the intensity variations are plotted on the vertical axis at each position and time point (space-time-intensity plot). For each time point in the 1 ps step image sequence, the intensity was averaged parallel to the shorter, vertical dimension of the red parallelogram and recorded at each pixel along the longer, horizontal dimension of the parallelogram from *x*0 to *x*1. Each slice of the image along the position axis thus corresponds to the intensity variation at that pixel over all time. Each slice of the image along the time axis corresponds to the intensity variation over each pixel in the length of the parallelogram at specific time points. These intensity variations were smoothed with a Savitzky-Golay FIR filter with an order of 3 and frame length of 21. To improve visibility and make the edges of the plot solid in the final plot, the edge values were set to the first percentile values. The FFT of this plot was computed and plotted from 40 to 60 GHz in Figure 3.6(d).

Similar to WSe_2 and TaS_2,[247,258] photoexcitation of the MoS_2 flake initially results in the generation of distinct, coherent in-plane wave trains at discrete structural features. The ridges of the space-time-intensity plot indicate that a wave train emerges from the lower-right edge of the flake and propagates away from the interface along a single wave

vector. To extract speeds, the space-time-intensity plot in Figure 3.6(c) was overlayed with a plot of the positions of intensity values above the 80th percentile to identify the ridges that are the contrast movement. I drew a rectangle around each of the first four ridges to identify the position of those ridges. The values at and above the 80th percentile within each box were fit with a line using a least squares algorithm. The fit of the third ridge was not accurate and was excluded. The remaining slopes of those lines were averaged to give the average velocity, and the error is the standard deviation. The average slope of the ridges gives an approximate group velocity of 7.3 ± 0.7 nm/ps along *x*. This speed is consistent with calculated speeds for acoustic phonons and experimental speeds for coherent longitudinal acoustic phonons.[178,251] Computing the FFT of the intensity variation at each pixel shown in Figure 3.6(d), we obtain a dominant frequency of oscillation of 50 GHz (20-ps period).

Within the analyzed region of interest, it can be seen that this coherent behavior evolves as the waves propagate across the entire flake; the onset of a distinct transition in behavior is marked by wave-train interference beginning at 140 ps (Figure 3.6(c)). Such effects take the form of the mixing of two wave trains, each propagating along a distinct wave vector within the region of interest (*i.e.*, having different slopes in the surface contour plot). Owing to relative wavefront orientations, wave-train velocities, and flake dimensions, the origin of the second wave train is likely a simultaneous emergence event at a separate structural feature (*e.g.*, vacuum/crystal or crystal/crystal interface). That is, though photoexcitation is uniform across the entire flake, each discrete structural feature

may act as a distinct wave-train nucleation site.

3.1.3 | Observation of 25-GHz Modes with Control Experiments

Although repeatable as shown in Section 3.1.4, imaging the 50-GHz oscillations was found to strongly depend on the imaging conditions for a particular day. In the following image sequences, only modes with frequencies less than 30 GHz were observed. The specimen was titled 4.99° around the main double-tilt holder axis and -1.32° around the orthogonal holder axis so that the contrast was similar to that observed in Figure 3.6; however, the exact zone axis was not known for the original experiment and thus could not be reproduced exactly. The images were acquired at 3,500x magnification, which corresponds to 1.5 nm/pixel, for 50 seconds for each image. The 2-mm diameter condenser aperture, spot size 1, and objective aperture of 100 μm centered on the direct beam in the diffraction pattern were used to produce higher image contrast while still providing sufficient signal to capture dynamics. The electron source was a 50-μm diameter LaB_6 flat surface embedded in graphite. Figure 3.7(a) is a representative BF UEM image with the three regions analyzed marked with blue (x_1), orange (x_2), and red (x_3) arrows.

The images were analyzed as in Section 3.1.1, where the intensity was averaged across 10 pixels and tracked in each image. In Figure 3.7(b), the oscillations in the counts are shown at a location 76 nm from the beginning of x_1, which shows much slower oscillations than before, with a period of 67 ps. Similarly, the period of the oscillations in the counts at a pixel 124 nm from the beginning of x_2 is 80 ps, as shown in Figure 3.7(c).

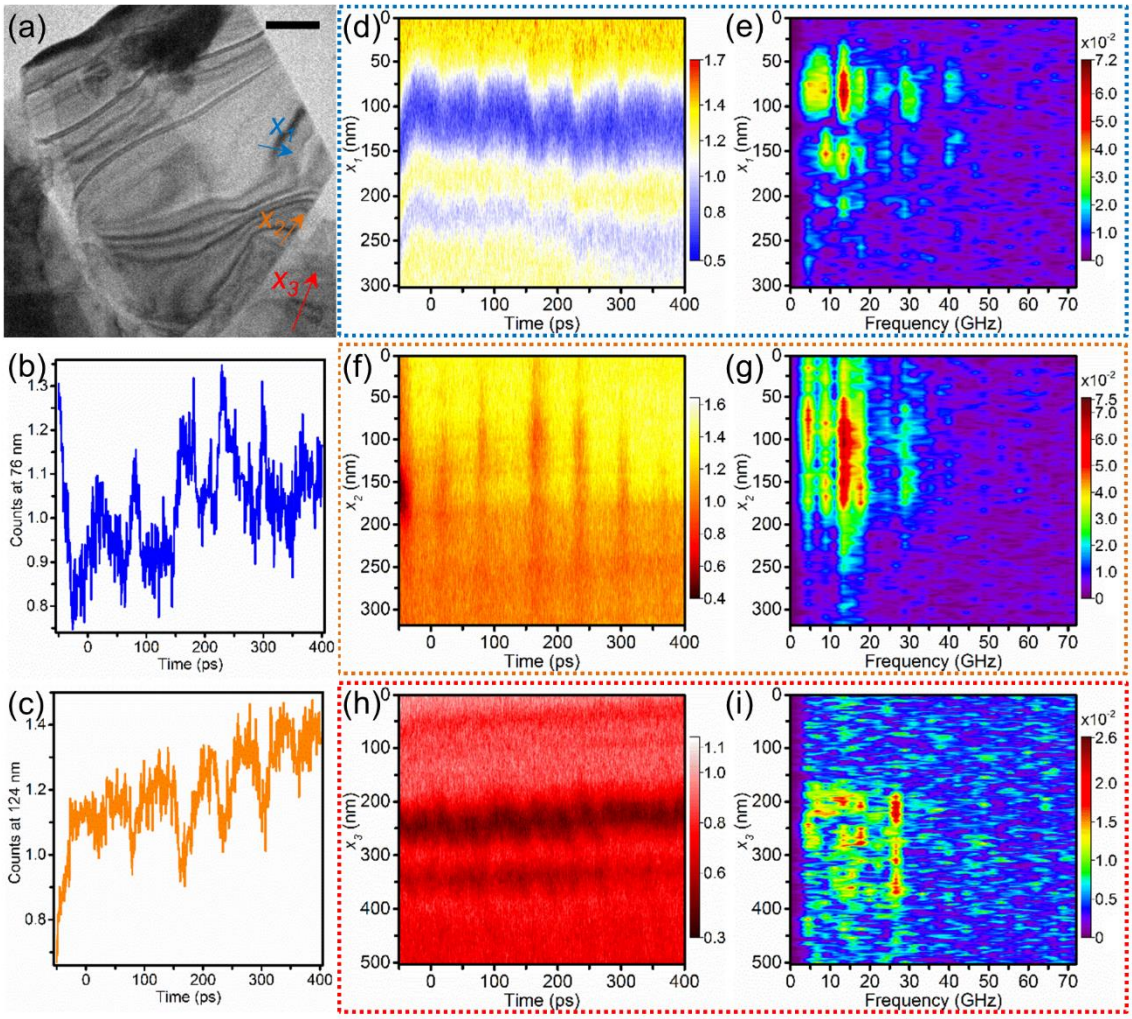

Figure 3.7 | **Observation of only 25-GHz modes.** (a) Representative BF UEM image, with three regions of interest marked by the arrows. Scale bar is 500 nm. (b) Scaled counts 76 nm along x_1 versus time. (c) Scaled counts 124 nm along x_3 versus time. (d), (f), and (h) all show intensity variation (color) at every pixel along x_n for each point in time, where n is 1 (blue), 2 (orange), and 3 (red). (e), (g), and (i) are the FFTs of the intensity variation at each point along x_n plotted from 0 to 72 GHz. In contrast to the two previous image sequences, the highest frequencies visible in each plot here are <30 GHz.

The oscillations in the image counts in the three regions of interest are shown in Figure 3.7(d), (f), and (h), and the corresponding FFTs performed over the regions over time are shown in Figure 3.7(e), (g), and (i). For the first region (Figure 3.7(e)), the largest frequency observed is 40 GHz, but the strongest frequency is 13 GHz, much slower than

observed in the other two image sequences. Similarly, in Figure 3.7(g), the highest frequency is 29 GHz, and the strongest frequency is 13 GHz. In the lower flake in Figure 3.7(i), similar frequencies are observed, namely 27 GHz as the highest frequency observed.

The oscillations in Figure 3.7(e) show a slightly different oscillation than observed previously. Rather than vertical translation from the initial position, this contrast feature changes contrast. This difference in contrast could be due to a different acoustic phonon mode. One possibility is a mode traveling along the [001] direction. Because the thickness is ~40 nm in that region, the wave would need to travel at 0.5 nm/ps, which is much lower than the speed of sound in the material.

Different oscillations on that lower flake were observed in the image sequence in Figure 3.8, which was acquired on a separate day at a 1,700x magnification (3.2 nm per pixel). The images were acquired with the 2-mm diameter condenser aperture, spot size

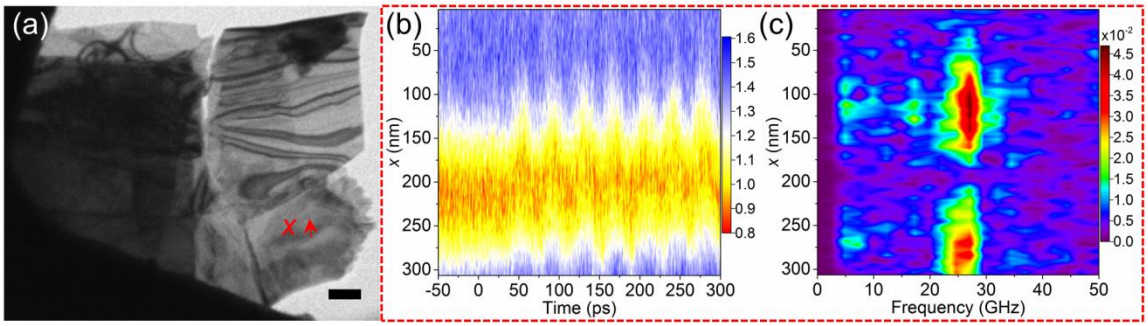

Figure 3.8 | **27-GHz oscillations in lower flake captured at lower magnification.** (a) Representative BF UEM image at 1,700x magnification, with region of interest marked by the red arrow. Scale bar represents 510 nm. (b) Scaled image counts at every pixel along *x* in each image. (c) FFT performed at each pixel along *x* and plotted between 0 and 50 GHz. The main frequency is 27 GHz.

1, and the 40-μm diameter objective aperture centered on the direct beam in the diffraction pattern. Each image was acquired for two minutes. The electron source was a 50-μm diameter LaB_6 flat surface embedded in graphite. The images were taken from -50 to 300 ps in 1 ps steps. A representative BF image is given in Figure 3.8(a) where the region analyzed is shown by the red arrow *x*. In Figure 3.8(b), the image contrast oscillations at every pixel along *x* are shown. Here, the contrast feature appears to expand every 37 ps, which is reflected in the main frequency observed in the FFT (27 GHz; see Figure 3.8(c)).

The control experiments taken on the same day as the image sequence in Figure 3.7 show that the observed dynamics captured are indeed due to the material photo-response rather than environmental fluctuations. Two control experiments were performed. In the first, the pump remained on the specimen at 73 ps delay while 100 images were acquired. The scaled image counts analyzed in several regions over that time frame are shown in Figure 3.9(b), (d), (f), and (h), along with the FFTs in Figure 3.9(c), (e), (g), and (i), assuming an image time step of 1 ps, as the image sequence in Figure 3.7. In the second control, the pump illumination was blocked, and 62 images were acquired. The scaled image counts analyzed in several regions over that time frame are shown in Figure 3.10(b), (d), (f), and (h), along with the FFTs in Figure 3.10(c), (e), (g), and (i), again assuming an image time step of 1 ps, as the image sequence in Figure 3.7. For both experiments, the same camera acquisition time and imaging conditions as the image sequence above in which dynamics were observed in Figure 3.7. In both

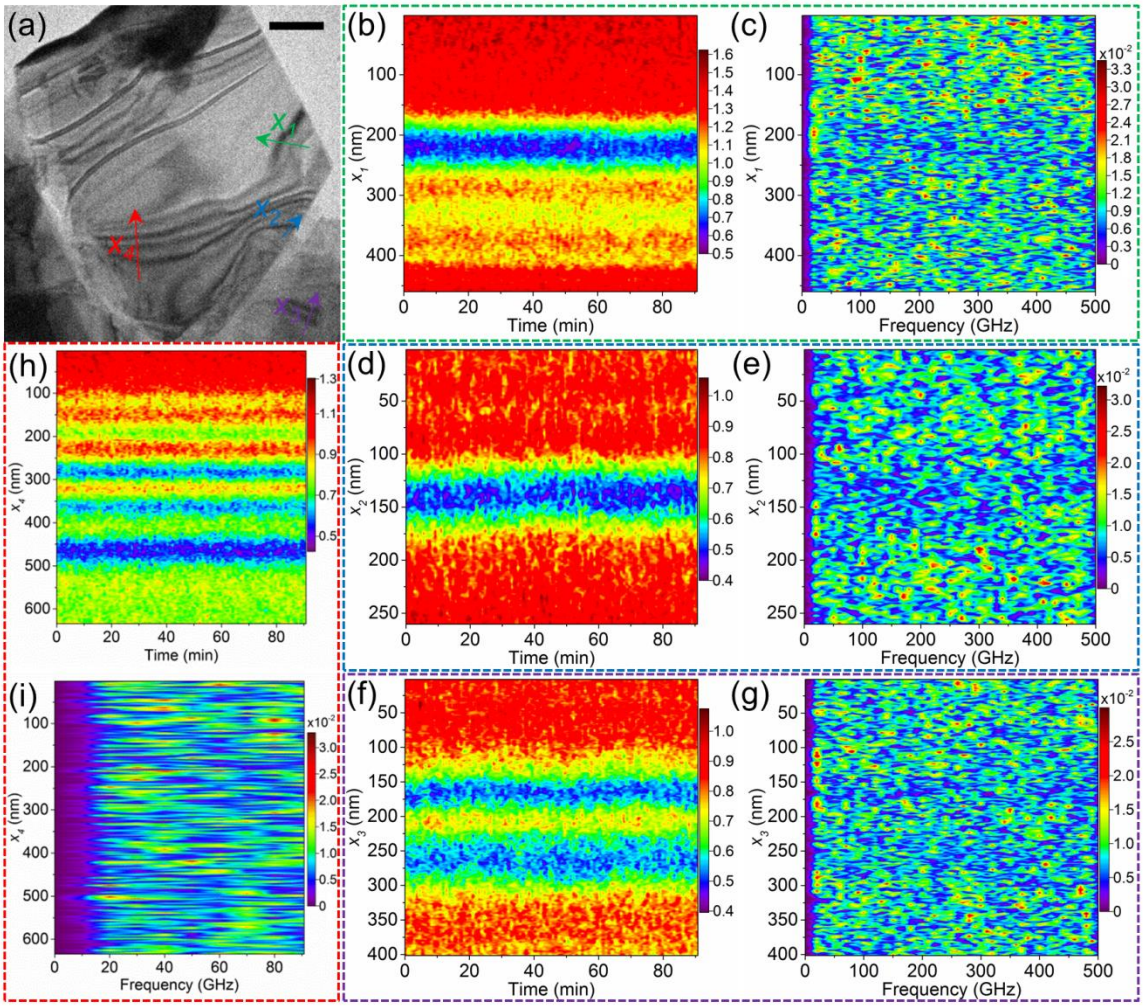

Figure 3.9 | **Control experiment without pump translation.** (a) Representative BF UEM image in which the pump-probe delay interval was 73 ps. Scale bar is 500 nm. The four regions analyzed are shown in green, blue, purple, and red. (b), (d), (f), and (h) Scaled image counts at every pixel along x_n at each point in time, where n = 1 (green), 2 (blue), 3 (purple), and 4 (red). The image contrast does not appreciably vary. (c), (e), (g), and (i) FFTs computed at each point along x_n assuming 1 ps time steps as above. No frequency is distinguishable.

control experiments, the diffraction contrast does not show oscillations, and, thus, image contrast oscillations and movement at these lower frequency modes can be assigned to the material photo-response.

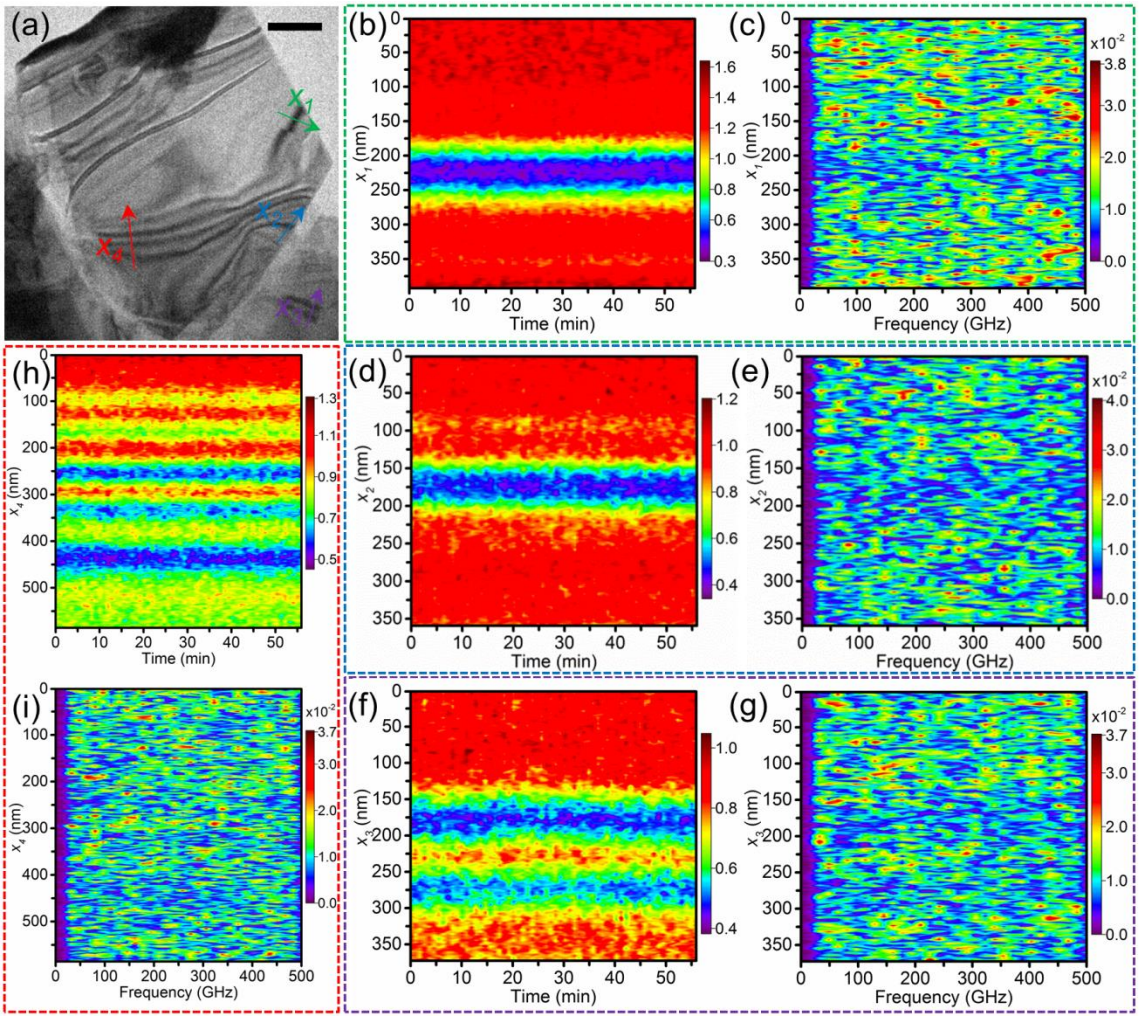

Figure 3.10 | **Control experiment with no pump irradiation.** (a) Representative BF UEM image during which the pump laser was blocked. Scale bar is 500 nm. Three regions analyzed shown in green, blue, purple, and red. (b), (d), (f), and (h) Scaled image counts at every pixel along x_n at each point in time, where n = 1 (green), 2 (blue), 3 (purple), and 4 (red). The image contrast does not appreciably vary. (c), (e), (g), and (i) FFTs computed at each point along x_n assuming 1 ps time steps as above. No frequency is distinguishable.

This observation suggests that the type of contrast oscillations strongly depend on the imaging conditions for a particular day. The specimen is repositioned in the holder for each experiment, which could lead to slightly different orientation of the specimen with respect to both the probe and pump beams and thus different orientations of the

planes near the diffraction condition with respect to the displacement directions. To ascertain that the high-frequency modes observed in the image sequence analyzed in Figure 3.6 are genuinely part of the material photo-response, another set of image sequences with control experiments was acquired.

3.1.4 | Observation of High-GHz Oscillations with Control Experiments

These image sequences show high frequency (>40 GHz) modes with the strong suggestion of low-GHz modes as well, which are explored in more detail in the next chapter. In the image sequence tracking dynamics, the images were acquired at 2,500x magnification, which corresponds to 2.1 nm/pixel, for 30 seconds each. The 2-mm condenser aperture, spot size one, and 40-μm diameter objective aperture were used, and the source was a 300-μm LaB_6 flat surface embedded in graphite. Images from -100 to 1,198 ps in 2 ps steps were acquired of the specimen titled so that the positions of contrast features on the flake was similar to that observed in Figure 3.6.

The image sequence shows >40 GHz oscillations as well as individual GHz oscillations, as in Figure 3.6. A representative BF UEM image is shown in Figure 3.11(a) with the three regions analyzed are marked by the red (x_1), blue (x_2), and green (x_3) arrows. 10, 10, and 25 pixels on either side of each line, respectively, were averaged to track the image contrast in each region. In Figure 3.11(b), a representative variation in image contrast is shown at a pixel 149 nm along x_1, a low frequency movement is immediately visible, where the period is approximately 750 ps (1.3 GHz). At the initial time points, outlined in purple in Figure 3.11(b) and magnified in Figure 3.11(c), higher

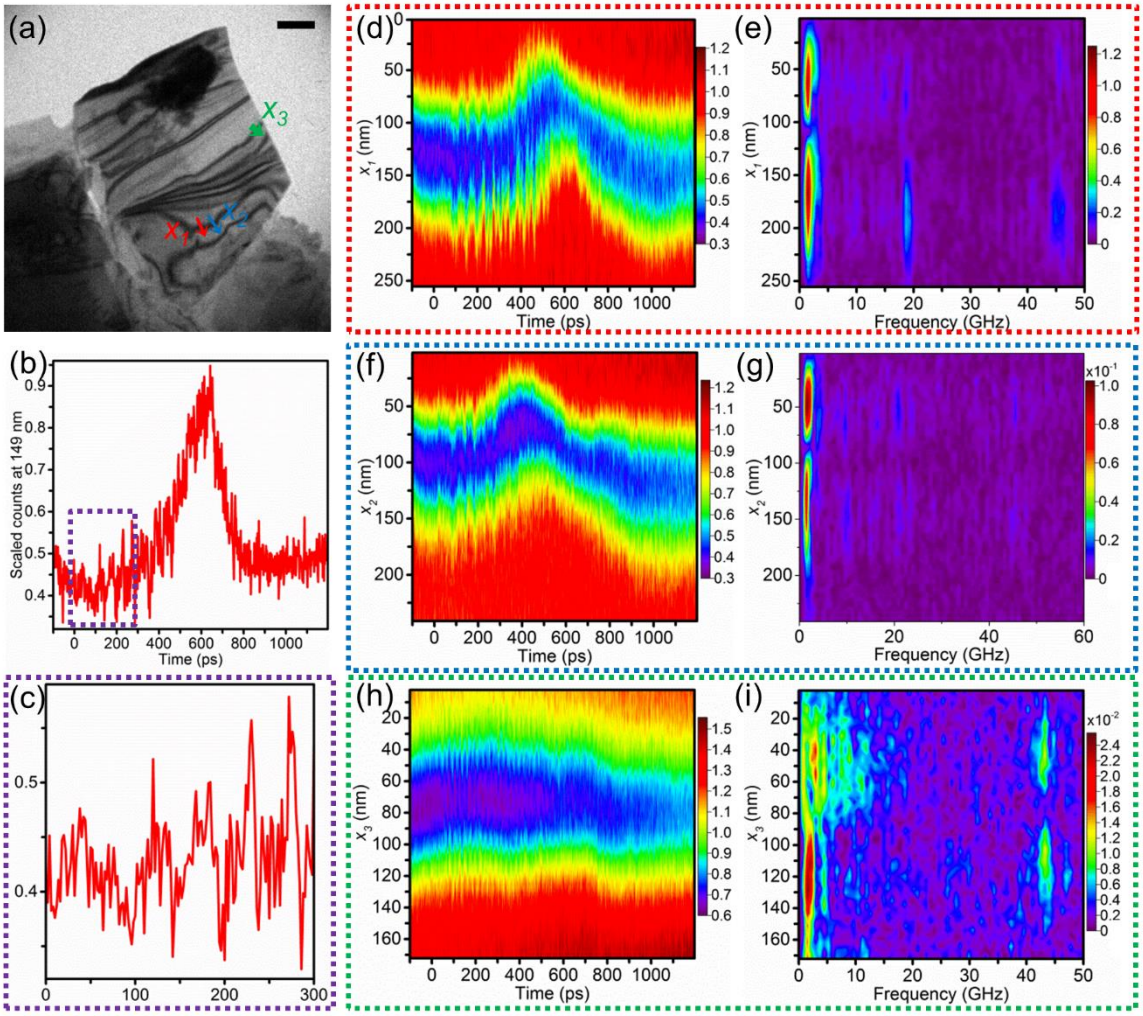

Figure 3.11 | **Acoustic phonons observed with control experiments.** (a) Representative BF UEM image with three regions of interest analyzed in the figure. Scale bar is 500 nm. (b) Scaled counts at a pixel 149 nm along x_1, which shows a low-frequency oscillation with a period of 750 ps. (c) A magnified view of the region outlined in purple in (b), which shows two oscillations – one with a period of ~50 ps and the other ~10 ps. (d), (f), and (h) Scaled counts plotted at each pixel along x_n and at each time point. (e), (g), and (i) FFTs computed at each pixel along x_n, which shows the three frequencies corresponding to the oscillations observed in (d), (f), and (g).

frequency oscillations are visible, with two periods. One is ~50 ps and is responsible for the ~20 GHz peaks in the FFTs. The second is close to the noise level and is ~10 ps, corresponding to the peaks >40 GHz in the FFTs. These oscillations are particularly

visible when the scaled image counts across x_n (where n = 1 (red), 2 (blue), and 3 (green)) are plotted versus time in the space-time-intensity plots in Figure 3.11(d), (f), and (g). The FFTs of these oscillations reveal strong oscillations at low frequencies and weaker oscillations at the high frequencies of Figure 3.6.

As in the previous section, two control experiments were conducted. The photoelectron beam had faded significantly between the image sequence above and the first first control experiment, and the laser position on the electron source was adjusted to produce more photoelectrons. First, the pump laser was left 642 ps, and 150 images were acquired at the same imaging conditions as the image sequence with varying pump-probe delay times. The image contrast was tracked over space and time in three different regions, and the resulting space-time-intensity plots and FFTs are plotted in Figure 3.12. These images were acquired for 35 seconds rather than 30.

In the second control experiment, the pump irradiation was removed from the specimen, and 120 images were acquired. Similarly, the acquisition time was 35 seconds. As for the other control experiment, the image contrast was tracked along each pixel for each image, and the FFT was calculated assuming a time step size of 2 ps. The results are plotted in Figure 3.13. As before, no dynamics are observed. Thus, we can conclude that the dynamics observed are due to the material photo-response.

3.2 | Discussion of Acoustic Phonon Dynamics

In the long wavelength limit, thermal energy carried in the acoustic phonons can be described by acoustic wave equations in an elastic continuum.[14] The modes are

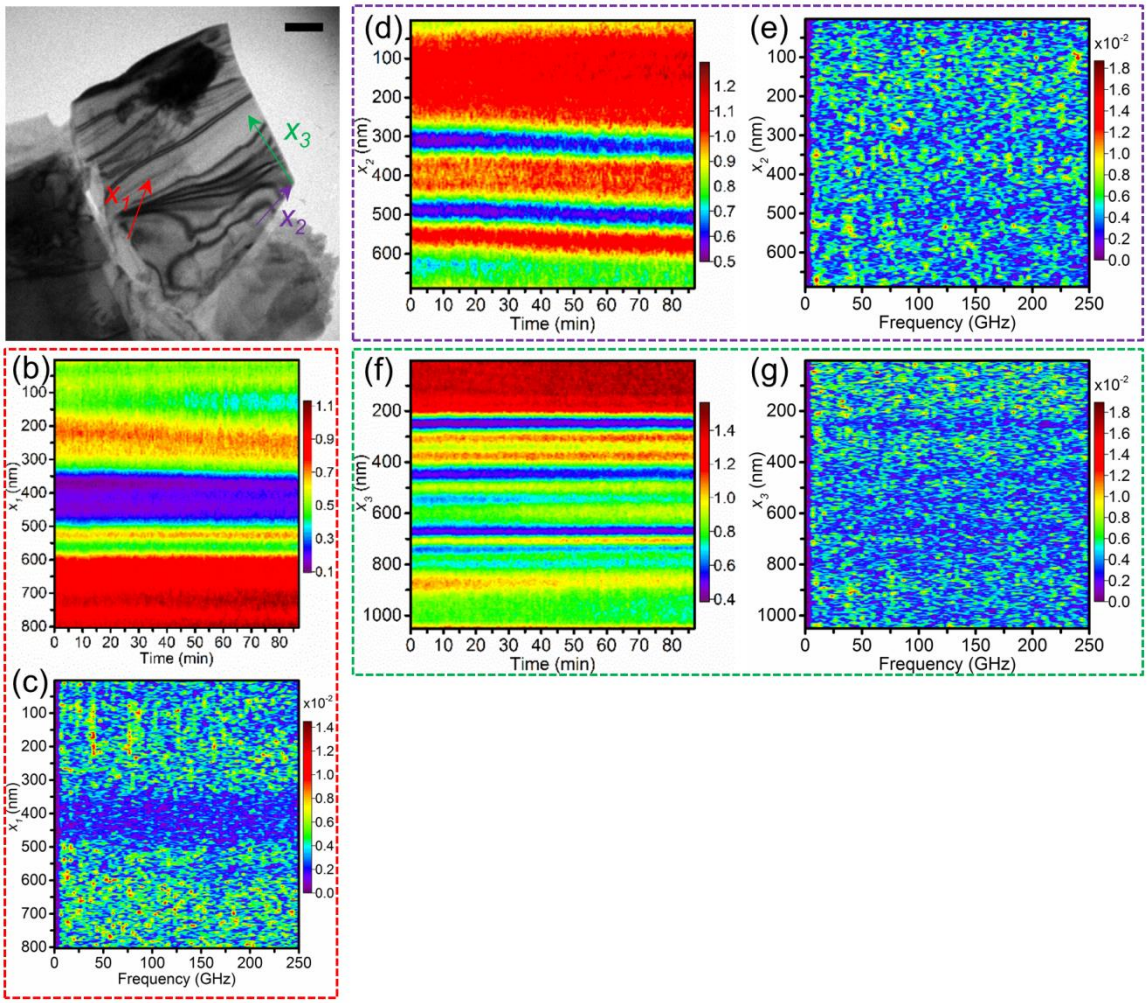

Figure 3.12 | **Control experiment with pump irradiation at 642 ps.** (a) Representative BF UEM image with three regions analyzed marked by x_n. Scale bar is 500 nm. (b), (d), (f) Scaled counts at each pixel along x_n in each image. (c), (e), and (g) FFT at each pixel along x_n plotted over the full frequency range, calculated assuming each time step was 2 ps. No dynamics are observed.

further classified based on the polarization of the wave with respect to its propagation direction and penetration depth into the specimen. The two most relevant to the discussion here are Rayleigh and Lamb modes. Rayleigh waves are surface waves, which require exponential decay of wave amplitude with distance from the surface, propagating at the interface of a solid approximated as an infinite half-space and vacuum.

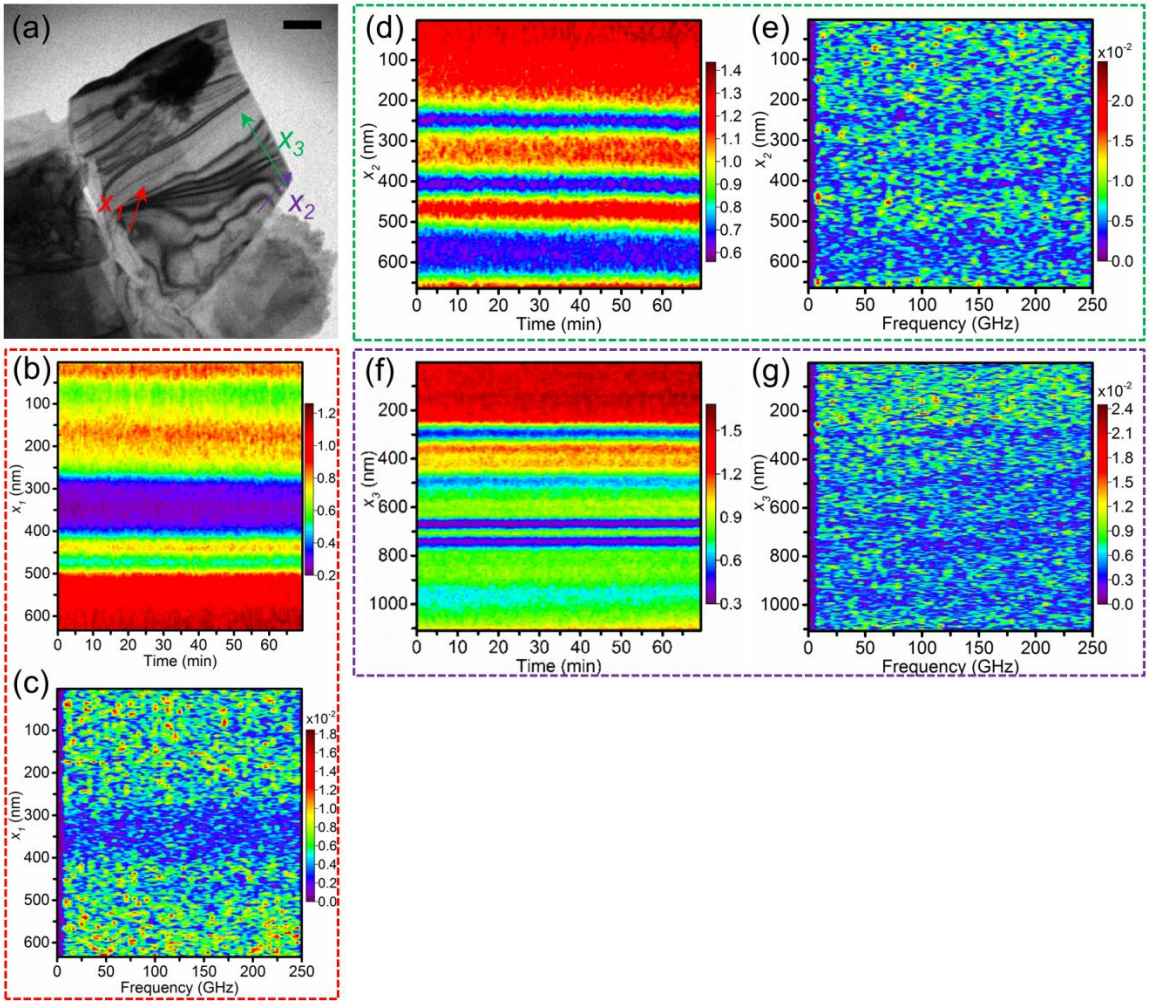

Figure 3.13 | **Control experiment with no pump irradiation.** (a) Representative BF UEM image with three regions analyzed marked by x_n. Scale bar is 500 nm. (b), (d), (f) Scaled counts at each pixel along x_n in each image. (c), (e), and (g) FFT at each pixel along x_n plotted over the full frequency range, calculated assuming each time step was 2 ps. No dynamics are observed.

In Rayleigh waves, the wave propagation direction and displacement direction (defined here as the polarization direction or polarization)[385] are in the same plane, and no disturbance propagates in the direction of the plane normal (*i.e.*, plane strain). In other words, Rayleigh waves have at least one component that is a vertically polarized transverse or shear wave.[386] These modes have been heavily studied and applied,

particularly in ultrasonic nondestructive evaluation methods because of their reflection from defects.[387-393] When excited with laser irradiation, these surface waves are observed in thick samples that can be approximated as infinite half-spaces, such as when the optical penetration depth is much smaller than the specimen thickness.[394-395]

As the specimen thickness decreases, the elastic displacements of the two free surfaces couple for vertically polarized transverse waves and are called Lamb waves.[394,396] Repeated reflections between the two plate surfaces result in a standing wave in the vertical direction and a propagating wave in the perpendicular direction along the plate (*i.e.*, a guided wave).[386,397] These modes are called Lamb modes and exist for finite values of λ/h where λ is the Lamb mode wavelength and h is the film thickness.[398] Unlike Rayleigh waves, these waves are dispersive.[386,398] The speed of sound depends on the direction of propagation due to changes in the mechanical properties and density of the material. Generally, the mode displacements are combinations of transverse and longitudinal modes. In the isotropic case, the transverse and longitudinal waves are uncoupled and thus known as pure modes. In anistropic materials, pure modes do not generally exist. For waves traveling along an axis of symmetry, one of the shear modes is uncoupled to produce a vertically polarized transverse wave coupled to a quasi-longitudinal wave, which is the Lamb wave in that direction, and a quasi-horizontally polarized transverse or shear wave.[385,399]

The behavior observed does not match that expected from Rayleigh waves. First, using the bulk absorption coefficient for MoS_2 (0.34×10^6 cm^{-1}),[400] the ($1/e$) extinction

distance is 29 nm. Even for a specimen thickness of 60 nm, 13% of the incident energy is still transmitted, which suggests that the film cannot be approximated as having elastic disturbance only near the surface of the film. More rigorously, calculations for Rayleigh waves in isotropic media suggest that Rayleigh waves are localized in the vertical distance corresponding to one to two times the wavelength. The phase velocity measured above is 7.3 nm/ps, and the phase velocity is the ratio of the angular frequency to the wavenumber. For a frequency of 50 GHz (angular frequency of 314 GHz), the corresponding wavenumber is 0.04 nm^{-1}, and the wavelength is ~100 nm. Thus, these waves are not surface waves but rather body waves in which the displacement of the bottom surface of the film is also important. Finally, Rayleigh wave velocities are nondispersive, and the phase velocity equation can be explicitly solved due to the symmetry in imaging along the [001] zone axis, as given by Royer and Dieulesaint[401] and described in Appendix F. In this experiment, the specimen is oriented so that a Rayleigh wave would propagate in the *x*-*z* plane and must decay along the [001] or *z*-axis, and the resulting Rayleigh wave speed is 1.9 nm/ps, which is much slower than observed here. We can thus conclude that the waves observed here are Lamb modes.

3.2.1 | Assignment of Lamb Modes

Knowing that the displacements must be Lamb modes, the next question to answer is which Lamb modes are observed. The Lamb modes can be split into two categories: symmetric (S_n) and anti-symmetric (A_n), which refer to the symmetry of the displacement with respect to the mid-plane of the specimen along [001], where the *n*

gives the order of the mode. For instance, Figure 3.14 shows schematics of plate deformation for the pure, zeroth order (a) symmetric (S_0) (a) or extensional and (b) anti-symmetric (A_0) or flexural Lamb modes.

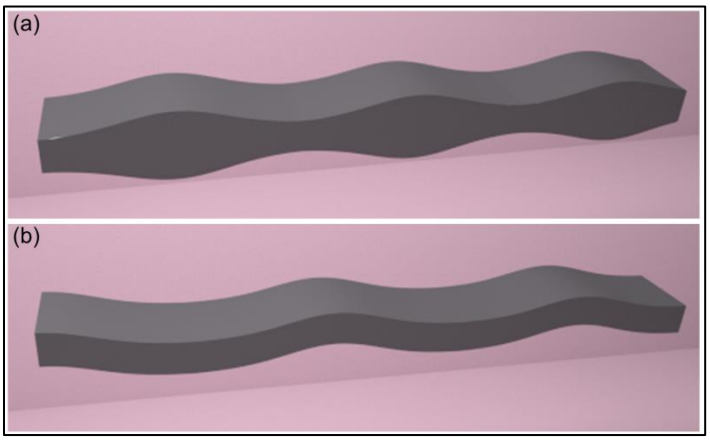

Figure 3.14 | **Pure zeroth order Lamb modes.** (a) Symmetric (S_0). (b) Anti-symmetric (A_0).

Because Lamb waves are dispersive and MoS_2 is anisotropic, the phase velocities and frequencies, which are determined by the mechanical properties in the direction of propagation, can be used to identify the Lamb mode. The phase velocities are given by the dispersion relation, ω/k, where ω is the angular frequency and k is the wavenumber. As a first approximation, the dispersion relation for MoS_2 as an isotropic material with the in-plane elastic modulus and Poisson's ratio (calculations shown in Appendix E) is calculated using the relation given by Rogers[402] and shown in Figure 3.15. In isotropic materials, the modes must be pure. As seen in the figure, zeroth order modes exist at all frequencies but propagate at lower phase velocities than higher modes, which can be used to differentiate them from high-frequency modes. In contrast, each high-order mode can propagate only at frequencies above a cut-off frequency.

Many features of this dispersion relation are preserved for the full anisotropic

solution while interesting new features arise. Even in fully anisotropic materials, the zeroth order modes propagate at all frequencies but at lower phase velocities, and the higher-order modes propagate only above cut-off frequencies. In anisotropic materials, however, the phase velocity now depends on the propagation direction, and the modes are no longer guaranteed to be purely transverse or longitudinal. Consequently, the group velocity, or the velocity of energy transfer, is not generally coincident with the propagation direction.

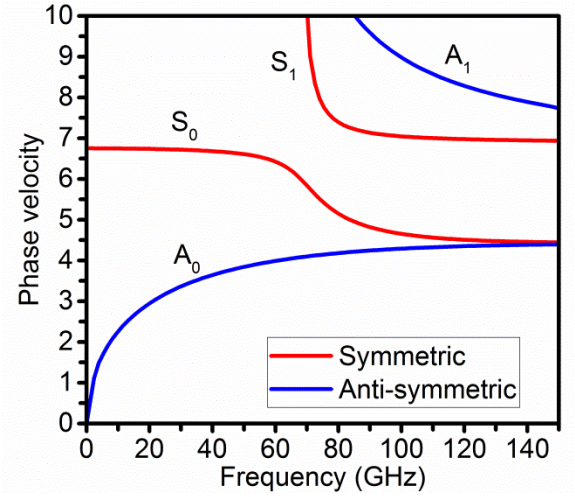

Figure 3.15 | **Dispersion relation for MoS_2 modeled as isotropic material.** MoS_2 is approximated as an isotropic material, and the dispersion relation is plotted for the zeroth and first order Lamb modes. S_0 and A_0 propagate at all frequencies, but S_1 and A_1 propagate only at frequencies above a cut-off frequency.

The cut-off frequencies for the symmetric and anti-symmetric modes can be calculated and used to identify the modes observed. Generally, the two quasi-transverse Lamb mode and quasi-longitudinal modes are coupled. However, when one mode travels down a crystallographic symmetric axis, the horizontally polarized shear wave can be uncoupled, and the cut-off frequencies are given analytically:[397]

$$f_n^s = \frac{n+\frac{1}{2}}{2h}\sqrt{\frac{c_{33}}{\rho}} \qquad n = 0, 1, 2 \ldots \tag{3.1}$$

$$f_n^s = \frac{m}{2h}\sqrt{\frac{c_{55}}{\rho}} \qquad m = 1, 2 \ldots \tag{3.2}$$

for the symmetric modes, and

$$f_n^a = \frac{n + \frac{1}{2}}{2h}\sqrt{\frac{c_{55}}{\rho}} \qquad n = 0, 1, 2 \ldots \tag{3.3}$$

$$f_n^a = \frac{m}{2h}\sqrt{\frac{c_{33}}{\rho}} \qquad m = 1, 2 \ldots \tag{3.4}$$

for the anti-symmetric modes, where c_{33} and c_{55} are stiffness tensor elements and h is the thickness.

Only the waves observed in Figure 3.1 and Figure 3.3 satisfy the conditions above. The crystallographic orientation was established by determining the rotation of the diffraction pattern relative to the BF image. Per established procedure,[403] a BF image was acquired at the desired magnification (1,700x), and the beam was defocused while in diffraction mode until a BF image was visible in the direct beam. The image in the direct beam of the DP was measured as rotated 20° clockwise relative to the BF image. Once rotated 20° counterclockwise, the DP was overlayed on the BF image, and the reciprocal lattice vectors drawn, which are perpendicular to the planes. The rotated DP and crystallographic axes drawn on the MoS_2 are shown in Figure 3.16. Comparing these axes to the direction of propagation of the observed waves, only the waves observed in Figure 3.1 and Figure 3.3 propagate along principal crystallographic axes, namely the [100] direction. Using h = 50 nm and the stiffness tensor elements given by Feldman,[43]

the cut-off frequencies in MoS_2 are calculated and shown in Table 3.1. The frequencies observed range from 44 to 60 GHz. The high frequency mode could be assigned to the second order anti-symmetric or second order symmetric mode. The cut-off frequencies depend inversely on thickness, and thus the uncertainties in thickness could account for the uncertainty in assignment.

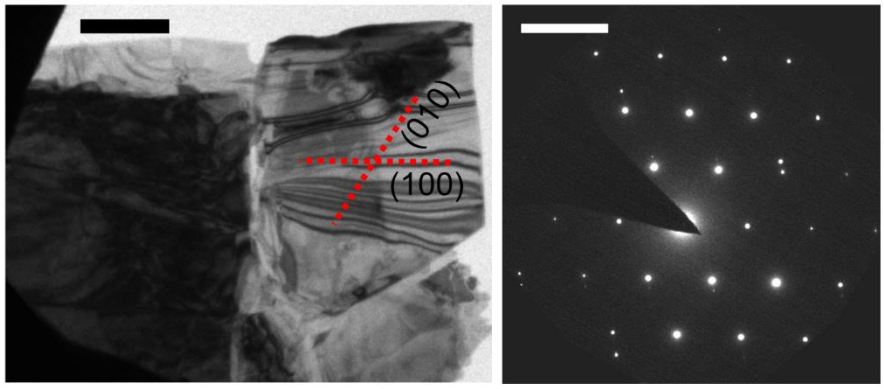

Figure 3.16 | **Crystallographic orientation of flake.** The diffraction pattern needed to be rotated 20° counterclockwise to coincide with the BF image. Scale bar in the BF image is 1 μm. Scale bar in the DP is 5 nm^{-1}.

The propagation direction appears to be influenced by the defects or strain inherent to the specimen before excitation. In all of the experiments described above, the waves were observed to propagate along existing or parallel to nearby bend contours. Similarly, acoustic waves

Antisymmetric mode	**Cut-off frequency (GHz)**	**Symmetric mode**	**Cut-off frequency (GHz)**
1	19	1	32
2	58	2	39

Table 3.1 | **Cut-off frequencies for two anti- and symmetric Lamb modes in 50-nm MoS_2.** For Lamb modes where one is propagating in the [100] direction, the cut-off frequencies are given by analytical functions depending on the stiffness constants in different directions. The cut-off frequencies for the first and second order anti- and symmetric Lamb modes are calculated for a specimen of thickness 50 nm.

have been observed to propagate along defects or strain in a wedge-polished silicon wedge, WSe_2, and TaS_2 in other UEM BF images.[247,258] This influence is not particularly surprising in that Lamb waves are guided surface waves and thus follow the surface contours, including around defects, which have led to their use to detect defects in paper[397] and aircraft parts.[388] Moreover, as described in the next section, the acoustic phonons are imaged *via* changes in diffraction contrast, which are most significant for regions near or at the diffraction condition (*e.g.*, bend contours). Therefore, the acoustic phonons will be most easily detected in regions near or on bend contours.

3.2.2 | Effect of Strain Due to Acoustic Phonons on Image Contrast

Phonons are, by definition, quantized strain in the lattice, and diffraction contrast is thus exquisitely sensitive to their presence. In static, conventional TEM images, diffraction contrast variations due to strain fields are used to identify defects and their orientations.[345,404-405] Because the zeroth order Lamb modes are present at all frequencies and the higher-order Lamb modes are harmonics of these modes, the effect of the displacement of these two modes on the image contrast is discussed below.

In the case of the anti-symmetric mode, the bending results in the appearance of bend contours when the specimen is close to the diffraction condition. A schematic of the bent specimen is shown in Figure 3.17(a), with several planes marked with dotted lines. Due to the thin specimens in TEM, the spots in the Ewald sphere are actually rods with variable intensity, known as reciprocal rods or relrods. Thus, the Ewald sphere will still intersect each relrod over a finite range of tilt angles, which is quantified by the

minimum distance from the Ewald sphere to the reciprocal lattice spot known as the excitation error or deviation vector (s), shown by the red arrows in Figure 3.17(b) and Figure 3.17(c). Assuming that the diffraction condition is exactly satisfied (s=0) for vertical planes such as those at the center of the fringe, the bending tilts the lattice and thus the reciprocal lattice (shown by the gray lines in Figure 3.17(b) and Figure 3.17(c)) farther from the diffraction condition (*i.e.*, increasing s for more deformed planes), and the Ewald sphere intersects the relrod farther from its center, resulting in a significant decrease in intensity. The intensity in the BF image will then increase in that particular location as fewer electrons are scattered at Bragg angles. Regions near the bent specimen may be bent into the diffraction condition, resulting in dark regions in the image. This

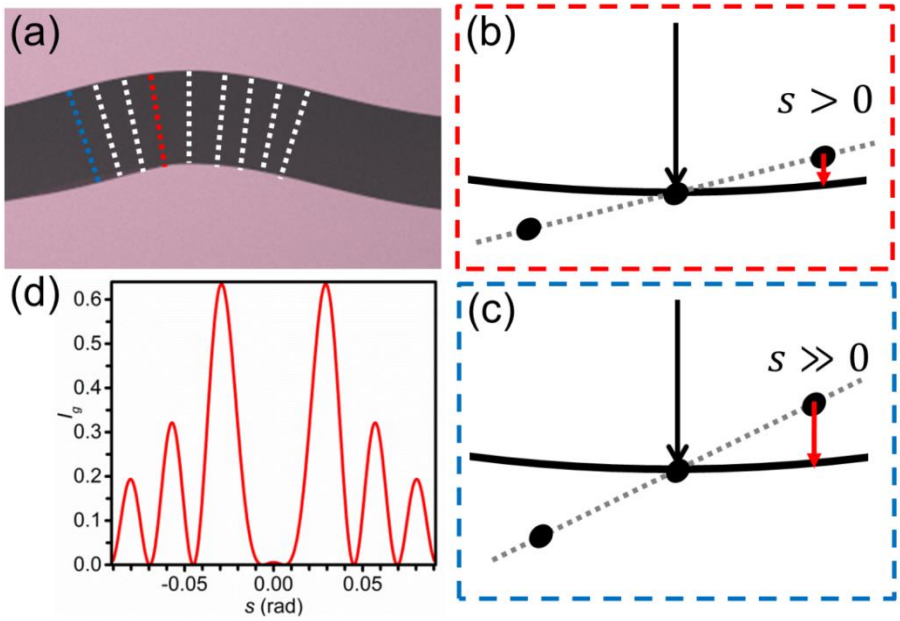

Figure 3.17 | **Diffraction contrast for pure anti-symmetric Lamb mode.** (a) Schematic of bent specimen with lattice planes shown in dotted lines. (b) Orientation of reciprocal lattice (gray line) relative to the Ewald sphere (black sphere) and incoming electron beam (black arrow) for plane in red in (a) with nonzero deviation parameter s (shown by red arrow). (c) Reciprocal space representation for plane in blue in (a) with larger tilt and thus larger s than (b). (d) Intensity in BF image plotted versus the deviation parameter in radians).

oscillation in diffraction condition would thus produce the movement of the bend contour from its initial position.[41]

A simple calculation shows that the image intensity is low at s=0 and higher otherwise, shown in Figure 3.17(d). Several approximations are made. First, the contributions to the diffracted and unscattered or direct beam are assumed to come from a small column with a radius of several nanometers rather than the entire specimen. Second, only the (100) diffraction peak and the direct beam are considered (*i.e.*, the two-beam condition). Dynamical theory, in which the diffracted and direct beam intensities are coupled, can then be used to derive the simple relation:

$$I_g = \left(\frac{\pi}{\xi}\right)^2 \frac{\sin^2(\pi s_{eff} t)}{\left(\pi s_{eff}\right)^2} \tag{3.5}$$

here I_g is the fraction of the total intensity in the (100) diffracted beam for which

$$I_0 = 1 - I_g \tag{3.6}$$

where I_0 is the fraction of the total intensity in the direct beam, t is the specimen thickness, and s_{eff} is the excitation error that accounts for absorption, given by

$$s_{eff} = \sqrt{s^2 + \frac{1}{\xi^2}} \tag{3.7}$$

where s is the excitation error, and ξ is the extinction distance for the (100) diffraction peak, defined as

$$\xi = \frac{\pi V}{\lambda F_g} \tag{3.8}$$

where V is the volume of the unit cell, λ is the electron wavelength, and F_g is the structure

factor for the (100) diffraction peak.[406] First, ξ was calculated. The volume of the unit cell was calculated from the experimentally measured lattice parameters, and the structure factor was calculated from the atomic scattering factors for Mo and S, calculated here using the Cromer Mann coefficients and converted from X-ray to electron scattering using the Mott formula. The value of relativistic λ for 200 keV electrons was taken from Williams and Carter.[265] Thus, ξ = 25 nm for the (100) diffraction peak. An average thickness of 50 nm was used. The various formulas and more details are given in Appendix G. I_g is plotted versus s in Figure 3.17(d), which shows that at s=0, the intensity is very low, leading to a dark band, as observed in the BF UEM images. However, as s increases, the intensity increases and then oscillates. This plot illustrates the mechanism by which pure anti-symmetric modes affect the image contrast.

In the case of anisotropy, as in MoS_2, the anti-symmetric Lamb modes also have a longitudinal component which magnifies this effect. The longitudinal wave distorts the (hk0) planes and thus moves them away or toward the direct beam depending on the point in the oscillation, which brings the Ewald sphere further away from or toward, respectively, the center of the relrod and affects the image contrast accordingly.

Because nearly all of these images were acquired where the electron beam was traveling down the specimen [001] axis, these images are not sensitive to pure symmetric Lamb modes. For a pure symmetric Lamb mode, the lattice is expanding and contracting in the vertical direction, leading to a change in the c lattice parameter. Thus, such changes could be observed in any spots with a z-component. However, as observed in

the diffraction pattern in Figure 2.17(c), none of these spots are allowed in patterns down the [001] zone axis. Moreover, the diffraction contrast features in this specimen can be traced back to the spots observed in the diffraction pattern, as seen in Figure 2.19, and thus such deformation would not be observed. The planes can also be modeled as tilting slightly, as shown in Figure 3.18(a), where the midplane is marked with the horizontal line. For vertical planes, the excitation error s is assumed to be negligible, as shown in Figure 3.18(b). The excitation error for the planes above the midplane is defined as positive since the excitation error falls within the Ewald sphere, as shown in Figure 3.18(c). In order for the mode to be symmetric, the planes below the midplane are tilted with the exact angle in the negative direction, producing an excitation error that is equal in magnitude but opposite in sign, as shown in Figure 3.18(d). The net result is that the pure

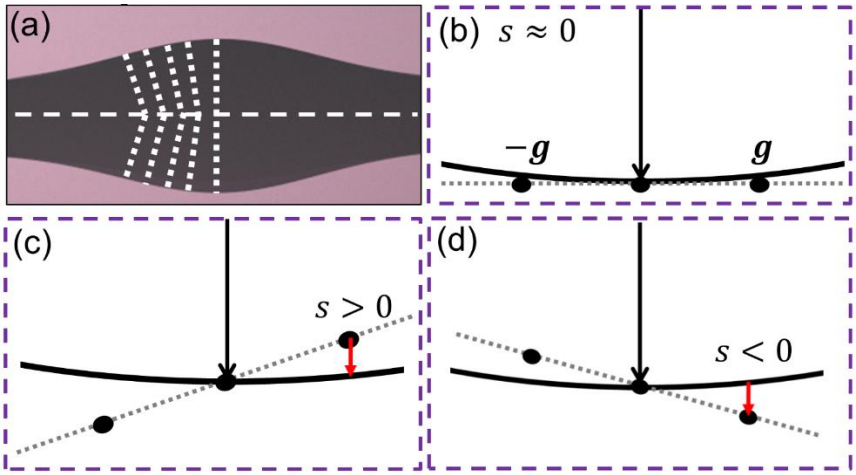

Figure 3.18 | **Diffraction contrast for pure symmetric Lamb mode**. (a) Schematic of the pure symmetric Lamb mode with horizontal midplane and tilted planes marked with dotted lines. Orientation of Ewald sphere and reciprocal lattice for the planes (b) for the vertical planes, where s is negligible, (c) above the midplane, where for g diffraction peak, s is defined as greater than 0 because it is inside the Ewald sphere, and (d) below the midplane, where for g diffraction peak, s is defined as less than 0 because it is inside the Ewald sphere. The magnitudes of s are equal in (c) and (d).

symmetric Lamb mode is invisible in this orientation of the specimen.

In anisotropic materials, however, the anti-symmetric shear wave is coupled to a longitudinal wave even when traveling down a symmetry axis, which decouples the horizontally polarized shear wave.[385,399] In this case, the longitudinal wave, because it is traveling in the plane of the layers, affects the (hk0) planes, which correspond to the diffraction contrast features. This change, however, is much smaller than observed for the anti-symmetric Lamb wave since the transverse wave cannot magnify the effect. Because the change is much smaller, the image signal must be sufficiently high relative to the noise to detect the Lamb wave reliably. This may be a contributing factor as to why waves traveling along bend contours are observed more frequently than those changing the contrast locally not on a bend contour as observed in Figure 3.6.

3.2.3 | Reflection and Interference

A second wave traveling in the opposite direction to the initial wave fronts observed was noted in Figure 3.6, beginning at 140 ps, and the question of the location of its launch is addressed here. The use of Lamb waves to map defects and interfaces stems from their scattering from those features, where the direction of propagation and wavenumber depend on the generalized Snell's law condition. The first candidate then is reflection of the initial wave from a defect. The most obvious defect in the path of propagation for the initial wave is the step edge connecting the two red arrows in Figure 3.19, characterized by the change in the thickness noted in Section 2.3.2 and in Figure 2.20. The step edge is a ~1 μm from *x*0. However, a reflection from this step is unlikely.

First, the wave propagation direction is not perpendicular to the step edge, and thus Snell's law requires that the reflection travels at an angle to the interface normal that is equal in magnitude to the angle of the incoming wave but opposite in sign, which does not allow the reflection to intersect the region analyzed. Moreover, traveling 1.5 μm (from *x*0 to the step edge and to *x*1) at 7.6 nm/ps requires 210 ps, and the appearance of the fringe is ~140 ps.

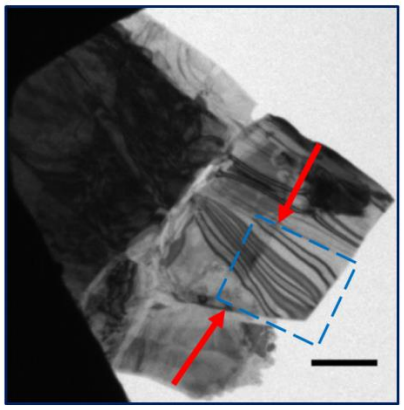

Figure 3.19 | **Nearby step edge.** Step edge from which wave could reflect or be launched connects the two red arrows. Blue rectangle indicates region in Figure 3.6(a). Scale bar represents 1 μm.

Another possibility is that this second wave was launched from the step edge itself at 0 ps. Acoustic waves have been observed to be launched from defects in previous work.[247,259] Traveling from the step edge to *x*1 at 7 nm/ps arrives at *x*1 at 90 ps. This time approximation is a rough approximation still because the second wave was assumed to travel at the same velocity as the first. However, the velocity in anisotropic materials depends on the definition of propagation. A third possibility is that the second wave was launched from another location entirely. Understanding the launch location and mechanisms is an ongoing area of research in the Flannigan research group.

The crossing of the waves suggests that these phonons are coherent acoustic phonons rather than thermal (incoherent) phonons. However, the intensity variations are close to the noise level, and true interference needs to be further probed to understand the

coherency of these waves.

3.2.4 | Broader Impacts

This work demonstrates the power of UEM to further sample characterization methods with Lamb waves. In conventional methods, the aggregate response of Lamb waves to many or large defects in the specimen is tracked, with limited spatial resolution depending on the placement and type of detectors or laser spots.[388,394,407] In UEM BF image sequences, Lamb modes can be tracked as they propagate across the specimen, and their interactions with individual defects can be probed by harnessing the high spatial resolution of TEM to characterize defects and the high temporal resolution of UEM to track the ultrafast interactions. Moreover, as demonstrated in this chapter, multiple Lamb waves in different sections of a specimen can be tracked simultaneously, leading to exquisite spatiotemporal resolution. As demonstrated in the next section, the launch mechanism can also be probed with the same instrument.

3.3 | Preliminary Work Probing Wave Launch Mechanism

It can be observed in Figure 3.6 and Figure 3.11 that the acoustic waves appear to be launched from the edges of the flake, which begs the questions of what the launch mechanism is and of whether waves are initially launched from edges. In this section, I will discuss potential launch mechanisms and my preliminary work determining theoretical time zero for the 515-nm pump line.

3.3.1 | Potential Launch Mechanisms

Gigahertz to terahertz acoustic waves are known to be launched *via* one of or

combinations of four mechanisms: deformation potential, thermoelasticity, inverse piezoelectric effect, and electrostriction. In the deformation potential mechanism, the electrons are promoted into empty energy levels; this change in the electron distribution modifies the interatomic forces. The forces, no longer balanced, produce lattice displacement from equilibrium positions (*i.e.*, strain waves or acoustic phonons), which can be compressive or expansive depending on the interaction. A higher electronic temperature thus results in a larger modification of the interactions and a higher density of phonons launched.[408-409] Thermoelasticity corresponds to a rapid lattice temperature increase. The swift thermal expansion launches strain waves.[408]

The latter two mechanisms can be disregarded in these experiments. In the inverse piezoelectric effect, an external electric field is applied to a piezoelectric sample, and the sample illuminated with a laser. As in the case of deformation potential, the photo-excited electrons modify the interatomic forces and thus change the effective electric field in the lattice, leading to changes in the equilibrium position of the lattice and thus the launch of strain waves. This effect depends on piezoelectricity,[408] which is present for only non-centrosymmetric, thin MoS_2.[118-120] Thus, inverse piezoelectricity was disregarded as a potential launch mechanism in these experiments. In electrostriction, the electric field of the incident light polarizes a transparent medium rather than being absorbed, and this polarization distorts the orbitals. This distortion produces a transient non-centrosymmetry, whereby piezoelectricity produces a lattice distortion and launches strain waves.[408] Even few-layer MoS_2 is strongly

absorbing,[94,158,160] and thus this mechanism is also discarded.

The dominant photogeneration mechanism for coherent acoustic phonons in semiconductors is normally the deformation potential due to generally higher charge carrier lifetimes.[408] For instance, in graphene, experiments and theoretical work suggest that deformation potential is the responsible mechanism for phonon emission in real systems with defects,[212,216,220,410] although some argue that a vector potential or combination of screened deformation and unscreened vector potentials is more accurate.[206,410] However, the deformation potential mechanism depends on a high excited charge carrier distribution and thus can be suppressed if the charge-carrier lifetimes are reduced, as in the case of high pump laser fluence. Moreover, as the carriers relax, they emit more incoherent acoustic phonons, leading to higher and more rapid local heating of the lattice and thus transition to thermoelasticity being the dominant mechanism. In MoS_2, thermalization processes have been found to hundreds of femtoseconds to single picoseconds.[231,235-237] As a result, thermoelasticity could dominate in these experiments.

The apparent launch location of the acoustic phonons also suggests that thermoelasticity could play a significant role in photogeneration of the acoustic phonons. From the analysis above, phonons appear to be launched from the edges of the flake or from defects. Similarly, phonons have been observed to be launched from the specimen-vaccuum interface or defects in similar systems in previous UEM experiments.[247,259] Because the specimen is uniformly illuminated, the charge carriers are expected to be evenly excited uniformly across the specimen, which would result in equal probability of

phonons being launched anywhere across the specimen. In contrast, thermoelasticity launches phonons from regions with high local stress. Stress is already present at defects (*i.e.*, step edges or sudden changes in thickness) or at the specimen-vacuum interface and thus reaching high enough local stress to launch phonons would occur first at these locations. I completed the first steps in researching the launch mechanism, as described below, and the question of the launch mechanism remains an area of ongoing work in the Flannigan research group.

To determine the photogeneration mechanism for coherent acoustic phonons in MoS_2, the charge carrier dynamics must be probed. In MoS_2, those dynamics have been found to occur within the first several picoseconds,[229,233,236] and thus, two experimental parameters – time zero and the instrument response time – must be determined before the experiments can be undertaken. Time zero must be accurately known to determine the timescales of electron excitation and relaxation, which determine not only the time at which phonons are launched (*i.e.*, electron-phonon coupling time) but also whether deformation potential or thermoelasticity dominates. The instrument response time must also be less than a picosecond to probe the dynamics and thus must be characterized and minimized. In the next section, I describe my work characterizing time zero and the instrument response time for the 515-nm pump with the procedure developed for the 1030-nm pump.[276]

3.3.2 | Time Zero and Instrument Response Characterization for Green Pump Line

The first experimental step to determining the acoustic phonon emission

mechanisms and timescales is to determine theoretical time zero and the instrument response for experiments pumping with 515-nm pulses. Theoretical time zero is often characterized with an electron energy-loss spectrometer.[297,411-413] Since the Flannigan laboratory currently does not have such a spectrometer, another approach utilizing the plasma lensing effect was employed. In this effect, a high-energy laser pulse incident on a metal grid produces a dense plasma, and the transient electric fields from that plasma repel the incident electron packets and thus change the image contrast on an ultrafast time scale. It has been found that the onset of the plasma (< 1 ps) is much faster than the pump pulse durations used in these experiments, and thus, the measured onset of the plasma lensing is a robust method for determining the theoretical time zero in our system.[276,414-415]

I first modified the system to produce 515-nm pump pulses with pulse energies of ~700 nJ at 200 kHz, which had been previously determined to produce the plasma lensing effect for infrared pump pulses.[276] The HIRO can produce two wavelengths from the base wavelength (1030 nm): 515 nm and 343 nm. To optimize 515-nm power, the HIRO was reconfigured according to the manufacturer's instructions so that the base wavelength was frequency-doubled only once to the 515-nm pulses, which greatly increased the amount of power available in the pump pulses. Next, the half-wave plate on the input for the HIRO module was rotated while measuring the green power output to optimize the orientation for 515-nm generation. Finally, in the previous laser setup, all of the 515-nm was directed into the BBO, and the remaining 515-nm after conversion,

which was a significant fraction, was used as the pump beam. However, the significant increase in the 515-nm pulse energy easily exceeded the damage threshold of the BBO. Three beam splitters were thus purchased from Thor Labs with 50/50, 90/10, and 70/30 reflection/transmission percentages, respectively. The beamsplitter was then inserted just before the mirror that directs the 515-nm light into the focusing optic before the BBO to minimize the path-length changes in this new beam path versus the old and ensure that time zero remained on the delay stage.

The standard operating procedure recently developed by Dayne Plemmons[276] was followed to find theoretical time zero and the instrument response. A 1000-mesh copper grid was pumped with 515-nm pump pulses with a pulse energy of 694 nJ at 200 kHz. Assuming a radius of 62 μm, the pump fluence was calculated to be 5.75 mJ/cm^2. Plasma lensing was observed while irradiating the 100-μm diameter LaB_6 flat surface embedded in graphite with a UV pulse energy of 77.65 nJ. The grid was observed at 120x magnification at spot size one, a condenser aperture with 2-mm diameter, and BF images were acquired with four-by-four binning to reduce the acquisition time to 1 second. Three runs were collected with the UV pulse energy 77.65 nJ to collect statistics. All image sequences have time steps of 250 femtoseconds and were taken in random order to deconvolute non-dynamic effects of the room environment from the plasma lensing. To calculate the number of electrons per pulse, 4 images without averaging were collected before and after each full scan, which contained 3 runs. The counts at each pixel were converted to number of electrons by assuming 4 counts equaled one electron,

as estimated by the camera manufacturer, Gatan. This quantity was then divided by the repetition rate and acquisition time of the individual image to give electrons per pulse per pixel. These values were then summed to give electrons per pulse. The electrons per pulse before and after each scan were then averaged to give the mean electrons per pulse.

As outlined in Figure 3.20, the time-dependent changes in image intensity around the copper grid bars were quantified to measure the time zero and the instrument response. The images in all the runs were first converted from dm4 to tif files. A median filter was applied to remove X-rays and reduce noise, and the images were interpolated to twice the original sampling rate. These images were drift-corrected using the template matching plugin as described in Section 2.4.2. These shifts were imported into MATLAB and applied to each image. Figure 3.20(a) shows a representative grid square for the image sequence taken at UV pulse energy of 77.65 nJ, which produced 5300 ± 200 electrons per pulse. The rectangle whose rows are averaged to show changes in intensity at each point along the horizontal grid bars is shown on top of an image of one of the grid squares in Figure 3.20(a). Figure 3.20(b) shows the resulting changes in intensity versus time at each position along the horizontal grid bars.

Time zero and the instrument response time were extracted from the images by fitting the image intensity with an error function. The time at which the error function has decayed to 50% of its initial value is defined as time zero, and the width of the error function corresponds to the instrument response, which is described by a Gaussian function in the weak interaction limit.[196] The images were then rotated so that the grid

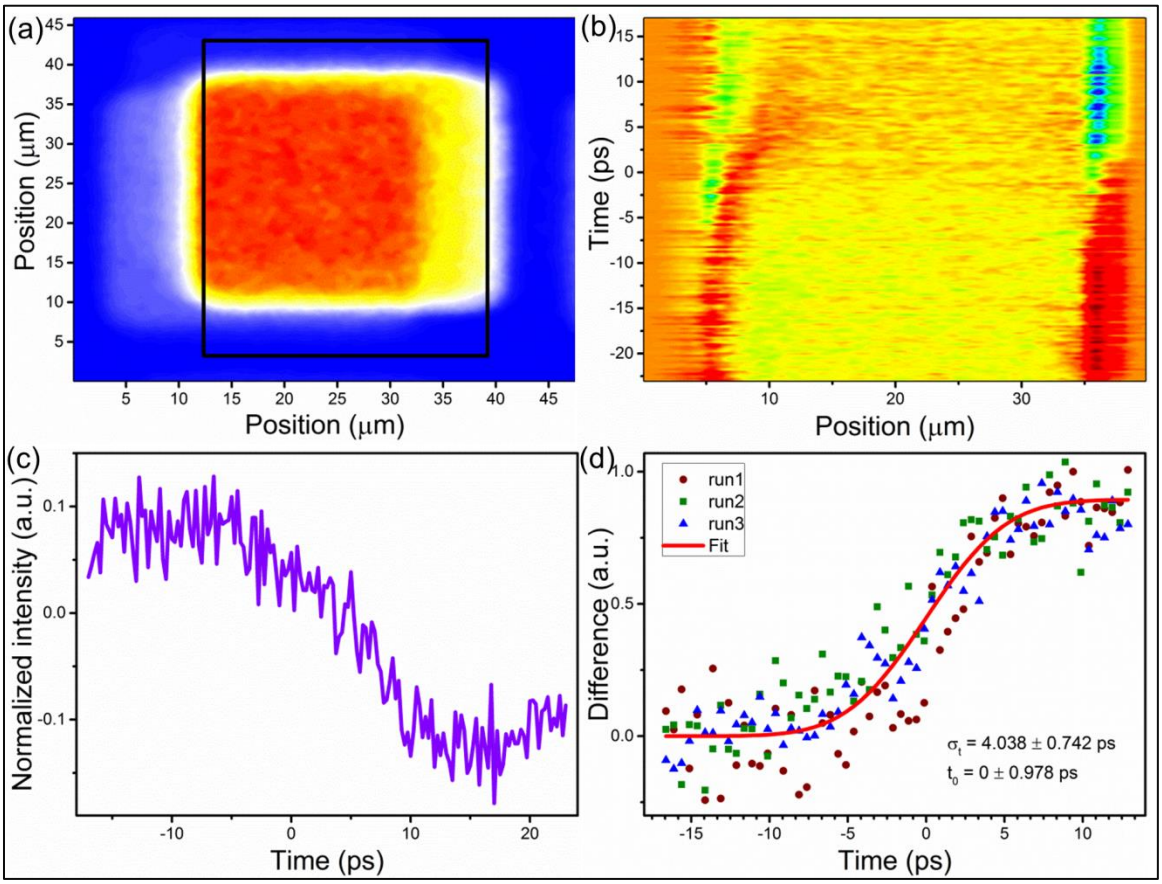

Figure 3.20 | **Characterization of time zero on the 515-nm pump line and instrument response time for pulses with thousands of photoelectrons.** (a) A representative BF UEM image of the copper grid square before the arrival of the pump pulse that shows the inside of the grid square (red) surrounded by the copper grid bars (blue). The black box shows the area whose rows were averaged to find the intensity variations in y. The black box indicates the region analyzed. (b) The intensity vs. time along the horizontal direction of the black box in (a). The maximum change occurs at the right edge. (c) The normalized intensity versus at the right edge of (b). (d) The intensity in three runs at the UV pulse energy 77.65 nJ (electrons per pulse = 5300 ± 200) in the same area on the grid and their mean error function fit, which results in the instrument response is fit to be σ_t = 4.0 ± 0.7 ps and time zero t_0 = 0 ± 1 ps.

bars were approximately vertical and horizontal to the image edges (24 degrees clockwise). For the same 5 grid squares in each image sequence, the intensity was averaged in the x- and y-direction. The location of maximum change in intensity at each grid square edge was computed. The maximum change in intensity (at the right edge of

Figure 3.20(b)) versus time is plotted in Figure 3.20(c). The intensity at these four locations was then inverted and normalized before being fit by an error function. The fits were then examined, and responses with amplitudes less than 0.85 and large residuals were excluded as poor representations of the instrument response. The fits for the data plotted in Figure 3.20(d) were then averaged to calculate the average instrument response time ($\sigma_t = 4.038 \pm 0.742$) and time zero ($t_0 = 0 \pm 0.978$ ps) given in Figure 3.20(d).

These results inform the experimental parameters needed to accurately measure the electron-phonon coupling time and phonon launch time. The instrument response for photoelectron packets containing thousands of photoelectrons is several picoseconds, which is on the order of electron-phonon coupling times reported in the literature.[229,233,236] Thus, much lower UV pulse energies must be used to probe the ultrafast dynamics due to the shorter instrument response time of the resulting smaller photoelectron packets. Further work to determine the minimum number of photoelectrons in each packet that still provide sufficient signal to image the launch of phonons will need to be conducted. The determination for time zero will be used to calculate the delay between arrival of the pump pulse and the launch of phonons, which would also be approximately equal to the electron-phonon coupling time.

3.4 | Summary and Conclusions

Propagating, high-GHz waves were observed in UEM BF images, traveling at phase velocities (7 nm/ps) close to the speed of sound in an MoS_2 flake. In particular, waves with frequencies of ~20-30 GHz and of 40-50 GHz were observed propagating

along or near bend contours. Control experiments in which a series of images were collected while the pump laser was left at a set time delay and in which a series of images were acquired after the pump laser was removed from the specimen showed that the dynamics were due to the material photo-response rather than environmental or photoelectron fluctuations.

The waves were identified as Lamb waves (guided surface waves in plates) rather than Rayleigh waves (guided surface waves in samples approximated as elastic half-spaces) due to their speed and specimen thickness. The Lamb modes were further identified using a calculated dispersion relation for an isotropic MoS_2 as an approximation and the cut-off frequency calculations for anisotropic solids. The 40-50 GHz waves were assigned to second order anti-symmetric or symmetric mode, depending on the symmetry of their displacements with respect to the midplane: symmetric and anti-symmetric. The effect of Lamb mode displacement on the image contrast was discussed in terms of the pure, zeroth order modes. The pure anti-symmetric Lamb mode, which is lower in frequency than the symmetric Lamb mode, changes the diffraction contrast *via* the same mechanism as bend contours (tilting of the planes closer or further from the diffraction condition depending on the specimen bending). The pure symmetric Lamb mode cannot be observed when the specimen is viewed down the [001] axis as in these experiments due to the contrast change only affecting the *c*-axis. However, in anisotropic materials, the symmetric Lamb modes are coupled to longitudinal waves, which change the diffraction condition in-plane and thus changes the contrast observed. A second wave

was identified in one of the image sequences and tentatively assigned to a wave launched from a nearby step-edge. Further work, however, is needed to clearly identify the source of this wave. Interference of the two waves suggested that the phonons are coherent rather than incoherent or thermal phonons.

Deformation potential (changes in the charge carrier distribution modifies interatomic interactions and results in the launch of strain waves) and thermoelasticity (high local heating leads to high local strain and the launch of strain waves) were identified as two potential launch mechanisms for these waves. The experiments suggest that strain waves are launched from defects and specimen-vacuum interfaces, which supports thermoelasticity as the launch mechanism in this case. To probe the launch mechanism, time zero on the 515-nm pump line and the instrument response time must be known. I presented my work modifying the 515-nm pump line so that plasma lensing could be used to determine time zero and characterize the instrument response time was presented. Time zero and the instrument response for certain experimental conditions were then determined experimentally.

This work furthers our understanding of the interactions between Lamb waves and specimen features such as defects. In addition, groundwork has been laid to probe the launch mechanism using the same instrument as that used to probe the propagation of the modes.

4 | TRANSITION FROM PHONON DYNAMICS TO MECHANICAL OSCILLATIONS

The experiments described in this chapter detail the second temporal regime of dynamics – the evolution from the coherent acoustic phonons in the previous chapter to chaotic, incoherent, lower-frequency oscillations after the initial hundred picoseconds. This coherent-to-incoherent transition over the span of a few nanoseconds is identified by monitoring the motion of bend contours in a BF UEM image series. The bend-contour motion transitions from (localized) nanoscale, high-GHz oscillations to low-GHz, larger-scale dynamics. Combined with the phonon dynamics detailed in Chapter 3 and the mechanical oscillations detailed in Chapter 5, this second temporal regime can be characterized as a transition region connecting local, relatively high-frequency coherent elastic strain waves to lower-frequency, whole-flake nano-mechanical motions via phonon-phonon scattering. The beginning of this regime is the interference and scattering of the phonons observed beginning at 140 ps after the first observation of dynamics in Figure 3.6 and is most obvious when the dynamics are imaged over several nanoseconds, as described here. Passages and figures of this chapter were taken from A. J. McKenna, J. K. Eliason, and D. J. Flannigan titled “Spatiotemporal Evolution of

Coherent Elastic Strain Waves in a Single MoS_2 Flake," which was recently accepted for publication in *Nano Letters*.[286]

4.1 | Transition Observed in Image Sequence with 2 and 5 ps Steps

4.1.1 | Dynamics Imaged

The images in this sequence (-100 to 1000 ps in 2 ps steps and 1000 to 2500 ps in 5 ps steps) were taken in random order as a control measure. The images were all acquired using a 200-μm diameter condenser aperture, spot size 1, and a 40-μm diameter objective aperture at 3,500x magnification, which corresponds to 1.5 nm/pixel. Each image was acquired for 30 seconds. The specimen was tilted 0.4° around the double-tilt holder axis and 0.93° around the orthogonal holder axis so that the diffraction contrast was similar to that observed in Figure 2.17(b). The source was 50-μm diameter flat surface LaB_6 embedded in graphite.

The dynamics were first qualitatively captured using difference images of a small region of the specimen. The image sequence was batch-converted and drift-corrected as described Section 2.4.1. Figure 4.1 is a magnified area of the region outlined in blue in Figure 2.17(b) at 572 ps in this image sequence. The region outlined in red in Figure 4.1 was used to capture the dynamics though difference images. The image of

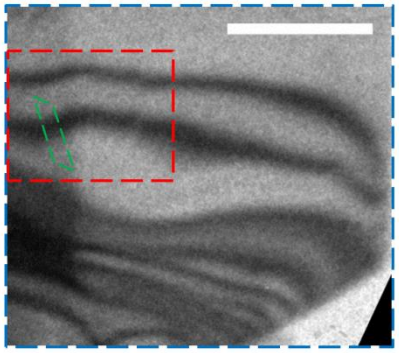

Figure 4.1 | **Representative BF UEM image of MoS_2 region outlined in blue in Figure 2.17(b).** The red dashed rectangle is the region in which contrast dynamics are highlighted in Figure 4.2. The green rectangle indicates the region in which subsequent analysis was performed. The scale bar represents 500 nm.

the region at -10 ps (shown as the first panel in Figure 4.2) was subtracted from the images at 0, 60, 82, 110, 314, 592, and 1,065 ps to produce the difference images, which were false-colored in Origin using a rainbow colormap.

The difference images in Figure 4.2 show that low-GHz as well as high-GHz oscillations are present on single ns timescales. A representative image of the region corresponding to -10 ps is shown in the first panel. At 0 ps, no change in intensity greater than a factor of one is observed (*i.e.*, no motion). By 60 ps, the intensity near the lower dark feature has changed by a factor of 2, meaning that the feature has moved down toward the bottom of the flake. By 82 ps, the intensity in the new position of the feature has changed by a factor of -1, showing that the feature has moved back to its initial position. By 110 ps, the intensity change indicates that the feature has completed a full period of motion and moved down toward the bottom of the specimen again. The period of this motion is approximately 24 ps. Similarly, the features display a much larger

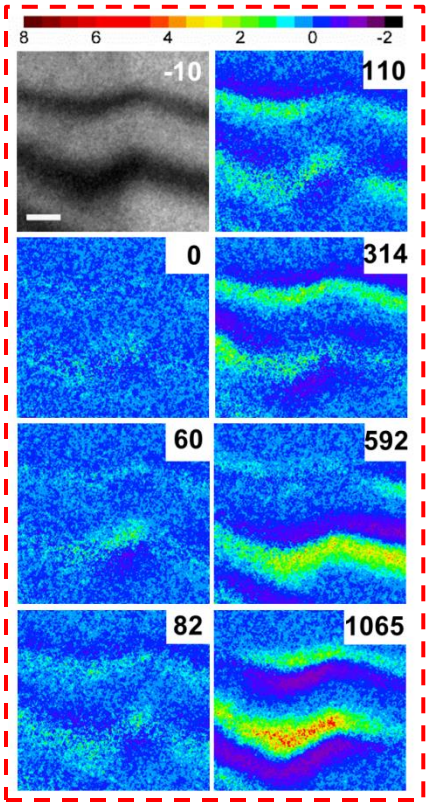

Figure 4.2 | **Contrast dynamics in transition from high-GHz propagating phonons to whole-flake mechanical oscillations.** Reference (-10 ps) and subsequent, false-colored difference images of the region highlighted in red in Figure 4.1. The time in ps relative to experimental time zero is shown in the upper-right corner of each frame. The color bar represents the factor by which the image counts have changed relative to pre-time-zero frames. The scale bar represents 100 nm.

spatial scale (tens of nm in some places), lower-frequency motion, in which the lower dark feature moves down toward the bottom of the flake by 314 ps, back towards its initial position by 592 ps, and down further by 1,065 ps. The period of this motion is less well-defined but closer to hundreds of picoseconds.

I quantified this lower-frequency motion by tracking the position of the dark feature in the green parallelogram in Figure 4.1. The images were drift-corrected, and the raw images were imported into MATLAB, where the intensity in each image was normalized by the average intensity across the entire image. I then drew a line approximately parallel to the movement of the diffraction contrast feature in Figure 4.1 (long edges of the green parallelogram). For each pixel along the long edge of the green parallelogram in Figure 4.1 in each image, the normalized counts within 25 pixels of either side of the line were averaged to produce an intensity versus space trace. This trace was smoothed using a Savitzky-Golay finite-duration impulse response filter, with an order of 3 and framelength of 33 to reduce high-frequency noise and X-rays. The diffraction contrast feature was identified as a minimum in the intensity, and the local minima were found in the intensity traces using the MATLAB function extrema. An appropriate fitting window that minimized errors in peak identification and fit was found to be the spatial range between two local maxima between which was a local minimum. The extrema were identified using the MATLAB function findpeaks. This minimum was then fit with a pseudo-Voigt function with negative amplitude using a nonlinear least squares solver, and the fitted center was recorded as the position of the contrast feature in

each image. The fitted centers before 0 ps were averaged to calculate an initial position, and the initial position was subtracted from the fitted centers to calculate the relative position. Any outlying points with low R^2 values were manually examined and found to be due to misidentifying the appropriate fitting window. This fitting window was manually specified, and the data were re-fit. The relative position was interpolated to 1 ps time steps and is plotted in Figure 4.3(a).

The relative position and FFT of the bend contour show that high-frequency waves are completely damped within approximately 1 ns and transition into increasingly incoherent, larger-scale motions. The high-frequency oscillations in position, magnified in the inset showing the first 500 ps of dynamics, are less than 10 nm in magnitude and are replaced by longer-period motions. The frequencies are determined by performing a fast Fourier transform (FFT) on the interpolated relative position to produce Figure 4.3(b). The displacement was padded to 2^{17} values with the average of the last 50 displacement values to increase frequency resolution. The low-frequency motions have frequencies on the order of 1 GHz, and the high frequency motions are shown in the inset from 40 to 51 GHz, which is consistent with the high-frequency motion evident in Figure 3.11 and similar figures.

The timescale of damping is captured using FFTs over different time windows. In Figure 4.3(c), the FFTs over windows of 0 to 0.5 ns (red curve), 0.501 to 1 ns (green curve), and 1.001 to 2.5 ns (blue curve) are shown for the high-frequency band between 40 and 51 GHz and illustrate that the higher-frequency mode becomes undetectable

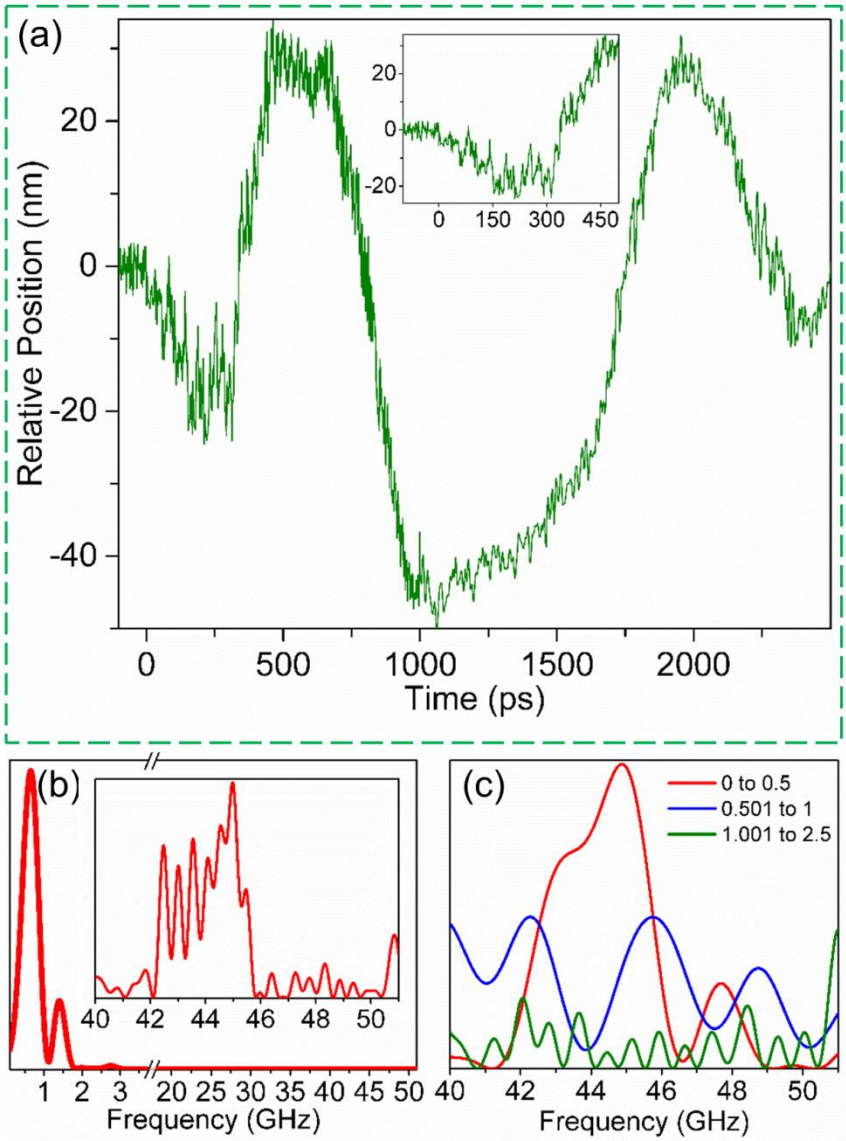

Figure 4.3 | **Quantification of transition from 50-GHz oscillations to 1-GHz oscillations.** (a) Relative position, as a function of time, of the bend contour highlighted in the green dashed parallelogram in Figure 4.1. The inset shows the first 500 ps of the contrast-feature dynamics. The axis labels are the same as the larger plot. (b) Fourier transform of the entire time trace in panel (a). The inset is a magnified view of the 40- to 51-GHz band showing the presence of low-magnitude, higher-frequency modes. (e) Fourier transform from three discrete time windows from the trace in (a) within the 40- to 51-GHz band. The units of the panel key are in nanoseconds, and the *y*-axes for the Fourier transforms are magnitude.

within approximately 1 ns. Owing to the observed wave-train interference effects within the first few hundred picoseconds (Figure 3.6), emergence of incoherent bend-contour motions is ascribed to wave-train reflections and in-plane strain-wave interactions. Incoherent phonons lead to lattice heating and thermal

expansion.[249] The specimen is constrained along the left and lower edges, which result in non-uniform deformation and ring-down of the energy. The fluctuating deformation would bring local parts of the specimen into and out of the diffraction condition, resulting in oscillation of the bend contours. This motion is similar to that observed when the specimen is tilted under thermionic illumination, leading to movement of contrast features (*e.g.*, bend contours).[41] To test such a hypothesis, future work includes tilting the specimen and correlating a change in position of the contrast features to a tilt angle, and modeling the thermal expansion and relaxation to determine if such a tilt is experimentally realizable under thermal stresses.

4.1.2 | Control Experiments

Two control experiments were conducted on the same day as the images above to eliminate environmental fluctuations as potentially contributing to the observed dynamics. First, the pump was left at 200 ps, and 120 images were acquired with the

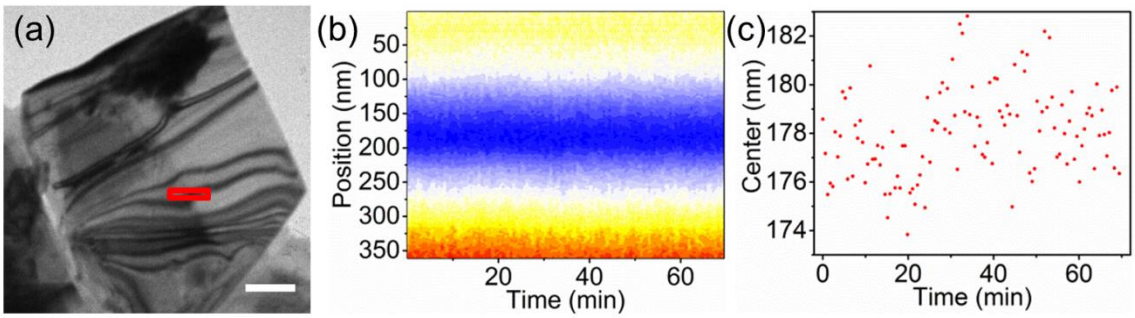

Figure 4.4 | **Control experiment with pump at 200 ps time delay.** (a) Representative BF UEM image with region analyzed outlined in red. Scale bar represents 500 nm. (b) Intensity as color plotted over time in minutes and position in nm, which shows no oscillations. (c) The center of the dark contrast feature in (a) over time, showing movement smaller than that observed in scans with varying time delays.

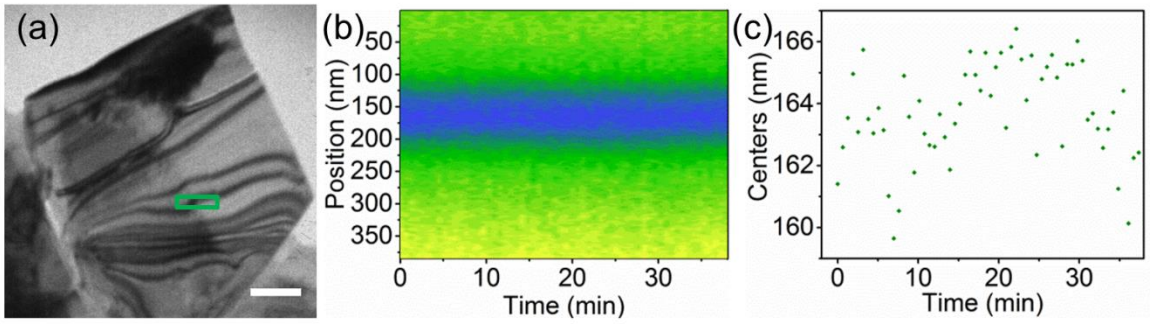

Figure 4.5 | **Control experiment with no pump irradiation.** (a) Representative BF UEM image with region analyzed outlined in green. Scale bar represents 500 nm. (b) Intensity as color plotted over time in minutes and position in nm, which shows no oscillations. (c) The center of the dark contrast feature in (a) over time, showing movement smaller than that observed in scans with varying time delays.

same imaging conditions as the image sequence above with an acquisition interval of 35 seconds. The images were batch converted and drift-corrected following the standard procedure, and the dm3 files were imported into MATLAB. I drew a line in approximately the same location as the green parallelogram in Figure 4.1, as shown by the red rectangle in Figure 4.4(a), and the intensity was averaged over 25 pixels on each side to produce an intensity trace. The intensity traces are plotted in Figure 4.4(b) and show no discernible movement. The noise can be quantified by fitting the valley in intensity with a negative-amplitude pseudo-Voigt function. The results are plotted in Figure 4.4(c) and show smaller magnitude oscillations than those observe in Figure 4.3(a). The second control experiment is a series of 60 images acquired with the same imaging parameters as above except that the pump laser was removed from the specimen. The acquisition interval was 38 seconds. The images were analyzed in the same manner as the first control experiment for the region outlined by the green rectangle in Figure 4.5(a). The intensity trace from each image is shown in Figure 4.5(b), and the fitted

centers are shown in Figure 4.5(c). Similarly, changes in the intensity and position are smaller than observed in Figure 4.3(a).

4.2 | Discussion of Chaotic Transition and Implications

This work is unique in that it probes the transition from coherent motion well-described by phonon dynamics and Lamb modes to coherent mechanical motion described by macroscopic mechanics. Coupling of strain-wave trains to the MHz whole-flake oscillations could provide a means for sensitive and predictable optomechanical control of MoS_2 membrane resonators for a variety of energy-harvesting and energy-conversion applications. However, combined spatial and temporal evolution of the deposited energy is challenging to elucidate, despite individual dynamic phenomena being amenable to study (*e.g.*, photogeneration of ultrasonic waves). This study demonstrates that UEM imaging enables more comprehensive studies to be performed, wherein dependence of strain-wave dynamics on discrete structural features and the mechanisms of coupling to lower-frequency, larger-scale oscillatory modes, can be elucidated.

Qualitatively, the observed behavior is expected to be universal for photoexcited freestanding multilayer MoS_2 flakes, though quantitative timescales and wave vectors strongly depend on overall spatial dimensions, structural morphology, and boundary conditions. This is because the number of wave trains initially launched following photoexcitation may depend upon the total number of discrete interfaces present within a flake, for example. This, combined with speed-of-sound wavefront velocities and

accounting for distances between discrete structural features, suggests the transition time from coherent to incoherent motion will depend upon the average distance traveled prior to the onset of significant reflection and interference (*i.e.*, the wave front mean free path).

4.3 | Summary and Conclusions

The high-frequency, propagating wave trains observed in Chapter 3 were found experimentally to scatter and result in increasingly incoherent, low-GHz oscillations. Images with 2 and 5 ps time steps were acquired out to 2.5 ns, and motions of bend contours were quantified. High-frequency (40-50 GHz) modes were observed to be completely damped within approximately 1 ns, and 1-GHz oscillations were found to dominate. Control experiments were used to eliminate environmental fluctuations as the potential source of these dynamics and to ascribe the dynamics to the material photo-response. This behavior is expected to be true in other freestanding multilayer specimens, although the timescales and magnitudes of the motion will depend on the specimen geometry, boundary conditions, and phonon mean free path. These experiments demonstrate the ability of UEM to image mode coupling and conversion across multiple temporal scales.

5 | MECHANICAL RINGDOWN

In the third temporal regime, the photo-excited oscillations decay into whole-flake, mechanical resonances. Fundamentally, the experiments in this chapter are of interest in understanding the ultimate evolution of the high-velocity, GHz strain waves. As demonstrated in Chapter 4, however, the dynamics were still plainly evolving in individual nanoseconds. To reach longer timescales, the nanosecond laser system and experiment logic described in Sections 2.1.2 and 2.1.5, respectively, were employed to acquire UEM BF image sequences with 0.5 and 10 ns steps. The 0.5 ns step image sequence captures the transition from the 1-GHz oscillations of Chapter 4 into the MHz mechanical oscillations, and the 10-ns step image sequence shows the rapid evolution into three, whole-flake mechanical resonances with microsecond lifetimes. The resonances are governed by the macroscopic material properties like Young's modulus and the boundary conditions and thereby connect ultrafast, nanoscopic dynamics to slower macroscopic counterparts across more than six orders of magnitude in time. Passages and figures from this chapter are taken from A. J. McKenna, J. K. Eliason, and D. J. Flannigan titled "Spatiotemporal Evolution of Coherent Elastic Strain Waves in a Single MoS_2 Flake," which was recently accepted for publication in *Nano Letters*.[286]

5.1 | Studies on Mechanical Oscillations of MoS_2

Micro- and nanomechanical resonators, like few- and monolayer MoS_2 can be employed as sensors and switches. Consequently, the mechanical properties need to be carefully characterized to understand their behavior before and after exposure to stimuli. Optical interferometry is one well-known, non-destructive technique to characterize material properties *via* photo-excited or driven mechanical resonance.[12,407] The resonance frequency depends on the material stiffness matrix, sample geometry, and the boundary conditions and is usually modeled using linear elastic continuum mechanics. Most experiments measuring the mechanical properties of MoS_2 specimens have used circular MoS_2 films that are clamped about their circumference, which simplifies the mathematics but reduces the applicability of the technique to measure properties in complicated device geometries.

Recently, a time-domain response study of the properties of a circular monolayer MoS_2 membrane demonstrated that time-domain and equilibrium oscillations are equally capable of accurate measurement of properties. For monolayer MoS_2, the mechanical ringdown lifetime for the 22.2 MHz resonant mode is 0.6 μs, and the quality factor is 41.8 ± 0.4, which compares well to that measured with the driven oscillations (41.5 ± 0.3). For five-layer MoS_2, the resonance frequency is 7.52 MHz and has a lifetime of 1.56 μs and a ringdown quality factor of 37.8 ± 0.2.[12] This study demonstrates that time-domain responses can be used to characterize a material, and a technique that can study the time-domain response of a more complicated geometry would be advantageous.

5.2 | Imaging Mechanical Ringdown with UEM

The mechanical ringdown of the MoS_2 specimen was observed in two image sequences: one with 0.5 ns time steps from -5 to 110 ns and the other with 10 ns time steps from -100 to 13,840 ns. I will henceforth refer to the former as the image sequence with 0.5 ns steps and the latter as the image sequence with 10 ns steps. The 0.5-ns step image sequence was acquired at 3,500x magnification (1.5 nm/pixel). Each image was acquired for 20 seconds using a fresh 15-μm-diameter flat LaB_6 with no graphite, a 2-mm diameter condenser aperture, a 40-μm diameter objective aperture, and spot size 1.

The motion imaged in the first 100 ns with 0.5 ns time steps is similarly chaotic to that observed in Chapter 4. A representative image from the image sequence is shown in Figure 5.1. The images were batch-converted and then drift-corrected using template matching, as described in Section 2.4.1. Each was imported into MATLAB, smoothed using a median filter, and divided by the mean intensity in the whole image. The images were rotated so that the flake was approximately vertical (116°). The first 11 images, corresponding pre- and time zero points, were averaged to produce an average pre-excitation image that was subtracted from all the images. The image was then divided by

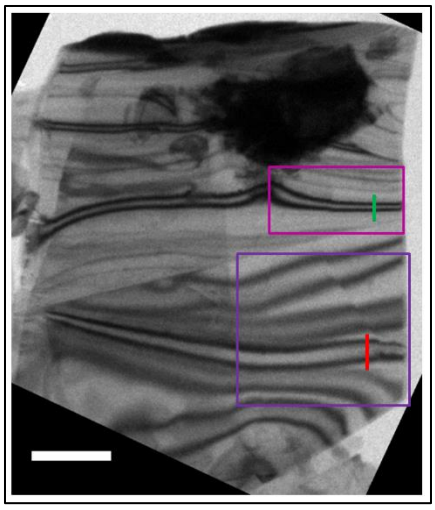

Figure 5.1 | **Representative image from 0.5 ns time step image sequence.** The pink and purple rectangles correspond to regions for which difference images were computed. The red and green rectangles correspond to regions for which the motion of the contrast was quantified. Scale bar is 500 nm.

this pre-excitation image to calculate the factor of change.

The resulting difference images for the pink and purple rectangles in Figure 5.1 are shown in Figure 5.2 and Figure 5.3, respectively. Positive factors (color closer to red) indicate an increase in intensity or movement of the fringe away from the location, and negative numbers (color closer to purple) indicate a decrease in intensity or feature movement into those regions. In both figures, the first panel shows a representative image at -5 ns in the region, followed by the region at 0 ns to show minimal contrast change. The first three panels afterward show the relatively high-frequency movement with periods of individual ns. The following five panels show lower-frequency movement with periods of tens of ns.

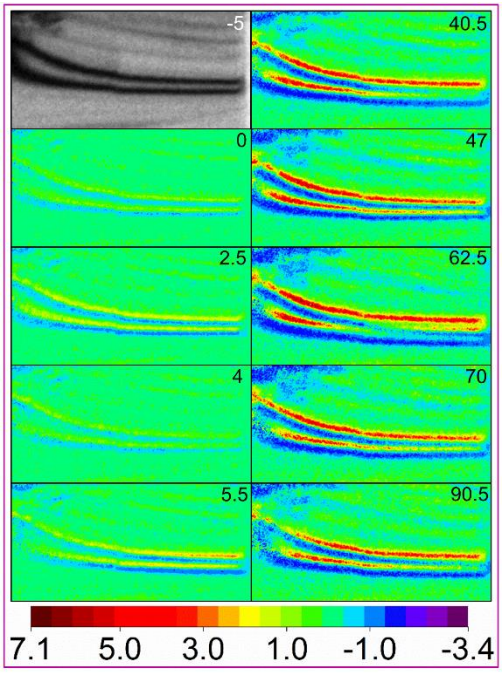

Figure 5.2 | **Difference images for region in pink rectangle in Figure 5.1.** The colorbar indicates factor of change in intensity. The numbers in the upper right hand corner indicate the time point in ns. The first panel is the region at -5 ns.

The motion is similar in Figure 5.3. For the bright feature between the two most prominent dark features, the contrast shows fractional changes in intensity at 0 ns. At 5.5 ns, the contrast feature has moved up toward the top of the flake, evidenced by the factor of 4 change in intensity (red within the fringe). By 10 ns, the feature has returned to its initial position. By 11.5 ns, the feature has completed a full period of oscillation by

moving again toward the top of the flake. The period of the motion is individual ns. The remaining five panels show similar motions of a larger magnitude and longer periods.

The motion can be quantified by tracking the displacement of two bright features in the red and green boxes in Figure 5.1. The BF images were imported into MATLAB and rotated 25° counterclockwise. To make each box, a line was then drawn across the bright feature (the long direction in Figure 5.1), and five pixels on either side were averaged together to reduce random noise in each image to produce an intensity versus space trace at each time point. The peaks and valleys were identified with the findpeaks command in MATLAB, and a peak preliminarily identified as that corresponding to the bright feature was then fit with a pseudo-Voigt function. The first 11 center values were averaged together to give an initial position, and the value was subtracted from all values to give the relative position. Approximately ten fits with R^2 values less than 0.8 or displacements that were larger than a factor of one from the nearby displacements were individually examined to check that the correct peak was fit and that the fit was not a straight line. If either of the two cases applied, the fitting window as manually specified, and the peak was re-fit. The positions of the contrast features are plotted in the left panels in Figure 5.4. The relative positions were padded to 2^{17} values, and the FFT was computed and is plotted in the right panels in Figure 5.4.

As can be seen in Figure 5.4, the movement of the contrast features is chaotic, which indicates the presence of multiple modes. The displacement of the fringe is observed to be much larger in the lower red box than in the upper green box. The FFTs

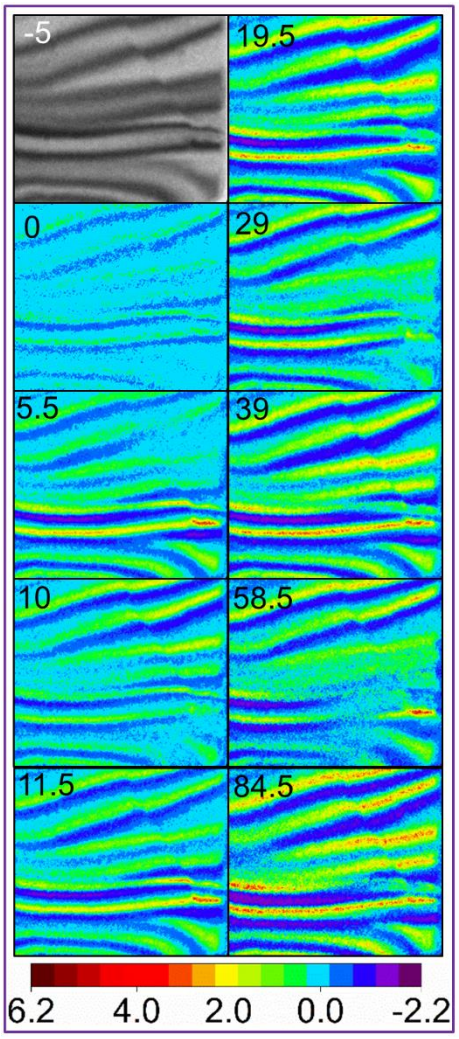

Figure 5.3 | **Differences images for region outlined in purple in Figure 5.1.** The colorbar indicates factor of change. The numbers in upper left hand corners indicate the time point in ns. The first panel is a representative image at -5 ns.

show the presence of multiple modes. For the green box, the main frequencies in the FFT are 3.2, 14.7, 34.5, and 62.3 MHz. For the red box, the three lowest frequencies with the highest amplitudes are 29, 127, and 150 MHz.

The ultimate dissipation of the energy can be extrapolated from the 10-ns step image sequence. This image sequence is a compilation of four scans, all acquired on the same day. 126 images from the first scan, 384 images from the second scan, 500 images from the third scan, and 385 images from the fourth scan were compiled. The photoelectron beam was adjusted between the second and third image sequences to improve intensity of the beam. The image sequences were acquired in temporal order using a 2-mm diameter condenser aperture and 40 μm-diameter objective aperture. The image sequences were acquired at 3,500 times magnification, which corresponds to 1.5 nm/pixel. Each image in the 10-ns step image sequence was acquired for 5 seconds using a 50-μm-diameter LaB_6 cylinder embedded in graphite.

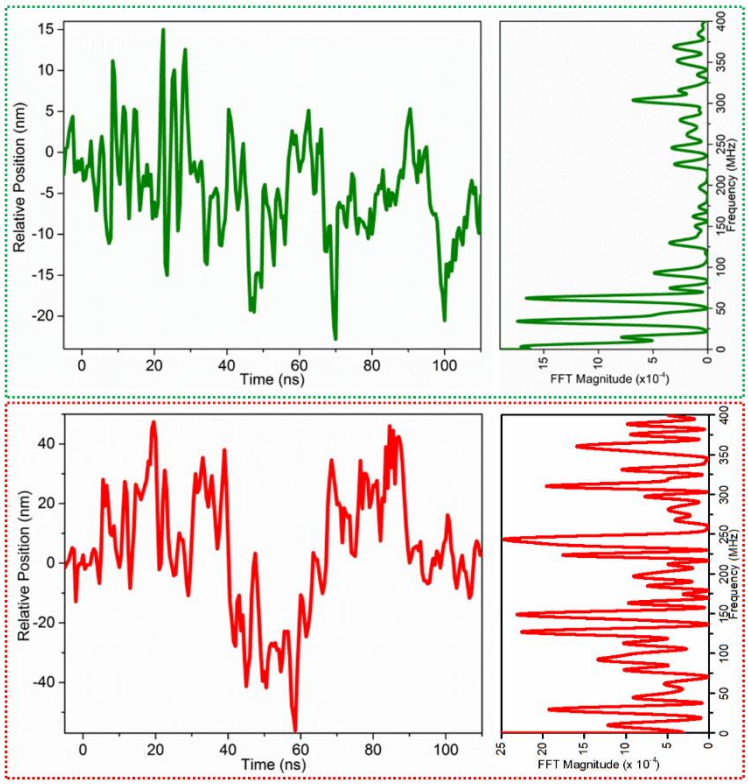

Figure 5.4 | **Position and FFTs of contrast feature movement for 0.5 ns step image sequence.** The two graphs outlined in green are the position of the bright fringe spanned by the green line in Figure 5.1 vs. time and the FFT magnitude vs. frequency. The two graphs outlined in red are the same for the bright fringed spanned by the red line in Figure 5.1.

Images were batch-converted and then drift-corrected using template matching, as described in Section 2.4.1, and saved as tiffs. Figure 5.5(a) is a magnified area of the region outlined in blue in Figure 2.17(b) at 0 ns in this image sequence. Representative images of the diffraction contrast movement due to the large-scale oscillations of the flake are shown at 0, 480, 490, and 520 ns in Figure 5.5(b). The black spheres used to mark the initial position of the lower dark feature in each image were manually placed in the 0 ps image and projected onto the other images using Origin. As observed in the difference images in Figure 5.2 and Figure 5.3, the movement is temporally uneven, evidencing the presence of more than one fundamental mode.

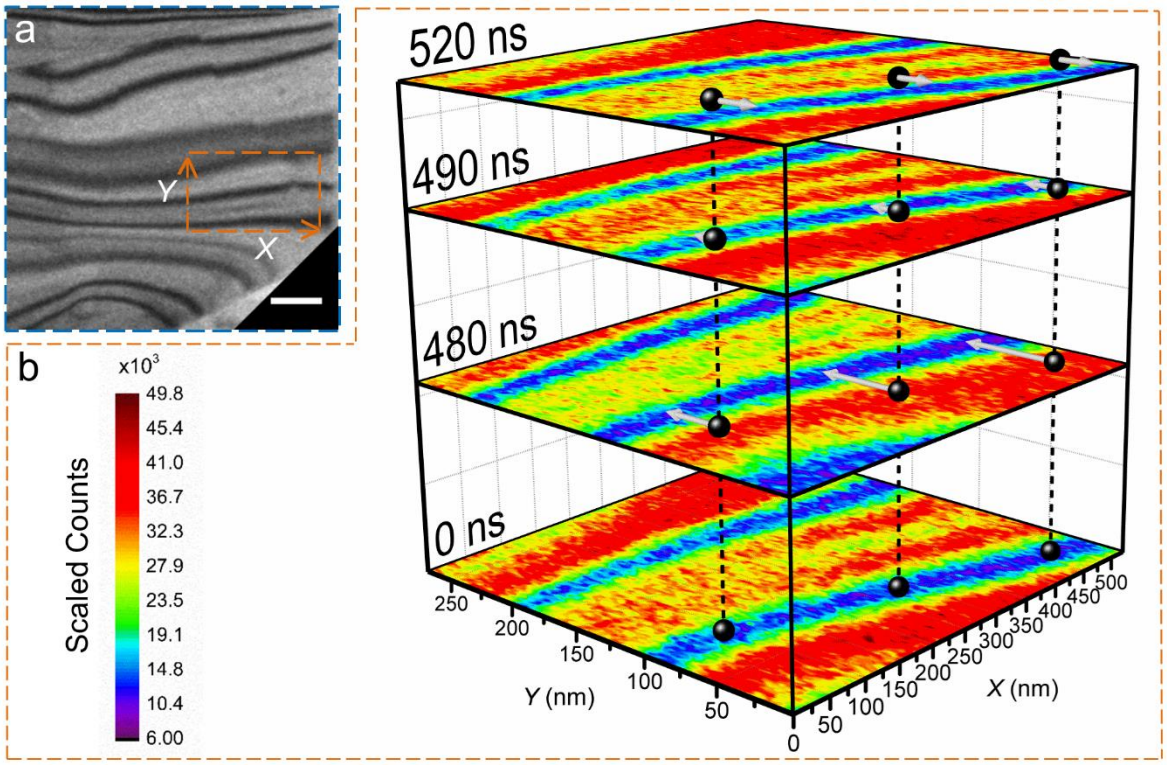

Figure 5.5 | **Images of whole-flake mechanical oscillations.** (a) Representative UEM BF image of the region of interest. The orange dashed rectangle denotes the region highlighted in panel (b), with the *X* and *Y* directions labeled. Scale bar represents 200 nm. (b) Select (false-colored) UEM images of the highlighted region in panel (a). The relative time at which each frame was obtained is shown to the left, and three black spheres mark the initial position at $t = 0$ ns of a bend contour of interest. Vectors in the plane of each image and extending from the spheres denote the displacement direction and magnitude relative to the $t = 0$ ns frame. The color bar corresponds to scaled image counts.

To quantify the multiple modes, the motion of a contrast feature was spatiotemporally mapped. A rectangle, as shown in green in Figure 5.6(a), was drawn on the drift-corrected images in Fiji. The intensity was averaged across the width of the box. These intensity line plots were exported from Fiji into MATLAB. In MATLAB, the data were first smoothed using a Savitzky-Golay filter of order 3 and framelength 25. The diffraction contrast feature was identified as a bright intensity feature (peak in intensity)

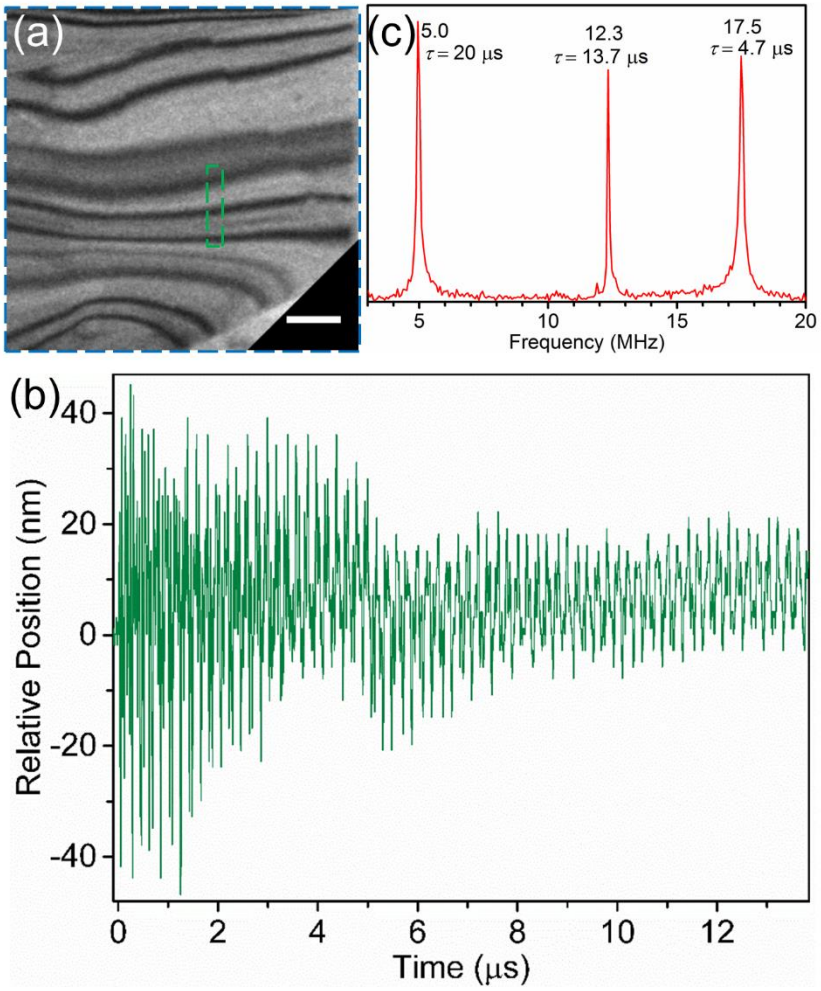

Figure 5.6 | **Whole-flake mechanical motion quantified.** (a) Representative UEM BF image of the MoS_2 region of interest. The green dashed rectangle denotes the region from which the contrast dynamics in panel (b) were quantified. Scale bar represents 200 nm. (b) Relative position of the bend contour highlighted in panel (a) as a function of time. (c) Fourier transform of the time trace in panel (d). Three distinct frequencies, with corresponding 1/*e* lifetimes (τ), are labeled.

between two low intensity features (dips in intensity). The peaks in the intensity versus space were identified using the MATLAB function findpeaks, and the dips in the intensity were identified using the MATLAB function extrema. The minima corresponding to the low intensity features were used to limit the fitting range and identify the peak corresponding to the bright feature, with if-loops to identify if the low intensity features were not present on one or both ends. The intensity was then fit with a pseudo-Voigt function, and the fitted center identified as the position of the peak. Any fits with low R^2

values were examined manually to ensure that the correct peak was fit, and the fitting window limits manually specified accordingly. The initial position was calculated by averaging the positions of the features in the image before 0 ns and was subtracted from every position value. The relative position versus time graph is in Figure 5.6(b). The FFT was calculated by padding the data with the average of the last 50 values out to 2^{14} values and is plotted in Figure 5.6(c). The MATLAB code used to analyze the intensity trace is included in Appendix F.

The relative position in Figure 5.6(b) most clearly shows beating as well as a slow damping of the oscillations. The envelope of the oscillations is an exponential decay. The motion within this decay envelope is initially chaotic, with the motion becoming more regular over time, indicate the presence initially of multiple modes with different damping.

The FFT in Figure 5.6(c) reveals three main frequencies: 5.0, 12.3, and 17.5 MHz. The displacement was bandpass-filtered in three ranges: 4 to 6, 11 to 13, and 16 to 18 MHz. The resulting oscillations were fit with a damped harmonic oscillator equation:

$$y = y_0 + Ae^{-Bt}cos(2\pi f + \beta) \tag{5.1}$$

where A is the amplitude, B is the damping constant, f is the frequency, and β is the phase, using a non-linear least squares solver. The fitted parameters are shown in Table 5.1. The bandpass-filtered oscillations and the fits are shown in Figure 5.7. The lifetimes τ of these oscillations ($1/e$) were found to be 20, 13.7, and 4.71 μs, for the 5.0, 12.3, and 17.5 megahertz (MHz) modes, respectively, as expected from the observations of the

relative position. The quality factors Q can be calculated using the classical formula:[416]

$$Q = \pi\tau f \tag{5.2}$$

and are shown in Table 5.1.

Band-pass start (MHz)	**Band-pass end (MHz)**	***f* (MHz)**	***A* (nm)**	***B* (1/s)**	***τ* (μs)**	***β* (rad)**	***y_0* (nm)**	***Q***
4	6	5.0	12.5	$4.9\text{x}10^4$	20	1.20	6.34	300
11	13	12.3	9.1	$7.3\text{x}10^4$	13.7	0.17	6.4	529
16	18	17.5	21.5	$2.1\text{x}10^5$	4.7	-2.87	6.35	260

Table 5.1 | **Fit parameters for fundamental mechanical modes.** The oscillations in Figure 5.6 were band-pass filtered over three ranges, and the resulting oscillations were fit with a damped oscillator equation, where f is the frequency, A is the amplitude, B is the damping constant, τ is the ($1/e$) lifetime, β is the phase, and y_0 is the offset. The quality factor Q for each mode was calculated using Equation 5.2.

These frequencies are in the range found by similar studies in MoS_2[12,40142,259-260] and in similar nanoscale systems[246,284] and have been imaged on microsecond timescales. In contrast to previous studies, in this dissertation, three fundamental modes were observed rather than one resonant frequency. A similar UEM study on graphite noted that at first multiple modes were present but quantified only the mode with the longest lifetime.[246] Here, a similar behavior is observed, and three modes and their lifetimes are actually resolved and reported. The lifetimes are much longer than that measured for a circular, monolayer membrane clamped on all sides. This can be attributed to the clamping of only two edges here rather than the entire circumference in the literature studies. The long lifetimes also emphasize the importance of measuring the ultimate relaxation timescales in ultrafast studies to allow sufficient time for the specimen to relax

completely. For this specimen, a conservative estimate of the complete relaxation requires a laser repetition rate of 40 kHz (25 μs relaxation time). Even assuming a complete relaxation time of 20 μs only allows the user to probe the specimen with a repetition rate of 50 kHz. Thus, the 10 kHz (100 μs relaxation time) repetition rate used in these experiments fulfills this requirement. A similar experiment completed at low repetition rates and analysis process can be used by future UEM users to determine appropriate repetition rates.

5.3 | Modeling Mechanical Modes

The mechanical modes observed were modeled using the Solid Mechanics module of COMSOL Multiphysics, version 5.1. The flake was constructed using the CAD drawing tools supplied in COMSOL. The specimen geometry was simplified into the seven polygons drawn in Figure 5.9, and Fiji drawing tools were used to measure the lengths (L_n) (see Figure 5.8) and angles (α_n) (see Figure 5.10) input into COMSOL. Thicknesses used in the COMSOL model are shown in Figure 5.11. The thickness h_1, h_2, h_3, and h_4 were extracted from the EELS thickness map in Figure 2.20. The other three thicknesses were estimated based on the mass-thickness contrast differences between the flakes compared to the flake with known thicknesses (h_1, h_2, h_3, and h_4) and preliminary modeling with COMSOL. Using these thickness values gave simulated frequencies that were within ~5% of the empirically determined counterparts (see Figure 5.12). Next, an eigenmode study was selected in the COMSOL model wizard. The geometry was constructed by drawing polygons in a two-dimensional work plane with the dimensions

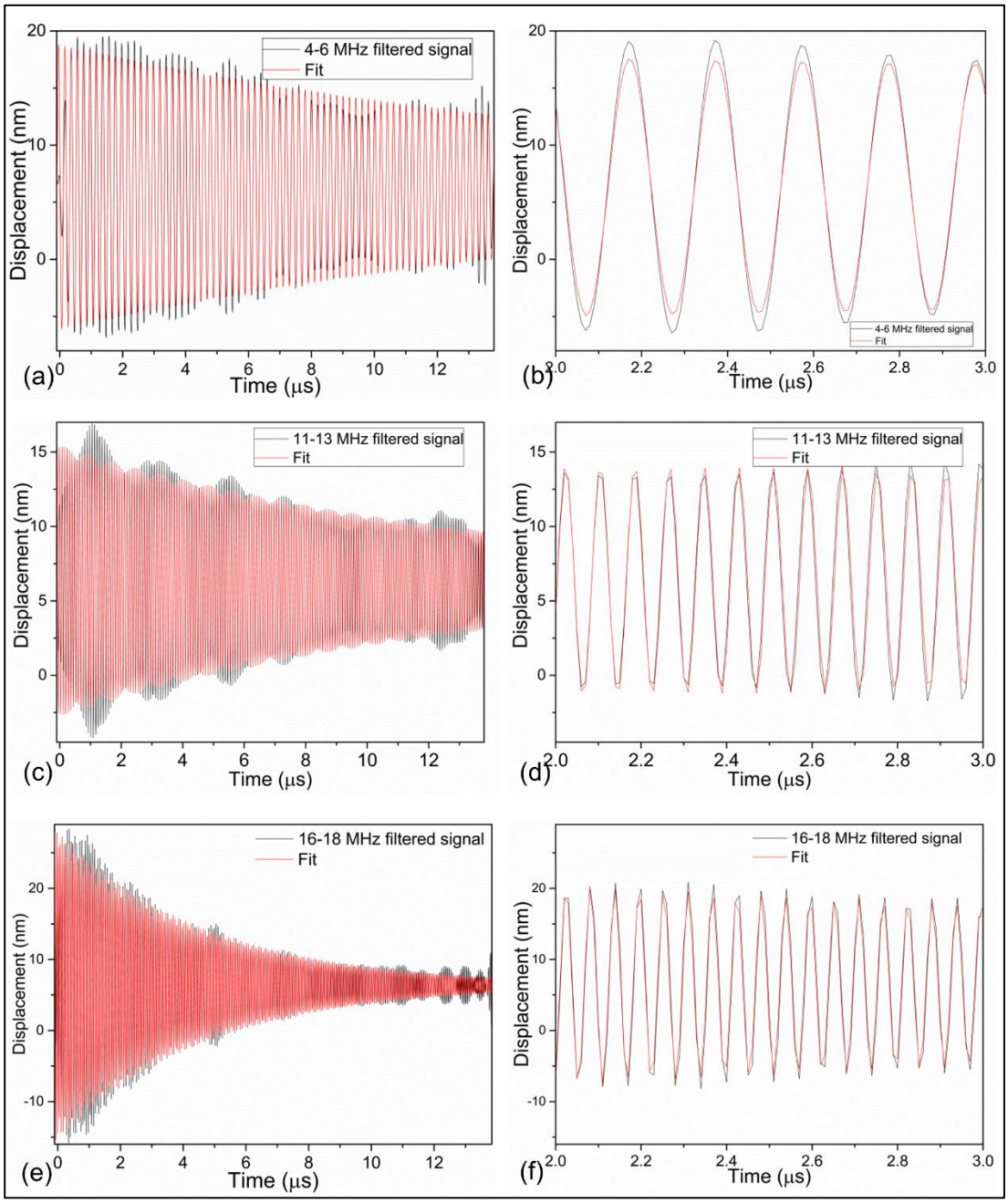

Figure 5.7 | **Isolation and quantification of resonant nanomechanical modes.** (a) Displacement of the bend contour in Figure 5.5 and Figure 5.6, Fourier-filtered over a window of 4 to 6 MHz and fit with a damped harmonic oscillator function (Eqn. 5.1). (b) A magnified view of (a) from 2 to 3 μs. (c) Same as in panel (a) but filtered over a window of 11 to 13 MHz. (d) A magnified view of (c) from 2 to 3 μs. (e) Same as in panel (c) but filtered over a window of 16 to 18 MHz. (f) A magnified view of (e) from 2 to 3 μs.

and angles described above and then extruding the shapes into three dimensions. The four polygons forming the main flake (red, light blue, green, and yellow polygons in Figure 5.9) were extruded in the positive vertical direction, whereas the other three polygons on the outside were extruded in the negative direction to be as close as possible to the original geometry. The shapes then undergo a form union operation in which the interior boundaries are not retained, and thus, one object results. The lower boundaries with lengths L_{16}, L_{18}, L_{19}, L_{20}, and L_{22} were set as clamped (*i.e.*, no movement), and all other boundaries and faces were left unconstrained. The material parameters and their sources used in the simulation are given in Table 5.2.

The Solid Mechanics COMSOL module solves for the eigenfrequencies of a

Property	**Value**	**Reference**
Young's modulus	E_p = 212 GPa E_t = 46.3 GPa	Calculated using stiffness matrix from Ref [43]
Poisson ratio	υ_p = -0.279 υ_{tp} = 0.124 υ_{pt} = 0.566	Calculated using stiffness matrix from Ref [43]
Lattice parameters	a = 3.1602 Å c = 12.294 Å	Ref [417]
Density	ρ = 5.0 g/cm^3	Calculated using lattice parameters above

Table 5.2 | **Material properties used in COMSOL simulations of eigenfrequencies.** The Young's moduli and Poisson ratios were calculated using the experimentally measured stiffness matrix.[43] Those calculations are shown in Appendix D. The lattice parameters were taken from Wildervanck and coworkers[417] and used to calculate the density.

structure based on elastic theory. Linear strains were not enforced. The equations of motion that COMSOL solves are as follows:

$$-\rho\omega^2\boldsymbol{u} = \boldsymbol{\nabla}\cdot S + \boldsymbol{F}v \qquad (5.3)$$

where ρ is the density, ω is the eigenfrequency, $\boldsymbol{u}$ is the displacement, S is the second Piola-Kirchoff stress in which the stress is related in the material rather than the spatial coordinate system, $\boldsymbol{F}$ is the deformation gradient tensor that relates changes in the material coordinate system with the spatial coordinate system, and v is the velocity field. S is given by

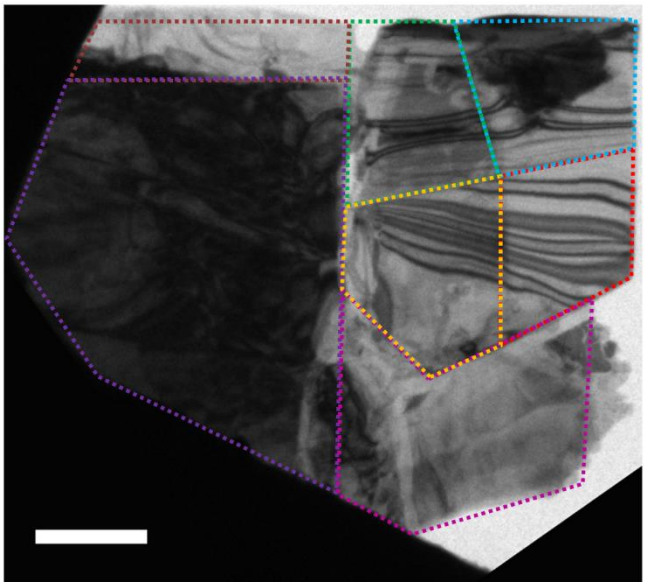

Figure 5.9 | **Simplified geometry for COMSOL modeling.** The geometry of the flake was simplified into seven regions outlined in different colors. Scale bar represents 1 μm.

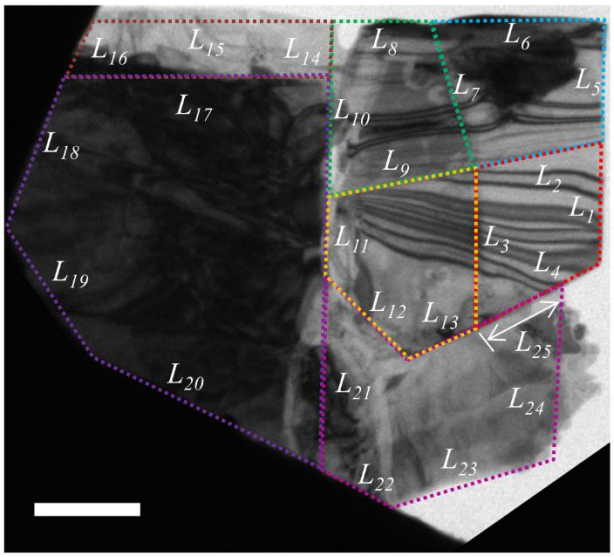

n	L_n (μm)	n	L_n (μm)	n	L_n (μm)
1	1.165	11	0.910	21	1.864
2	1.241	12	0.882	22	0.941
3	1.45	13	0.776	23	1.605
4	1.277	14	0.537	24	1.605
5	1.093	15	2.364	25	0.777
6	1.564	16	0.543		
7	1.493	17	2.579		
8	0.815	18	1.771		
9	1.359	19	1.279		
10	1.093	20	2.391		

Figure 5.8 | **Lengths of polygons used in COMSOL simulations**. The lengths were measured in Fiji and input into COMSOL in the simulations. Scale bar represents 1 μm.

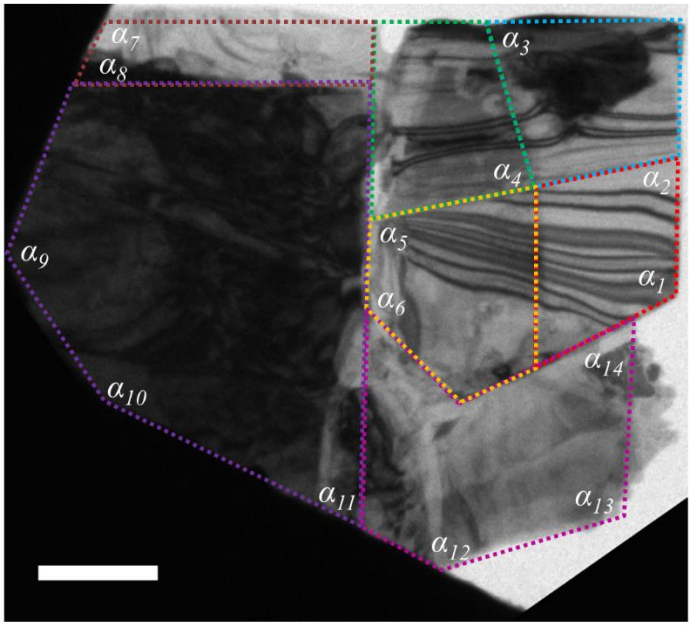

n	α_n (°)	n	α_n (°)
1	121.43	10	154.642
2	78.102	11	63.204
3	71.131	12	132.96
4	85.382	13	105.909
5	104.113	14	64.136
6	129.472		
7	117.350		
8	62.439		
9	124.613		

Figure 5.10 | **Angles in polygons used in COMSOL simulations**. The angles were measured in Fiji and input into COMSOL in the simulations. Scale bar represents 1 µm.

$$S = S_0 + S_{ext} + S_q + C : \varepsilon_{el} \tag{5.4}$$

where S_0 is the initial stress, S_{ext} is the external stress, S_q is the stress due to viscous damping. The main component of the stress is due to the elastic strain ε_{el} computed with the elastic constants tensor C. The elastic stress is calculated using:

$$\varepsilon_{el} = \varepsilon - \varepsilon_{inel} \tag{5.5}$$

where ε is the total strain that is related to $\boldsymbol{u}$ by

$$\varepsilon = \frac{1}{2}[(\nabla \boldsymbol{u})^T + \nabla \boldsymbol{u}] \tag{5.6}$$

and ε_{inel} is the inelastic strain, which is given by

$$\varepsilon_{inel} = \varepsilon_0 + \varepsilon_{th} + \varepsilon_{hs} + \varepsilon_{pl} + \varepsilon_{cr} \tag{5.7}$$

where ε_0 is the initial strain, ε_{th} is the thermal strain, ε_{hs} is the hygroscopic strain, ε_{pl} is the plastic strain, and ε_{cr} is the viscoplastic strain. In this simple case, most of these

terms are zero. For instance, no fluid was involved (*i.e.*, $\varepsilon_{th} = \varepsilon_{hs} = 0$). A tetragonal, physics-controlled mesh with a "fine" mesh size was used. The eigenfrequencies were solved for using the MUMPS (a MUltifrontal Massively Parallel sparse direct Solver) solver.

The three lowest simulated eigenmode frequencies were found to be 4.639, 11.597, and 17.974 MHz. These eigenfrequencies are in reasonable agreement with the empirically determined ones (5.0, 12.3, and 17.5 MHz), and the solution could be improved by further thickness characterization on the two outer flakes in Figure 5.9. The displacement corresponding to each mode is shown in Figure 5.12, where the position of the undeformed specimen is shown in the wire frame. In the 4.6 MHz mode, the entire specimen curves in a single arc. In the 12 MHz, mode the specimen folds into an *s* shape, with the largest displacements along the top edge. In the 18 MHz mode, the specimen folds into an *s* shape along the right edge. The total displacements here are qualitative rather than absolute due to normalization in COMSOL and have been further normalized to the largest displacement.

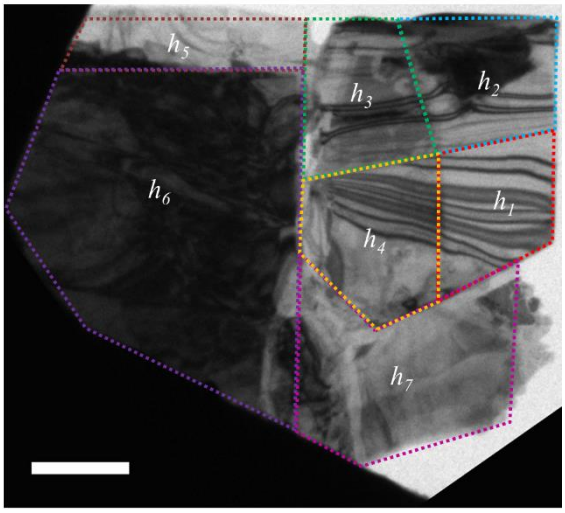

n	h_n (nm)
1	30
2	43
3	55
4	42
5	20
6	80
7	30

Figure 5.11 | **Thicknesses of the various polygons input into COMSOL simulation.** Thicknesses were estimated from EEL spectra where available, relative contrast, and variation in the model. Scale bar represents 1 μm.

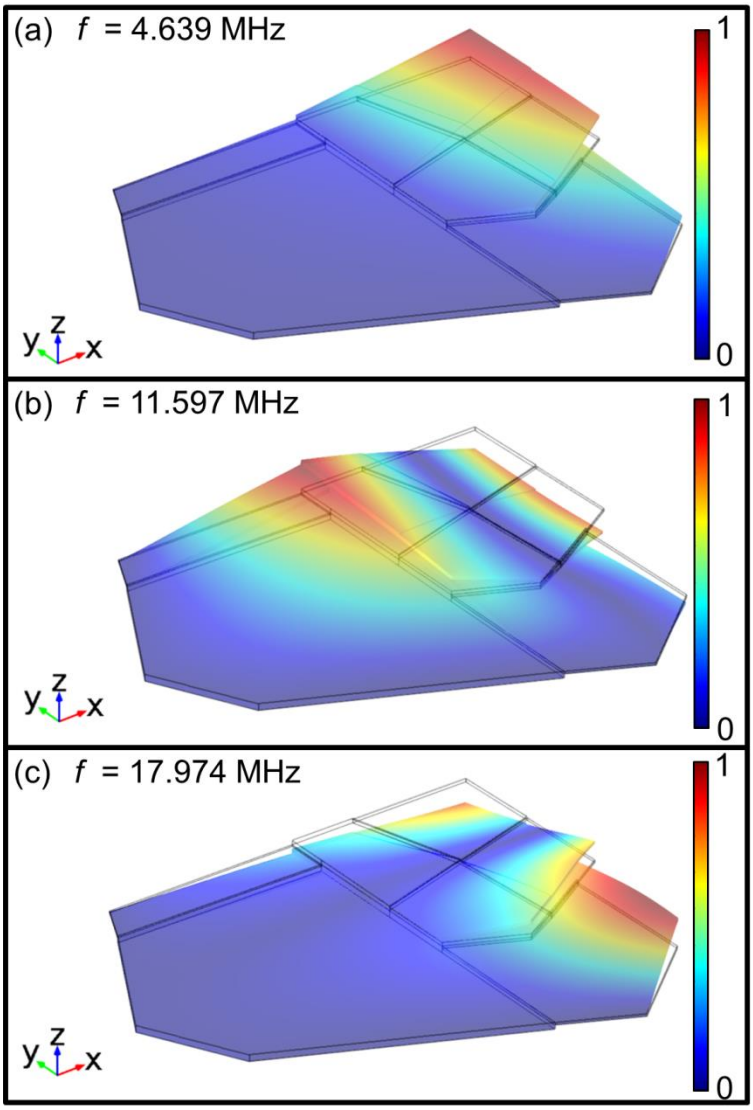

Figure 5.12 | **Simulated mechanical eigenmodes.** The total displacement at each eigenfrequency. The displacement is qualitative (not absolute) due to normalization in COMSOL and has been normalized to the largest displacement in each mode. (a) The lowest frequency eigenmode, 4.6 MHz. (b) The second lowest eigenfrequency, 11.6 MHz. (c) The third lowest frequency, 17.9 MHz. All frequencies show reasonable agreement with experimental results (5.0, 12.3, and 17.5 MHz).

This research has implications both fundamentally and empirically. Fundamentally, this work images the transition between ultrafast laser excitation and ultimate ringdown and shows that the ultimate relaxation is determined by the specimen geometry and macroscopic material properties. Unlike the ultrafast dynamics, the mechanical ringdown is well-described by continuum elastic theory and thus can be tuned with varying thicknesses and boundary conditions. In applications, the presence of these three modes with

different lifetimes suggests that the sensor may not need to be a single flake of a single thickness. Different geometries with varying thicknesses could be used to tune the sensitivity, modes, and lifetimes of nanomechanical motion in a material.

5.4 | Chapter Summary and Conclusions

In this chapter, I have described my experiments and simulations investigating the mechanical ringdown of a photo-excited MoS_2 flake. I have directly imaged the mechanical ringdown of the specimen through two image sequences, one with 0.5 ns steps in the initial 100 ns and the other with 10 ns steps out to almost 14 μs. The first image sequence showed chaotic motion similar to that observed in image sequences in Chapter 4. The second image sequence showed that on longer time scales, the motion decayed into three fundamental eigenfrequencies: 5.0, 12.3, and 17.5 MHz. These eigenfrequencies were simulated with elastic continuum mechanics in COMSOL and were assigned to the three lowest-frequency mechanical modes. This research directly images the mechanical ringdown of a specimen, which is of interest for sensors. Moreover, the study suggests that the mechanical modes can be tuned using different geometries and thicknesses even in one flake.

6 | Conclusions and Future Work

In this chapter, I will discuss future work extending the experiments and modeling presented in this dissertation and will summarize conclusions. I will first propose experiments to probe the launch mechanism of the acoustic phonons observed, including fluence studies, experiments in reciprocal space, layer studies, and specimen lifetime studies. Second, I will suggest simulations for correlating diffraction contrast to phonon dynamics and thermal expansion. Next, I will discuss simulations to understand energy relation processes in the transition between the high-frequency modes to the whole-flake mechanical oscillations. Fourth, a combination of nanosecond UEM experiments and modeling to determine mechanical properties in complex nanostructures will be described. Fifth, I will discuss other experimental systems, namely $MoSe_2$ and TMD heterostructures, to which the work presented here could be compared and contrasted. Finally, I will summarize the conclusions that can be drawn from this dissertation.

6.1 | Future Work

6.1.1 | Probing Launch Mechanism: Fluence and Reciprocal-space Studies

As noted in Chapters 1 and 3, the photo-carrier structural dynamics in MoS_2 depend on the excitation fluence. At low excitation fluences in thin specimens, the

material behaves as a semiconductor, and the primary acoustic phonon launch mechanism is expected to be deformation potential. The optical phonon emission is likewise effective due to the low phonon population. At high excitation fluences in thin specimens, however, fast local photo-carrier relaxation leads to large, localized lattice temperature rises (*i.e.*, thermoelastic stress) that launch acoustic waves, and thermoelasticity becomes dominant acoustic phonon emission mechanism. By changing the fluence on the same specimen, three regimes may theoretically be probed: deformation potential dominant, transition, and thermoelastic stress dominant launch. In the regime of deformation potential dominant launch, I would expect the phonons to be launched from nearly anywhere in the specimen unless the photo-carriers were pinned by some defect. In the other limit in which thermoelastic stress dominates, I would expect areas with initial local strain, such as pinned edges or defects such as tears or step-edges to launch first due to a faster buildup to a high local stress than non-stressed areas of the specimen. In the transition regime, I would expect to see a chaotic mixture of both expectations above. In addition, simulations to determine the effect on BF image contrast due to the different mechanisms will need to be conducted.

An important compliment to these BF UEM image sequences will be image sequences in reciprocal space, due to the sensitivity of reciprocal space to electron-phonon coupling dynamics. Once time zero is determined as described in Section 3.3.2, the electron-phonon coupling time can be measured in reciprocal space using the Debye-Waller effect, in which coherent diffraction decays and incoherent scattering increases as

the excited electrons oscillate farther from their equilibrium positions.[418-421] This method is used widely in the ultrafast diffraction community to measure electron-phonon coupling times,[244,422] which are related to the carrier lifetimes that determine the launch mechanism. The time interval between time zero and the sudden decay of diffraction peak intensity corresponds to the electron-phonon coupling time, and this interval and oscillations in diffraction peak spacing can be monitored at different fluences relative to BF contrast change to determine the launch mechanisms and the charge carrier populations and lifetimes. Simulations will need to be completed to determine the electron-phonon coupling time correlation to launch mechanism regimes.

6.1.2 | Probing Launch Mechanism: Number of Layers

Nearly every property of MoS_2 depends on the number of layers, and thus a systematic study of the dependence of structural dynamics on the number of layers could be undertaken. As stated in Chapter 3, the frequencies and velocities at which Lamb modes travel depend on thickness. A systematic study could thus be undertaken to determine if these acoustic phonons are indeed accurately described by Lamb modes and at what thicknesses the Lamb modes transition into Rayleigh (surface) waves instead. Using the bulk absorption coefficient (3.4×10^5 cm^{-1}), the optical penetration depth is 29 nm, and a simple calculation using Beer's Law is plotted in Figure 6.1, which plots the fraction of light transmitted versus the thickness of the specimen. Beer's Law predicts that 5% or less of the incident light is transmitted for thicknesses of 147 layers or more (88.2 nm, assuming a layer thickness of 0.6 nm). Thus, I expect that the crossover region

to be approximately 150 layers. These thicknesses are usually still electron-transparent, and thus experiments in which the wave modes are now Rayleigh or surface modes rather than Lamb modes can also be probed.

6.1.3 | Probing Launch Mechanism: Specimen Lifetime

Although most exfoliated and synthetically grown MoS_2 is chemically stable in ambient atmosphere, at least one study has found that the samples can degrade over time due to the adsorption and oxidation along grain boundary edges.[423] The high-GHz oscillation frequency ranged from 40 to 50 GHz in images acquired over 11 months. Between experiments, the specimen was stored in ambient atmosphere and was probed many times in other experiments. Adsorption of contaminants is ruled out because the specimen is placed in vacuum during the experiments and repeatedly heated, but defects remaining if water intercalated between layers at the edge or oxidation due to water adsorption cannot be ruled out or increasing sulfur vacancies without a systematic study. A systematic study is thus proposed in which a map of the specimen chemical composition is collected and dynamics probed every two months to determine the lifetime of a specimen stored in ambient atmosphere and the effect of chemical defects on the specimen. Concurrently, the same data should be collected on a specimen stored in a desiccator or under vacuum as a control. Such experiments would help

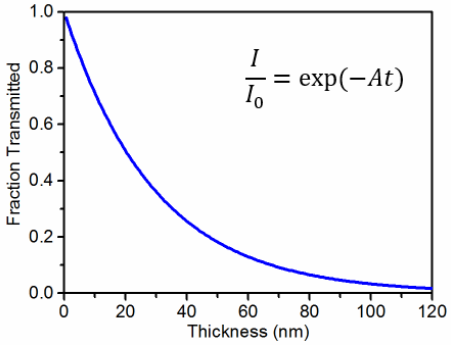

Figure 6.1 | **Fraction of transmitted intensity versus thickness.** Using bulk properties and Beer's Law, the intensity of transmitted light is plotted versus the sample thickness.

determine the time interval over which the material photo-response is reversible.

6.1.4 | Correlating Diffraction Contrast to Specimen Dynamics

The image sequences in this dissertation suggest that acoustic waves and structural dynamics are imaged primarily by their interaction with planes near the diffraction condition. This observation leads to future work determining the sets of planes involved in the acoustic wave trains. Coupled with frequency determination, such knowledge would indicate the nature of the Lamb modes (*i.e.*, longitudinal or transverse). The experiments involve indexing the diffraction contrast features in the BF image and then acquiring BF image and DP sequences at different tilt angles, corresponding to different zone axes so that different sets of planes are near the diffraction condition. Unpublished work suggests the contrast change is most evident when the specimen is slightly off a zone axis.

Concurrently, modeling of the diffraction contrast can be undertaken. The electron wavefunction for the direct beam and diffracted beams are integrated over the thickness of the material, and the amplitude is the image intensity. For a flake of this thickness (where the thickness is larger than the extinction distance), dynamical theory must be used, although the column approximation, in which only a scattering within a column with a radius of a few nm contributes to the wavefunction, can be used. For ease of implementation in MATLAB, the problem can be formulated as an eigenvalue problem.[404,424] Preliminary code is included in Appendix H.9. This code currently considers only the direct beam and the (100) diffracted beam for MoS_2 and computes the

diffracted intensity and the direct intensity given the product of the extinction distance and the excitation error is 1.5 over one spatial dimension. Since the diffraction condition does not change over that spatial dimension, the code currently computes a constant value for both intensities. However, it is written to accommodate more beams, and suggestions are provided to include strain or defect fields.

6.1.5 | Mechanical Characterization of Complex Nanostructures

A niche application of UEM is the time-domain mechanical characterization of nanoscopic structures. As demonstrated in Chapter 5, the mechanical properties, boundary conditions, and thickness determine the eigenfrequencies. For nanoscopic structures with known geometry and eigenfrequencies measured with UEM, the mechanical properties could then be extracted, such as the Young's modulus and the Q-factor. The advantage is that this non-destructive technique offers two orders of magnitude better spatial resolution than current optical techniques and similar temporal resolution as that of such time domain measurements.[12] Moreover, the UEM can be operated as a TEM, and the nanoscale morphology of the specimen carefully characterized.

6.1.6 | $MoSe_2$ and TMD Heterostructures

Although similar to MoS_2 in structure, nine-layer $MoSe_2$ rather than monolayer $MoSe_2$ has been found to undergo an indirect-to-direct bandgap transition as the temperature rises above ~250 K.[92] The experiments presented in this dissertation demonstrate that heat in the form of phonons can be localized on femtosecond to

picosecond timescales and nanometer spatial scales. This ability could be harnessed to dynamically tune the bandgap of $MoSe_2$. First, a study comparing the acoustic phonon dynamics in $MoSe_2$ and an identical specimen (*i.e.*, same number of layers and similar lateral dimensions) of MoS_2 would elucidate the extent of local, ultrafast bandgap tuning possible more clearly. Studies in the literature have shown that the presence of the direct bandgap increases radiative recombination at the expense of nonradiative recombination, and thus local tuning of the bandgap could result in the suppression of emission of coherent acoustic phonons in UEM BF image sequences. A pump fluence study could be used to determine the onset of bandgap shift and the resulting differences in photo-carrier relaxation time scales. Second, the repetition rate could be selected so that the few-layer $MoSe_2$ specimen does not have sufficient time to fully relax, leading to steady-state heating, which could be modeled using COMSOL *a priori*, and thus variable bandgap tuning. Studying the response and comparing it to lower repetition rates would help determine the dominant relaxation mechanisms.

Another area of interest is structural dynamics of TMD heterostructures. In these experiments, heterostructures can be fabricated by stacking different TMDs vertically or horizontally, and the resulting interlayer coupling has been shown to have significant impacts on electronic bandstructure and thus on the dominant relaxation mechanisms. Layers stacked in the [001] direction are the most common device architecture. Thus, studying heat transport and boundary resistance across that interface would be of interest to understand the underlying mechanism responsible for the lowering of thermal

conductivity and the dissipation of heat in electronic devices. Comparing these results to a similar experiment for heterostructures connected in the [100] or [010] direction would be of fundamental interest to understand coupling and thermal conductivity and of practical interest to understand what makes a better architecture.

Specimen preparation will need to be carefully considered for these experiments. Heterostructures in either geometry can be grown with chemical vapor deposition by varying the growth conditions.[425] To make these structures into TEM specimens, they must be transferred from the growth substrate onto a TEM grid to be electron transparent. Because of the small lateral size of these structures, the TEM grid must have a membrane to support the specimens. The geometric pinning of the TEM membrane on the heterostructure, however, greatly reduces the magnitude of the structural dynamics. While membranes with periodic holes are available, contact between suspended lateral heterostructures would need to be preserved.

In addition to thermal conductivity, directly imaging charge carriers such as excitons that become important at the interface[426-427] would be a rewarding experiment. The Bohr radius of excitons in MoS_2 is ~1 nm,[428-429] and the lifetimes can be as short as hundreds of femtoseconds, depending on the defect densities and specimen geometry. Such experiments would require higher magnifications than used in this work and thus more attention to the temporal and spatial coherency of the electron packets, as required for the imaging of lattice fringes outlined in Chapter 2. These results, however, would enhance our fundamental knowledge of excitons, as the visualization of acoustic phonons

has enhanced our understanding of phonons.

Heterostructures allow for experiments to probe mode coupling and conversion at interfaces between two dissimilar materials. Such interfaces could be used to determine the mode of the incident wave by simulating how which scattered modes that can propagate across the interface unless the wave is incident at critical angles. In addition, interfaces would allow multiple modes, which would be transmitted or reflected, to be probed in one image sequence.[385]

Work in nanophononics and the Flannigan research has demonstrated that heat propagation pathways can be manipulated with structure and defects. High-resolution work understanding the defects such as dislocations or steps and visualizing their effects on phonon and ultimately heat transport is currently underway by coworkers in the Flannigan research group. In addition, defects can be introduced with a high-brightness electron beam in thin layers and their effects on the structural dynamics probed.[29] Based on work by coworkers in the Flannigan group[247,259] and by the quenching of photoluminescence by defects,[23] I expect the phonons to be pinned or stopped at certain defect sites, resulting in higher localized heating around defects. In contrast, step edges have been observed to partly reflect and to partly transmit the acoustic waves in this dissertation as is desired in phononic structures, and thus, the theoretical design of phononic structures can be directly visualized experimentally. Such knowledge would aid in design of phononic structures to protect sensitive instruments from sound waves and to dissipate heat more quickly. The challenging part of this project then is the design

and fabrication of the structures themselves.

6.2 | Conclusions

The photo-induced structural dynamics of MoS_2 over seven orders of magnitude in time – individual picoseconds (10^{-12} seconds) to tens of microseconds (10^{-5} seconds) – in real space with 10 nanometer (10^{-9} meter) spatial resolution or better have been directly imaged using ultrafast electron microscopy. Following photo-excitation with 515-nm light, propagating, 50-GHz strain wave trains appeared to be launched from the specimen-vacuum interface and step edge defects. These acoustic waves traveled at the speed of sound near or along diffraction contrast features and were identified as Lamb modes, which are plate waves. For the wave trains traveling along the [100] direction, a dispersion relation for 50-nm thick MoS_2 approximated as an isotropic plate and the cut-off frequencies for an anisotropic plate suggest that the wave trains are second order anti-symmetric or symmetric Lamb modes, differentiated by their symmetry with respect to a plane perpendicular to the thickness direction of the plate. Because MoS_2 is transversely isotropic, however, the Lamb modes are generally combinations of longitudinal or transverse waves. The contrast mechanism was identified as the tilting of planes into and out of the diffraction condition for anti-symmetric waves and the change in inter-planar spacing for symmetric waves with a longitudinal component. Second, the wave trains were found to undergo phonon scattering and damp completely in several nanoseconds, ultimately leading to the dominance of 1-GHz, incoherent oscillations. Finally, three mechanical eigenmodes evolved with MHz frequencies and microsecond lifetimes, which

could be well-described by COMSOL simulations.

This work is expected to apply to the relaxation of photo-excitation in freestanding, multilayer, semiconducting specimens. Lamb modes are plate waves that can be observed in any plate, although the dispersion relation and wavenumbers supported depend on the mechanical properties of the material. Thus, the experiments elucidating the interaction of Lamb modes with specimen features (*i.e.*, launch of strain wavetrains from the specimen-vacuum interface) will also apply in other systems. Thermoelasticity (high local heating) and deformation potential (changes in electronic distribution), identified as the most likely launch mechanisms, are observed in other films, although their relative importance depends on whether the specimen is metallic, semiconducting, piezoelectric, or transparent. Consequently, future work includes similar experiments in other TMDs and TMD heterostructures. In addition, preliminary work determining theoretical time zero on the 515-nm pump line and the instrument response time for similar imaging conditions can be built upon to probe the launch mechanism more quantitatively, such as through varying fluence and studying these dynamics in reciprocal space where different planes are close to the diffraction condition. Future work can also extend the understanding of mode conversion through simulations and experiments in different specimens, where the timescales and magnitudes of motion are expected to vary due to changes in phonon mean free path.

7 | REFERENCES

1. Citarella, R.; Cricrì, G.; Lepore, M.; Perrella, M. Thermo-mechanical Crack Propagation in Aircraft Engine Vane by Coupled FEM–DBEM Approach. *Advances in Engineering Software* **2014**, *67*, 57-69.
2. Yang, L.; Zhou, Y. C.; Lu, C. Damage Evolution and Rupture Time Prediction in Thermal Barrier Coatings Subjected to Cyclic Heating and Cooling: An Acoustic Emission Method. *Acta Mater.* **2011**, *59*, 6519-6529.
3. Tang, W. Z.; Yang, L.; Zhu, W.; Zhou, Y. C.; Guo, J. W.; Lu, C. Numerical Simulation of Temperature Distribution and Thermal-stress Field in a Turbine Blade with Multilayer-structure TBCs by a Fluid–solid Coupling Method. *J. Mater. Sci. Technol.* **2016**, *32*, 452-458.
4. Lubimova, E. A.; Magnitzky, V. A. Thermoelastic Stresses and the Energy of Earthquakes. *J. Geophys. Res.* **1964**, *69*, 3443-3447.
5. Poli, P.; Prieto, G.; Rivera, E.; Ruiz, S. Earthquakes Initiation and Thermal Shear Instability in the Hindu Kush Intermediate Depth Nest. *Geophs. Res. Lett.* **2016**, *43*, 1537-1542.
6. Markoff, J., IBM Discloses Working Version of a Much Higher-capacity Chip. *The New York Times* July 9, 2015, 2015, p B2.
7. Chakraborty, P. S.; Cardoso, A. S.; Wier, B. R.; Omprakash, A. P.; John D. Cressler, F.; Kaynak, M.; Tillack, B. A 0.8 THz f_{MAX} SiGe HBT Operating at 4.3 K. *IEEE Electron Devices Letters* **2014**, *35*, 151-153.
8. Ferrari, A. C.; Bonaccorso, F.; Fal'ko, V.; Novoselov, K. S.; Roche, S.; Boggild, P.; Borini, S.; Koppens, F. H.; Palermo, V.; Pugno, N.; Garrido, J. A.; Sordan, R.; Bianco, A.; Ballerini, L.; Prato, M.; Lidorikis, E.; Kivioja, J.; Marinelli, C.; Ryhanen, T.; Morpurgo, A.; Coleman, J. N.; Nicolosi, V.; Colombo, L.; Fert, A.; Garcia-Hernandez, M.; Bachtold, A.; Schneider, G. F.; Guinea, F.; Dekker, C.; Barbone, M.; Sun, Z.; Galiotis, C.; Grigorenko, A. N.; Konstantatos, G.; Kis, A.; Katsnelson, M.; Vandersypen, L.; Loiseau, A.; Morandi, V.; Neumaier, D.; Treossi, E.; Pellegrini, V.; Polini, M.; Tredicucci, A.; Williams, G. M.; Hong, B. H.; Ahn, J. H.; Kim, J. M.; Zirath, H.; van Wees, B. J.; van der Zant, H.; Occhipinti, L.; Di Matteo, A.; Kinloch, I. A.; Seyller, T.; Quesnel, E.; Feng, X.; Teo, K.; Rupesinghe, N.; Hakonen, P.; Neil, S. R.; Tannock, Q.; Lofwander, T.; Kinaret, J. Science and Technology Roadmap for Graphene, Related Two-dimensional Crystals, and Hybrid Systems. *Nanoscale* **2015**, *7*, 4598-4810.
9. Maasilta, I.; Minnich, A. J. Heat under the Microscope. *Phys. Today* **2014**, *67*, 27-32.

10. Eichler, A.; Moser, J.; Chaste, J.; Zdrojek, M.; Wilson-Rae, L.; Bachtold, A. Nonlinear Damping in Mechanical Resonators Made from Carbon Nanotubes and Graphene. *Nat. Nanotechnol.* **2011**, *6*, 339-342.
11. Cleland, A. N.; Roukes, M. L. Noise Processes in Nanomechanical Resonators. *J. Appl. Phys.* **2002**, *92*, 2758-2769.
12. van Leeuwen, R.; Castellanos-Gomez, A.; Steele, G. A.; van der Zant, H. S. J.; Venstra, W. J. Time-domain Response of Atomically Thin MoS_2 Nanomechanical Resonators. *Appl. Phys. Lett.* **2014**, *105*, 041911.
13. Barnard, A. W.; Sazonova, V.; van der Zande, A. M.; McEuen, P. L. Fluctuation Broadening in Carbon Nanotube Resonators. *Proc. Natl. Acad. Sci. U. S. A.* **2012**, *109*, 19093-19096.
14. Chen, G. *Nanoscale Energy Transport and Conversion*. Oxford University Press, Inc.: Oxford, 2005; p 531.
15. Lin, Z.; Carvalho, B. R.; Kahn, E.; Lv, R.; Rao, R.; Terrones, H.; Pimenta, M. A.; Terrones, M. Defect Engineering of Two-dimensional Transition Metal Dichalcogenides. *2D Mater.* **2016**, *3*, 022002.
16. Splendiani, A.; Sun, L.; Zhang, Y.; Li, T.; Kim, J.; Chim, C. Y.; Galli, G.; Wang, F. Emerging Photoluminescence in Monolayer MoS_2. *Nano Lett.* **2010**, *10*, 1271-1275.
17. Mak, K. F.; Lee, C.; Hone, J.; Shan, J.; Heinz, T. F. Atomically Thin MoS_2: A New Direct-Gap Semiconductor. *Phys. Rev. Lett.* **2010**, *105*, 136805.
18. Xie, J.; Zhang, H.; Li, S.; Wang, R.; Sun, X.; Zhou, M.; Zhou, J.; Lou, X. W.; Xie, Y. Defect-rich MoS_2 Ultrathin Nanosheets with Additional Active Edge Sites for Enhanced Electrocatalytic Hydrogen Evolution. *Adv. Mater.* **2013**, *25*, 5807-5813.
19. Kibsgaard, J.; Chen, Z.; Reinecke, B. N.; Jaramillo, T. F. Engineering the Surface Structure of MoS_2 to Preferentially Expose Active Edge Sites for Electrocatalysis. *Nat. Mater.* **2012**, *11*, 963-969.
20. Addou, R.; McDonnell, S.; Barrera, D.; Guo, Z.; Azcatl, A.; Wang, J.; Zhu, H.; Hinkle, C. L.; Quevedo-Lopez, M.; Alshareef, H. N.; Colombo, L.; Hsu, J. W.; Wallace, R. M. Impurities and Electronic Property Variations of Natural MoS_2 Crystal Surfaces. *ACS Nano* **2015**, *9*, 9124-9133.
21. Addou, R.; Colombo, L.; Wallace, R. M. Surface Defects on Natural MoS_2. *ACS Appl. Mater. Interfaces* **2015**, *7*, 11921-11929.
22. Kong, D.; Wang, H.; Cha, J. J.; Pasta, M.; Koski, K. J.; Yao, J.; Cui, Y. Synthesis of MoS_2 and $MoSe_2$ Films with Vertically Aligned Layers. *Nano Lett.* **2013**, *13*, 1341-1347.
23. Chow, P. K.; Jacobs-Gedrim, R. B.; Gao, J.; Lu, T.-M.; Yu, B.; Terrones, H.; Koratkar, N. Defect-induced Photoluminescence in Monolayer Semiconducting Transition Metal Dichalcogenides. *Nano Lett.* **2015**, *9*, 1520-1527.
24. Karunadasa, H. I.; Montalvo, E.; Sun, Y.; Majda, M.; Long, J. R.; Chang, C. J. A Molecular MoS_2 Edge Site Mimic for Catalytical Hydrogen Generation. *Science*

2012, *335*, 698-702.

25. Jaramillo, T. F.; Jørgensen, K. P.; Bonde, J.; Nielsen, J. H.; Horch, S.; Chorkendorff, I. Identification of Active Edge Sites for Electrochemical H_2 Evolution from MoS_2 Nanocatalysts. *Science* **2007**, *317*, 100-102.
26. Hinnemann, B.; Moses, P. G.; Bonde, J.; Jørgensen, K. P.; Nielsen, J. H.; Horch, S.; Chorkendorff, I.; Nørskov, J. K. Biomimetic Hydrogen Evolution: MoS_2 Nanoparticles as Catalyst for Hydrogen Evolution. *J. Am. Chem. Soc.* **2005**, *127*, 5308-5309.
27. Lau, V. W.; Masters, A. F.; Bond, A. M.; Maschmeyer, T. Ionic-liquid-mediated Active-site Control of MoS_2 for the Electrocatalytic Hydrogen Evolution Reaction. *Chem. - Eur. J.* **2012**, *18*, 8230-8239.
28. Benck, J. D.; Chen, Z.; Kuritzky, L. Y.; Forman, A. J.; Jaramillo, T. F. Amorphous Molybdenum Sulfide Catalysts for Electrochemical Hydrogen Production: Insights into the Origin of their Catalytic Activity. *ACS Catal.* **2012**, *2*, 1916-1923.
29. Komsa, H. P.; Kotakoski, J.; Kurasch, S.; Lehtinen, O.; Kaiser, U.; Krasheninnikov, A. V. Two-dimensional Transition Metal Dichalcogenides under Electron Irradiation: Defect Production and Doping. *Phys. Rev. Lett.* **2012**, *109*, 035503.
30. Novoselov, K. S.; Jiang, D.; Schedin, F.; Booth, T. J.; Khotkevich, V. V.; Morozov, S. V.; Geim, A. K. Two-dimensional Atomic Crystals. *Proc. Natl. Acad. Sci. U. S. A.* **2005**, *102*, 10451-10453.
31. Wang, Q. H.; Kalantar-Zadesh, K.; Kis, A.; Coleman, J. N.; Strano, M. S. Electronics and Optoelectronics of Two-Dimensional Transition Metal Dichalcogenides. *Nat. Nanotechnol.* **2012**, *7*, 699-712.
32. Chhowalla, M.; Shin, H. S.; Eda, G.; Li, L.-J.; Loh, K. P.; Zhang, H. The Chemistry of Two-dimensional Layered Transition Metal Dichalcogenide Nanosheets. *Nat. Chem.* **2013**, *5*, 263-275.
33. Bhimanapati, G. R.; Lin, Z.; Meunier, V.; Jung, Y.; Cha, J. J.; Das, S.; Xiao, D.; Son, Y.; Strano, M. S.; Cooper, V. R.; Liang, L.; Louie, S. G.; Ringe, E.; Zhou, W.; Sumpter, B. G.; Terrones, H.; Xia, F.; Wang, Y.; Zhu, J.; Akinwande, D.; Alem, N.; Schuller, J. A.; Schaak, R. E.; Terrones, M.; Robinson, J. A. Recent Advances in Two-Dimensional Materials Beyond Graphene. *ACS Nano* **2015**, *9*, 11509-11539.
34. Bonaccorso, F.; Colombo, L.; Yu, G.; Stoller, M.; Tozzini, V.; Ferrari, A. C.; Ruoff, R. S.; Pellegrini, V. Graphene, Related Two-dimensional Crystals, and Hybrid Systems for Energy Conversion and Storage. *Science* **2015**, *347*, 1246501.
35. Huang, X.; Zeng, Z.; Zhang, H. Metal Dichalcogenide Nanosheets: Preparation, Properties and Applications. *Chem. Soc. Rev.* **2013**, *42*, 1934-1946.
36. Ponraj, J. S.; Xu, Z. Q.; Dhanabalan, S. C.; Mu, H.; Wang, Y.; Yuan, J.; Li, P.; Thakur, S.; Ashrafi, M.; McCoubrey, K.; Zhang, Y.; Li, S.; Zhang, H.; Bao, Q. Photonics and Optoelectronics of Two-dimensional Materials beyond Graphene.

Nanotechnol. **2016**, *27*, 462001.
37. Bertolazzi, S.; Brivio, J.; Kis, A. Stretching and Breaking of Ultrathin MoS_2. *ACS Nano* **2011**, *5*, 9703-9709.
38. Jiang, J. W.; Qi, Z.; Park, H. S.; Rabczuk, T. Elastic Bending Modulus of Single-layer Molybdenum Disulfide (MoS_2): Finite Thickness Effect. *Nanotechnol.* **2013**, *24*, 435705.
39. Castellanos-Gomez, A.; Poot, M.; Steele, G. A.; Zant, H. S. J. v. d.; Agraït, N.; Rubio-Bollinger, G. Elastic Properties of Freely Suspended MoS_2 Nanosheets. *Adv. Mater.* **2012**, *24*, 772-775.
40. Castellanos-Gomez, A.; Singh, V.; van der Zant, H. S. J.; Steele, G. A. Mechanics of Freely-suspended Ultrathin Layered Materials. *Ann. Phys. (Berlin)* **2015**, *527*, 27-44.
41. Williams, D. B.; Carter, C. B. Thickness and Bending Effects. In *Transmission Electron Microscopy*, 2 ed.; Springer Science+Business Media, LLC: New York, 2009; Vol. 3, pp 407-417.
42. Xiong, S.; Cao, G. Bending Response of Single Layer MoS_2. *Nanotechnol.* **2016**, *27*, 105701.
43. Feldman, J. L. Elastic Constants of 2H-MoS_2 and 2H-$NbSe_2$ Extracted From Measured Dispersion Curves and Linear Compressibilities. *J. Phys. Chem. Solids* **1976**, *37*, 1141-1144.
44. Bosi, M. Growth and Synthesis of Mono and Few-layers Transition Metal Dichalcogenides by Vapour Techniques: A Review. *RSC Adv.* **2015**, *5*, 75500-75518.
45. Butler, S. Z.; Hollen, S. M.; Cao, L.; Cui, Y.; Gupta, J. A.; Gutiérrez, H. R.; Heinz, T. F.; Hong, S. S.; Huang, J.; Ismach, A. F.; Johnston-Halperin, E.; Kuno, M.; Plashnitsa, V. V.; Robinson, R. D.; Ruoff, R. S.; Salahuddin, S.; Shan, J.; Shi, L.; Spencer, O. M. G.; Terrones, M.; Windl, W.; Goldberger, J. E. Progress, Challenges, and Opportunities in Two-Dimensional Materials Beyond Graphene. *ACS Nano* **2013**, *7*, 2898-2926.
46. Xu, M.; Liang, T.; Shi, M.; Chen, H. Graphene-like Two-dimensional Materials. *Chem. Rev.* **2013**, *113*, 3766-3798.
47. Fleischauer, P. D. Fundamental Aspects of the Electronic Structure, Materials Properties and Lubrication Performance of Sputtered MoS_2 Films. *Thin Solid Films* **1987**, *154*, 309-322.
48. Donnet, C.; Erdemir, A. Historical Developments and New Trends in Tribological and Solid Lubricant Coatings. *Surf. Coat. Technol.* **2004**, *180-181*, 76-84.
49. Polcar, T.; Cavaleiro, A. Self-adaptive Low Friction Coatings Based on Transition Metal Dichalcogenides. *Thin Solid Films* **2011**, *519*, 4037-4044.
50. Castellanos-Gomez, A.; Buscema, M.; Molenaar, R.; Singh, V.; Janssen, L.; van der Zant, H. S. J.; Steele, G. A. Deterministic Transfer of Two-dimensional Materials by All-dry Viscoelastic Stamping. *2D Mater.* **2014**, *1*, 011002.
51. Lee, C.; Yan, H.; Brus, L. E.; Heinz, T. F.; Hone, J.; Ryu, S. Anomalous Lattice

Vibrations of Single- and Few-Layer MoS_2. *ACS Nano* **2010**, *4*, 2695-2700.

52. Radisavljevic, B.; Kis, A. Mobility Engineering and a Metal-Insulator Transition in Monolayer MoS_2. *Nat. Mater.* **2013**, *12*, 815-820.
53. Radisavljevic, B.; Radenovic, A.; Brivio, J.; Giacometti, V.; Kis, A. Single-layer MoS_2 Transistors. *Nat. Nanotechnol.* **2011**, *6*, 147-150.
54. Radisavljevic, B.; Whitwick, M. B.; Kis, A. Integrated Circuits and Logic Operations Based on Single-Layer MoS_2. *ACS Nano* **2011**, *5*, 9934-9938.
55. Mlack, J. T.; Masih Das, P.; Danda, G.; Chou, Y. C.; Naylor, C. H.; Lin, Z.; Lopez, N. P.; Zhang, T.; Terrones, M.; Johnson, A. T.; Drndic, M. Transfer of Monolayer TMD WS_2 and Raman Study of Substrate Effects. *Sci. Rep.* **2017**, *7*, 43037.
56. Coleman, J. N.; Lotya, M.; O'Neill, A.; Bergin, S. D.; King, P. J.; Khan, U.; Young, K.; Gaucher, A.; De, S.; Smith, R. J.; Shvets, I. V.; Arora, S. K.; Stanton, G.; Kim, H.-Y.; Lee, K.; Kim, G. T.; Duesberg, G. S.; Hallam, T.; Boland, J. J.; Wang, J. J.; Donegan, J. F.; Grunlan, J. C.; Moriarty, G.; Shmeliov, A.; Nicholls, R. J.; Perkins, J. M.; Grieveson, E. M.; Theuwissen, K.; McComb, D. W.; Nellist, P. D.; Nicolos, V. Two-dimensional Nanosheets Produced by Liquid Exfoliation of Layered Materials. *Science* **2011**, *331*, 568-571.
57. Zhou, K. G.; Mao, N. N.; Wang, H. X.; Peng, Y.; Zhang, H. L. A Mixed-solvent Strategy for Efficient Exfoliation of Inorganic Graphene Analogues. *Angew. Chem., Int. Ed.* **2011**, *50*, 10839-10842.
58. Cunningham, G.; Lotya, M.; Cucinotta, C. S.; Sanvito, S.; Bergin, S. D.; Menzel, R.; Shaffer, M. S. P.; Coleman, J. N. Solvent Exfoliation of Transition Metal Dichalcogenides: Dispersibility of Exfoliated Nanosheets Varies Only Weakly between Compounds. *ACS Nano* **2012**, *6*, 3468-3480.
59. Smith, R. J.; King, P. J.; Lotya, M.; Wirtz, C.; Khan, U.; De, S.; O'Neill, A.; Duesberg, G. S.; Grunlan, J. C.; Moriarty, G.; Chen, J.; Wang, J.; Minett, A. I.; Nicolosi, V.; Coleman, J. N. Large-scale Exfoliation of Inorganic Layered Compounds in Aqueous Surfactant Solutions. *Adv. Mater.* **2011**, *23*, 3944-3948.
60. Nicolosi, V.; Chhowalla, M.; Kanatzidis, M. G.; Strano, M. S.; Coleman, J. N. Liquid Exfoliation of Layered Materials. *Science* **2013**, *340*, 1226419.
61. Lee, Y. H.; Yu, L.; Wang, H.; Fang, W.; Ling, X.; Shi, Y.; Lin, C. T.; Huang, J. K.; Chang, M. T.; Chang, C. S.; Dresselhaus, M.; Palacios, T.; Li, L. J.; Kong, J. Synthesis and Transfer of Single-layer Transition Metal Disulfides on Diverse Surfaces. *Nano Lett.* **2013**, *13*, 1852-1857.
62. Liu, K. K.; Zhang, W.; Lee, Y. H.; Lin, Y. C.; Chang, M. T.; Su, C. Y.; Chang, C. S.; Li, H.; Shi, Y.; Zhang, H.; Lai, C. S.; Li, L. J. Growth of Large-area and Highly Crystalline MoS_2 Thin Layers on Insulating Substrates. *Nano Lett.* **2012**, *12*, 1538-1544.
63. Yun, S. J.; Chae, S. H.; Kim, H.; Park, J. C.; Park, J.-H.; Han, G. H.; Lee, J. S.; Kim, S. M.; Oh, H. M.; Seok, J.; Jeong, M. S.; Kim, K. K.; Lee, Y. H. Synthesis of Centimeter-scale Monolayer Tungsten Disulfide Film on Gold Foils. *ACS*

Nano **2015**, *9*, 5510-5519.

64. Perez-Hoyos, E.; Young, J.; Chilcote, M.; Barone, M.; Mueller, S.; Kawakami, R.; Johnston-Halperin, E. In *Uniform Wafer-scale Growth of Stencil Templated, High-quality Monolayer MoS_2*, American Physical Society Graduate Education & Bridge Program Conference, College Park, Maryland, February 11, 2017; College Park, Maryland, 2017.
65. Zhan, Y.; Liu, Z.; Najmaei, S.; Ajayan, P. M.; Lou, J. Large-area Vapor-phase Growth and Characterization of MoS_2 Atomic Layers on a SiO_2 Substrate. *Small* **2012**, *8*, 966-971.
66. Zhang, F.; Momeni, K.; AlSaud, M. A.; Azizi, A.; Hainey, M. F.; Redwing, J. M.; Chen, L.-Q.; Alem, N. Controlled Synthesis of 2D Transition Metal Dichalcogenides: From Vertical to Planar MoS_2. *2D Mater.* **2017**, *4*, 025029.
67. Lembke, D.; Bertolazzi, S.; Kis, A. Single-layer MoS_2 Electronics. *Acc. Chem. Res.* **2015**, *48*, 100-110.
68. Jariwala, D.; Sangwan, V. K.; Lauhon, L. J.; Marks, T. J.; Hersam, M. C. Emerging Device Applications for Semiconducting Two-dimensional Transition Metal Dichalcogenides. *ACS Nano* **2014**, *8*, 1102-1120.
69. Bersch, B. M.; Lin, Y.-C.; Zhang, K.; Eichfeld, S. M.; Leach, J. H.; Metzger, R.; Evans, K.; Robinson, J. A. In *Two-dimensional Materials for Low Power and High Frequency Devices*, Proc. SPIE 9467, Micro- and Nanotechnology Sensors, Systems, and Applications VII, Baltimore, Maryland, May 22, 2015; Baltimore, Maryland, 2015; pp 94670T-94670T-94679.
70. Liu, Y.; Weiss, N. O.; Duan, X.; Cheng, H.-C.; Huang, Y.; Xiangfeng, D. Van der Waals Heterostructures and Devices. *Nat. Rev. Mater.* **2016**, *1*, 16042.
71. Nichols, B. M.; Mazzoni, A. L.; Chin, M. L.; Shah, P. B.; Najmaei, S.; Burke, R. A.; Dubey, M. Advances in 2D Materials for Electronic Devices. *Semicond. Semimetals* **2016**, *95*, 221-277.
72. Novoselov, K. S.; Mishchenko, A.; Carvalho, A.; Castro Neto, A. H. 2D Materials and van der Waals Heterostructures. *Science* **2016**, *353*, aac9439.
73. Zhang, K.; Eichfeld, S.; Leach, J.; Metzger, B.; Lin, Y.-C.; Evans, K.; Robinson, J. A. In *Synthesis of Two-dimensional Materials for Beyond Graphene Devices*, SPIE Micro- and Nanotechnology Sensors, Systems, and Applications VII, Baltimore, Maryland, Baltimore, Maryland, 2015; p 94670O.
74. Mak, K. F.; Shan, J. Photonics and Optoelectronics of 2D Semiconductor Transition Metal Dichalcogenides. *Nat. Photonics* **2017**, *10*, 216-226.
75. Jiang, J.-W. Graphene Versus MoS_2: A Short Review. *Front. Phys.* **2015**, *10*, 287-302.
76. Wilson, J. A.; Yoffe, A. D. The Transition Metal Dichalcogenides: Discussion and Interpretation of the Observed Optical, Electrical, and Structural Properties. *Adv. Phys.* **1969**, *18*, 193-335.
77. Wilson, J. A.; Di Salvo, F. J.; Mahajan, S. Charge-density Waves and Superlattices in the Metallic Layered Transition Metal Dichalcogenides. *Adv.*

Phys. **1975**, *24*, 117-201.
78. McMillan, W. L. Landau Theory of Charge-density Waves in Transition-metal Dichalcogenides. *Phys. Rev. B* **1975**, *12*, 1187-1196.
79. Sipos, B.; Kusmartseva, A. F.; Akrap, A.; Berger, H.; Forro, L.; Tutis, E. From Mott State to Superconductivity in 1T-TaS_2. *Nat. Mater.* **2008**, *7*, 960-965.
80. Withers, R. L.; Wilson, J. A. An Examination of the Formation and Characteristics of Charge-density Waves in Inorganic Materials with Special Reference to the Two- and One-dimensional Transition-metal Dichalcogenides. *J. Phys. C: Solid State Phys.* **1986**, *19*, 4809-4845.
81. Castro Neto, A. H. Charge Density Wave, Superconductivity, and Anomalous Metallic Behavior in 2D Transition Metal Dichalcogenides. *Phys. Rev. Lett.* **2001**, *86*, 4382-4385.
82. Rossnagel, K. On the Origin of Charge-density Waves in Select Layered Transition-metal Dichalcogenides. *J. Phys.: Condens. Matter* **2011**, *23*, 213001.
83. Carvalho, A.; Ribeiro, R. M.; Castro Neto, A. H. Band Nesting and the Optical Response of Two-dimensional Semiconducting Transition Metal Dichalcogenides. *Phys. Rev. B* **2013**, *88*, 115205.
84. Gutiérrez, H. R.; Perea-López, N.; Elías, A. L.; Berkdemir, A.; Wang, B.; Lv, R.; López-Urías, F.; Crespi, V. H.; Terrones, H.; Terrones, M. Extraordinary Room-temperature Photoluminescence in Triangular WS_2 Monolayers. *Nano Lett.* **2012**, *13*, 3447-3454.
85. Hanbicki, A. T.; McCreary, K. M.; Currie, M.; Kioseoglou, G.; Hellberg, C. S.; Friedman, A. L.; Jonker, B. T. In *Tuning the Trion Photoluminescence Polarization in Monolayer WS_2*, American Physical Society March Meeting 2016, Baltimore, Maryland, March 14 - 18, 2016; Baltimore, Maryland, 2016.
86. Zhao, W.; Ribeiro, R. M.; Toh, M.; Carvalho, A.; Kloc, C.; Castro Neto, A. H.; Eda, G. Origin of Indirect Optical Transitions in Few-layer MoS_2, WS_2, and WSe_2. *Nano Lett.* **2013**, *13*, 5627-5634.
87. Castellanos-Gomez, A.; Roldán, R.; Cappelluti, E.; Buscema, M.; Guinea, F.; Zant, H. S. J. v. d.; Steele, G. A. Local Strain Engineering in Atomically Thin MoS_2. *Nano Lett.* **2013**, *13*, 5361-5366.
88. Conley, H. J.; Wang, B.; Ziegler, J. I.; Haglund, R. F., Jr.; Pantelides, S. T.; Bolotin, K. I. Bandgap Engineering of Strained Monolayer and Bilayer MoS_2. *Nano Lett.* **2013**, *13*, 3626-3630.
89. Keum, D. H.; Cho, S.; Kim, J. H.; Choe, D.-H.; Sung, H.-J.; Kan, M.; Kang, H.; Hwang, J.-Y.; Kim, S. W.; Yang, H.; Chang, K. J.; Lee, Y. H. Bandgap Opening in Few-layered Monoclinic $MoTe_2$. *Nat. Phys.* **2015**, *11*, 482-486.
90. Li, H.; Duan, X.; Duan, X.; Pan, A. In *Band Gap Engineering of Atomic Layer Semiconductor Nanosheets*, International Conference on the Physics of Semiconductors, Beijing, China, July 31 - August 5, 2016; Beijing, China, 2016; p 1.
91. Wang, Y.; Cong, C.; Yang, W.; Shang, J.; Peimyoo, N.; Chen, Y.; Kang, J.;

Wang, J.; Huang, W.; Yu, T. Strain-induced Direct-indirect Band Gap Transition and Phonon Modulation in Monolayer WS_2. *Nano Res.* **2015**, *8*, 2562-2572.

92. Tongay, S.; Zhou, J.; Ataca, C.; Lo, K.; Matthews, T. S.; Li, J.; Grossman, J. C.; Wu, J. Thermally Driven Crossover from Indirect toward Direct Bandgap in 2D Semiconductors: $MoSe_2$ versus MoS_2. *Nano Lett.* **2012**, *12*, 5576-5580.
93. Gehlmann, M.; Aguilera, I.; Bihlmayer, G.; Nemšák, S.; Nagler, P.; Gospodarič, P.; Zamborlini, G.; Eschbach, M.; Feyer, V.; Kronast, F.; Młyńczak, E.; Korn, T.; Plucinski, L.; Schüller, C.; Blügel, S.; Schneider, C. M. Direct Observation of the Band Gap Transition in Atomically Thin ReS_2. **2017**, arXiv:1702.04176 [cond-mat.mtrl-sci].
94. Bernardi, M.; Palummo, M.; Grossman, J. C. Extraordinary Sunlight Absorption and One Nanometer Thick Photovoltaics Using Two-dimensional Monolayer Materials. *Nano Lett.* **2013**, *13*, 3664-3670.
95. Gourmelon, E.; Lignier, O.; Hadouda, H.; Couturier, G.; Bernède, J. C.; Tedd, J.; Pouzet, J.; Salardenne, J. MS_2 (M = W, Mo) Photosensitive Thin Films for Solar Cells. *Sol. Energy Mater. Sol. Cells* **1997**, *46*, 115-121.
96. Ortiz-Quiles, E. O.; Cabrera, C. R. Exfoliated Molybdenum Disulfide for Dye Sensitized Solar Cells. *FlatChem* **2017**, *2*, 1-7.
97. Palummo, M.; Bernardi, M.; Grossman, J. C. Exciton Radiative Lifetimes in Two-dimensional Transition Metal Dichalcogenides. *Nano Lett.* **2015**, *15*, 2794-2800.
98. Sang, Y.; Zhao, Z.; Zhao, M.; Hao, P.; Leng, Y.; Liu, H. From UV to Near-Infrared, WS2 Nanosheet: A Novel Photocatalyst for Full Solar Light Spectrum Photodegradation. *Adv. Mater.* **2015**, *27*, 363-369.
99. Singh, E.; Kim, K. S.; Yeom, G.-Y.; Nalwa, H. S. Atomically Thin-layered Molybdenum Disulfide (MoS_2) for Bulk-Heterojunction Solar Cells. *ACS Appl. Mater. Interfaces* **2017**, *9*, 3223-3245.
100. Cui, Y.; Xin, R.; Yu, Z.; Pan, Y.; Ong, Z. Y.; Wei, X.; Wang, J.; Nan, H.; Ni, Z.; Wu, Y.; Chen, T.; Shi, Y.; Wang, B.; Zhang, G.; Zhang, Y. W.; Wang, X. High-Performance Monolayer WS_2 Field-effect Transistors on High-kappa Dielectrics. *Adv. Mater.* **2015**, *27*, 5230-5234.
101. Duesberg, G. S.; Hallam, T.; O'Brien, M.; Gatensby, R.; Kim, H.-Y.; Lee, K.; Berner, N. C.; McEvoy, N.; Yim, C., Investigation of 2D Transition Metal Dichalcogenide Films for Electronic Devices. In *2015 Joint International EUROSOI Workshop and International Conference on Ultimate Integration on Silicon (EUROSOI-ULIS)*, IEEE: Bologna, Italy, 2015; pp 73-76.
102. Fuhrer, M. S.; Hone, J. Measurement of Mobility in Dual-gated MoS_2 Transistors. *Nat. Nanotechnol.* **2013**, *8*, 146-147.
103. Georgiou, T.; Jalil, R.; Belle, B. D.; Britnell, L.; Gorbachev, R. B.; Morozov, S. V.; Kim, Y.-J.; Gholinia, A.; Haigh, S. J.; Makarovsky, O.; Eaves, L.; Ponomarenko, L. A.; Geim, A. K.; Novoselov, K. S.; Mishchenko, A. Vertical Field-effect Transistor Based on Graphene-WS_2 Heterostructures for Flexible and Transparent Electronics. *Nat. Nanotechnol.* **2012**, *8*, 100-103.

104. Jo, S.; Ubrig, N.; Berger, H.; Kuzmenko, A. B.; Morpurgo, A. F. Mono- and Bilayer WS_2 Light-emitting Transistors. *Nano Lett.* **2014**, *14*, 2019-2025.
105. Kaul, A. B. In *Van der Waals Solids: Properties and Device Applications*, SPIE Micro- and Nanotechnology Sensors, Systems, and Applications VII, Baltimore, Maryland, Baltimore, Maryland, 2015; p 94670N.
106. Lee, C. H.; McCulloch, W.; Lee, E. W.; Ma, L.; Krishnamoorthy, S.; Hwang, J.; Wu, Y.; Rajan, S. Transferred Large Area Single Crystal MoS_2 Field Effect Transistors. *Appl. Phys. Lett.* **2015**, *107*, 193503.
107. Leitao, L.; Bala Kumar, S.; Yijian, O.; Guo, J. Performance Limits of Monolayer Transition Metal Dichalcogenide Transistors. *IEEE Trans. Electron Devices* **2011**, *58*, 3042-3047.
108. Liu, X.; Hu, J.; Yue, C.; Fera, N. D.; Ling, Y.; Mao, Z.; Wei, J. High Performance Field-Effect Transistor Based on Multilayer Tungsten Disulfide. *ACS Nano* **2014**, *8*, 10396-10402.
109. Schwierz, F. In *Graphene and Beyond: Two-dimensional Materials for Transistor Applications*, SPIE Micro- and Nanotechnology Sensors, Systems, and Applications VII, Baltimore, Maryland, Baltimore, Maryland, 2015; p 94670W.
110. Sik Hwang, W.; Remskar, M.; Yan, R.; Protasenko, V.; Tahy, K.; Doo Chae, S.; Zhao, P.; Konar, A.; Xing, H.; Seabaugh, A.; Jena, D. Transistors with Chemically Synthesized Layered Semiconductor WS_2 Exhibiting 10^5 Room Temperature Modulation and Ambipolar Behavior. *Appl. Phys. Lett.* **2012**, *101*, 013107.
111. Yoon, Y.; Ganapathi, K.; Salahuddin, S. How Good Can Monolayer MoS_2 Transistors Be? *Nano Lett.* **2011**, *11*, 3768-3773.
112. Zhang, Y.; Li, H.; Wang, H.; Xie, H.; Liu, R.; Zhang, S. L.; Qiu, Z. J. Thickness Considerations of Two-Dimensional Layered Semiconductors for Transistor Applications. *Sci. Rep.* **2016**, *6*, 29615.
113. Zhang, Y.; Ye, J.; Matsuhashi, Y.; Iwasa, Y. Ambipolar MoS_2 Thin Flake Transistors. *Nano Lett.* **2012**, *12*, 1136-1140.
114. Lopez-Sanchez, O.; Lembke, D.; Kayci, M.; Radenovic, A.; Kis, A. Ultrasensitive Photodetectors Based on Monolayer MoS_2. *Nat. Nanotechnol.* **2013**, *8*, 497-501.
115. Wang, H.; Zhang, C.; Chan, W.; Tiwari, S.; Rana, F. Ultrafast Response of Monolayer Molybdenum Disulfide Photodetectors. *Nat. Commun.* **2015**, *6*, 8831.
116. Yu, Y.; Hu, S.; Su, L.; Huang, L.; Liu, Y.; Jin, Z.; Purezky, A. A.; Geohegan, D. B.; Kim, K. W.; Zhang, Y.; Cao, L. Equally Efficient Interlayer Exciton Relaxation and Improved Absorption in Epitaxial and Nonepitaxial MoS_2/WS_2 Heterostructures. *Nano Lett.* **2015**, *15*, 486-491.
117. Tongay, S.; Zhou, J.; Ataca, C.; Liu, J.; Kang, J. S.; Matthews, T. S.; You, L.; Li, J.; Grossman, J. C.; Wu, J. Broad-range Modulation of Light Emission in Two-dimensional Semiconductors by Molecular Physisorption Gating. *Nano Lett.* **2013**, *13*, 2831-2836.
118. Duerloo, K.-A. N.; Ong, M. T.; Reed, E. J. Intrinsic Piezoelectricity in Two-

Dimensional Materials. *J. Phys. Chem. Lett.* **2012**, *3*, 2871-2876.
119. Zhu, H.; Wang, Y.; Xiao, J.; Liu, M.; Xiong, S.; Wong, Z. J.; Ye, Z.; Ye, Y.; Yin, X.; Zhang, X. Observation of Piezoelectricity in Free-standing Monolayer MoS_2. *Nat. Nanotechnol.* **2015**, *10*, 151-155.
120. Wu, W.; Wang, L.; Li, Y.; Zhang, F.; Lin, L.; Niu, S.; Chenet, D.; Zhang, X.; Hao, Y.; Heinz, T. F.; Hone, J.; Wang, Z. L. Piezoelectricity of Single-atomic-layer MoS_2 for Energy Conversion and Piezotronics. *Nature* **2014**, *514*, 470-474.
121. Feng, J.; Graf, M.; Liu, K.; Ovchinnikov, D.; Dumcenco, D.; Heiranian, M.; Nandigana, V.; Aluru, N. R.; Kis, A.; Radenovic, A. Single-layer MoS_2 Nanopores as Nanopower Generators. *Nature* **2016**, *536*, 197-200.
122. Rezk, A. R.; Carey, B.; Chrimes, A. F.; Lau, D. W.; Gibson, B. C.; Zheng, C.; Fuhrer, M. S.; Yeo, L. Y.; Kalantar-Zadeh, K. Acoustically-driven Trion and Exciton Modulation in Piezoelectric Two-Dimensional MoS_2. *Nano Lett.* **2016**, *16*, 849-855.
123. Zeng, M.; Li, Y. Recent Advances in Heterogeneous Electrocatalysts for Hydrogen Evolution Reaction. *J. Mater. Chem. A* **2015**, *3*, 14942-14962.
124. Zhang, N.; Gan, S.; Wu, T.; Ma, W.; Han, D.; Niu, L. Growth Control of MoS_2 Nanosheets on Carbon Cloth for Maximum Active Edges Exposed: An Excellent Hydrogen Evolution 3D Cathode. *ACS Appl. Mater. Interfaces* **2015**, *7*, 12193-12202.
125. Bernardi, M.; Vigil-Fowler, D.; Ong, C. S.; Neaton, J. B.; Louie, S. G. Ab Initio Study of Hot Electrons in GaAs. *Proc. Natl. Aacd. Sci. U. S. A.* **2015**, *112*, 5291-5296.
126. Bratschitsch, R. In *Ultrafast Valley Dynamics in Atomically Thin Transition Metal Dichalcogenides*, SPIE Spintronics IX, San Diego, California, San Diego, California, 2016; p 99313D.
127. Cao, T.; Wang, G.; Han, W.; Ye, H.; Zhu, C.; Shi, J.; Niu, Q.; Tan, P.; Wang, E.; Liu, B.; Feng, J. Valley-selective Circular Dichroism of Monolayer Molybdenum Disulphide. *Nat. Commun.* **2012**, *3*, 887.
128. Jones, A. M.; Yu, H.; Ghimire, N. J.; Wu, S.; Aivazian, G.; Ross, J. S.; Zhao, B.; Yan, J.; Mandrus, D. G.; Xiao, D.; Yao, W.; Xu, X. Optical Generation of Excitonic Valley Coherence in Monolayer WSe_2 *Nat. Nanotechnol.* **2013**, *8*, 634-638.
129. Kumar, N.; He, J.; He, D.; Wang, Y.; Zhao, H. Valley and Spin Dynamics in $MoSe_2$ Two-dimensional Crystals. *Nanoscale* **2014**, *6*, 12690-12695.
130. Mai, C.; Barrette, A.; Yu, Y.; Semenov, Y. G.; Kim, K. W.; Cao, L.; Gundogdu, K. Many-body Effects in Valleytronics: Direct Measurement of Valley Lifetimes in Single-layer MoS_2. *Nano Lett.* **2014**, *14*, 202-206.
131. Mak, K. F.; He, K.; Shan, J.; Heinz, T. F. Control of Valley Polarization in Monolayer in MoS_2 by Optical Helicity. *Nat. Nanotechnol.* **2012**, *7*, 494-498.
132. Wang, Q.; Ge, S.; Li, X.; Qiu, J.; Ji, Y.; Feng, J.; Sun, D. Valley Carrier Dynamics in Monolayer Molybdenum Disulfide from Helicity-resolved Ultrafast

Pump-Probe Spectroscopy. *ACS Nano* **2013**, *7*, 11087-11093.

133. Xiao, D.; Liu, G.-B.; Feng, W.; Xu, X.; Yao, W. Coupled Spin and Valley Physics in Monolayers of MoS_2 and Other Group-VI Dichalcogenides. *Phys. Rev. Lett.* **2012**, *108*, 196802.
134. Zeng, H.; Dai, J.; Yao, W.; Xiao, D.; Cui, X. Valley Polarization in MoS_2 Monolayers by Optical Pumping. *Nat. Nanotechnol.* **2012**, *7*, 490-493.
135. Zeng, H.; Liu, G. B.; Dai, J.; Yan, Y.; Zhu, B.; He, R.; Xie, L.; Xu, S.; Chen, X.; Yao, W.; Cui, X. Optical Signature of Symmetry Variations and Spin-valley Coupling in Atomically Thin Tungsten Dichalcogenides. *Sci. Rep.* **2013**, *3*, 1608.
136. Xu, X.; Yao, W.; Xiao, D.; Heinz, T. F. Spin and Pseudospins in Layered Transition Metal Dichalcogenides. *Nat. Phys.* **2014**, *10*, 343-350.
137. Dickinson, R. G.; Pauling, L. The Crystal Structure of Molybdenite. *J. Am. Chem. Soc.* **1926**, *46*, 1466-1471.
138. Cooper, R. C.; Lee, C.; Marianetti, C. A.; Wei, X.; Hone, J.; Kysar, J. W. Nonlinear Elastic Behavior of Two-dimensional Molybdenum Disulfide. *Phys. Rev. B* **2013**, *87*, 035423.
139. Li, T. Ideal Strength and Phonon Instability in Single-layer MoS_2. *Phys. Rev. B* **2012**, *85*, 235407.
140. Wagner, P.; Ivanovskaya, V. V.; Rayson, M. J.; Briddon, P. R.; Ewels, C. P. Mechanical Properties of Nanosheets and Nanotubes Investigated Using a New Geometry Independent Volume Definition. *J. Phys.: Condens. Matter* **2013**, *25*, 155302.
141. Wang, Z.; Lee, J.; Feng, P. X.-L. In *Exploiting Irregular MoS_2 Nanostructures for Very High Frequency (VHF) Nanomechanical Resonators with Mode Shape Engineering and Frequency Control*, 2013 Joint European Frequency and Time Forum & International Frequency Control Symposium (EFTF/IFC), 2013; pp 551-554.
142. Lee, J.; Wang, Z.; He, K.; Shan, J.; Feng, P. X.-L. High Frequency MoS_2 Nanomechanical Resonators. *ACS Nano* **2013**, *7*, 6086-6091.
143. Ganatra, R.; Zhang, Q. Few-layer MoS_2: A Promising Layered Semiconductor. *ACS Nano* **2014**, *8*, 4074-4099.
144. Kuc, A.; Zibouche, N.; Heine, T. Influence of Quantum Confinement on the Electronic Structure of the Transition Metal Sulfide TS_2. *Phys. Rev. B* **2011**, *83*, 245213.
145. Wang, L.; Wang, Z.; Wang, H. Y.; Grinblat, G.; Huang, Y. L.; Wang, D.; Ye, X. H.; Li, X. B.; Bao, Q.; Wee, A. S.; Maier, S. A.; Chen, Q. D.; Zhong, M. L.; Qiu, C. W.; Sun, H. B. Slow Cooling and Efficient Extraction of C-exciton Hot Carriers in MoS_2 Monolayer. *Nat. Commun.* **2017**, *8*, 13906.
146. Johari, P.; Shenoy, V. B. Tuning the Electronic Properties of Semiconducting Transition Metal Dichalcogenides by Applying Mechanical Strains. *ACS Nano* **2012**, *6*, 5449-5456.
147. Peelaers, H.; Van de Walle, C. G. Effects of Strain on Band Structure and

Effective Masses in MoS_2. *Phys. Rev. B* **2012**, *86*, 241401(R).
148. Coehoorn, R.; Haas, C.; de Groot, R. A. Electronic Structure of $MoSe_2$, MoS_2, and WSe_2. II. The Nature of the Optical Band Gaps. *Phys. Rev. B* **1987**, *35*, 6203-6206.
149. Coehoorn, R.; Haas, C.; Dijkstra, J.; Flipse, C. J. F.; de Groot, R. A.; Wold, A. Electronic Structure of $MoSe_2$, MoS_2, and WSe_2. I. Band-structure Calculations and Photoelectron Spectroscopy. *Phys. Rev. B* **1987**, *35*, 6195-6202.
150. Cheiwchanchamnangij, T.; Lambrecht, W. R. L. Quasiparticle Band Structure Calculation of Monolayer, Bilayer, and Bulk MoS_2. *Phys. Rev. B* **2012**, *85*, 205302.
151. Molina-Sánchez, A.; Sangalli, D.; Hummer, K.; Marini, A.; Wirtz, L. Effect of Spin-orbit Interaction on the Optical Spectra of Single-layer, Double-layer, and Bulk MoS_2. *Phys. Rev. B* **2013**, *88*, 045412.
152. Hill, H. M.; Rigosi, A. F.; Roquelet, C.; Chernikov, A.; Berkelbach, T. C.; Reichman, D. R.; Hybertsen, M. S.; Brus, L. E.; Heinz, T. F. Observation of Excitonic Rydberg States in Monolayer MoS_2 and WS_2 by Photoluminescence Excitation Spectroscopy. *Nano Lett.* **2015**, *15*, 2992-2997.
153. Berkelbach, T. C.; Hybertsen, M. S.; Reichman, D. R. Theory of Neutral and Charged Excitons in Monolayer Transition Metal Dichalcogenides. *Phys. Rev. B* **2013**, *88*, 045318.
154. Ross, J. S.; Wu, S.; Yu, H.; Ghimire, N. J.; Jones, A. M.; Aivazian, G.; Yan, J.; Mandrus, D. G.; Xiao, D.; Yao, W.; Xu, X. Electrical Control of Neutral and Charged Excitons in a Monolayer Semiconductor. *Nat. Commun.* **2013**, *4*, 1474.
155. Mak, K. F.; He, K.; Lee, C.; Lee, G. H.; Hone, J.; Heinz, T. F.; Shan, J. Tightly Bound Trions in Monolayer MoS_2. *Nat. Mater.* **2013**, *12*, 207-211.
156. Lui, C. H.; Frenzel, A. J.; Pilon, D. V.; Lee, Y. H.; Ling, X.; Akselrod, G. M.; Kong, J.; Gedik, N. Trion-induced Negative Photoconductivity in Monolayer MoS_2. *Phys. Rev. Lett.* **2014**, *113*, 166801.
157. Zhu, Z. Y.; Cheng, Y. C.; Schwingenschlögl, U. Giant Spin-orbit-induced Spin Splitting in Two-dimensional Transition-metal Dichalcogenide Semiconductors. *Phys. Rev. B* **2011**, *84*, 153402.
158. Britnell, L.; Ribeiro, R. M.; Eckmann, A.; Jalil, R.; Belle, B. D.; Mishchenko, A.; Kim, Y.-J.; Gorbachev, R. B.; Georgiou, T.; Morozov, S. V.; Grigorenko, A. N.; Keim, A. K.; Casiraghi, C.; Castro Neto, A. H.; Novoselov, K. S. Strong Light-matter Interactions in Heterostructures of Atomically Thin Films. *Science* **2013**, *340*, 1311-1314.
159. Kozawa, D.; Kumar, R.; Carvalho, A.; Amara, K. K.; Zhao, W.; Wang, S.; Toh, M.; Ribeiro, R. M.; Castro Neto, A. H.; Matsuda, K.; Eda, G. Photocarrier Relaxation Pathway in Two-dimensional Semiconducting Transition Metal Dichalcogenides. *Nat. Commun.* **2014**, *5*, 4543.
160. Kumar, R.; Verhbitskiy, I.; Eda, G. Strong Optical Absorption and Photocarrier Relaxation in 2-D Semiconductors. *IEEE J. Quantum Electron.* **2015**, *51*,

0600206.

161. Zhu, X. Y.; Monahan, N. R.; Gong, Z.; Zhu, H.; Williams, K.; Nelson, C. A. Charge Transfer Excitons at van der Waals Interfaces. *J. Am. Chem. Soc.* **2015**, *137*, 8313-8320.
162. Koppens, F. H. L.; Mueller, T.; Avouris, P.; Ferrari, A. C.; Vitiello, M. S.; Pollini, M. Photodetectors Based on Graphene, Other Two-dimensional Materials and Hybrid Systems. *Nat. Nanotechnol.* **2014**, *9*, 780-793.
163. Sun, Z.; Chang, H. Graphene and Graphene-like Two-dimensional Materials in Photodetection: Mechanisms and Methodology. *ACS Nano* **2014**, *8*, 4133-4156.
164. Li, H.; Zhang, Q.; Yap, C. C. R.; Tay, B. K.; Edwin, T. H. T.; Olivier, A.; Baillargeat, D. From Bulk to Monolayer MoS_2: Evolution of Raman Scattering. *Adv. Funct. Mater.* **2012**, *22*, 1385-1390.
165. Konstantopoulou, A.; Sgouros, A. P.; Sigalas, M. M. Computation Study of Phononic Resonators and Waveguides in Monolayer Transition Metal Dichalcogenides. *Phys. Chem. Chem. Phys.* **2017**, *19*, 8082-8090.
166. Molina-Sánchez, A.; Wirtz, L. Phonons in Single-layer and Few-layer MoS_2 and WS_2. *Phys. Rev. B* **2011**, *84*, 155413.
167. Liu, J.; Choi, G.-M.; Cahill, D. G. Measurement of the Anisotropic Thermal Conductivity of Molybdenum Disulfide by the Time-resolved Magneto-optic Kerr Effect. *J. Appl. Phys.* **2014**, *116*, 233107.
168. Yan, R.; Simpson, J. R.; Bertolazzi, S.; Brivio, J.; Watson, M.; Wu, X.; Kis, A.; Luo, T.; Walker, A. R. H.; Xing, H. G. Thermal Conductivity of Monolayer Molybdenum Disulfide Obtained from Temperature-Dependent Raman Spectroscopy. *ACS Nano* **2014**, *8*, 986-993.
169. Sahoo, S.; Gaur, A. P. S.; Ahmadi, M.; Guinel, M. J. F.; Katiyar, R. S. Temperature-dependent Raman Studies and Thermal Conductivity of Few-layer MoS_2. *J. Phys. Chem. C* **2013**, *117*, 9042-9047.
170. Jo, I.; Pettes, M. T.; Ou, E.; Wu, W.; Shi, L. Basal-plane Thermal Conductivity of Few-layer Molybdenum Disulfide. *Appl. Phys. Lett.* **2014**, *104*, 201902.
171. Muratore, C.; Varshney, V.; Gengler, J. J.; Hu, J.; Bultman, J. E.; Roy, A. K.; Farmer, B. L.; Voevodin, A. A. Thermal Anisotropy in Nano-crystalline MoS_2 Thin Films. *Phys. Chem. Chem. Phys.* **2014**, *16*, 1008-1014.
172. Sledzinska, M.; Graczykowski, B.; Placidi, M.; Reig, D. S.; Sachat, A. E.; Reparaz, J. S.; Alzina, F.; Mortazavi, B.; Quey, R.; Colombo, L.; Roche, S.; Torres, C. M. S. Thermal Conductivity of MoS_2 Polycrystalline Nanomembranes. *2D Mater.* **2016**, *3*, 035016.
173. Zhang, J.; Meguid, S. Piezoelectricity of Two-dimensional Nanomaterials: Characterization, Properties and Applications. *Semicond. Sci. Technol.* **2017**, *32*, 043006.
174. Molina-Sánchez, A.; Hummer, K.; Wirtz, L. Vibrational and Optical Properties of MoS_2: From Monolayer to Bulk. *Surf. Sci. Rep.* **2015**, *70*, 554-586.
175. Late, D. J.; Huang, Y.-K.; Acharya, B. L. J.; Shirodkar, S. N.; Luo, J.; Yan, A.;

Charles, D.; Waghmare, U. V.; Dravid, V. P.; Rao, C. N. R. Sensing Behavior of Atomically Thin-layered MoS_2 Transistors. *ACS Nano* **2013**, *7*, 4879-4891.

176. Castellanos-Gomez, A.; Cappelluti, E.; Roldan, R.; Agrait, N.; Guinea, F.; Rubio-Bollinger, G. Electric-field Screening in Atomically Thin Layers of MoS_2: The Role of Interlayer Coupling. *Adv. Mater.* **2013**, *25*, 899-903.
177. Kim, S.; Konar, A.; Hwang, W. S.; Lee, J. H.; Lee, J.; Yang, J.; Jung, C.; Kim, H.; Yoo, J. B.; Choi, J. Y.; Jin, Y. W.; Lee, S. Y.; Jena, D.; Choi, W.; Kim, K. High-mobility and Low-power Thin-film Transistors Based on Multilayer MoS_2 Crystals. *Nat. Commun.* **2012**, *3*, 1011.
178. Kaasbjerg, K.; Thygesen, K. S.; Jacobsen, K. W. Phonon-limited Mobility in *n*-type Single-layer MoS_2 from First Principles. *Phys. Rev. B* **2012**, *85*, 115317.
179. Choi, W.; Cho, M. Y.; Konar, A.; Lee, J. H.; Cha, G. B.; Hong, S. C.; Kim, S.; Kim, J.; Jena, D.; Joo, J.; Kim, S. High-detectivity Multilayer MoS_2 Phototransistors with Spectral Response from Ultraviolet to Infrared. *Adv. Mater.* **2012**, *24*, 5832-5836.
180. Korn, T.; Heydrich, S.; Hirmer, M.; Schmutzler, J.; Schüller, C. Low-temperature Photocarrier Dynamics in Monolayer MoS_2. *Appl. Phys. Lett.* **2011**, *99*, 102109.
181. Zhang, Y.; Li, H.; Wang, L.; Wang, H.; Xie, X.; Zhang, S. L.; Liu, R.; Qiu, Z. J. Photothermoelectric and Photovoltaic Effects Both Present in MoS_2. *Sci. Rep.* **2015**, *5*, 7938.
182. Zhu, C. R.; Wang, G.; Liu, B. L.; Marie, X.; Qiao, X. F.; Zhang, X.; Wu, X. X.; Fan, H.; Tan, P. H.; Amand, T.; Urbaszek, B. Strain Tuning of Optical Emission Energy and Polarization in Monolayer and Bilayer MoS_2. *Phys. Rev. B* **2013**, *88*, 121301(R).
183. Nayeri, M.; Fathipour, M.; Yazdanpanah Goharrizi, A. The Effect of Uniaxial Strain on the Optical Properties of Monolayer Molybdenum Disulfide. *J. Phys. D: Appl. Phys.* **2016**, *49*, 455103.
184. Zhao, Y.; Zhang, Z.; Ouyang, G. Lattice Strain Effect on the Band Offset in Single-layer MoS_2: An Atomic-Bond-Relaxation Approach. *J. Phys. Chem. C* **2017**, *121*, 5366-5371.
185. McCreary, A.; Ghosh, R.; Amani, M.; Wang, J.; Duerloo, K. A.; Sharma, A.; Jarvis, K.; Reed, E. J.; Dongare, A. M.; Banerjee, S. K.; Terrones, M.; Namburu, R. R.; Dubey, M. Effects of Uniaxial and Biaxial Strain on Few-layered Terrace Structures of MoS_2 Grown by Vapor Transport. *ACS Nano* **2016**, *10*, 3186-3197.
186. He, X.; Li, H.; Zhu, Z.; Dai, Z.; Yang, Y.; Yang, P.; Zhang, Q.; Li, P.; Schwingenschlogl, U.; Zhang, X. Strain Engineering in Monolayer WS_2, MoS_2, and the WS_2/MoS_2 Heterostructure. *Appl. Phys. Lett.* **2016**, *109*, 173105.
187. Lloyd, D.; Liu, X.; Christopher, J. W.; Cantley, L.; Wadehra, A.; Kim, B. L.; Goldberg, B. B.; Swan, A. K.; Bunch, J. S. Band Gap Engineering with Ultralarge Biaxial Strains in Suspended Monolayer MoS_2. *Nano Lett.* **2016**, *16*, 5836-5841.
188. Yang, L.; Cui, X.; Zhang, J.; Wang, K.; Shen, M.; Zeng, S.; Dayeh, S. A.; Feng, L.; Xiang, B. Lattice Strain Effects on the Optical Properties of MoS_2 Nanosheets.

Sci. Rep. **2014**, *4*, 5649.
189. Scalise, E.; Houssa, M.; Pourtois, G.; Afanas'ev, V.; Stesmans, A. Strain-induced Semiconductor to Metal Transition in the Two-dimensional Honeycomb Structure of MoS_2. *Nano Res.* **2011**, *5*, 43-48.
190. Ghorbani-Asl, M.; Borini, S.; Kuc, A.; Heine, T. Strain-dependent Modulation of Conductivity in Single-layer Transition-metal Dichalcogenides. *Phys. Rev. B* **2013**, *87*, 235434.
191. López-Suárez, M.; Neri, I.; Rurali, R. Band Gap Engineering of MoS_2 upon Compression. *J. Appl. Phys.* **2016**, *119*, 165105.
192. Guzman, D. M.; Strachan, A. Role of Strain on Electronic and Mechanical Response of Semiconducting Transition-metal Dichalcogenide Monolayers: An Ab-initio Study. *J. Appl. Phys.* **2014**, *115*, 243701.
193. Ouyang, B.; Mi, Z.; Song, J. Bandgap Transition of 2H Transition Metal Dichalcogenides: Predictive Tuning via Inherent Interface Coupling and Strain. *J. Phys. Chem. C* **2016**, *120*, 8927-8935.
194. Corkum, P. B.; Krausz, F. Attosecond Science. *Nat. Phys.* **2007**, *3*, 381-387.
195. Kun Zhao, Q. Z., Michael Chini, Yi Wu, Xiaowei Wang, Zenghu Chang Tailoring a 67 Attosecond Pulse through Advantageous Phase-mismatch. *Opt. Lett.* **2012**, *37*, 3891-3893.
196. Plemmons, D. A.; Suri, P. K.; Flannigan, D. J. Probing Structural and Electronic Dynamics with Ultrafast Electron Microscopy. *Chem. Mater.* **2015**, *27*, 3178-3192.
197. Othonos, A. Probing Ultrafast Carrier and Phonon Dynamics in Semiconductors. *J. Appl. Phys.* **1998**, *83*, 1789-1830.
198. Meyer, J. C.; Geim, A. K.; Katsnelson, M. I.; Novoselov, K. S.; Booth, T. J.; Roth, S. The Structure of Suspended Graphene Sheets. *Nature* **2007**, *446*, 60-63.
199. Geim, A. K. Random Walk to Graphene. *International Journal of Modern Physics B* **2011**, *25*, 4055-4080.
200. Huang, J.; Alexander-Webber, J. A.; Janssen, T. J.; Tzalenchuk, A.; Yager, T.; Lara-Avila, S.; Kubatkin, S.; Myers-Ward, R. L.; Wheeler, V. D.; Gaskill, D. K.; Nicholas, R. J. Hot Carrier Relaxation of Dirac Fermions in Bilayer Epitaxial Graphene. *J. Phys.: Condens. Matter* **2015**, *27*, 164202.
201. Neto, A. H. C.; Guinea, F.; Peres, N. M. R.; Novoselov, K. S.; Geim, A. K. The Electronic Properties of Graphene. *Rev. Mod. Phys.* **2009**, *81*, 109-162.
202. Sarma, S. D.; Adam, S.; Hwang, E. H.; Rossi, E. Electronic Transport in Two-dimensional Graphene. *Rev. Mod. Phys.* **2011**, *83*, 407-470.
203. Tse, W.-K.; Das Sarma, S. Energy Relaxation of Hot Dirac Fermions in Graphene. *Phys. Rev. B* **2009**, *79*, 235406.
204. Borzenets, I. V.; Coskun, U. C.; Mebrahtu, H. T.; Bomze, Y. V.; Smirnov, A. I.; Finkelstein, G. Phonon Bottleneck in Graphene-based Josephson Junctions at Millikelvin Temperatures. *Phys. Rev. Lett.* **2013**, *111*, 027001.
205. Fong, K. C.; Wollman, E. E.; Ravi, H.; Chen, W.; Clerk, A. A.; Shaw, M. D.;

Leduc, H. G.; Schwab, K. C. Measurement of the Electronic Thermal Conductance Channels and Heat Capacity of Graphene at Low Temperature. *Phys. Rev. X* **2013**, *3*, 041008.

206. Bhargavi, K. S.; Kubakaddi, S. S. High Field Transport Properties of a Bilayer Graphene. *Phys. E (Amsterdam, Neth.)* **2014**, *56*, 123-129.
207. Song, J. C.; Reizer, M. Y.; Levitov, L. S. Disorder-assisted Electron-phonon Scattering and Cooling Pathways in Graphene. *Phys. Rev. Lett.* **2012**, *109*, 106602.
208. Breusing, M.; Ropers, C.; Elsaesser, T. Ultrafast Carrier Dynamics in Graphite. *Phys. Rev. Lett.* **2009**, *102*, 086809.
209. Bonini, N.; Lazzeri, M.; Marzari, N.; Mauri, F. Phonon Anharmonicities in Graphite and Graphene. *Phys. Rev. Lett.* **2007**, *99*, 176802.
210. Harb, M.; Enquist, H.; Jurgilaitis, A.; Tuyakova, F. T.; Obraztsov, A. N.; Larsson, J. Phonon-phonon Interactions in Photoexcited Graphite Studied by Ultrafast Electron Diffraction. *Phys. Rev. B* **2016**, *93*, 104104.
211. Ishida, Y.; Togashi, T.; Yamamoto, K.; Tanaka, M.; Taniuchi, T.; Kiss, T.; Nakajima, M.; Suemoto, T.; Shin, S. Non-thermal Hot Electrons Ultrafastly Generating Hot Optical Phonons in Graphite. *Sci. Rep.* **2011**, *1*, 64.
212. Viljas, J. K.; Heikkilä, T. T. Electron-phonon Heat Transfer in Monolayer and Bilayer Graphene. *Phys. Rev. B* **2010**, *81*, 245404.
213. Hwang, E. H.; Adam, S.; Sarma, S. D. Carrier Transport in Two-dimensional Graphene Layers. *Phys. Rev. Lett.* **2007**, *98*, 186806.
214. Schedin, F.; Geim, A. K.; Morozov, S. V.; Hill, E. W.; Blake, P.; Katsnelson, M. I.; Novoselov, K. S. Detection of Individual Gas Molecules Adsorbed on Graphene. *Nat. Mater.* **2007**, *6*, 652-655.
215. Katsnelson, M. I.; Geim, A. K. Electron Scattering on Microscopic Corrugations in Graphene. *Philos. Trans. R. Soc., A* **2008**, *366*, 195-204.
216. Betz, A. C.; Vialla, F.; Brunel, D.; Voisin, C.; Picher, M.; Cavanna, A.; Madouri, A.; Feve, G.; Berroir, J. M.; Placais, B.; Pallecchi, E. Hot Electron Cooling by Acoustic Phonons in Graphene. *Phys. Rev. Lett.* **2012**, *109*, 056805.
217. Stauber, T.; Peres, N. M. R.; Guinea, F. Electronic Transport in Graphene: A Semiclassical Approach Including Midgap States. *Phys. Rev. B* **2007**, *76*, 205423.
218. Peres, N. M. R.; Lopes dos Santos, J. M. B.; Stauber, T. Phenomenological Study of the Electronic Transport Coefficients of Graphene. *Phys. Rev. B* **2007**, *76*, 073412.
219. Bistritzer, R.; MacDonald, A. H. Electronic Cooling in Graphene. *Phys. Rev. Lett.* **2009**, *102*, 206410.
220. Baker, A. M. R.; Alexander-Webber, J. A.; Altebaeumer, T.; Nicholas, R. J. Energy Relaxation for Hot Dirac Fermions in Graphene and Breakdown of the Quantum Hall Effect. *Phys. Rev. B* **2012**, *85*, 115403.
221. Kubakaddi, S. S. Interaction of Massless Dirac Electrons with Acoustic Phonons in Graphene at Low Temperatures. *Phys. Rev. B* **2009**, *79*, 075417.

222. Graham, M. W.; Shi, S.-F.; Ralph, D. C.; Park, J.; McEuen, P. L. Photocurrent Measurements of Supercollision Cooling in Graphene. *Nat. Phys.* **2013**, *9*, 103-108.
223. Betz, A. C.; Jhang, S. H.; Pallecchi, E.; Ferreira, R.; Fève, G.; Berroir, J.-M.; Plaçais, B. Supercollision Cooling in Undoped Graphene. *Nat. Phys.* **2013**, *9*, 109-112.
224. Baker, A. M. R.; Alexander-Webber, J. A.; Altebaeumer, T.; McMullan, S. D.; Janssen, T. J. B. M.; Tzalenchuk, A.; Lara-Avila, S.; Kubatkin, S.; Yakimova, R.; Lin, C. T.; Li, L. J.; Nicholas, R. J. Energy Loss Rates of Hot Dirac Fermions in Epitaxial, Exfoliated, and CVD Graphene. *Phys. Rev. B* **2013**, *87*, 045414.
225. Kampfrath, T.; Perfetti, L.; Schapper, F.; Frischkorn, C.; Wolf, M. Strongly Coupled Optical Phonons in the Ultrafast Dynamics of the Electronic Energy and Current Relaxation in Graphite. *Phys. Rev. Lett.* **2005**, *95*, 187403.
226. Ma, Q.; Gabor, N. M.; Andersen, T. I.; Nair, N. L.; Watanabe, K.; Taniguchi, T.; Jarillo-Herrero, P. Competing Channels for Hot-electron Cooling in Graphene. *Phys. Rev. Lett.* **2014**, *112*, 247401.
227. Dai, Y. M.; Bowlan, J.; Li, H.; Miao, H.; Wu, S. F.; Kong, W. D.; Shi, Y. G.; Trugman, S. A.; Zhu, J. X.; Ding, H.; Taylor, A. J.; Yarotski, D. A.; Prasankumar, R. P. Ultrafast Carrier Dynamics in the Large-magnetoresistance Material WTe_2. *Phys. Rev. B* **2015**, *92*, 161104(R).
228. Wang, R.; Ruzicka, B. A.; Kumar, N.; Bellus, M. Z.; Chiu, H.-Y.; Zhao, H. Ultrafast and Spatially Resolved Studies of Charge Carriers in Atomically Thin Molybdenum Disulfide. *Phys. Rev. B* **2012**, *86*, 045406.
229. Kumar, N.; He, J.; He, D.; Wang, Y.; Zhao, H. Charge Carrier Dynamics in Bulk MoS_2 Crystal Studied by Transient Absorption Microscopy. *J. Appl. Phys.* **2013**, *113*, 133702.
230. Sun, D.; Rao, Y.; Reider, G. A.; Chen, G.; You, Y.; Brézin, L.; Harutyunyan, A. R.; Heinz, T. F. Observation of Rapid Exciton-exciton Annihilation in Monolayer Molybdenum Disulfide. *Nano Lett.* **2014**, *14*, 5625-5629.
231. Shi, H.; Yan, R.; Bertolazzi, S.; Brivio, J.; Gao, B.; Kis, A.; Jena, D.; Xing, H. G.; Huang, L. Exciton Dynamics in Suspended Monolayer and Few-layer MoS_2 2D Crystals. *ACS Nano* **2013**, *7*, 1072-1080.
232. Sim, S.; Park, J.; Song, J.-G.; In, C.; Lee, Y.-S.; Kim, H.; Choi, H. Exciton Dynamics in Atomically Thin MoS_2: Interexcitonic Interaction and Broadening Kinetics. *Phys. Rev. B* **2013**, *88*, 075434.
233. Mannebach, E. M.; Duerloo, K.-A. N.; Pellouchoud, L. A.; Sher, M.-J.; Nah, S.; Kuo, Y. H.; Yu, Y.-H.; Marshall, A. F.; Cao, L.; Reed, E. J.; Lindenberg, A. M. Ultrafast Electronic and Structural Response of Monolayer MoS_2 under Intense Photoexcitation Conditions. *ACS Nano* **2014**, *8*, 10734-10742.
234. Chernikov, A.; Ruppert, C.; Hill, H. M.; Rigosi, A. F.; Heinz, T. F. Population Inversion and Giant Bandgap Renormalization in Atomically Thin WS_2 Layers. *Nat. Photonics* **2015**, *9*, 466-470.

235. Tanaka, A.; Watkins, N. J.; Gao, Y. Hot-electron Relaxation in the Layered Semiconductor 2H−MoS_2 Studied by Time-resolved Two-photon Photoemission Spectroscopy. *Phys. Rev. B* **2003**, *67*, 113315.
236. Nie, Z.; Long, R.; Sun, L.; Huang, C.-C.; Zhang, J.; Xiong, Q.; Hewak, D. W.; Shen, Z.; Prezhdo, O. V.; Loh, Z.-H. Ultrafast Carrier Thermalization and Cooling Dynamics in Few-Layer MoS_2. *ACS Nano* **2014**, *8*, 10931-10940.
237. Nie, Z.; Long, R.; Teguh, J. S.; Huang, C.-C.; Hewak, D. W.; Yeow, E. K. L.; Shen, Z.; Prezhdo, O. V.; Loh, Z.-H. Ultrafast Electron and Hole Relaxation Pathways in Few-layer MoS_2. *J. Phys. Chem. C* **2015**, *119*, 20698–20708.
238. Kaasbjerg, K.; Bhargavi, K. S.; Kubakaddi, S. S. Hot-electron Cooling by Acoustic and Optical Phonons in Monolayers of MoS_2 and Other Transition-metal Dichalcogenides. *Phys. Rev. B* **2014**, *90*, 165436.
239. Ruppert, C.; Chernikov, A.; Hill, H. M.; Rigosi, A. F.; Heinz, T. F. The Role of Electronic and Phononic Excitation in the Optical Response of Monolayer WS_2 after Ultrafast Excitation. *Nano Lett.* **2017**, *17*, 644-651.
240. Carbone, F.; Baum, P.; Rudolf, P.; Zewail, A. Erratum: Structural Preablation Dynamics of Graphite Observed by Ultrafast Electron Crystallography [Phys. Rev. Lett. 100, 035501 (2008)]. *Phys. Rev. Lett.* **2011**, *106*.
241. Carbone, F.; Baum, P.; Rudolf, P.; Zewail, A. H. Structural Preablation Dynamics of Graphite Observed by Ultrafast Electron Crystallography. *Phys. Rev. Lett.* **2008**, *100*, 035501.
242. Raman, R. K.; Murooka, Y.; Ruan, C. Y.; Yang, T.; Berber, S.; Tomanek, D. Direct Observation of Optically Induced Transient Structures in Graphite using Ultrafast Electron Crystallography. *Phys. Rev. Lett.* **2008**, *101*, 077401.
243. Schäfer, S.; Liang, W.; Zewail, A. H. Primary Structural Dynamics in Graphite. *New J. Phys.* **2011**, *13*, 063030.
244. Mannebach, E. M.; Li, R.; Duerloo, K.-A. N.; Nyby, C.; Zalden, P.; Vecchione, T.; Ernst, F.; Reid, A. H.; Chase, T.; Shen, X.; Weathersby, S.; Hast, C.; Hettel, R.; Coffee, R.; Hartmann, N.; Fry, A. R.; Yu, Y.; Cao, L.; Heinz, T. F.; Reed, E. J.; Dürr, H. A.; Wang, X.; Lindenberg, A. M. Dynamic Structural Response and Deformations of Monolayer MoS_2 Visualized by Femtosecond Electron Diffraction. *Nano Lett.* **2015**, *15*, 6889–6895.
245. Chatelain, R. P.; Morrison, V. R.; Klarenaar, B. L.; Siwick, B. J. Coherent and Incoherent Electron-phonon Coupling in Graphite Observed with Radio-frequency Compressed Ultrafast Electron Diffraction. *Phys Rev Lett* **2014**, *113*, 235502.
246. Kwon, O.-H.; Barwick, B.; Park, H. S.; Baskin, J. S.; Zewail, A. H. Nanoscale Mechanical Drumming Visualized by 4D Electron Microscopy. *Nano Lett.* **2008**, *8*, 3557-3562.
247. Cremons, D. R.; Plemmons, D. A.; Flannigan, D. J. Femtosecond Electron Imaging of Defect-modulated Phonon Dynamics. *Nat. Commun.* **2016**, *7*, 11230.
248. Scheuch, M.; Kampfrath, T.; Wolf, M.; von Volkmann, K.; Frischkorn, C.;

Perfetti, L. Temperature Dependence of Ultrafast Phonon Dynamics in Graphite. *Appl. Phys. Lett.* **2011**, *99*, 211908.

249. Jeong, T. Y.; Jin, B. M.; Rhim, S. H.; Debbichi, L.; Park, J.; Jang, Y. D.; Lee, H. R.; Chae, D.-H.; Lee, D.; Kim, Y.-H.; Jung, S.; Yee, K. J. Coherent Lattice Vibrations in Mono- and Few-Layer WSe_2. *ACS Nano* **2016**, *10*, 5560–5566.
250. Tanaka, S.; Matsunami, M.; Kimura, S. An Investigation of Electron-phonon Coupling via Phonon Dispersion Measurements in Graphite Using Angle-resolved Photoelectron Spectroscopy. *Sci. Rep.* **2013**, *3*, 3031.
251. Ge, S.; Liu, X.; Qiao, X.; Wang, Q.; Xu, Z.; Qiu, J.; Tan, P.-H.; Zhao, J.; Sun, D. Coherent Longitudinal Acoustic Phonon Approaching THz Frequency in Multilayer Molybdenum Disulphide. *Sci. Rep.* **2014**, *4*, 5722.
252. He, B.; Zhang, C.; Zhu, W.; Li, Y.; Liu, S.; Zhu, X.; Wu, X.; Wang, X.; Wen, H. H.; Xiao, M. Coherent Optical Phonon Oscillation and Possible Electronic Softening in WTe_2 Crystals. *Sci. Rep.* **2016**, *6*, 30487.
253. Ma, L.; Ye, C.; Yu, Y.; Lu, X. F.; Niu, X.; Kim, S.; Feng, D.; Tomanek, D.; Son, Y. W.; Chen, X. H.; Zhang, Y. A Metallic Mosaic Phase and the Origin of Mott-insulating State in 1T-TaS_2. *Nat. Commun.* **2016**, *7*, 10956.
254. Sun, S.; Wei, L.; Li, Z.; Cao, G.; Liu, Y.; Lu, W. J.; Sun, Y. P.; Tian, H.; HuaixinYang; Li, J. Direct Observation of an Optically Induced Charge Density Wave Transition in 1*T*-$TaSe_2$. *Phys. Rev. B* **2015**, *92*, 224303.
255. Haupt, K.; Eichberger, M.; Erasmus, N.; Rohwer, A.; Demsar, J.; Rossnagel, K.; Schwoerer, H. Ultrafast Metamorphosis of a Complex Charge-density Wave. *Phys. Rev. Lett.* **2016**, *116*, 016402.
256. Mutka, H.; Housseau, N.; Zuppiroli, L.; Pelissieb, J. The Pinning of the Charge Density Wave to Irradiation-induced Defects. *Philos. Mag. B* **1982**, *45*, 361-373.
257. Li, L. J.; Lu, W. J.; Liu, Y.; Qu, Z.; Ling, L. S.; Sun, Y. P. Influence of Defects on Charge-density-wave and Superconductivity in 1T-TaS_2 and 2H-TaS_2 Systems. *Phys. C* **2013**, *492*, 64-67.
258. Cremons, D. R.; Plemmons, D. A.; Flannigan, D. J. Defect-mediated Phonon Dynamics in TaS_2 and WSe_2. *Struct. Dyn.* **2017**, *4*, 044019.
259. Yurtsever, A.; Zewail, A. H. Kikuchi Ultrafast Nanodiffraction in Four-dimensional Electron Microscopy. *Proc. Natl. Acad. Sci. U. S. A.* **2011**, *108*, 3152-3156.
260. Castellanos-Gomez, A.; van Leeuwen, R.; Buscema, M.; van der Zant, H. S.; Steele, G. A.; Venstra, W. J. Single-layer MoS_2 Mechanical Resonators. *Adv. Mater.* **2013**, *25*, 6719-6723.
261. Wang, Z.; Lee, J.; He, K.; Shan, J.; Feng, P. X. Embracing Structural Nonidealities and Asymmetries in Two-dimensional Nanomechanical Resonators. *Sci. Rep.* **2014**, *4*, 3919.
262. Zheludev, N. I. What Diffraction Limit? *Nat. Mater.* **2008**, *7*, 420-422.
263. Xiangsheng Xie, Y. C., Ken Yang, and Jianying Zhou Harnessing the Point-Spread Function for High-Resolution Far-Field Optical Microscopy. *Phys. Rev.*

Lett. **2014**, *113*, 263901.
264. Rogers, E. T. F.; Zheludev, N. I. Optical Super-oscillations: Sub-wavelength Light Focusing and Super-resolution Imaging. *J. Opt.* **2013**, *15*, 094008.
265. Williams, D. B.; Carter, C. B. *Transmission Electron Microscopy: A Textbook for Materials Science*. 2nd ed.; Springer Science + Business Media, LLC: New York, 2009; Vol. 1.
266. Azizi, A.; Zou, X.; Ercius, P.; Zhang, Z.; Elias, A. L.; Perea-Lopez, N.; Stone, G.; Terrones, M.; Yakobson, B. I.; Alem, N. Dislocation Motion and Grain Boundary Migration in Two-dimensional Tungsten Disulphide. *Nat. Commun.* **2014**, *5*, 4867.
267. Vanacore, G. M.; Fitzpatrick, A. W. P.; Zewail, A. H. Four-dimensional Electron Microscopy: Ultrafast Imaging, Diffraction and Spectroscopy in Materials Science and Biology. *Nano Today* **2016**, *11*, 228-249.
268. Barwick, B.; Zewail, A. H. Photonics and Plasmonics in 4D Ultrafast Electron Microscopy. *ACS Photonics* **2015**, 150924080031000.
269. Shorokhov, D.; Zewail, A. H. Perspective: 4D Ultrafast Electron Microscopy - Evolutions and Revolutions. *J. Chem. Phys.* **2016**, *144*, 080901.
270. Zewail, A. H. The New Age of Structural Dynamics. *Acta. Crystallogr. A.* **2010**, *66*, 135-136.
271. Zewail, A. H. Micrographia of the Twenty-first Century: From Camera Obscura to 4D Microscopy. *Philos. Trans. R. Soc., A* **2010**, *368*, 1191-1204.
272. Zewail, A. H. Filming the Invisible in 4-D. *Sci. Am.* **2010**, *303*, 74-81.
273. Zewail, A. H. Four-Dimensional Electron Microscopy. *Science* **2010**, *328*, 187-193.
274. Zewail, A. H. Ultrafast Light and Electrons: Imaging the Invisible. In *Optics in Our Time*, Al-Amri, M. D.; El-Gomati, M.; Zubairy, M. S., Eds. Springer International Publishing: Cham, 2016; pp 43-68.
275. Adhikari, A.; Eliason, J. K.; Sun, J.; Bose, R.; Flannigan, D. J.; Mohammed, O. F. Four-dimensional Ultrafast Electron Microscopy: Insights into an Emerging Technique. *ACS Appl. Mater. Interfaces* **2017**, *9*, 3-16.
276. Plemmons, D. A.; Flannigan, D. J. Ultrafast Electron Microscopy: Instrument Response from the Single-electron to High Bunch-charge Regimes. *Chem. Phys. Lett.* **2017**, 10.1016/j.cplett.2017.1001.1055 (in press).
277. King, W. E.; Campbell, G. H.; Frank, A.; Reed, B.; Schmerge, J. F.; Siwick, B. J.; Stuart, B. C.; Weber, P. M. Ultrafast Electron Microscopy in Materials Science, Biology, and Chemistry. *J. Appl. Phys.* **2005**, *97*, 111101.
278. Armstrong, M. R.; Boyden, K.; Browning, N. D.; Campbell, G. H.; Colvin, J. D.; DeHope, W. J.; Frank, A. M.; Gibson, D. J.; Hartemann, F.; Kim, J. S.; King, W. E.; LaGrange, T. B.; Pyke, B. J.; Reed, B. W.; Shuttlesworth, R. M.; Stuart, B. C.; Torralva, B. R. Practical Considerations for High Spatial and Temporal Resolution Dynamic Transmission Electron Microscopy. *Ultramicroscopy* **2007**, *107*, 356-367.

279. van der Veen, R. M.; Kwon, O.-H.; Tissot, A.; Hauser, A.; Zewail, A. H. Single-nanoparticle Phase Transitions Visualized by Four-dimensional Electron Microscopy. *Nat. Chem.* **2013**, *5*, 395-402.
280. Grinolds, M. S.; Lobastov, V. A.; Weissenrieder, J.; Zewail, A. H. Four-dimensional Ultrafast Electron Microscopy of Phase Transitions. *Proc. Natl. Aacd. Sci. U. S. A.* **2006**, *103*, 18427-18431.
281. Kwon, O.-H.; Ortalan, V.; Zewail, A. H. Macromolecular Structural Dynamics Visualized by Pulsed Dose Control in 4D Electron Microscopy. *Proc. Natl. Acad. Sci. U. S. A.* **2011**, *108*, 6026-6031.
282. Park, S. T.; Flannigan, D. J.; Zewail, A. H. 4D Electron Microscopy Visualization of Anisotropic Atomic Motions in Carbon Nanotubes. *J. Am. Chem. Soc.* **2012**, *134*, 9146-9149.
283. Vanacore, G. M.; van der Veen, R. M.; Zewail, A. H. Origin of Axial and Radial Expansion in Carbon Nanotubes Revealed by Ultrafast Diffraction and Spectroscopy. *ACS Nano* **2015**.
284. Flannigan, D. J.; Cremons, D. R.; Valley, D. T. Multimodal Visualization of the Optomechanical Response of Silicon Cantilevers with Ultrafast Electron Microscopy. *J. Mater. Res.* **2017**, *32*, 239-247.
285. McKenna, A. J.; Eliason, J. K.; Flannigan, D. J. In *Imaging Photoinduced Structural and Morphological Dynamics of a Single MoS_2 Flake With Ultrafast Electron Microscopy*, Microsc. Microanal., Columbus Ohio, Columbus Ohio, 2016; pp 1662-1663.
286. McKenna, A. J.; Eliason, J. K.; Flannigan, D. J. Spatiotemporal Evolution of Coherent Elastic Strain Waves in a Single MoS_2 Flake. *Nano Lett.* 10.1021/acs.nanolett.1027b01565 (in press).
287. Valley, D. T.; Ferry, V. E. F., D. J. Imaging Intra- and Interparticle Acousto-plasmonic Vibrational Dynamics with Ultrafast Electron Microscopy. *Nano Lett.* **2016**, *16*, 7302-7308.
288. Kwon, O.-H.; Zewail, A. H. 4D Electron Tomography. *Science* **2010**, *328*, 1668-1673.
289. Su, D. S. Electron Tomography: From 3D Statics to 4D Dynamics. *Angew. Chem., Int. Ed.* **2010**, *49*, 9569-9571.
290. Kwon, O. H.; Park, H. S.; Baskin, J. S.; Zewail, A. H. Nonchaotic Nonlinear Motion Visualized in Complex Nanostructures by Stereographic 4D Electron Microscopy. *Nano Lett.* **2010**, *10*, 3190-3198.
291. Carbone, F.; Kwon, O. H.; Zewail, A. H. Dynamics of Chemical Bonding Mapped by Energy-resolved 4D Electron Microscopy. *Science* **2009**, *325*, 181-184.
292. Carbone, F.; Barwick, B.; Kwon, O.-H.; Park, H. S.; Spencer Baskin, J.; Zewail, A. H. EELS Femtosecond Resolved in 4D Ultrafast Electron Microscopy. *Chem. Phys. Lett.* **2009**, *468*, 107-111.
293. van der Veen, R. M.; Penfold, T. J.; Zewail, A. H. Ultrafast Core-loss

Spectroscopy in Four-dimensional Electron Microscopy. *Struct. Dyn.* **2015**, *2*, 024302.

294. Barwick, B.; Flannigan, D. J.; Zewail, A. H. Photon-induced Near-field Electron Microscopy. *Nature* **2009**, *462*, 902-906.
295. Park, S. T.; Lin, M.; Zewail, A. H. Photon-induced Near-field Electron Microscopy (PINEM): Theoretical and Experimental. *New J. Phys.* **2010**, *12*, 123028.
296. Park, S. T.; Zewail, A. H. Relativistic Effects in Photon-induced Near Field Electron Microscopy. *J. Phys. Chem. A* **2012**, *116*, 11128-11133.
297. Plemmons, D. A.; Tae Park, S.; Zewail, A. H.; Flannigan, D. J. Characterization of Fast Photoelectron Packets in Weak and Strong Laser Fields in Ultrafast Electron Microscopy. *Ultramicroscopy* **2014**, *146*, 97-102.
298. Yurtsever, A.; Baskin, J. S.; Zewail, A. H. Entangled Nanoparticles: Discovery by Visualization in 4D Electron Microscopy. *Nano Lett.* **2012**, *12*, 5027-5032.
299. Yurtsever, A.; Zewail, A. H. Direct Visualization of Near-fields in Nanoplasmonics and Nanophotonics. *Nano Lett.* **2012**, *12*, 3334-3338.
300. Feist, A.; Echternkamp, K. E.; Schauss, J.; Yalunin, S. V.; Schäfer, S.; Ropers, C. Quantum Coherent Optical Phase Modulation in an Ultrafast Transmission Electron Microscope. *Nature* **2015**, *521*, 200-203.
301. Nikolova, L.; LaGrange, T.; Reed, B. W.; Stern, M. J.; Browning, N. D.; Campbell, G. H.; Kieffer, J. C.; Siwick, B. J.; Rosei, F. Nanocrystallization of Amorphous Germanium Films Observed with Nanosecond Temporal Resolution. *Appl. Phys. Lett.* **2010**, *97*, 203102.
302. Nikolova, L.; LaGrange, T.; Stern, M. J.; MacLeod, J. M.; Reed, B. W.; Ibrahim, H.; Campbell, G. H.; Rosei, F.; Siwick, B. J. Complex Crystallization Dynamics in Amorphous Germanium Observed with Dynamic Transmission Electron Microscopy. *Phys. Rev. B* **2013**, *87*, 064105.
303. Nikolova, L.; Stern, M. J.; MacLeod, J. M.; Reed, B. W.; Ibrahim, H.; Campbell, G. H.; Rosei, F.; LaGrange, T.; Siwick, B. J. In Situ Investigation of Explosive Crystallization in a-Ge: Experimental Determination of the Interface Response Function Using Dynamic Transmission Electron Microscopy. *J. Appl. Phys.* **2014**, *116*, 093512.
304. King, W. E.; Armstrong, M. R.; Bostanjoglo, O.; Reed, B. W. High-Speed Electron Microscopy. In *Science of Microscopy*, Hawkes, P. W.; Spence, J. C. H., Eds. Springer: New York, 2007; Vol. 1, pp 406-444.
305. LaGrange, T.; Reed, B. W.; King, W. E.; Kim, J. S.; Campbell, G. H. Dynamic Transmission Electron Microscopy. In *In-Situ Electron Microscopy: Applications in Physics, Chemistry and Materials Science*, Dehm, G.; Howe, J. M.; Zweck, J., Eds. Wiley-VCH Verlag GmbH & Co. KGaA: Weinheim, Germany, 2012; pp 71-97.
306. LaGrange, T.; Campbell, G. H.; Reed, B. W.; Taheri, M.; Pesavento, J. B.; Kim, J. S.; Browning, N. D. Nanosecond Time-resolved Investigations Using the In

Situ of Dynamic Transmission Electron Microscope (DTEM). *Ultramicroscopy* **2008**, *108*, 1441-1449.

307. LaGrange, T.; Reed, B. W.; DeHope, W.; Shuttlesworth, R.; Huete, G. In *Movie Mode Dynamic Transmission Electron Microscopy (DTEM): Multiple Frame Movies of Transient States in Materials with Nanosecond Time Resolution*, Microsc. Microanal., Nashville, Tennessee, Nashville, Tennessee, 2011.
308. Yang, D.-S.; Mohammed, O. F.; Zewail, A. H. Scanning Ultrafast Electron Microscopy. *Proc. Natl. Acad. Sci. U. S. A.* **2010**, *107*, 14993-14998.
309. Mohammed, O. F.; Yang, D. S.; Pal, S. K.; Zewail, A. H. 4D Scanning Ultrafast Electron Microscopy: Visualization of Materials Surface Dynamics. *J. Am. Chem. Soc.* **2011**, *133*, 7708-7711.
310. Yang, D.-S.; Mohammed, O. F.; Zewail, A. H. Environmental Scanning Ultrafast Electron Microscopy: Structural Dynamics of Solvation at Interfaces. *Angew. Chem., Int. Ed.* **2013**, *52*, 2897-2901.
311. Cho, J.; Hwang, T. Y.; Zewail, A. H. Visualization of Carrier Dynamics in p(n)-type GaAs by Scanning Ultrafast Electron Microscopy. *Proc. Natl. Aacd. Sci. U. S. A.* **2014**, *111*, 2094-2099.
312. Najafi, E.; Scarborough, T. D.; Tang, J.; Zewail, A. H. Four-dimensional Imaging of Carrier Interface Dynamics in p-n Junctions. *Science* **2015**, *347*, 164-167.
313. Sun, J.; Melnikov, V. A.; Khan, J. I.; Mohammed, O. F. Real-space Imaging of Carrier Dynamics of Materials Surfaces by Second-generation Four-dimensional Scanning Ultrafast Electron Microscopy. *J. Phys. Chem. Lett.* **2015**, *6*, 3884-3890.
314. Sun, J.; Adhikari, A.; Shaheen, B. S.; Yang, H.; Mohammed, O. F. Mapping Carrier Dynamics on Material Surfaces in Space and Time Using Scanning Ultrafast Electron Microscopy. *J. Phys. Chem. Lett.* **2016**, *7*, 985-994.
315. Khan, J. I.; Adhikari, A.; Sun, J.; Priante, D.; Bose, R.; Shaheen, B. S.; Ng, T. K.; Zhao, C.; Bakr, O. M.; Ooi, B. S.; Mohammed, O. F. Enhanced Optoelectronic Performance of a Passivated Nanowire-based Device: Key Information from Real-Space Imaging Using 4D Electron Microscopy. *Small* **2016**, *12*, 2313-2320.
316. Bose, R.; Sun, J.; Khan, J. I.; Shaheen, B. S.; Adhikari, A.; Ng, T. K.; Burlakov, V. M.; Parida, M. R.; Priante, D.; Goriely, A.; Ooi, B. S.; Bakr, O. M.; Mohammed, O. F. Real-space Visualization of Energy Loss and Carrier Diffusion in a Semiconductor Nanowire Array Using 4D Electron Microscopy. *Adv. Mater.* **2016**, *28*, 5106-5111.
317. Bose, R.; Bera, A.; Parida, M. R.; Adhikari, A.; Shaheen, B. S.; Alarousu, E.; Sun, J.; Wu, T.; Bakr, O. M.; Mohammed, O. F. Real-space Mapping of Surface Trap States in CIGSe Nanocrystals Using 4D Electron Microscopy. *Nano Lett.* **2016**, *16*, 4417-4423.
318. Lahme, S.; Kealhofer, C.; Krausz, F.; Baum, P. Femtosecond Single-electron Diffraction. *Struct. Dyn.* **2014**, *1*, 034303.
319. Weathersby, S. P.; Brown, G.; Centurion, M.; Chase, T. F.; Coffee, R.; Corbett, J.; Eichner, J. P.; Frisch, J. C.; Fry, A. R.; Guhr, M.; Hartmann, N.; Hast, C.;

Hettel, R.; Jobe, R. K.; Jongewaard, E. N.; Lewandowski, J. R.; Li, R. K.; Lindenberg, A. M.; Makasyuk, I.; May, J. E.; McCormick, D.; Nguyen, M. N.; Reid, A. H.; Shen, X.; Sokolowski-Tinten, K.; Vecchione, T.; Vetter, S. L.; Wu, J.; Yang, J.; Durr, H. A.; Wang, X. J. Mega-electron-volt Ultrafast Electron Diffraction at SLAC National Accelerator Laboratory. *Rev. Sci. Instrum.* **2015**, *86*, 073702.

320. van Oudheusden, T.; de Jong, E. F.; van der Geer, S. B.; 't Root, W. P. E. M. O.; Luiten, O. J.; Siwick, B. J. Electron Source Concept for Single-shot Sub-100 fs Electron Diffraction in the 100 keV Range. *J. Appl. Phys.* **2007**, *102*, 093501.
321. van Oudheusden, T.; Pasmans, P. L.; van der Geer, S. B.; de Loos, M. J.; van der Wiel, M. J.; Luiten, O. J. Compression of Subrelativistic Space-charge-dominated Electron Bunches for Single-shot Femtosecond Electron Diffraction. *Phys. Rev. Lett.* **2010**, *105*, 264801.
322. Chatelain, R. P.; Morrison, V. R.; Godbout, C.; Siwick, B. J. Ultrafast Electron Diffraction with Radio-frequency Compressed Electron Pulses. *Appl. Phys. Lett.* **2012**, *101*, 081901.
323. Han, J.-H. Production of a Sub-10 fs Electron Beam with 10^7 Electrons. *Phys. Rev. Spec. Top. - Accel. Beams* **2011**, *14*, 050101.
324. Li, R. K.; Musumeci, P.; Bender, H. A.; Wilcox, N. S.; Wu, M. Imaging Single Electrons to Enable the Generation of Ultrashort Beams for Single-shot Femtosecond Relativistic Electron Diffraction. *J. Appl. Phys.* **2011**, *110*, 074512.
325. Chatelain, R. P.; Morrison, V. R.; Klarenaar, B. L.; Siwick, B. J. Coherent and Incoherent Electron-phonon Coupling in Graphite Observed with Radio-frequency Compressed Ultrafast Electron Diffraction. *Phys. Rev. Lett.* **2014**, *113*, 235502.
326. Chase, T.; Trigo, M.; Reid, A. H.; Li, R.; Vecchione, T.; Shen, X.; Weathersby, S.; Coffee, R.; Hartmann, N.; Reis, D. A.; Wang, X. J.; Dürr, H. A. Ultrafast Electron Diffraction from Non-equilibrium Phonons in Femtosecond Laser Heated Au Films. *Appl. Phys. Lett.* **2016**, *108*, 041909.
327. Bostanjoglo, O. Multiple Phase Transitions in GeTe Films: Dynamics and Film Structure. *Phys. Status Solidi A* **1983**, *76*, 525-531.
328. Bostanjoglo, O.; Endruschat, F. E.; Tornow, W. Time Resolved TEM of Laser-Induced Phase Transitions in a-Ge and a-Si/Al-Films. *Mater. Res. Soc. Symp. Proc.* **1986**, *71*, 345-350.
329. Bostanjoglo, O.; Heinricht, F. A Reflection Electron Microscope for Imaging of Fast Phase Transitions on Surfaces. *Rev. Sci. Instrum.* **1990**, *61*, 1223-1229.
330. Bostanjoglo, O.; Hořinek, W. R. Pulsed TEM-A New Method to Detect Transient Structures in Fast Phase Transitions. *Optik* **1983**, *65*, 361-367.
331. Bostanjoglo, O.; Kornitzky, J.; Tornow, R. P. Nanosecond Double-frame Electron Microscopy of Fast Phase Transitions. *J. Phys. E: Sci. Instrum.* **1989**, *22*, 1008-1011.
332. Bostanjoglo, O.; Liedtke, R. Tracing Fast Phase Transitions by Electron

Microscopy. *Phys. Status Solidi A* **1980**, *60*, 451-455.
333. Bostanjoglo, O.; Penschke, V. Kinetics of Laser-Induced Phase Transitions in Ni-Al Alloys. *J. Appl. Phys.* **1993**, *73*, 8201-8205.
334. Bostanjoglo, O.; Thomsen-Schmidt, P. Laser-Induced Multiple Phase Transitions in Ge-Te Films Traced by Time-Resolved TEM. *Appl. Surf. Sci.* **1989**, *43*, 136-141.
335. Browning, N. D. Electron Microscopy: Phase Transition Singled Out. *Nat. Chem.* **2013**, *5*, 363-364.
336. Park, H. S.; Kwon, O.-H.; Baskin, J. S.; Barwick, B.; Zewail, A. H. Direct Observation of Martensitic Phase-Transformation Dynamics in Iron by 4D Single-Pulse Electron Microscopy. *Nano Lett.* **2009**, *9*, 3954-3962.
337. Morrison, V. R.; Chatelain, R. P.; Tiwari, K. L.; Hendaoui, A.; Bruhács, A.; Chaker, M.; Siwick, B. J. A Photoinduced Metal-like Phase Monoclinc VO_2 Revealed by Ultrafast Electron Diffraction. *Science* **2014**, *346*, 445-448.
338. Siwick, B. J.; Dwyer, J. R.; Jordan, R. E.; Miller, R. J. D. Femtosecond Electron Diffraction Studies of Strongly Driven Structural Phase Transitions. *Chem. Phys.* **2004**, *299*, 285-305.
339. Harb, M.; Ernstorfer, R.; Dartigalongue, T.; Hebeisen, C. T.; Jordan, R. E.; Miller, R. J. D. Carrier Relaxation and Lattice Heating Dynamics in Silicon Revealed by Femtosecond Electron Diffraction. *J. Phys. Chem. B* **2006**, *110*, 23508-25313.
340. Yang, J.; Beck, J.; Uiterwaal, C. J.; Centurion, M. Imaging of Alignment and Structural Changes of Carbon Disulfide Molecules Using Ultrafast Electron Diffraction. *Nat. Commun.* **2015**, *6*, 8172.
341. Paschotta, R. Pulse Pickers. https://www.rp-photonics.com/pulse_pickers.html (accessed January 27, 2017).
342. Lobastov, V. A.; Srinivasan, R.; Zewail, A. H. Four-dimensional Ultrafast Electron Microscopy. *Proc. Natl. Acad. Sci. U. S. A.* **2005**, *102*, 7069-7073.
343. Barwick, B.; Park, H. S.; Kwon, O. H.; Baskin, J. S.; Zewail, A. H. 4D Imaging of Transient Structures and Morphologies in Ultrafast Electron Microscopy. *Science* **2008**, *322*, 1227-1231.
344. Lehmann, M.; Lichte, H., Electron Waves, Interference, & Coherence. In *Transmission Electron Microscopy: Diffraction, Imaging, and Spectrometry*, Carter, C. B.; Williams, D. B., Eds. Springer International Publishing: Switzerland, 2016; pp 197-214.
345. Williams, D. B.; Carter, C. B. *Transmission Electron Microscopy: A Textbook for Materials Science*. 2 ed.; Springer Science+Business Media, LLC: New York, 2009; Vol. 3.
346. Zhang, H. R.; Egerton, R. F.; Malac, M. Local Thickness Measurement through Scattering Contrast and Electron Energy-loss Spectroscopy. *Micron* **2012**, *43*, 8-15.
347. Malis, T.; Cheng, S. C.; Egerton, R. F. EELS Log-ratio Technique for Specimen-

thickness Measurement in the TEM. *J. Electron Microsc. Tech.* **1988**, *8*, 193-200.
348. Iakoubovskii, K.; Mitsuishi, K.; Nakayama, Y.; Furuya, K. Thickness Measurements with Electron Energy Loss Spectroscopy. *Microsc. Res. Tech.* **2008**, *71*, 626-631.
349. Johannes Schindelin, I. A.-C., Erwin Frise, Verena Kaynig, Mark Longair, Tobias Pietzsch, Stephan Preibisch, Curtis Rueden, Stephan Saalfeld, Benjamin Schmid, Jean-Yves Tinevez, Daniel James White, Volker Hartenstein, Kevin Eliceiri, Pavel Tomancak, Albert Cardona Fiji: An Open-source Platform for Biological-image Analysis. *Nat. Methods* **2012**, *9*, 676-682.
350. Robert Fisher, S. P., Ashley Walker, Erik Wolfart Contrast Stretching. http://homepages.inf.ed.ac.uk/rbf/HIPR2/stretch.htm#1) (accessed March 19, 2017).
351. Miró, P.; Ghorbani-Asl, M.; Heine, T. Spontaneous Ripple Formation in MoS_2 Monolayers: Electronic Structure and Transport Effects. *Adv. Mater.* **2013**, *25*, 5473-5475.
352. Rice, C.; Young, R.; Zan, R.; Bangert, U.; Wolverson, D.; Georgiou, T.; Jalil, R.; Novoselov, K. Raman-scattering Measurements and First-principles Calculations of Strain-induced Phonon Shifts in Monolayer MoS_2. *Phys. Rev. B* **2013**, *87*, 081307(R).
353. van der Zande, A. M.; Kunstmann, J.; Chernikov, A.; Chenet, D. A.; You, Y.; Zhang, X.; Huang, P. Y.; Berkelbach, T. C.; Wang, L.; Zhang, F.; Hybertsen, M. S.; Muller, D. A.; Reichman, D. R.; Heinz, T. F.; Hone, J. C. Tailoring the Electronic Structure in Bilayer Molybdenum Disulfide via Interlayer Twist. *Nano Lett.* **2014**, *14*, 3869-3875.
354. Qin, C.; Gao, Y.; Qiao, Z.; Xiao, L.; Jia, S. Atomic-Layered MoS_2 as a Tunable Optical Platform. *Adv. Opt. Mater.* **2016**, *4*, 1429-1456.
355. Akinwande, D.; Brennan, C. J.; Bunch, J. S.; Egberts, P.; Felts, J. R.; Gao, H.; Huang, R.; Kim, J.-S.; Li, T.; Li, Y.; Liechti, K. M.; Lu, N.; Park, H. S.; Reed, E. J.; Wang, P.; Yakobson, B. I.; Zhang, T.; Zhang, Y.-W.; Zhou, Y.; Zhu, Y. A Review on Mechanics and Mechanical Properties of 2D Materials — Graphene and Beyond. *Extreme Mech. Lett.* **2017**, *13*, 42-77.
356. Shi, H.; Pan, H.; Zhang, Y.-W.; Yakobson, B. I. Quasiparticle band structures and optical properties of strained monolayer MoS_2 and WS_2. *Phys. Rev. B* **2013**, *87*, 155304.
357. He, K.; Poole, C.; Mak, K. F.; Shan, J. Experimental Demonstration of Continuous Electronic Structure Tuning via Strain in Atomically Thin MoS_2. *Nano Lett.* **2013**, *13*, 2931-2936.
358. Wang, Y.; Cong, C.; Qiu, C.; Yu, T. Raman Spectroscopy Study of Lattice Vibration and Crystallographic Orientation of Monolayer MoS_2 under Uniaxial Strain. *Small* **2013**, *9*, 2857-2861.
359. Ding, Z.; Pei, Q.-X.; Jiang, J.-W.; Zhang, Y.-W. Manipulating the Thermal Conductivity of Monolayer MoS_2 via Lattice Defect and Strain Engineering. *J.*

Phys. Chem. C **2015**, *119*, 16358-16365.

360. Nayak, A. P.; Pandey, T.; Voiry, D.; Liu, J.; Moran, S. T.; Sharma, A.; Tan, C.; Chen, C.-H.; Li, L.-J.; Chhowalla, M.; Lin, J.-F.; Singh, A. K.; Akinwande, D. Pressure-dependent Optical and Vibrational Properties of Monolayer Molybdenum Disulfide. *Nano Lett.* **2015**, *15*, 346-353.
361. Shin, B. G.; Han, G. H.; Yun, S. J.; Oh, H. M.; Bae, J. J.; Song, Y. J.; Park, C.-Y.; Lee, Y. H. Indirect Bandgap Puddles in Monolayer MoS_2 by Substrate-induced Local Strain. *Adv. Mater.* **2016**, *28*, 9378-9384.
362. Cai, Y.; Lan, J.; Zhang, G.; Zhang, Y.-W. Lattice Vibrational Modes and Phonon Thermal Conductivity of Monolayer MoS_2. *Phys. Rev. B* **2014**, *89*, 035438.
363. Ding, Y.; Xiao, B. Thermal Expansion Tensors, Gruneisen Parameters and Phonon Velocities of Bulk MT_2 (M = W and Mo; T = S and Se) from First Principles Calculations. *RSC Adv.* **2015**, *5*, 18391-18400.
364. Xiaoming, F.; Farhad, K.; Vahid, R.; Mariyappan, S.; Masoud, L.; Jacek, J.; Robert, W. C.; Eugene, T.; Balaji, P. MoS_2 Actuators: Reversible Mechanical Responses of MoS_2 - Polymer Nanocomposites to Photons. *Nanotechnol.* **2015**, *26*, 261001.
365. Lagarde, D.; Bouet, L.; Marie, X.; Zhu, C. R.; Liu, B. L.; Amand, T.; Tan, P. H.; Urbaszek, B. Carrier and Polarization Dynamics in Monolayer MoS_2. *Phys. Rev. Lett.* **2014**, *112*, 047401.
366. Wang, H.; Zhang, C.; Rana, F. Ultrafast Dynamics of Defect-assisted Electron-hole Recombination in Monolayer MoS_2. *Nano Lett.* **2015**, *15*, 339-345.
367. Grubišić Čabo, A.; Miwa, J. A.; Grønborg, S. S.; Riley, J. M.; Johannsen, J. C.; Cacho, C.; Alexander, O.; Chapman, R. T.; Springate, E.; Grioni, M.; Lauritsen, J. V.; King, P. D. C.; Hofmann, P.; Ulstrup, S. Observation of Ultrafast Free Carrier Dynamics in Single Layer MoS_2. *Nano Lett.* **2015**, *15*, 5883-5887.
368. Czech, K. J.; Thompson, B. J.; Kain, S.; Ding, Q.; Shearer, M. J.; Hamers, R. J.; Jin, S.; Wright, J. C. Measurement of Ultrafast Excitonic Dynamics of Few-Layer MoS_2 Using State-Selective Coherent Multidimensional Spectroscopy. *ACS Nano* **2015**, *9*, 12146-12157.
369. Wang, H.; Zhang, C.; Rana, F. Surface Recombination Limited Lifetimes of Photoexcited Carriers in Few-Layer Transition Metal Dichalcogenide MoS_2. *Nano Lett.* **2015**, *15*, 8204-8210.
370. Ceballos, F.; Zhao, H. Ultrafast Laser Spectroscopy of Two-dimensional Materials beyond Graphene. *Adv. Funct. Mater.* **2016**, *1604509*, 10.1002/adfm.201604509.
371. Plechinger, G.; Heydrich, S.; Eroms, J.; Weiss, D.; Schüller, C.; Korn, T. Raman Spectroscopy of the Interlayer Shear Mode in Few-layer MoS_2 Flakes. *Appl. Phys. Lett.* **2012**, *101*, 101906.
372. Zeng, H.; Zhu, B.; Liu, K.; Fan, J.; Cui, X.; Zhang, Q. M. Low-frequency Raman modes and electronic excitations in atomically thin MoS_2 films. *Phys. Rev. B* **2012**, *86*, 241301.

373. Zhao, Y.; Luo, X.; Li, H.; Zhang, J.; Araujo, P. T.; Gan, C. K.; Wu, J.; Zhang, H.; Quek, S. Y.; Dresselhaus, M. S.; Xiong, Q. Interlayer Breathing and Shear Modes in Few-trilayer MoS_2 and WSe_2. *Nano Lett.* **2013**, *13*, 1007-1015.
374. Huang, S.; Liang, L.; Ling, X.; Puretzky, A. A.; Geohegan, D. B.; Sumpter, B. G.; Kong, J.; Meunier, V.; Dresselhaus, M. S. Low-Frequency Interlayer Raman Modes to Probe Interface of Twisted Bilayer MoS_2. *Nano Lett.* **2016**, *16*, 1435-1444.
375. Flannigan, D. J.; Samartzis, P. C.; Yurtsever, A.; Zewail, A. H. Nanomechanical Motions of Cantilevers: Direct Imaging in Real Space and Time with 4D Electron Microscopy. *Nano Lett.* **2009**, *9*, 875-881.
376. Bugayev, A.; Esmail, A.; Abdel-Fattah, M.; Elsayed-Ali, H. E. Coherent Phonons in Bismuth Film Observed by Ultrafast Electron Diffraction. *AIP Adv.* **2011**, *1*, 012117.
377. Vanacore, G. M.; Hu, J.; Liang, W.; Bietti, S.; Sanguinetti, S.; Zewail, A. H. Diffraction of Quantum Dots Reveals Nanoscale Ultrafast Energy Localization. *Nano Lett.* **2014**, *14*, 6148-6154.
378. Eichberger, M.; Schafer, H.; Krumova, M.; Beyer, M.; Demsar, J.; Berger, H.; Moriena, G.; Sciaini, G.; Miller, R. J. D. Snapshots of Cooperative Atomic Motions in the Optical Suppression of Charge Density Waves. *Nature* **2010**, *468*, 799-802.
379. Zhu, P. F.; Cao, J.; Zhu, Y.; Geck, J.; Hidaka, Y.; Pjerov, S.; Ritschel, T.; Berger, H.; Shen, Y.; Tobey, R.; Hill, J. P.; Wang, X. J. Dynamic Separation of Electron Excitation and Lattice Heating during the Photoinduced Melting of the Periodic Lattice Distortion in 2H-$TaSe_2$. *Appl. Phys. Lett.* **2013**, *103*, 071914.
380. Sun, S. S.; Wei, L. L.; Li, Z. W.; Cao, G. L.; Liu, Y.; Lu, W. J.; Sun, Y. P.; Tian, H. F.; Yang, H. X.; Li, J. Q. Direct Observation of an Optically Induced Charge Density Wave Transition in 1*T*-$TaSe_2$. *Phys. Rev. B* **2015**, *92*, 224303.
381. Laulhe, C.; Cario, L.; Corraze, B.; Janod, E.; Huber, T.; Lantz, G.; Boulfaat, S.; Ferrer, A.; Mariager, S. O.; Johnson, J. A.; Grubel, S.; Lubcke, A.; Ingold, G.; Beaud, P.; Johnson, S. L.; Ravy, S. X-Ray Study of Femtosecond Structural Dynamics in the 2D Charge Density Wave Compound 1T-TaS_2. *Phys. B* **2015**, *460*, 100-104.
382. Olaoye, O.; Erasmus, N.; Haupt, K.; Schwoerer, H. Femtosecond Dynamics of Decoupled Superlattice Zones in $4H_b$–$TaSe_2$ Single Crystals. *J. Phys. B* **2016**, *49*, 064011.
383. Wei, L.; Sun, S.; Guo, C.; Li, Z.; Sun, K.; Liu, Y.; Lu, W.; Sun, Y.; Tian, H.; Yang, H.; Li, J. Dynamic Diffraction Effects and Coherent Breathing Oscillations in Ultrafast Electron Diffraction in Layered 1T-TaSeTe. *Struct. Dyn.* **2017**, *4*, 044012.
384. Waldecker, L.; Bertoni, R.; Hübener, H.; Brumme, T.; Vasileiadis, T.; Zahn, D.; Rubio, A.; Ernstorfer, R. A Momentum-Resolved View on Electron-Phonon Coupling in Multilayer WSe_2. **2017**, arXiv:1703.03496.

385. Nayfeh, A. H. *Wave Propagation in Layered Anisotropic Media with Applications to Composites*. Elsevier Science B. V.: Amsterdam, 1995; Vol. 39, p 332.
386. Achenbach, J. D. *Wave Propagation in Elastic Solids*. North-Holland Publishing Company: Amsterdam, 1973; Vol. 16, p 425.
387. Susan E. Burrows, B. D., and Steve Dixon Laser Generation of Lamb Waves for Defect Detection: Experimental Methods and Finite Element Modeling. *IEEE Trans. Sonics Ultrason.* **2012**, *59*, 82-89.
388. Kessler, S. S.; Spearing, S. M.; Soutis, C. Damage Detection in Composite Materials Using Lamb Wave Methods. *Smart Mater. Struct.* **2002**, *11*, 269-278.
389. Burrows, S. E.; Rashed, A.; Almond, D. P.; Dixon, S. Combined Laser Spot Imaging Thermography and Ultrasonic Measurements for Crack Detection. *Nondestr. Test. Eval.* **2007**, *22*, 217-227.
390. Bernstein, J. R.; Spicer, J. B. Hybrid Laser/Broadband EMAT Ultrasonic System for Characterizing Cracks in Metals. *J. Acoust. Soc. Am.* **2002**, *111*, 1685-1691.
391. Broda, D.; Staszewski, W. J.; Martowicz, A.; Uhl, T.; Silberschmidt, V. V. Modelling of Nonlinear Crack-wave Interactions for Damage Detection Based on Ultrasound - A Review. *J. Sound Vib.* **2014**, *333*, 1097-1118.
392. Quaegebeur, N.; Bouslama, N.; Bilodeau, M.; Masson, P.; Maslouhi, A.; Micheau, P. In *Guided Wave Scattering by a Geometrical or Damage Feature: Application to Fatigue Crack and Machined Notch*, SPIE Health Monitoring of Structural and Biological Systems, Portland, Oregon, April 5, 2017; Kundu, T., Ed. Portland, Oregon, 2017.
393. Canle, D. V.; Salmi, A.; Hæggström, E. In *Flaw Detection in Rotating Structures by Lamb Waves*, IEEE International Ultrasonics Symposium (IUS), Tours, France, Tours, France, 2016; pp 1-3.
394. Chimenti, D. E. Guided Waves in Plates and Their Use in Materials Characterization. *Appl. Mech. Rev.* **1997**, *50*, 247-284.
395. Hess, P. Surface Acoustic Waves in Materials Science. *Phys. Today* **2002**, *55*, 42-47.
396. Lamb, H. On Waves in an Elastic Plate. *Proc. R. Soc. A* **1917**, *93*, 114-128.
397. Cheng, J.-C.; Berthelot, Y. H. Theory of Laser-generated Transient Lamb Waves in Orthotropic Plates. *J. Phys. D: Appl. Phys.* **1996**, *29*, 1857-1867.
398. Cheeke, J. D. N., Fundamentals and Applications of Ultrasonic Waves. CRC Press: Baton Rouge, USA, 2012. (accessed April 19, 2017).
399. Wang, L.; Yuan, F. G. Group Velocity and Characteristic Wave Curves of Lamb Waves in Composites: Modeling and Experiments. *Compos. Sci. Technol.* **2007**, *67*, 1370-1384.
400. Beal, A. R.; Hughes, H. P. Kramers-Kronig Analysis of the Reflectivity Spectra of 2H-MoS_2, 2H-$MoSe_2$, and 2H-$MoTe_2$. *J. Phys. C: Solid State Phys.* **1979**, *12*, 881-890.
401. Royer, D.; Dieulesaint, E. Rayleigh Wave Velocity and Displacement in Orthorhombic, Tetragonal, Hexagonal, and Cubic Crystals. *J. Acoust. Soc. Am.*

1984, *76*, 1438-1444.
402. Rogers, W. P. Elastic Property Measurement Using Rayleigh-Lamb Waves. *Res. Nondestr. Eval.* **1995**, *6*, 185-208.
403. Williams, D. B.; Carter, C. B. Transmission Electron Microscopy: A Textbook for Materials Science. In *Part 1: The Basics*, Springer Science+Business Media: New York, 2009; Vol. 1, pp 167-168.
404. Reimer, L.; Kohl, H. *Transmission Electron Microscopy: Physics of Image Formation*. 5 ed.; Springer Science+Business Media, LLC: New York, 2008; p 587.
405. Head, A. K.; Humble, P.; Clarebrough, L. M.; Morton, A. J.; Forwood, C. T. *Computed Electron Micrographs and Defect Identification*. North-Holland Publishing Compnay: Amsterdam, 1973; Vol. 7, p 400.
406. Fultz, B.; Howe, J. *Transmission Electron Microscopy and Diffractometry of Materials*. 2 ed.; Springer: Berlin, Germany, 2002; p 748.
407. Krishnaswamy, S. Theory and Applications of Laser-Ultrasonic Techniques. In *Ultrasonic Nondestructive Evaluation*, Kundu, T., Ed. CRC Press LLC: Boca Raton, FL, 2004; pp 436-493.
408. Ruello, P.; Gusev, V. E. Physical Mechanisms of Coherent Acoustic Phonons Generation by Ultrafast Laser Action. *Ultrasonics* **2015**, *56*, 21-35.
409. Volz, S.; Ordonez-Miranda, J.; Shchepetov, A.; Prunnila, M.; Ahopelto, J.; Pezeril, T.; Vaudel, G.; Gusev, V.; Ruello, P.; Weig, E. M.; Schubert, M.; Hettich, M.; Grossman, M.; Dekorsy, T.; Alzina, F.; Graczykowski, B.; Chavez-Angel, E.; Sebastian Reparaz, J.; Wagner, M. R.; Sotomayor-Torres, C. M.; Xiong, S.; Neogi, S.; Donadio, D. Nanophononics: State of the Art and Perspectives. *Eur. Phys. J. B* **2016**, *89*.
410. Chen, W.; Clerk, A. A. Electron-phonon Mediated Heat Flow in Disordered Graphene. *Phys. Rev. B* **2012**, *86*, 125443.
411. Piazza, L.; Masiel, D. J.; LaGrange, T.; Reed, B. W.; Barwick, B.; Carbone, F. Design and Implementation of a fs-resolved Transmission Electron Microscope Based on Thermionic Gun Technology. *Chem. Phys.* **2013**, *423*, 79-84.
412. Piazza, L.; Lummen, T. T. A.; Quiñonez, E.; Murooka, Y.; Reed, B. W.; Barwick, B.; Carbone, F. Simultaneous Observation of the Quantization and the Interference Pattern of a Plasmonic Near-field. *Nat. Commun.* **2015**, *6*, 6407.
413. Bücker, K.; Picher, M.; Crégut, O.; LaGrange, T.; Reed, B. W.; Park, S. T.; Masiel, D. J.; Banhart, F. Electron Beam Dynamics in an Ultrafast Transmission Electron Microscope with Wehnelt Electrode. *Ultramicroscopy* **2016**, *171*, 8-18.
414. Scoby, C. M.; Li, R. K.; Musumeci, P. Effect of an Ultrafast Laser Induced Plasma on a Relativistic Electron Beam to Determine Temporal Overlap in Pump-probe Experiments. *Ultramicroscopy* **2013**, *127*, 14-18.
415. Jason R. Dwyer, C. T. H., Ralph Ernstorfer, Maher Harb, Vatche B. Deyirmenjian, Robert E. Jordan, R. J. Dwayne Miller Femtosecond Electron Diffraction: "Making the Molecular Movie". *Philos. Trans. R. Soc., A* **2006**, *364*,

741-778.
416. Taylor, J. R. *Classical Mechanics*. University Science Books: South Orange, New Jersey, 2005.
417. Wildervanck, J. C.; Jellinek, F. Preparation and Crystallinity of Molybdenum and Tunsten Sulfides. *Z. Anorg. Allg. Chem.* **1964**, *328*, 309-318.
418. Housley, R. M.; Hess, F. Analysis of Debye-Waller-Factor and Mössbauer-Thermal-Shift Measurements. I. General Theory. *Phys. Rev.* **1966**, *146*, 517-526.
419. Levi, A. C.; Suhl, H. Quantum Theory of Atom-Surface Scattering: Debye-Waller Factor. *Surface Science* **1979**, *88*, 221-254.
420. Lipkin, H. J. Physics of Debye-Waller Factors. *arXiv:cond-mat/0405023 [cond-mat.mes-hall]* **2004**.
421. Maradudin, A. A.; Flinn, P. A. Anharmonic Contributions to the Debye-Waller Factor. *Phys. Rev.* **1963**, *129*, 2529-2547.
422. Cremons, D. R.; Flannigan, D. J. Direct In Situ Thermometry: Variations in Reciprocal-lattice Vectors and Challenges with the Debye-Waller Effect. *Ultramicroscopy* **2016**, *161*, 10-16.
423. Gao, J.; Li, B.; Tan, J.; Chow, P.; Lu, T. M.; Koratkar, N. Aging of Transition Metal Dichalcogenide Monolayers. *ACS Nano* **2016**, *10*, 2628-2635.
424. Metherell, A. J. F. Diffraction of Electrons by Perfect Crystals. In *Electron Microscopy in Materials Science*, Valdré, U.; Ruedl, E., Eds. Commission of the European Communities: Luxembourg, 1975; Vol. 2, pp 401-552.
425. Yoo, Y.; Degregorio, Z. P.; Johns, J. E. Seed Crystal Homogeneity Controls Lateral and Vertical Hetereoepitaxy of Monolayer MoS_2 and WS_2. *J. Am. Chem. Soc.* **2015**, *137*, 14281-14287.
426. Schaibley, J. In *Control of Interlayer Valley Excitons in Atomically-thin $MoSe_2$-WSe_2 Heterostructures*, Proc. SPIE: Ultrafast Phenomena and Nanophotonics XXI, San Francisco, CA, Betz, M.; Elezzabi, A. Y., Eds. San Francisco, CA, 2017.
427. Fang, H.; Battaglia, C.; Carraro, C.; Nemsak, S.; Ozdol, B.; Kang, J. S.; Bechtel, H. A.; Desai, S. B.; Kronast, F.; Unal, A. A.; Conti, G.; Conlon, C.; Palsson, G. K.; Martin, M., C.; Minor, A. M.; Fadley, C. S.; Yablonovitch, E.; Maboudian, R.; Javey, A. Strong Interlayer Coupling in van der Waals Heterostructures Built from Single-layer Chalcogenides. *Proc. Natl. Acad. Sci. U. S. A.* **2014**, *111*, 6198-6202.
428. Thilagam, A. Exciton Complexes in Low Dimensional Transition Metal Dichalcogenides. *J. Appl. Phys.* **2014**, *116*, 053523.
429. Yu, Y.; Yu, Y.; Cai, Y.; Li, W.; Gurarslan, A.; Peelaers, H.; Aspnes, D. E.; Walle, C. G. V. d.; Nguyen, N. V.; Zhang, Y.-W.; Cao, L. Exciton-dominated Dieletric Function of Atomically Thin MoS_2 Films. *Sci. Rep.* **2015**, *5*, 16996.
430. Paschotta, R., Beam Radius. In *Encyclopedia of Laser Physics and Technology*, 2012.
431. Bower, A. F., Constitutive Models - Relations between Stress and Strain. In

Applied Mechanics of Solids, CRC Press: Boca Raton, FL, 2012.

432. Tilley, R. J. D. *Crystals and Crystal Structures*. John Wiley & Sons, Inc.: Hoboken, NJ, 2007.
433. Rupp, B. Atomic Scattering Factors. http://www.ruppweb.org/cgi-bin/webscat_linux?E1=Mo&B=5.0&Occupation_factor=1.0&B1=Submit (accessed May 1).
434. Rupp, B. Atomic Scattering Factor. http://www.ruppweb.org/cgi-bin/webscat_linux?E1=S&B=5.0&Occupation_factor=1.0&B1=Submit (accessed May 1).

Appendix A | List of Publications and Presentations

A.1 | Publications

McKenna, A. J.; Eliason, J. K.; Flannigan, D. J. Spatiotemporal Evolution of Coherent Elastic Strain Waves in a Single MoS_2 Flake. *Nano Lett*., 10.1021/acs.nanolett.7b01565 (in press).

McKenna, A. J.; Eliason, J. K.; Flannigan, D. J. Imaging Photoinduced Structural and Morphological Dynamics of a Single MoS_2 Flake with Ultrafast Electron Microscopy. *Microscopy and Microanalysis* **2016**, *22* (Suppl. 3), 1662-1663.

McKenna, A. J.; Flannigan, D. J. Seeing is Educating: The Case for Electron-Microscopy Videos in the Classroom. *Microscopy Today* **2016**, *24*, 46-47.

Plemmons, D. A.; **McKenna, A. J.**; Flannigan, D. J. Effects of Quantized Chromatic Aberrations in Ultrafast Electron Microscopy. *Microscopy and Microanalysis* **2015**, *21* (Suppl. 3), 805-806.

A.2 | Oral Presentations

Presenter name is underlined.

Flannigan, D. J.; Cremons, D. R.; **McKenna, A. J.**; Plemmons, D. A.; Valley, D. T. "Coherent Photoexcited Structural Dynamics in Nanostructured and Nanoscale Materials." Electron Microscopy with High Temporal Resolution, Strasbourg, France, May 29-31, 2017.

McKenna, A. J., *et al.* Group H – What Questions Should Be Asked and Measurements Monitored in Order for Institutions to Analyze Safety Climate and Safety Culture. *Safety By Design: Improving Safety in Research Laboratories*, National Institutes of Health, Bethesda, Maryland, April 10-12, 2016.

A.3 | Poster Presentations

Presenter name is underlined.

McKenna, A. J.; Eliason, J. K.; Flannigan, D. J. "Photoexcited Structural Evolution of Few-Layer MoS_2 – From Coherent Acoustic Phonons to Large-Scale Mechanical Oscillations." Materials Research Society, Boston, MA, November 27-December 2, 2016.

McKenna, A. J.; Eliason, J. K.; Flannigan, D. J. "Imaging Photoinduced Structural and Morphological Dynamics of a Single MoS_2 Flake with Ultrafast Electron Microscopy" Microscopy and Microanalysis Meeting, Columbus, OH, July 24-28, 2016.

Plemmons, D. A.; **McKenna, A. J.**; Flannigan, D. J. "Effects of Quantized Chromatic Aberrations in Ultrafast Electron Microscopy" Microscopy and Microanalysis Meeting, Portland, OR, August 2-6, 2015. (poster)

Appendix B | Copyright Permissions

Figure 1.2 adapted by permission from Macmillan Publishers Ltd: *Nature Nanotechnology*, Ref [31]), © 2012.

Figure 1.3 reprinted with permission from Kuc, A.; Zibouche, N.; Heine, T. *Phys. Rev. B* **2011**, *83*, 245213. © 2011 by the American Physical Society.

Figure 1.4 reprinted with permission from Cheiwchanchamnangij, T.; Lambrecht, W. R. L. *Phys. Rev. B* **2012**, *85*, 205302. © 2012 by the American Physical Society.

Figure 1.5 adapted with permission from Ref [83] © American Physical Society.

Figure 1.6 adapted with permission from Ref [166]© American Physical Society

Figure 1.7 reprinted from *Surf. Sci. Rep.*, *70*, A. Molina-Sánchez, K. Hummer, and L. Wirtz, Vibrational and Optical Properties of MoS_2: From Monolayer to Bulk, 554-586, © 2015, with permission from Elsevier.

Figure 1.8 reprinted by permission from Macmillan Publishers Ltd: *Nature Materials*, Ref [79], © 2008.

Figure 2.5 is courtesy of Daniel Cremons.

Figure 2.6 is courtesy of Daniel Cremons.

Passages of and several figures in Chapters 3 – 5 were reprinted or adapted with permission from McKenna, A. J.; Eliason, J. K.; Flannigan, D. J. Spatiotemporal Evolution of Coherent Elastic Strain Waves in a Single MoS_2 Flake. *Nano Lett.*, 10.1021/acs.nanolett.7b01565 (in press). © 2017, American Chemical Society.

Appendix C | Common Acronyms

BBO	Beta barium borate
BF	Bright-field
CCD	Charge-coupled device
CDW	Charge density wave
CCDW	Commensurate CDW
CVD	Chemical vapor deposition
DP	Diffraction pattern
DF	Dark-field
DTEM	Dynamic transmission electron microscopy or microscope
EELS	Electron energy-loss spectroscopy or spectrometer
FFT	Fast Fourier transform
fs	Femtosecond
FWHM	Full-width at half-maximum
GHz	Gigahertz (10^9 s^{-1})
GPa	Gigapascal (10^9 Pa)
ICCDW	Incommensurate CDW
kHz	Kilohertz
km	Kilometer
LA	Longitudinal acoustic
LBO	Lithium triborate
LED	Light-emitting diode
MEMS	Micro-electromechanical system
MHz	Megahertz (10^6 s^{-1})
mJ	milliJoule
mrad	milliradian
ms	millisecond
NCCDW	Nearly commensurate CDW
NEMS	Nano-electromechanical system
μm	Micrometer or micron (10^{-6} m)
μs	Microsecond (10^{-6} s)
nm	Nanometer (10^{-9} m)
ns	Nanosecond (10^{-9} s)
PINEM	Photon-induced near-field electron microscopy
ps	Picosecond (10^{-12} s)
s	Second
SAD	Selected area diffraction
SCOP	Strongly-coupled optical phonon
SUEM	Scanning ultrafast electron microscope or microscopy
TEM	Transmission electron microscope or microscopy
THz	Terahertz (10^{12} s^{-1})
TMD	Transition metal dichalcogenide

TPa	Terapascal (10^{12} Pa)
UED	Ultrafast electron diffraction
UEM	Ultrafast electron microscope or microscopy
UV	Ultraviolet

Appendix D | Pump Beam Radius and Pump Fluence

The FWHM of the 515-nm pump beam was measured to be 124 μm using a knife-edge experiment on a beam profiler just outside the pump periscope on the UEM. The beam radius (w), the half of the width when the intensity has decayed to $1/e^2$ of its initial value is thus related to the FWHM by[430]

$$0.5 = e^{\frac{2\left(\frac{FWHM}{2}\right)^2}{w^2}} \tag{D.1}$$

Here, w = 105 μm, which can be used to calculate the average fluence (energy per area) given the average power for each experiment and that the repetition rate for every experiment was 10 kHz:

Figures	Average power (mW)
Figure 3.1 through Figure 3.5	2.7
Figure 3.6	2.76
Figure 3.7, Figure 3.9, Figure 3.10	2.68
Figure 3.8	2.75
Figure 3.11 through Figure 3.13	2.5
Chapter 4, all figures	2.37
Figure 5.1 through Figure 5.4	2.64
Figure 5.5 through Figure 5.7	2.71

Appendix E | Mechanical Property Calculations

For a transversely isotropic solid, the linear elastic stress-strain relationship is given by

$$\begin{bmatrix}\sigma_{11}\\ \sigma_{22}\\ \sigma_{33}\\ \sigma_{23}\\ \sigma_{13}\\ \sigma_{12}\end{bmatrix} = \begin{bmatrix} c_{11} & c_{12} & c_{13} & 0 & 0 & 0 \\ c_{12} & c_{11} & c_{13} & 0 & 0 & 0 \\ c_{13} & c_{13} & c_{33} & 0 & 0 & 0 \\ 0 & 0 & 0 & c_{44} & 0 & 0 \\ 0 & 0 & 0 & 0 & c_{44} & 0 \\ 0 & 0 & 0 & 0 & 0 & \frac{1}{2}(c_{11}-c_{12}) \end{bmatrix} \begin{bmatrix}\epsilon_{11}\\ \epsilon_{22}\\ \epsilon_{33}\\ \epsilon_{23}\\ \epsilon_{13}\\ \epsilon_{12}\end{bmatrix} \tag{E.1}$$

where σ is the engineering stress, ε is the engineering strain, and c_{nn} are the stiffness constants for MoS_2 from Feldman.[43] The elastic moduli E_n, Poisson ratios υ_n, and bulk moduli G_n are given by[431]

$$E_1 = E_2 = E_p \tag{E.2}$$

$$E_p = \frac{c_{11}^2 c_{33} + 2c_{13}^2 c_{12} - 2c_{11}c_{13}^2 - c_{33}c_{12}^2}{c_{11}c_{33} - c_{13}^2} \tag{E.3}$$

$$E_3 = E_t = \frac{c_{11}^2 c_{33} + 2c_{13}^2 c_{12} - 2c_{11}c_{13}^2 - c_{33}c_{12}^2}{c_{11}^2 - c_{12}^2} \tag{E.4}$$

$$\nu_{12} = \nu_{21} = \nu_p = \frac{c_{12}c_{33} - c_{13}^2}{c_{11}c_{33} - c_{13}^2} \tag{E.5}$$

$$\nu_{31} = \nu_{32} = \nu_{tp} = \frac{c_{13}c_{11} - c_{12}c_{13}}{c_{11}^2 - c_{12}^2} \tag{E.6}$$

$$\nu_{13} = \nu_{23} = \nu_{pt} = \frac{c_{11}c_{13} - c_{12}c_{13}}{c_{11}c_{33} - c_{13}^2} \tag{E.7}$$

$$G_{13} = G_{23} = c_{44} \tag{E.8}$$

$$G_{12} = \frac{1}{2}(c_{11} - c_{12}) \tag{E.9}$$

Appendix F | Rayleigh Wave Speed

The Rayleigh velocity equation for Rayleigh waves traveling in a semi-infinite slab without bounds in direction x_1 and x_3 and with the free surface at $x_2 = 0$ in a plane perpendicular to an inverse diad axis, derived in Royer and Dieulesaint,[401] is

$$f(\xi) \equiv \xi - \left(\frac{c_{22}}{c_{66}}\frac{c_{22}-\xi}{c_{11}-\xi}\right)^{\frac{1}{2}}(c-\xi) = 0 \tag{F.1}$$

where ξ is given by

$$\xi = \rho V^2 \tag{F.2}$$

where ρ is the density, and V is the phase velocity, c_{ij} is the stiffness tensor with respect to the system axes rather than the crystallographic axes and obtained from c_{kl}^R (the stiffness tensor with respect to the crystallographic axes) by transformations depending on the experiment geometry, and c is given by

$$c \equiv c_{11} - \frac{c_{12}^2}{c_{22}} > \xi \tag{F.3}$$

The equation can be rearranged in a more convenient form and the roots found:

$$c_{22}c_{66}\xi^2(c_{11}-\xi) = (c_{66}-\xi)[c_{22}(c_{11}-\xi) - c_{12}^2]^2 \tag{F.4}$$

There are three roots, but the only root that has physical meaning in that it gives decaying waves in the x_2 direction is ξ_R given by two conditions

$$0 < \xi_R = \rho V_R^2 < \xi_m \tag{F.5}$$

where ξ_m is the minimum of c_{66} or c, and ξ_R cannot have a value between c_{66} and c_{11}.

The next step is to determine the values of c_{ij} for the experiment. In this case, x_2 is

parallel to the crystallographic *Z* or [001] direction. For a hexagonal system,

$$\begin{aligned} c_{jj} &= c_{33}^{R} \\ c_{kk} &= c_{11}^{R} \\ c_{12} &= c_{13}^{R} \\ c_{66} &= c_{44}^{R} \end{aligned} \tag{F.6}$$

where $j \neq 3$, $k \neq 3$, and $k \neq j$. Using the stiffness matrix values given by Feldman,[43] the roots were found using MATLAB, and the only root satisfying the conditions given above yields a phase velocity of 1.9 km/s (nm/ps). The solving code is given in H.6.

Appendix G | Calculation of Atomic Scattering Factors, Extinction Distance, and Diffraction Contrast Variation

The structure factor $F_g(hkl)$ is given by

$$F_g(hkl) = \sum_{n=1}^{N} f_n \, e^{2\pi i(hx_n + khy_n + lz_n)} \tag{G.1}$$

where *N* indicates the total number of atoms in each unit cell, f_n is the atomic scattering factor for the n^{th} atom, *hkl* indicate the plane for which the structure factor is being computed, and x_n, y_n, and z_n indicate the position of the n^{th} atom in the unit cell. The atomic scattering factors can be referenced from experimentally measured plots if available but were computed here for Mo and S using the Cromer-Mann coefficients in the equation[432]

$$f_n^X = \sum_{i=1}^{4} a_i \, e^{-b_i\left(\frac{\sin(\theta)}{\lambda}\right)^2} + c \tag{G.2}$$

where the Cromer-Mann coefficients for Mo and S are

Element	**Mo**[433]	**S**[434]
Z	42	16
a_1, a_2, a_3, a_4	3.703, 17.236, 12.8888, 3.743	6.905, 5.203, 1.438, 1.586
b_1, b_2, b_3, b_4	0.277, 1.096, 11.004, 61.658	1.468, 22.215, 0.254, 56.172
c	4.387	0.867

where the scattering curves were fitted to the Cromer-Mann equation to extract the parameters, θ is the scattering semi-angle, and λ is the wavelength of the incident radiation in Å. The Cromer-Mann coefficients describe X-ray scattering from atoms, and the atomic scattering factors for electrons scattering from atoms can be calculated from

the atomic scattering factors for X-rays using the Mott formula:

$$f_n^e = \frac{1 + \frac{E_0}{m_0 c^2}}{8\pi a_0^2}\left(\frac{\sin(\theta)}{\lambda}\right)^2 (Z - f_n^X) \tag{G.3}$$

where E_0 is the beam energy in keV, m_0 is the electron rest mass, c is the speed of light, Z is the atomic number of the atom, and a_0 is the Bohr radius given by

$$a_0 = \frac{h^2 \varepsilon_0}{\pi m_0 e^2} \tag{G.4}$$

where h is Planck's constant and ε_0 is the vacuum (electrical) permittivity.[403] For the (100) scattering in MoS_2, these quantities were computed using the MATLAB code in Appendix H.7. The structure factor was then calculated using the following atomic positions for Mo: ±(1/3,2/3,1/4) and for S: ±(2/3,1/3,*z*) and ±(2/3,1/3,1/2-*z*), where *z* is an internal parameter describing how the unit cell is defined.[174]

The extinction distance is defined as

$$\xi = \frac{\pi V}{\lambda F_g(hkl)} \tag{G.5}$$

where V is the volume of the hexagonal unit cell computed using:[432]

$$V = \frac{\sqrt{3}}{2} ac \tag{G.6}$$

where a and c are the unit cell parameters. For 200 kV electron beam, λ = 0.0251 Å. Using these values, the extinction distance was calculated to be 25 nm.

Using these values, the fraction of intensity in a bend contour can be simulated from the equation

$$I_g = \left(\frac{\pi}{\xi}\right)^2 \frac{\sin^2(\pi s_{eff} t)}{\left(\pi s_{eff}\right)^2} \tag{G.7}$$

where t is thickness and s_{eff} is given by

$$s_{eff} = \sqrt{s^2 + \frac{1}{\xi^2}} \tag{G.8}$$

where s is the excitation error. This equation assumes that only one diffraction beam and the direct beam are strongly excited and that the intensity is affected by the dynamics of the electrons in a column of material with a radius of several nm.[406] The excitation error was approximated as only its component parallel to the direct electron beam direction, and the tilt angles were assumed to be small (-225 to 225 mrad) so that the small angle approximation for computation of the sine function could be made. The MATLAB code used to compute the intensity of a bend contour vs. s is given in Appendix H.8.

Appendix H | MATLAB Code

H.1 | Code to Sum Counts in Images

```
[path, files, nimages, bn, tifbool] = dataGetter();
imagenames =
['stepsize1_10.dm3';'stepsize1_15.dm3';'stepsize1_18.dm3';'stepsize1_20.
dm3'];
nimages = 4;

for i = 1:nimages
% [image_struct] = DM3Import(strcat(path,'photoelectron beam
drift2.',num2str(i),'.dm3'));
% [image_struct] = DM3Import(strcat(path,'stepsize',num2str(i),'.dm3'));
[image_struct] = DM3Import(strcat(path,imagenames(i,:)));
DP = image_struct.image_data .* image_struct.intensity.scale;
DP=imrotate(DP,-90);
a=fliplr(DP);
sumI(i) = sum(a(:));
end

plot(sumI)
% newsumI = sumI(:)-sumIavg;

save(strcat(path,'sum of images.mat'),'sumI')
```

H.2 | dataGetter.m

```
function [path, files, nimages, bn, tifbool] = dataGetter()
% written by Ryan Gnabasik
tifbool = false;
path = strcat(uigetdir,'\'); %opens a dialog box to get the directory
where the files are stored
% files = dir(strcat(path,'\*.tiff'));
files = dir(strcat(path,'\*.dm3'));
if isempty(files)
    files = dir(strcat(path,'\*.tif'));
    disp('Tif files are being used')
    tifbool = true;
end
nimages = numel(files); %number of images
bn = strtok(files(1).name,'0'); %base name for the image files to be
read in assuming that the files have been bulk renamed to start at 0

end
```

H.3 | Code to Analyze 10 ns Step Image Sequence (Chapter 5)

```
clear lowindex highindex ans f fittedparams Gausswidthguess j i imin
imax ymin ymax

data = box2; %data to analyze
numCurves = size(data,2); %number of curves
pixlenline = size(data,1); %number of pixels in each curve
convfact = 0.66527023; %pixels per nm
xinpix = [1:pixlenline]'; %x in pixels
T = 10^-9; %timestep size in s

smoothdata = zeros(pixlenline,numCurves);

% Smooth data using a Savitzky-Golay filter.  This filter fits
successive
% sub-sets (which MATLAB calls frames) of the data to a low-degree
% polynomial using linear least squares.  Here I have specified a third
% degree polynomial with a frame size of 25 data values.
for i = 1:numCurves
    smoothdata(:,i) = sgolayfilt(data(:,i),3,25);
end

options = optimset('Display','off');
fittedparamsbox4 = zeros(numCurves,6);
rsbox4 = zeros(numCurves,1);
centersbox4 = zeros(numCurves,1);

for i = 1:numCurves

    clear peaks locs locs2 widths prominences ymax imax ymin imin
highindices lowindices indices

    i

    % Find the peaks and minima
[peaks,locs,widths,prominences]=findpeaks(smoothdata(:,i),'MinPeakDistan
ce',40,'WidthReference','halfheight','SortStr','ascend');

    [ymax,imax,ymin,imin] = extrema(smoothdata(:,i));

    figure(1);plot(smoothdata(:,i));
    hold on
    plot(locs,peaks,'or')
    plot(imin,ymin,'r*');
    hold off

    numPeaks = size(peaks,1);
```

```
    % If there are 3 peaks,
    if numPeaks == 3
        locs2 = locs;  % save the locs as a second variable
        % Find max and min peak locations and save their positions
        lowerpkind = find(locs==min(locs));
        lowerpkpos = locs(lowerpkind);
        highpkind = find(locs==max(locs));
        highpkpos = locs(highpkind);

        % Now find the middle peak (our band) location and save position
as
        bandpkind = find(locs>min(locs) & locs<max(locs));
        locs(1) = locs(bandpkind);
        widths(1) = widths(bandpkind);

        % Now find the lowest/highest minima surrounding the middle peak
        % and save as lowindex and highindex, which define our fitting
        % window.
        lowindices = find(imin<locs(1) & imin>lowerpkpos & imin<locs(1)-
10);
        lowmin = imin(lowindices);
        lowymins = ymin(lowindices);
        sortedlowymins = sort(lowymins);
        lowminind = find(lowymins==sortedlowymins(1));
        lowindex = lowmin(lowminind);
        highindices = find(imin>locs(1) & imin>locs(1)+10 &
imin<highpkpos);
        highmin = imin(highindices);
        highymins = ymin(highindices);
        sortedhighymins = sort(highymins);
        highminind = find(highymins==sortedhighymins(1));
        highindex = highmin(highminind);
    end

    % If there are not 3 peaks, define the lower or higher peak position
by
    % any values in locs that are not equal to the band peak, which we
    % assume is the middle/lowest peak.
    if numPeaks~=3
        lowerpkpos = max(locs(locs<locs(1)));
        highpkpos = min(locs(locs>locs(1)));

        % If no peak before band peak,
        if isempty(lowerpkpos)==1
            % the lower limit of fitting window (lowindex) should be max
of minima
            % less than the center position guessed of the band peak.
            indices = find(imin<locs(1) & imin<locs(1)-10);
            lowmin = imin(indices);
            lowymins = ymin(indices);
            sortedlowymins = sort(lowymins);
```

```
            lowminind = find(lowymins==sortedlowymins(1));
            lowindex = lowmin(lowminind);
%             clear indices

            % if there is also no peak above the band peak,
            if isempty(highpkpos)==1
                highindices = find(imin>locs(1) & imin>locs(1)+10);
                highmin = imin(highindices);
                highymins = ymin(highindices);
                sortedhighymins = sort(highymins);
                highminind = find(highymins==sortedhighymins(1));
                highindex = highmin(highminind);
            end

            %If there is a peak above the band peak,
            if isempty(highpkpos)==0
                highindices = find(imin>locs(1) & imin>locs(1)+10 &
imin<highpkpos);
                highmin = imin(highindices);
                highymins = ymin(highindices);
                sortedhighymins = sort(highymins);
                highminind = find(highymins==sortedhighymins(1));
                highindex = highmin(highminind);
            end
        end

        %If there is a peak before the band peak,
        if isempty(lowerpkpos)==0
            indices = find(imin<locs(1) & imin>lowerpkpos &
imin<locs(1)-10);
            lowmin = imin(indices);
            lowymins = ymin(indices);
            sortedlowymins = sort(lowymins);
            lowminind = find(lowymins==sortedlowymins(1));
            lowindex = lowmin(lowminind);

            % if there is also no peak above the band peak,
            if isempty(highpkpos)==1
                highindices = find(imin>locs(1) & imin>locs(1)+10);
                highmin = imin(highindices);
                highymins = ymin(highindices);
                sortedhighymins = sort(highymins);
                highminind = find(highymins==sortedhighymins(1));
                highindex = highmin(highminind);
            end

            %If there is a peak above the band peak,
            if isempty(highpkpos)==0
                highindices = find(imin>locs(1) & imin>locs(1)+10 &
imin<highpkpos);
                highmin = imin(highindices);
```

```
                highymins = ymin(highindices);
                sortedhighymins = sort(highymins);
                highminind = find(highymins==sortedhighymins(1));
                highindex = highmin(highminind);
            end
        end
    end

    if highindex>length(x)
        highindex = length(x);
    end

    if lowindex < 1
        lowindex = 1;
    end

    centerguess = locs(1);
    widthguess = widths(1);
    x0 = [peaks(1)/2 peaks(1)/2  centerguess widthguess widthguess
10^4];
    xupperbound = [peaks(1) peaks(1) highindex 2*widths(1) 2*widths(1)
10^5];
    xlowerbound = [0 0 lowindex 0.0001 0.0001 0];
    ydata = smoothdata(lowindex:highindex,i);
    xdata = xinpix(lowindex:highindex);


    [peakparams] =
lsqcurvefit(@PseudoVoigt,x0,xdata,ydata,xlowerbound,xupperbound,options)
;
    f = PseudoVoigt(peakparams,xdata);
    fittedparamsbox4(i,:) = peakparams;
    ymean=mean(mean(ydata));
    ssres = sum((ydata-f).^2);
    sstot=sum((ydata-ymean).^2);
    rsbox4(i) = 1-(ssres/sstot);
    figure(2);plot(xdata,ydata,xdata,f);

    centersbox4(i) = x(round(peakparams(3))).*1000; % factor puts the
center positions in terms of nm instead of um

end


% make a time vector in s
timens = [-100:10:13840]';
time = timens.*10^-9;

% find the initial position of the peak
initialpos = mean(centersbox2(1:11));
```

```
% compute displacement from that initial position
dispfrominitial = centersbox4(:)-initialpos;
% plot the results
figure;plot(timens,dispfrominitial);
ylabel('center peak position (nm)');
xlabel('time (ns)');

% Now compute the Fourier transform of the signal to get an idea of the
% major frequencies

T = 10*10^-9;
Fs = 1/T;  % sampling frequency
m = length(dispfrominitial);
padArray = ones(2^14-m,1).*mean(dispfrominitial(m-50:50,1));
paddeddata = cat(1,dispfrominitial,padArray);
L = size(paddeddata,1); % length of signal
m = length(paddeddata);          % Window length
n = 2^14;   % Transform length
y = fft(dispfrominitial,n);           % DFT
power = y.*conj(y)/n;   % Power of the DFT
phase = angle(y);
allfreqinHz = [0:1:n-1].*(Fs/n);
middlefreq = ceil(n/2);
onesidedpower = power(1:middlefreq);
f0 = allfreqinHz(1:middlefreq);
phase0 = phase(1:middlefreq);

% plot the FT:
figure(1); plot(f0,onesidedpower)
title('Single-Sided Power Spectrum of X(t)')
xlabel('f (Hz)')
ylabel('|P1(f)|')
```

H.4 | Pseudo-Voigt Function

```
function f=PseudoVoigt(x,xdata)

    L0=x(1); G0=x(2); x0=x(3); Gw=x(4); Lw=x(5); f0=x(6);

    L=L0*(0.5*Lw./((xdata-x0).^2+(0.5*Lw)^2));
    G=G0*exp(-((xdata-x0).^2)./(2*Gw^2));

    f=L+G+f0;

end
```

H.5 | Fit of Fourier-filtered Relative Position

```
clear all
```

```
%% First frequency
t = time; %time vector
F1 = FREQ1; %first Fourier-filtered displacement

LB = [0 1e3 -10 -pi 4*10^6]; %lower bound for fit variable in weird
alphabetical order - uppercase first [A B D c w] according to fit
function below

UB = [20 6*10^6 10 pi 6*10^6]; %upper bound for fit variable in weird
alphabetical order - uppercase first [A B D c w]

ST = [15 5*10^4 0 0 5*10^6]; %starting value for fit variable in weird
alphabetical order - uppercase first [A B D c w]
%good starting values are needed for the fit to converge

OPTIONS = fitoptions('Method','NonlinearLeastSquares',...
    'Lower',LB,...
    'Upper',UB,...
    'Startpoint',ST,...
    'Display','iter');  %these specify type of fitting scheme and bounds
and starting values for all fit variables

TYPE=fittype('A*exp(-B*x).*cos(2*pi*w*x+c)+D;','options',OPTIONS);
%here you enter your custom fit function - always use 'x' as the
dependent variable

[c.gs,gof] = fit(t,F1,TYPE)  %fit data - don't use ';' if you want to
see iterations and final fit values

fitteddata = c.gs.A*exp(-c.gs.B*t).*cos(2*pi*c.gs.w*t+c.gs.c)+c.gs.D;
%reconstruct fitted data


figure(10);plot(t,F1,'r','MarkerSize',5)      %plot model funciton
hold on
plot(t,fitteddata,'b','LineWidth',1)  %plot fitted function
hold off

%% Second frequency
F1 = FREQ2; %second Fourier-filtered position
t = time; %time vector


LB = [5 1e3 -10 -pi 1e7]; %lower bound for fit variable in weird
alphabetical order - uppercase first [A B D c w] according to fit
function below
```

```
UB = [20 1e6 10 pi 1.5e7]; %upper bound for fit variable in weird
alphabetical order - uppercase first [A B D c w]

ST = [15 5*10^4 0 0 1.2e7]; %starting value for fit variable in weird
alphabetical order - uppercase first [A B D c w]
%good starting values are needed for the fit to converge

OPTIONS = fitoptions('Method','NonlinearLeastSquares',...
    'Lower',LB,...
    'Upper',UB,...
    'Startpoint',ST,...
    'Display','iter');  %these specifies type of fitting scheme and
bounds and starting values for all fit variables


TYPE=fittype('A*exp(-B*x).*cos(2*pi*w*x+c)+D;','options',OPTIONS);
%here you enter your custom fit function - always use 'x' as the
dependent variable

[c.gs,gof] = fit(t,F1,TYPE)  %fit data - don't use ';' if you want to
see iterations and final fit values

fitteddata = c.gs.A*exp(-c.gs.B*t).*cos(2*pi*c.gs.w*t+c.gs.c)+c.gs.D;
%reconstruct fitted data


figure(11);plot(t,F1,'r','MarkerSize',5)      %plot model function
hold on
plot(t,fitteddata,'b','LineWidth',1)  %plot fitted function
hold off

%% Third frequency
F1 = FREQ3; %third Fourier-filtered relative position with same time
vector as above

LB = [5 1e3 -10 -pi 1.5e7]; %lower bounds
UB = [25 1e6 10 pi 1.9e7]; %upper bounds
%good starting values are needed for the fit to converge
ST = [20 5*10^3 0 0 1.75e7];


OPTIONS = fitoptions('Method','NonlinearLeastSquares',...
    'Lower',LB,...
    'Upper',UB,...
    'Startpoint',ST,...
    'Display','iter');  %these specifies type of fitting scheme and
bounds and starting values for all fit variables
```

```
TYPE=fittype('A*exp(-B*x).*cos(2*pi*w*x+c)+D;','options',OPTIONS);
%here you enter your custom fit function - always use 'x' as the
dependent variable

[c.gs,gof] = fit(t,F1,TYPE)  %fit data - don't use ';' if you want to
see iterations and final fit values

fitteddata = c.gs.A*exp(-c.gs.B*t).*cos(2*pi*c.gs.w*t+c.gs.c)+c.gs.D;
%reconstruct fitted data


figure(12);plot(t,F1,'r','MarkerSize',5)      %plot model function
hold on
plot(t,fitteddata,'b','LineWidth',1)  %plot fitted function
hold off
```

H.6 | Code Solving for Rayleigh Speed in MoS_2

```
% This function finds the roots of the Rayleigh wave equation given in
% Royer, D.; Dieulesant, E.  J. Acoust. Soc. Am. 1984, 76, 1438-1444,
for
% hexagonal MoS2 where the Rayleigh waves propagate in the basal plane
and
% decay along the [001] zone axis.
%%

clear all
clc

rho = 5000; %density of MoS2 in kg m^-3
f = 10^9;  %factor to convert GPa stiffness matrix values to Pa
c11R = 238*f;  %original values in GPa
c12R = -54*f;
c13R = 23*f;
c33R = 52*f;
c44R = 19*f;
c55R = c44R*f;
c66R = 0.5*(c11R-c12R);

c22 = c33R;  %stiffness matrix values for experiment
c11 = c11R;
c12 = c13R;
c66 = c44R;

% ksi values:
syms xi

% Find the coefficients of the Rayleigh wave equation when set equal to
```

```
% zero
cy = coeffs(c22*c66*(xi^2)*(c11-xi)-(c66-xi)*((c22*(c11-xi)-
c12^2)^2),xi);

% Find the roots of the equation, where the coefficients have to be in
% descending order
solxi = roots(fliplr(cy));

% Convert the symbolic roots into numbers
numsol = double(solxi);

% Find the phase velocities
phasev = sqrt(numsol./rho);
```

H.7 | Atomic Scattering Factors

```
clear all
clc

% % Cromer-Mann coefficients for Mo:
% a = [3.703 17.236 12.888 3.743];
% b = [0.277 1.096 11.004 61.658];
% c = 4.387;
% %atomic number:
% Z = 42;

% Cromer-Mann coefficients for S:
a = [6.905 5.203 1.438 1.586];
b = [1.468 22.215 0.254 56.172];
c = 0.867;
% atomic number
Z = 16;

% % Cromer-Mann coefficients for Au
% a = [16.882 18.591 25.558 5.860];
% b = [0.461 8.622 1.483 36.396];
% c = 12.066;
% %atomic number
% Z = 79;

for i = 1:4

    infac(i) = a(i)*exp(-b(i)*((4.57*10^-3)/(0.0251))^2); % for (100)
scattering
% infac(i) = a(i)*exp(-b(i)*0.212^2);  % for Au (111) plane


end
```

```
fx = sum(infac)+ c;

m0 = 9.109*10^-31; % electron rest mass in kg
h = 6.626*10^-34; % Planck's constant in J*s
ec = 1.602*10^-19; % in C
e0 = 8.854*10^-12; % in F/m
E0 = 100*10^3*1.602*10^-19; % in J
c = 3*10^8;
hbar = h/(2*pi);
% lambda = h/sqrt(2*m0*E0*(1+E0/(2*m0*c^2)));
lambda = 0.00251*10^-9*10^10;
m = m0*(1+100/511);

a0 = (h^2*e0)/(pi*m0*ec^2)*10^10;

fe = (1+E0/(m0*c^2))/(8*pi^2*a0)*(Z-fx)/(0.212^2)
```

H.8 | Bend Contour

```
% Bend contour

clear all
clc
close all

g = (4*pi)/(sqrt(3)*0.31602); % in nm^-1
t = 50; % thickness in nm
xig = 25.3; % extinction distance in nm^-1

% use the small-angle approximation
s = [-225:1:225].*g*pi/180*10^-3;
npts = length(s);

for i = 1:npts

    seff(i) = sqrt(s(i)^2+xig^(-2));

    Ig(i) = (pi/xig)^2*(sin(pi*seff(i)*t)/(pi*seff(i)))^2;

end

figure;plot(s,Ig);title('s vs. Ig')
```

H.9 | Diffraction Contrast

```
clear all
```

```
clc

eg = [0 25.3*10^-7]; %extinction distances corresponding to the
reciprocal lattice points included in cm
s0 = [0 1.5/eg(2)]; %excitation error in inverse nm
Psyattop = zeros(length(eg),1);
Psyattop(1) = 1; % Boundary condition
h = 0.25*eg(2); %thickness in nm
w = 1.5;
g = [1 0 0];
gR = [1 0.3];%dot product of g and R
ec = 1.602*10^-19; %elementary charge
lambda = 0.00251*10^-7; %wavelength in cm
elemC = 1.602*10^-19; % elementary charge
m0 = 9.109*10^-31; %in kg
E0 = m0*(3*10^8)^2;
% V0 = 1.602*10^-19*C(1,2);
hcon = 6.626*10^-34; %Plank's constant in J*s
BE = 200*10^3*elemC; %beam energy in J
K = (1/100)*(1/hcon)*sqrt(2*m0*BE*(1+BE/(2*511*10^3*elemC)));
thetaB = 4.57*10^-3;
% A = diag(s);

x = [-100:1:100].*10^-7;

strain = 10;
a = 0.03*10^-7;
c = 1.2*10^-7;
kx = 1/(5*10^-7);
beta = 1/(100*10^-7);

% This section needs to be re-worked for the particular defect/strain
% you're modeling.  I never got this working properly.
% Rc = zeros(3,size(x,2));
%
% for i = size(Rc,2)
% Rc(1,:) = strain*a.*cos(kx.*x);
% end
% figure;plot(x,Rc(1,:))
%
% changeinRc = zeros(3,length(x));
% changeinRc(1,:) = strain*a.*(kx.*sin(-kx.*x));
% figure;plot(x,changeinRc(1,:))

for i = 1:length(x)
    % The change for including deformation:
%         for k = 1:(length(s0)-1)
%     sR(i,k+1) = s0(k+1) + thetaB*dot(g,changeinRc(:,i));
%     end
%         A(:,:,i) = diag(sR(i,:));
```

```
        A(:,:,i) = diag(s0);
    for m = 1:length(eg)
        for l = 1:length(eg)
            if m==l

            else
                Ugh = 1/(lambda*eg((abs(m-l)+1)));
                % Assuming a centrosymmetric crystal:
                A(m,l,i) = Ugh/(2*K);
            end
        end
    end
    [C1,gamma1]=eig(A(:,:,i));
    C(:,:,i) = C1;
    gamma(:,:,i) = gamma1;
    invC(:,:,i) = inv(C1);
end
% figure;plot(x,changeinRc)

%%

eigexp = zeros(size(gamma,2),size(gamma,2),length(x));

for i = 1:length(x)
for j = 1:size(gamma,2)
    eigexp(j,j,i) = exp(2*pi*1i*gamma(j,j,i)*h);
end
end

Psy = zeros(size(gamma,2),size(x,2),length(x));

for j = 1:size(x,2)
Psy(:,j) = C(:,:,j)*eigexp(:,:,j)*inv(C(:,:,j))*Psyattop;

Inew0(j) = Psy(1,j)*conj(Psy(1,j));
Inewg(j) = Psy(2,j)*conj(Psy(2,j));
end

figure;plot(x,Inew0)
figure;plot(x,Inewg)
```